AFRL-RY-HS-TR-2008-0026 Volume II

PROCEEDINGS OF THE 2008 ANTENNA APPLICATIONS SYMPOSIUM
Volume II of II

Daniel Schaubert et al.

University of Massachusetts at Amherst
Electrical and Computer Engineering
100 Natural Resources Road
Amherst MA 01003

Final Report

20 December 2008

APPROVED FOR PUBLIC RELEASE; DISTRIBUTION UNLIMITED

AIR FORCE RESEARCH LABORATORY
Sensors Directorate
Electromagnetics Technology Division
80 Scott Drive
Hanscom AFB MA 01731-2909

NOTICE AND SIGNATURE PAGE

Using Government drawings, specifications, or other data included in this document for any purpose other than Government procurement does not in any way obligate the U.S. Government. The fact that the Government formulated or supplied the drawings, specifications, or other data does not license the holder or any other person or corporation; or convey any rights or permission to manufacture, use, or sell any patented invention that may relate to them.

This report was cleared for public release by the 66th Air Base Wing Public Affairs Office for the Air Force Research Laboratory Electromagnetic Technology Division and is available to the general public, including foreign nationals. Copies may be obtained from the Defense Technical Information Center (DTIC) (http://www.dtic.mil).

AFRL-RY-HS-TR-2009- 0026 HAS BEEN REVIEWED AND IS APPROVED FOR PUBLICATION IN ACCORDANCE WITH ASSIGNED DISTRIBUTION STATEMENT.

DAVID D. CURTIS
Chief, Antenna Technology Branch

MICHAEL N. ALEXANDER
Technical Advisor
Electromagnetic Technology Division

This report is published in the interest of scientific and technical information exchange, and its publication does not constitute the Government's approval or disapproval of its ideas or findings.

REPORT DOCUMENTATION PAGE

Form Approved
OMB No. 0704-0188

Public reporting burden for this collection of information is estimated to average 1 hour per response, including the time for reviewing instructions, searching existing data sources, gathering and maintaining the data needed, and completing and reviewing this collection of information. Send comments regarding this burden estimate or any other aspect of this collection of information, including suggestions for reducing this burden to Department of Defense, Washington Headquarters Services, Directorate for Information Operations and Reports (0704-0188), 1215 Jefferson Davis Highway, Suite 1204, Arlington, VA 22202-4302. Respondents should be aware that notwithstanding any other provision of law, no person shall be subject to any penalty for failing to comply with a collection of information if it does not display a currently valid OMB control number. **PLEASE DO NOT RETURN YOUR FORM TO THE ABOVE ADDRESS.**

1. REPORT DATE *(DD-MM-YYYY)*	**2. REPORT TYPE**	**3. DATES COVERED** *(From - To)*
20-12-2008	FINAL REPORT	16 Sep 2008 - 18 Sep 2008

4. TITLE AND SUBTITLE

Proceedings of the 2008 Antenna Applications Symposium, Volume II

5a. CONTRACT NUMBER
F33615-02-D-1283

5b. GRANT NUMBER

5c. PROGRAM ELEMENT NUMBER

6. AUTHOR(S)

Daniel Schaubert et al.

5d. PROJECT NUMBER

5e. TASK NUMBER

5f. WORK UNIT NUMBER

7. PERFORMING ORGANIZATION NAME(S) AND ADDRESS(ES)
University of Massachusetts Amherst
Electrical and Computer Engineering
100 Natural Resources Road
Amherst, MA 01003

8. PERFORMING ORGANIZATION REPORT

9. SPONSORING / MONITORING AGENCY NAME(S) AND ADDRESS(ES)
Electromagnetics Technology Division
Sensors Directorate
Air Force Research Laboratory
80 Scott Drive
Hanscom AFB MA 01731-2909

10. SPONSOR/MONITOR'S ACRONYM(S)
AFRL-RY-HS

11. SPONSOR/MONITOR'S REPORT NUMBER(S)
AFRL-RY-HS-TR-2008-0026

12. DISTRIBUTION / AVAILABILITY STATEMENT
APPROVED FOR PUBLIC RELEASE; DISTRIBUTION UNLIMITED

13. SUPPLEMENTARY NOTES
Volume I contains pages 1 – 269
Volume II contains pages 270 – 524
Public Affairs release Number 66ABW-2009-0055

14. ABSTRACT

The Proceedings of the 2007 Antenna Applications Symposium is a collection of state-of-the art papers relating to antenna arrays, millimeter wave antennas, simulation and measurement of antennas, integrated antennas, and antenna bandwidth and radiation improvements.

15. SUBJECT TERMS
Antennas, phased arrays, digital beamforming, millimeter waves, antenna measurements, airborne antenna applications, Vivaldi antennas, waveguide antenna arrays, broadband arrays, electrically small antennas

16. SECURITY CLASSIFICATION OF:			**17.LIMITATION OF ABSTRACT**	**18.NUMBER OF PAGES**	**19a. NAME OF RESPONSIBLE PERSON**
a. REPORT	**b. ABSTRACT**	**c. THIS PAGE**			**19b. TELEPHONE NUMBER** *(include area code)*
Unclassified	Unclassified	Unclassified	UU	265	David D. Curtis N/A

Standard Form 298 (Rev. 8-98)
Prescribed by ANSI Std. Z39.18

Table of Contents

2008 ANTENNA APPLICATIONS SYMPOSIUM (Volumes I and II)
16-18 September 2008, Monticello, Illinois

Advances in the Development of Electronically Scanned Arrays of Balanced Antipodal Vivaldi Antennas **1**
M.W. Elsallal, D.H. Schaubert, and J.B. West

Comparison of the Broadband Properties of Arrays Having Time-Delayed Four- and Eight-Element Polyomino Subarrays **17**
R.J. Mailloux, S.G. Santarelli, T.M. Roberts and D. Luu

Broadband Array Antenna **42**
M. Stasiowski and D. Schaubert

Stripline Fed Low Profile Radiating Elements for Use in Integrated Arrays **60**
M.J. Buckley, L.M. Paulsen, J.D. Wolf and J.B. West

Antenna Element Pattern Reconfigurability in Adaptive Arrays **86**
T.L. Roach and J.T. Bernhard

μ-Coaxial Phased Arrays for Ka-Band Communications **104**
D. Filipovic, G.Potvin, D. Fontaine, Y. Saito, J-M. Rollin, Z. Popovic, M. Lukic, K. Vanhille and C. Nichols

Phased Array for Multi-Direction Secure Communication **116**
M.P. Daly and J.T. Bernhard

A Wideband, Dual-Polarized, Differentially-Fed Cavity-Backed Slot Antenna **132**
R.C. Paryani, P.F. Wahid and N. Behdad

Miniaturized Microstrip Patch Antennas for Dual Band GPS Operation **143**
S.S. Holland and D.H. Schaubert

On the Use of Spiral Antennas for Electronic Attack **154**
M.J. Radway, W.N. Kefauver and D.S. Filipovic

A Class of Electrically Small Spherical Antennas with Near-Minimum Q **165**
J.J. Adams and J.T. Bernhard

Metamaterials and Their RF Properties **176**
J.S. Derov, E.E. Crisman and A.J. Drehman

Scan Impedance for an Infinite Dipole Array: Accurate Theory Model Versus Numerical Software **190**
S.N. Makarov, A. Puzella and V. Iyer

Novel Hybrid Tolerance Analysis Method with Application to the Low Cost Manufacture of Edge Slot Waveguide Arrays **222**
B.J. Herting, M.W. Elsallal, J.C. Mather and J.B. West

Design of Coplanar Waveguide Fed Tapered-Slot Antenna Arrays for High-Power Space Distributed Amplifier Applications **233**
A. Rivera-Albino and R.A. Rodriguez-Solis

Efficient Global Optimization for Antenna Design **250**
H.L. Southall, T.H. O'Donnell and B. Kaanta

Helicopter Mounted Radar Installed Characterisation Assessments: Theoretical Predictions and Measurements **270**
C. McCartney

The RF Cuttlefish: Overview of Biologically Inspired Concepts for Smart Skins and Reconfigurable Antennas **291**
G.H. Huff, S. Goldberger and S.A. Long

Investigation of the Null Steering Capability of Yagi-Uda Arrays with Variable Reactive Loads **306**
D.F. Kelley and T.J. Destan

Non-Foster Matching of Electrically-Small Antennas to Transmitters **326**
S.E. Sussman-Fort and R.M. Rudish.

Using Series Resonators in Parallel to Achieve Broadband Performance in Inductively Loaded Antennas **343**
P.E. Mayes, P.W. Klock and S. Barot

Design and Limitations of Ku/Ka Band Compact Feeds Employing Dielectric Loaded Corrugated Horns **363**
J.P. Creticos and D.H. Schaubert

A Tunable Dielectric Patch Antenna **388**
E.M.A. Oliveira, S.N. Makarov, C. Dill and R. Ludwig

Investigation of a Reconfigurable Stacked Patch with Beamsteering Capabilities **410**
J.E. Ruyle and J.T. Bernhard

A Structurally-Functionalizable Archimedean Spiral Aperchassis **426**
G.H. Huff

Evaluation of Human Body Interaction for the Enhancement of a Broadband Body-Borne Radio Geolocation System **436**
A. Lalezari, F. Lalezari, B. Jeong and D. Filipovic

Investigation of Ground Plane Slot Designs for Isolation of Cosited Microstrip Antennas **454**
K.C. Kerby and J.T. Bernhard

A New Radio Direction Finder for Wildlife Research II **463**
T.A. Borrowman, S.J. Franke and G.W. Swenson, Jr.

Pillbox Antenna with a Dipole Feed **472**
W.R. Pickles and M.G. Parent

The State-of-the-Art in Small Wideband Antennas **492**
S.R. Best

Identifiers for Proceedings of Symposia

The USAF Antenna Research and Development Program

Year	Symp. No.	Identifier
1951	First	_____
1952	Second	ADB870006
1953	Third	ADB283180
1954	Fourth	AD63139
1955	Fifth	AD90397
1956	Sixth	AD114702
1957	Seventh	AD138500
1958	Eighth	AD301151
1959	Ninth	AD314721
1960	Tenth	AD244388 (Vol. 1) AD319613 (Vol. 2)
1961	Eleventh	AD669109 (Vol. 1) AD326549 (Vol. 2)
1962	Twelfth	AD287185 (Vol. 1) AD334484 (Vol. 2)
1963	Thirteenth	AD421483
1964	Fourteenth	AD609104
1965	Fifteenth	AD474238L
1966	Sixteenth	AD800524L
1967	Seventeenth	AD822894L
1968	Eighteenth	AD846427L
1969	Nineteenth	AD860812L
1970	Twentieth	AD875973L
1971	Twenty-First	AD888641L
1972	Twenty-Second	AD904360L
1973	Twenty-Third	AD914238L

Antenna Applications Symposium

Year	Symposium	Technical Report #	Identifier
1977	First	None	ADA 955413
1978	Second	None	ADA 955416
1979	Third	_____	ADA 077167
1980	Fourth	_____	ADA 205907
1981	Fifth	_____	ADA 205816
1982	Sixth	_____	ADA 129356
1983	Seventh	_____	ADA 142003; 142754
1984	Eighth	85-14	ADA 153257; 153258
1985	Ninth	85-242	ADA 166754; 165535
1986	Tenth	87-10	ADA 181537; 181536
1987	Eleventh	88-160	ADA 206705; 206704
1988	Twelfth	89-121	ADA 213815; 211396
1989	Thirteenth	90-42	ADA 26022; 226021
1990	Fourteenth	91-156	ADA 37056; 237057
1991	Fifteenth	92-42	ADA 253681; 253682
1992	Sixteenth	93-119	ADA 268167; 266916
1993	Seventeenth	94-20	ADA 277202; 277203
1994	Eighteenth	95-47	ADA 293258; 293259
1995	Nineteenth	96-100	ADA 309715; 309723
1996	Twentieth	97-189	ADA 341737
1997	Twenty First	1998-143	ADA 355120
1998	Twenty Second	1999-86	ADA 364798
1999	Twenty Third	2000-008 (I) (II)	ADA 386476; 386477
2000	Twenty Fourth	2002-001 Vol I & II	ADA 405537; 405538
2001	Twenty Fifth	2002-002 Vol I & II	ADA 405328; 405327
2002	Twenty Sixth	2005-001 Vol I & II	ADA 427799; 427800
2003	Twenty Seventh	2005-005 Vol I & II	ADA 429122
2004	Twenty Eighth	2005-016 Vol I & II	ADA431338; 431339
2005	Twenty Ninth	2005-039 Vol I & II	ADM001873
2006	Thirtieth	2006-0047 Vol I & II	ADA464059
2007	Thirty First	2007-0037 Vol I & II	ADA475327, 475333

2008 Author Index

Adams, J.J. 165
Barot, S. 343
Behdad, N. 132
Bernhard, J.T. 86, 116, 165, 410, 454
Best, S.R. 492
Borrowman, T.A. 463
Buckley, M.J. 60
Creticos, J.P. 363
Crisman, E.E. 176
Daly, M.P. 116
Derov, J.S. 176
Destan, T.J. 306
Dill, C. 388
Drehman, A.J. 176
Elsallal, M.W. 1, 222
Filipovic, D. 104, 154, 436
Fontaine, D. 104
Franke, S.J. 463
Goldberger, S. 291
Herting, B.J. 222
Holland, S.S. 143
Huff, G.H. 291, 426
Iyer, V. 190
Jeong, B. 436
Kaanta, B. 250
Kefauver, W.N. 154
Kelley, D.F. 306
Kerby, K.C. 454
Klock, P.W. 343
Lalezari, A. 436
Lalezari, F. 436
Long, S.A. 291
Ludwig, R. 388
Lukic, M. 104
Luu D. 17
Mailloux, R.J. 17
Makarov, S.N. 190, 388
Mather, J.C. 222
Mayes, P.E. 343
McCartney, C. 270
Nichols, C. 104
O'Donnell, T.H. 250
Oliveira, E.M.A. 388
Parent, M.G. 472
Paryani, R.C. 132
Paulsen, L.M. 60
Pickles, W.R. 472
Popovic, Z. 104
Potvin, G. 104
Puzella, A. 190
Radway, M.J. 154
Rivera-Albino, A. 233
Roach, T.L. 86
Roberts, T.M. 17
Rodriguez-Solis, R.A. 233
Rollin, J-M. 104
Rudish, R.M. 326
Ruyle, J.E. 410
Saito, Y. 104
Santarelli, S.G. 17
Schaubert, D.H. 1, 42, 143, 363
Southall, H.L. 250
Stasiowski, M. 42
Sussman-Fort, S.E. 326
Swenson, Jr., G.W. 463
Vanhille, K. 104
Wahid, P.F. 132
West, J.B. 1, 60, 222
Wolf, J.D. 60

HELICOPTER MOUNTED RADAR INSTALLED CHARACTERISATION ASSESSMENTS THEORETICAL PREDICTIONS AND MEASUREMENTS

Colin McCartney BSc, C.Eng, MIEE
Cobham Advanced Composites
Horizon Technology Park
Stevenage SG1 2DH
United Kingdom

Abstract

This paper reports the theoretical predictions obtained from computer modelling carried out on a helicopter under-body with a belly mounted radar antenna and radome installed. The major effects are the reflections and blockages caused by the helicopter structure and the reflection lobe from the radome. Comparisons are made with measurements carried out on a full size 'mock-up' of the helicopter body and there is reasonable agreement between measurement and theory. Generally, the change in the directivity, beam shift and distortion of the radar antenna beam are predicted with reasonable correlation with the values obtained from the measurements carried out on the full scale 'mock up'.

1. Introduction

Radar performance of helicopter belly mounted systems has proved to be troublesome under certain conditions. This paper reports the output from a series of predictions of a computer model of a radar system antenna and radome mounted in the centre of the underside of a helicopter. The radar system performance when installed is a function of many complex characteristics. The prime components, as far as the radiation pattern of the installed antenna is concerned, are the antenna aperture distribution inside the radome, the radome transmission and reflection characteristics and the interference effects of the helicopter. The first two components are controlled by individual component specifications but there is not normally a specification for the effects of the helicopter body or any other obstruction. Knowledge of the interference effects of the helicopter assembly is necessary for the overall installed

performance of the system. There are two methods that can be employed to ascertain these effects – measurements on a full scale model and computer predictions - neither of which is quick or easy - but both approaches have been carried out and the results compared and reported here.

Normally, computer modelling of the antenna and radome combination would be carried out during the radome design phase, but would not include the interference effects of the helicopter and its associated obstacles. Recent advances in the modelling software developed at Cobham Advanced Composites have enabled the helicopter modelling problem to be attempted.

The measurement of the full-scale 'mock-up' involves producing a representative structure of the body of the helicopter and all the relevant obstructions and then measuring the changes in the radiation pattern of the antenna due to the helicopter. In order to make radiation pattern measurements of the antenna mounted on a large 8m long by 2.5m wide structure a suitable test site is required that can cope with such a large effective RF aperture. It is not practical to use conventional far field ranges since the range length would need to be of the order of 4km for measurements at 10GHz. A compact range with a quiet zone big enough would need a reflector size approaching 20m across which was not available. Near field measurements techniques, however, do allow such large structures to be measured and the large indoor cylindrical scanner at Cobham Advanced Composites was selected for the work.

2. Modelling Software

The introduction of the improved software tools developed over the last four years at Cobham Advanced Composites has meant that modelling of the effects of obstacles and blockages can be attempted. The main software tool developed for use at Cobham, called 'File Oriented Radome/Antenna Modelling' (or FORAM),[1] has a number of functions or 'building blocks' which calculate, inter alia, the surface geometry of the problem, the electromagnetic properties of the materials, surface currents, near fields and the transformations into the far field. Each function, or 'block', is self-contained with input and output data files that are easily read. By combining various building blocks, a comprehensive model of the problem may be generated.

2.1 FORAM Concepts

FORAM is a software tool which has been created to provide the user with an 'environment' within which to work out solutions to problems in electromagnetics. FORAM does not attempt to provide a 'black-box' solution to every radome / antenna modelling problem. Rather, the approach adopted in FORAM attempts to encourage

the user to move away from 'black box' solutions (which are not generally available) towards solutions which require a certain amount of judgement and thought as to how to frame and solve the problem in hand: FORAM allows a more heuristic approach to problem solving, enabling the user to make appropriate choices as to what tactics should be employed: in general finding solutions to problems in electromagnetics requires working in a domain which is difficult.

Clearly FORAM requires some understanding of what processes are involved in a given problem, i.e. an understanding of what is going on physically. This should not be seen as a negative thing however since having a good understanding of the processes involved leads to a good understanding of how to solve the problem and consequently gives confidence in the eventual solution obtained. This approach has resulted in an improved ability to tackle complex configurations by breaking them down into smaller sections.

2.2 Separation of Data and Processes

The key idea behind the FORAM software package is one of separation of data and processes. This recognises the fact that typical antenna / radome (electromagnetic) problems involve

(a) large amounts of data and
(b) usually several distinct processes.

The processes referred to are called commands in FORAM. These commands are the building blocks referred to above. As an example, the computation of the far-field pattern of an antenna might involve the computation of a large set of points over the antenna surface, the computation of a large set of currents at these points and the computation of the radiated field at one or more far-field points. FORAM uses a file-oriented approach to modelling: distinct processes (i.e. FORAM commands / building blocks) are available which generate certain items of data (e.g. a set of surface points or surface currents) and these data are passed from process to process (i.e. FORAM command to FORAM command) via data files. Importantly, these data files contain human-readable text which facilitates checking / inspection of intermediate results. There are several advantages to this approach, of which the three principal advantages are

(a) the breaking down of complex calculations into several distinct stages,
(b) the ability to stop a calculation between stages and look at intermediate results
(c) the ability to re-use intermediate results for different subsequent calculations.

2.3 Housekeeping and Complex Models: F-Language

FORAM itself provides the building blocks with which models can be constructed. FORAM commands are tailored as required by specifying supporting command data, for example a spherical surface requires a radius and so on. In a complicated model it is often necessary to specify a large amount of supporting data across a large number of commands; some parts of a calculation may be repeated and various sets of results may be produced. In this case it is desirable to have some sort of over-arching control of the FORAM building blocks and their supporting data. F-Language is provided for this purpose.

F-Language is a scripting or control language which allows complex models to be constructed using a mixture of FORAM building blocks (to create surfaces, sources of radiation etc), and general (BASIC-like) programming language statements. The latter can be used, for example, to loop over frequencies, antenna scan angles etc and perform general housekeeping operations - for example creating file names which change according to some variable (e.g. scan angle or frequency). F-Language provides all the usual capabilities of a high level programming language. Combining F-Language and FORAM provides a powerful environment in which to construct complex models.

3. Model Components

3.1 Helicopter Body

The main shape of the helicopter lower body was based on CATIA files from the helicopter designers. Figure 1 is an extract from the CATIA files

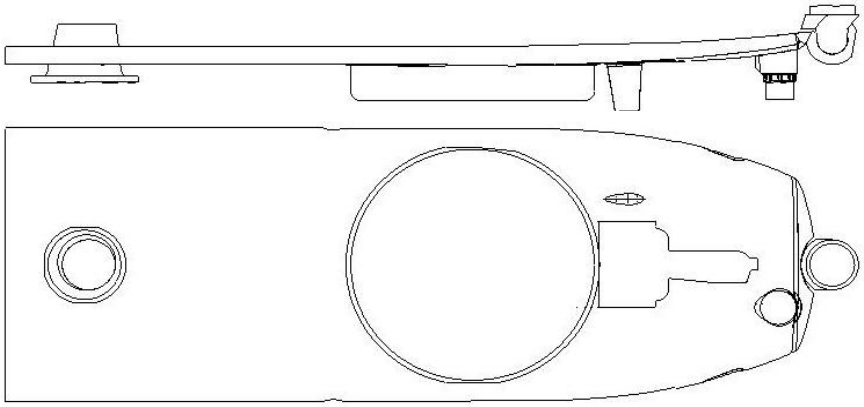

Figure 1 Extract from the Helicopter CATIA Files

For the computer model, the three dimensional surface was divided into elements with dimensions less than half a wavelength, and the whole surface modelled as a conducting surface (except the radome!). During normal flight the helicopter undercarriage retracts into a wheel bay but there is no cover over this wheel bay. This hole in the conducting surface was directly in front of the radar and therefore had to be simulated in the computer model. The shape of the wheel bay hole was taken from the CATIA file, but, unlike the mock up for the test configuration, the computer model did not include the complex shapes of the undercarriage itself. Figure 2 is the computer model equivalent of the body shape.

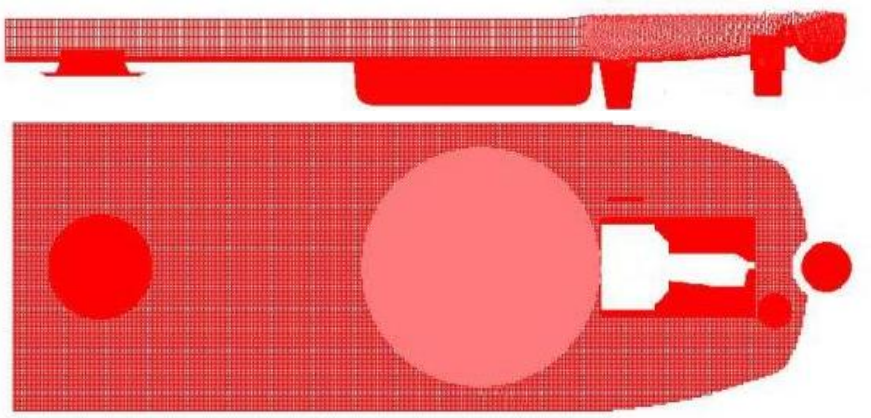

Figure 2 Computer Model of the Helicopter Body

For weight as well as availability reasons it was not possible to mount a real helicopter body on the test rig. So for the test programme, a lightweight foam shape was constructed and then metal sprayed with aluminium to give a good conducting surface.

Figure 3 The Test Body Under Construction.

3.2 Antenna

The initial simple model of the radar antenna had a rectangular array of elements based on the locations in eleven rows of seventy six radiating waveguide slots. The basic form of the aperture amplitude distribution was taken as a Taylor type (-27dB, n=6) in azimuth and (-27dB, n=3) in elevation. The predicted major plane patterns for this first antenna model are shown in Figures 4 and 5 together with the measurement results from the test antenna.

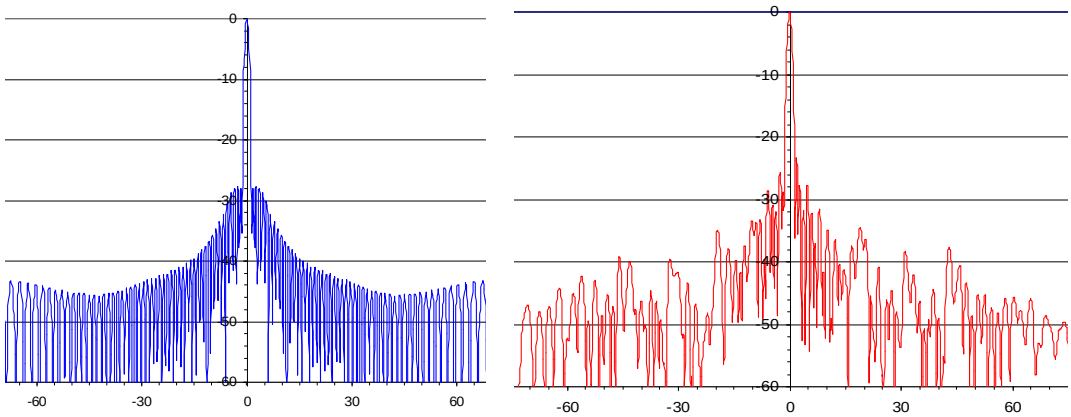

Figure 4 Initial Antenna Model and Measured Azimuth Patterns

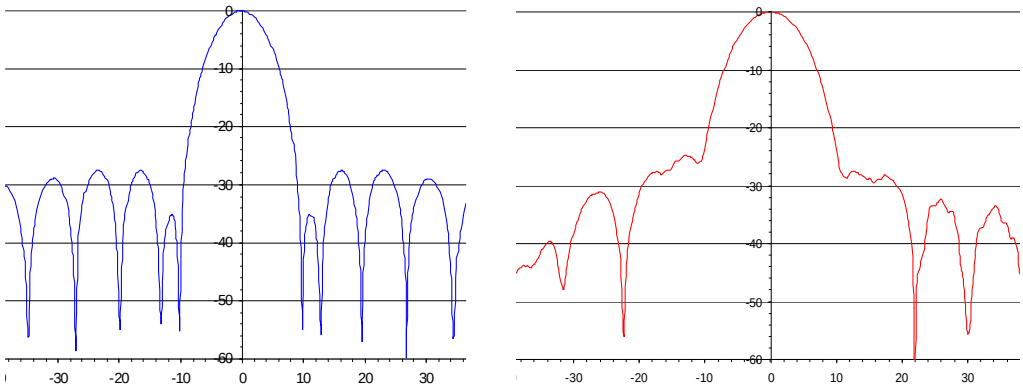

Figure 5 Initial Antenna Model and Measured Elevation Patterns

Clearly the computer model is idealistic and not really representative of the test antenna. This was due, in part, to the fact that some of the radiating slots in the test antenna were missing and so when these were removed from the model, the final computed antenna patterns of Figure 6 and 7 were obtained and the comparison with the test results is much better. There still is a difference however, particularly in the

elevation pattern, which may be due to some manufacturing phase errors in the test antenna. The comparison of the sidelobe levels, however, is very much better for the azimuth plane.

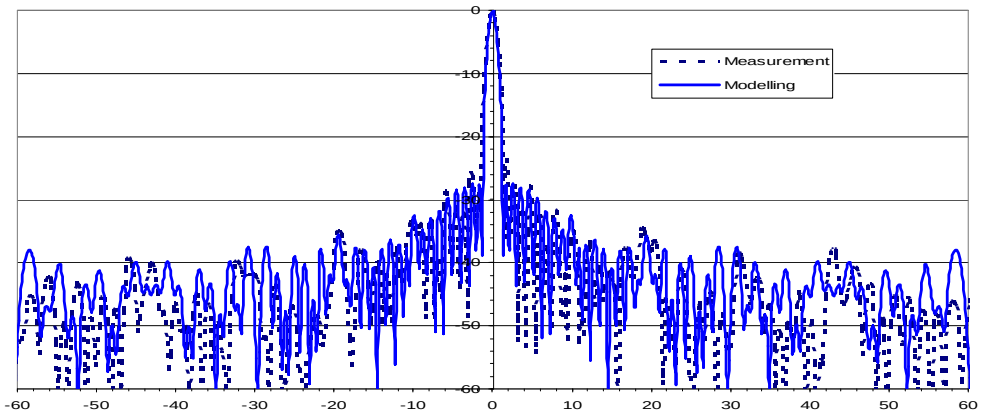

Figure 6 Final Antenna Model and Measured Azimuth Patterns

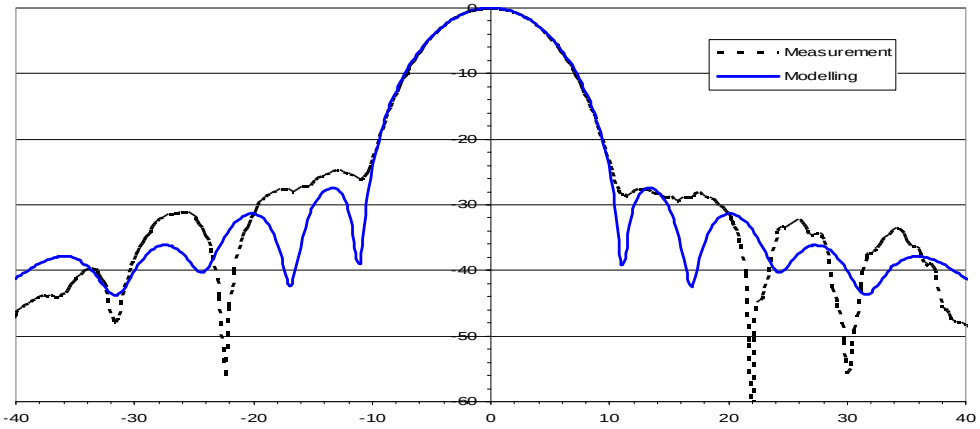

Figure 7 Final Antenna Model and Measured Elevation Patterns

3.3 Radome

The full multi-layer radome is included in the computer model. Each of the radome layers was modelled in terms of thickness, dielectric constant and loss tangent with the thickness at any point a function of the radial position in order to correctly model the phase compensation tapers within the radome build. For the test programme, a production standard radome was mounted on the helicopter mock-up.

FORAM Flow Diagrams

The overall logic for the computer model is shown in Figure 8. The ***.flp blocks are F-Language routines which set up the configurations and then control the way the ***.foram blocks are implemented. The input parameters to the radar.flp block are frequency and antenna elevation angle. (Azimuth angle is only required when running the helicopter.flp). The outputs of the radar.foram block are the surfaces of the antenna and radome, the antenna radiating field and the bare antenna patterns.

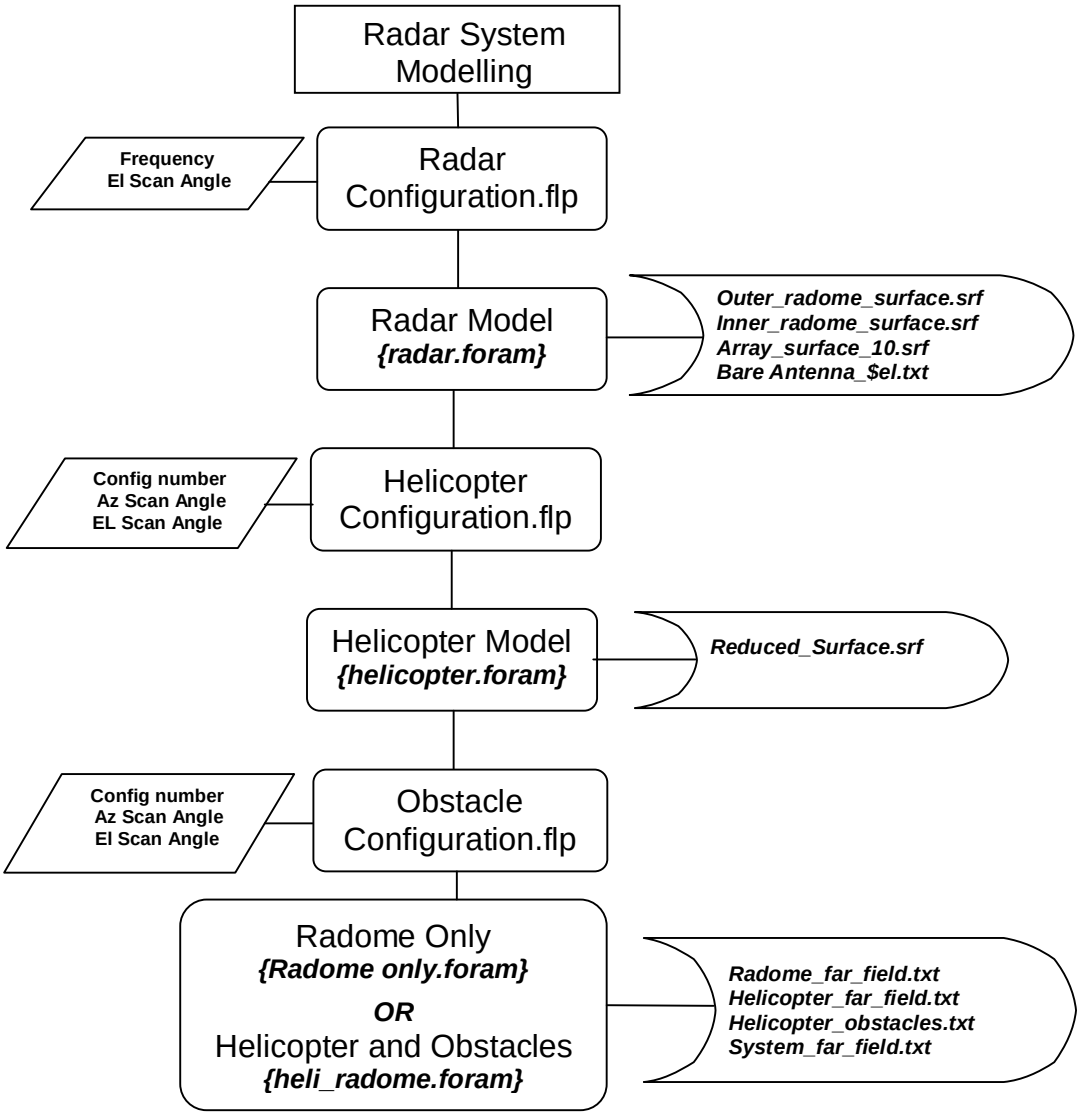

Figure 8 Overall FORAM Logic for the Helicopter Modelling

Figure 9 is the logic for the radar.foram and lists the FORAM commands that are invoked in order to model the antenna and radome and also lists where the output files come from.

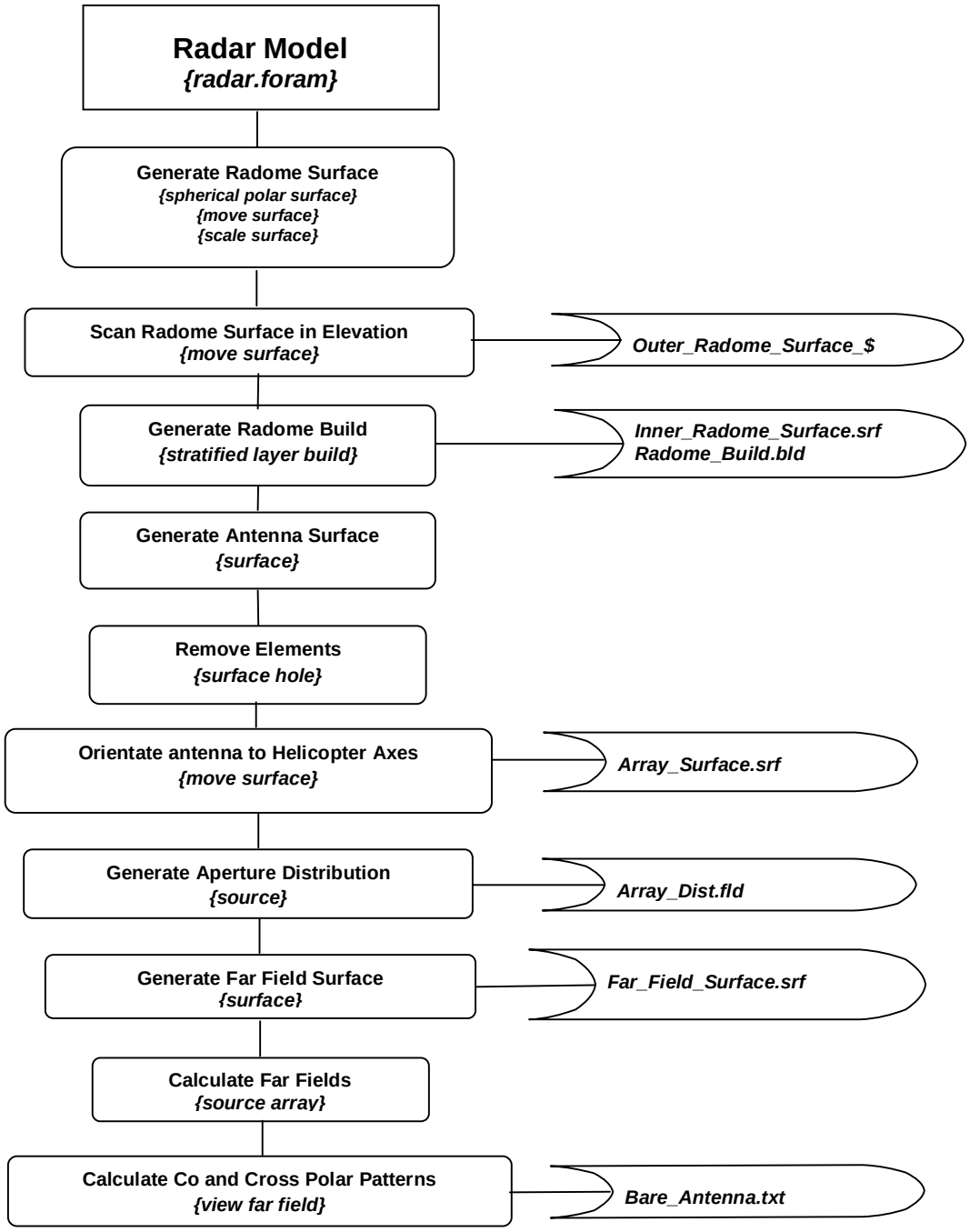

Figure 9 Overall FORAM Logic for the Radar Model

The helicopter.flp runs the helicopter.foram which establishes the illumination levels on the helicopter surface and discards any of the surface which has an illumination level below –60dB with respect to the peak illumination level. This is to minimise the model size and therefore reduce the computation times. (The discarded surface is generally some of the helicopter which is behind the radar antenna). Figure 10 is the logic for the helicopter.foram.

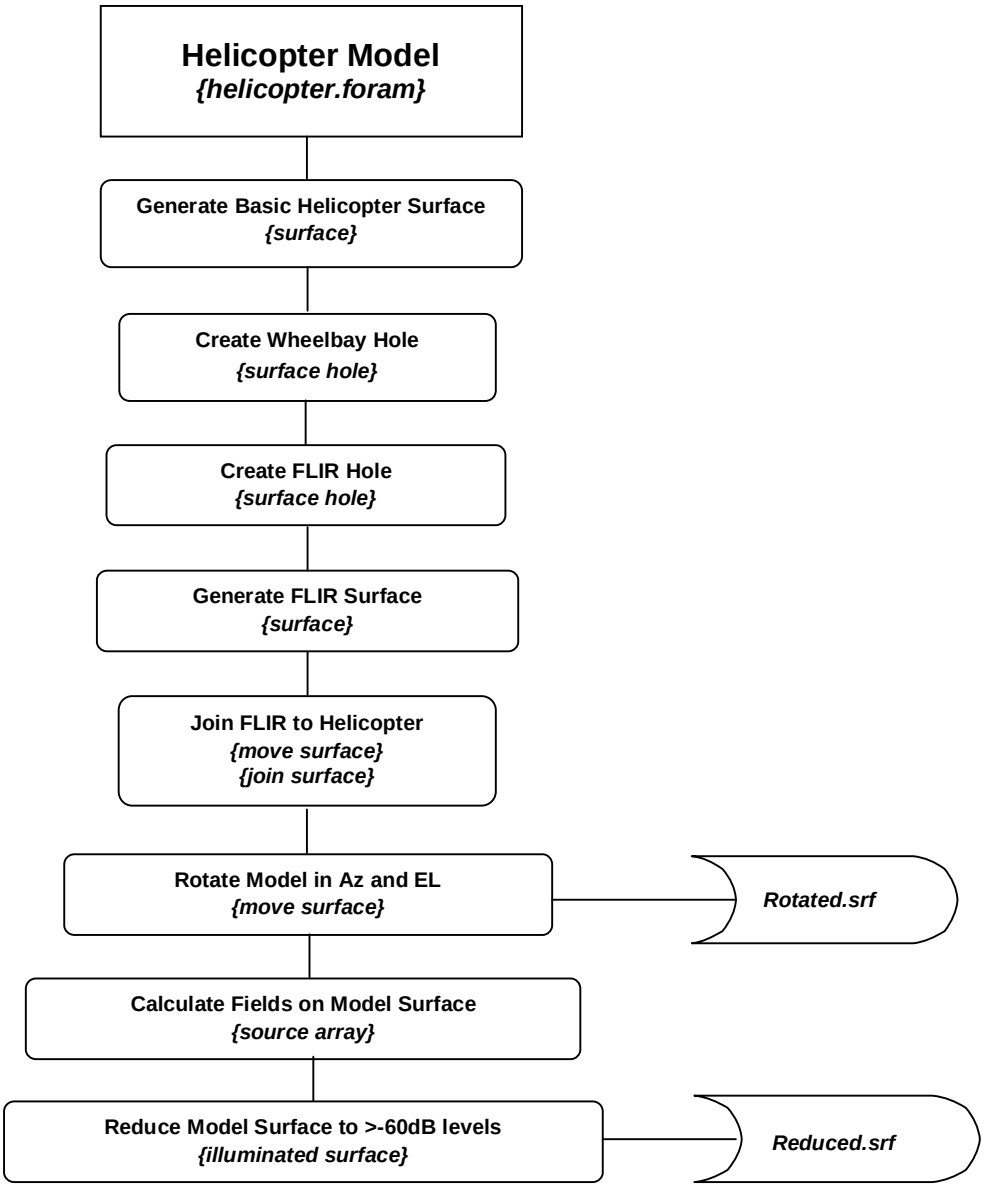

Figure 10 Overall FORAM Logic for the Helicopter Model

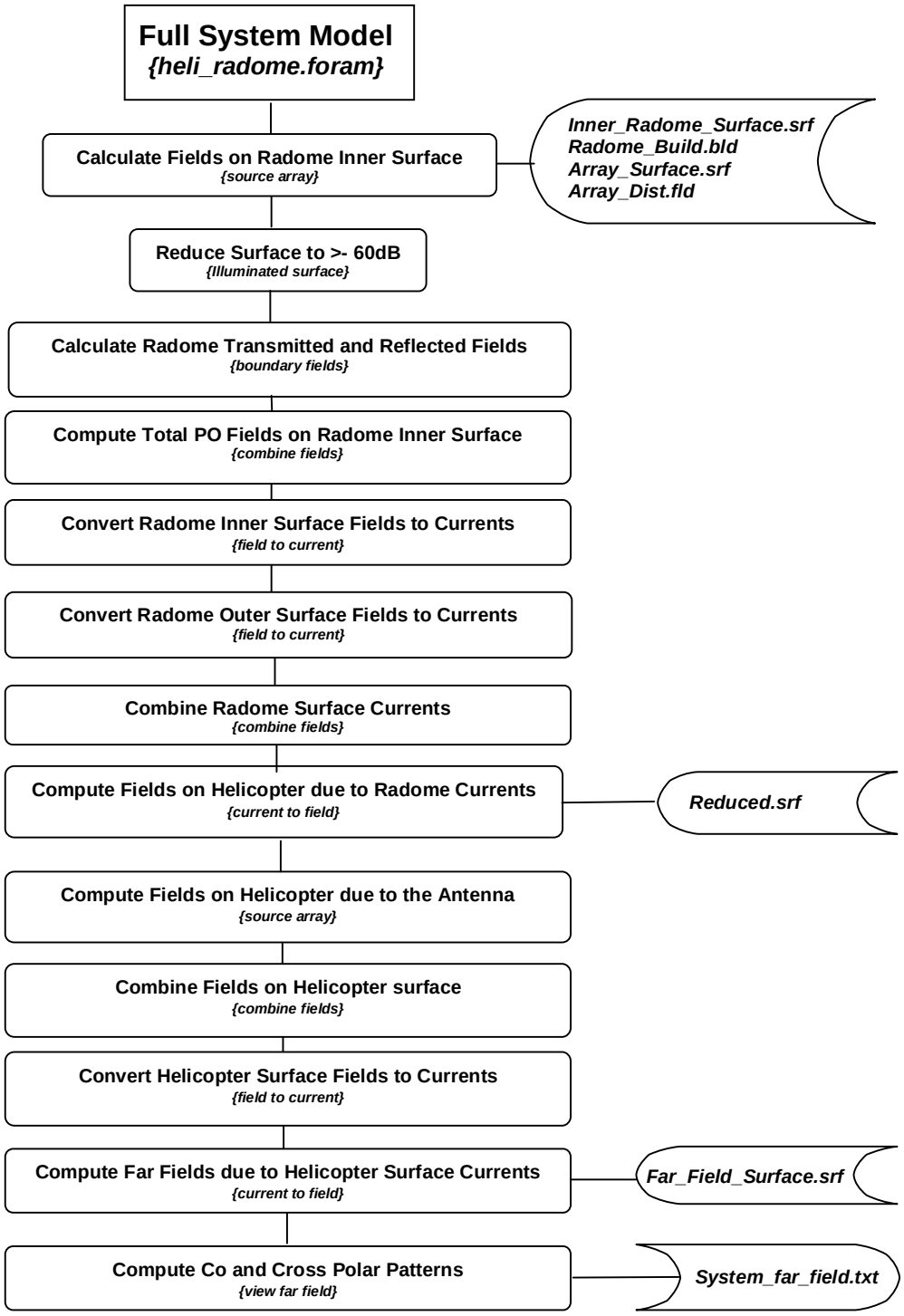

Figure 11 Overall FORAM Logic for the Full System Model

The obstacle configuration.flp then runs the 'obstacle'.foram depending on the model chosen. For example

a) Config 1 - Radome Only - this enables the comparison with measurements carried out on the qualification and production radomes without any influence of the helicopter.
b) Config 2 - Helicopter and Radome - this carries out the calculations to see the effect of the helicopter and radome with the radar facing rearward.
c) Config 3 - Helicopter and Radome (Bank Angle Effects) - this is for the full helicopter system model with the antenna facing sideways.

Figure 11 is the logic for full helicopter system option taking input files from the radar and helicopter routines. The final output is the text file that contains the co- and cross-polar patterns for the configuration being modelled.

4 Full Scale Testing

4.1 Near Field Cylindrical Scanner System

The near field scanner system comprises of a 360^{o} azimuth turntable on which the device under test is mounted and a vertical scanned probe with a scan range of 6m. The motions of both the turntable and the probe are controlled by the NSI 2000© system controller with positional data collated with the RF test data to produce a cylindrical near field data set. The radius of the scanned cylindrical surface is chosen to be the smallest that totally encloses the test item in order to minimise the number of sample points required. For this series of tests the cylinder radius was 4m.

4.2 Test Fixture

The purpose of the test fixture is to hold the gimbaled test antenna and the helicopter assembly in the correct orientation with minimum interference by the test fixture of the radiated fields. The antenna azimuth axis must be in line with the azimuth axis of the test scanner system and elevation axis of the antenna must lie in the horizontal plane and pass through the azimuth axis of the test scanner system. The whole of the antenna and helicopter assembly is mounted on the large ring plate which in turn is supported by a large stiff frame. This frame can be elevated using the automatic jacking system and the elevation angle accurately measured using an angle encoder system mounted on the elevation axis. (Note that the tests are carried out with the complete helicopter assembly inverted). For all measurements the antenna radiating face is positioned to lie in a vertical plane and the helicopter body is then moved to give the required angular relationship with the antenna. Figure 12 shows the test

support fixture with the partially assembled helicopter mock-up mounted together with the antenna assembly and radome in the test site..

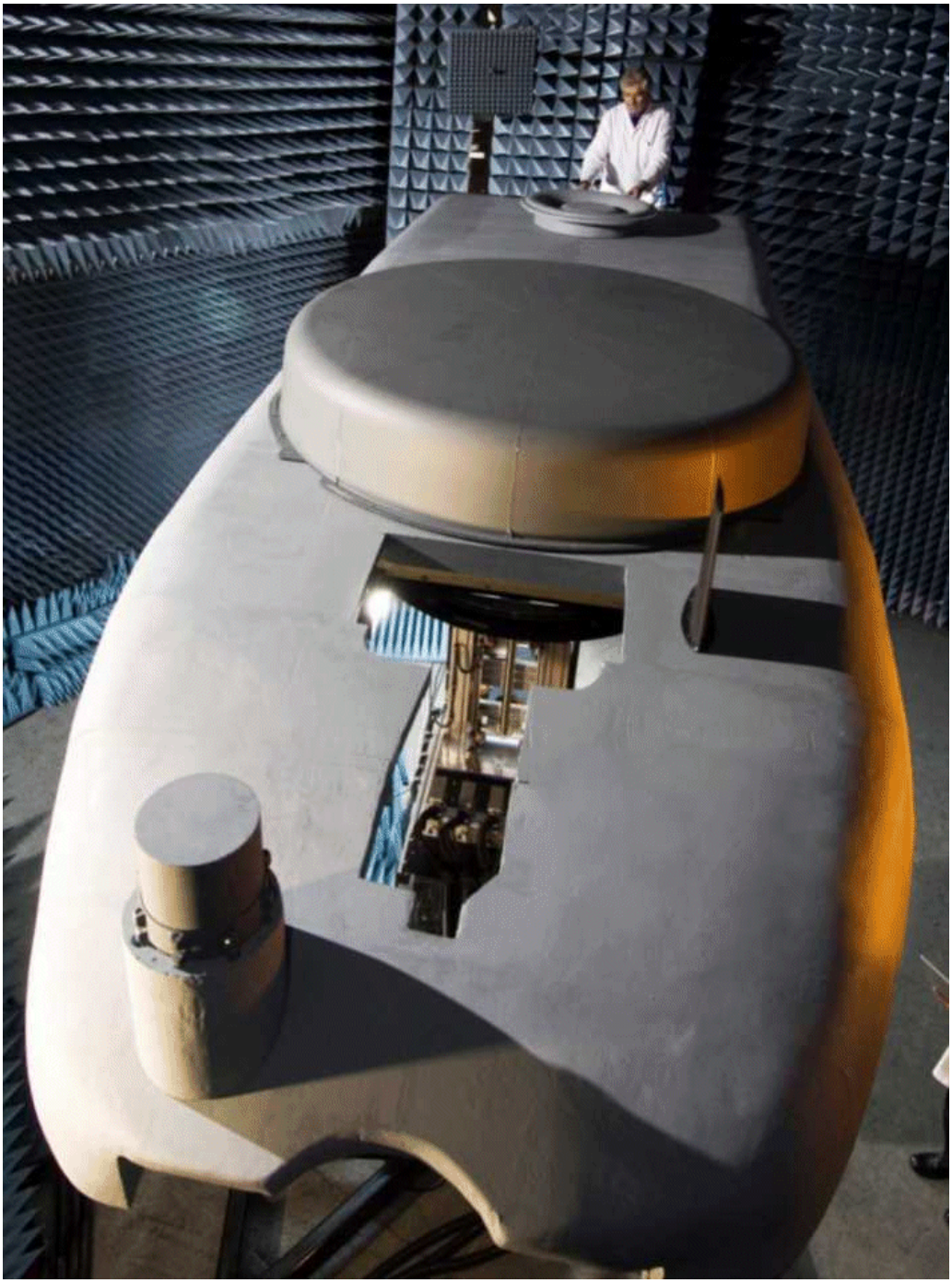

Figure 12 Partially Assembled Helicopter Mounted in the Test Site

4.3 Microwave Test System

The microwave system, shown in Figure 13, is based on the Agilent 8530 test system, driven by the NSI Controller, comprising of the following:

8530A Microwave Receiver
83621B Frequency Synthesizer (two off)
85309A LO/IF Distribution Unit
85320A Test Mixer
B5320B Reference Mixer
85320B 10dB coupler
OEWG Measurement Probe
Microwave Coax Rotary Joint
Appropriate interconnection cables

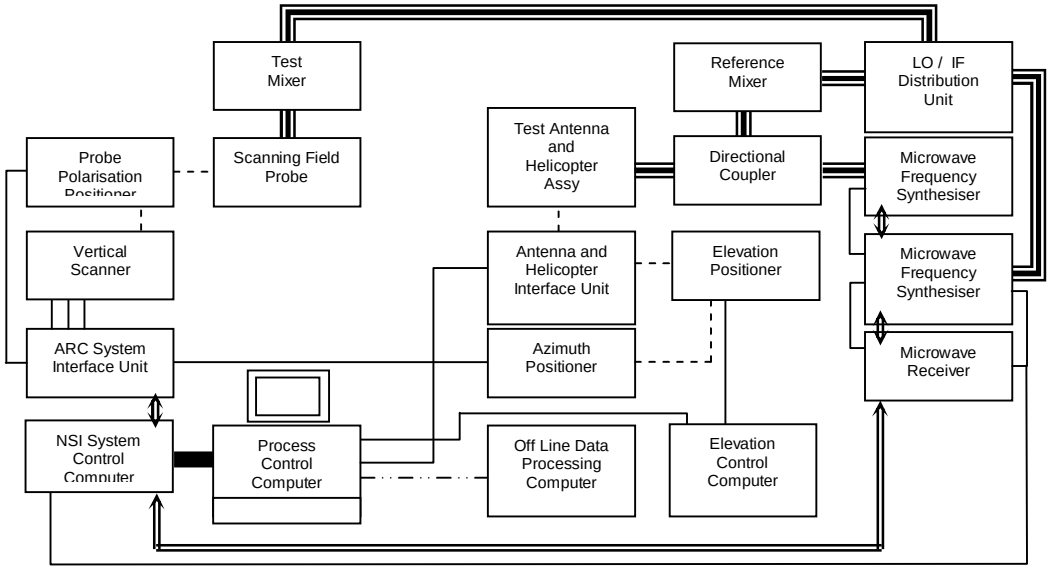

Figure 13 6m Scanner and Microwave Test System Block Diagram

4.4 Test System Software

The main controlling software is NSI 2000 Rev 4.0.18 running on the system PC. This has a Windows© based interface with software links to the controller and then on to the cylindrical scanning positioners and microwave test system. The setting of all scan parameters, frequencies, data logging and far field transformations are carried out using the NSI 2000 software together with scripts written specifically for the test programme.

4.5 Near Field Data

The near field data is collected in terms of amplitude and phase for each measurement point on the cylindrical surface. Figure 14 shows typical grey scale plots of the near field amplitude, plotted in terms of azimuth angle ($\pm 90^{o}$)and cylinder height (±2.5m), for the bare antenna and also when the helicopter is present. This data is stored in the control computer and is further processed offline. Each file contains all data for a particular antenna set angle with respect to the helicopter including the scan conditions, ranges, and near field pattern data for each frequency. These files are then processed using the NSI2000 FFT software.

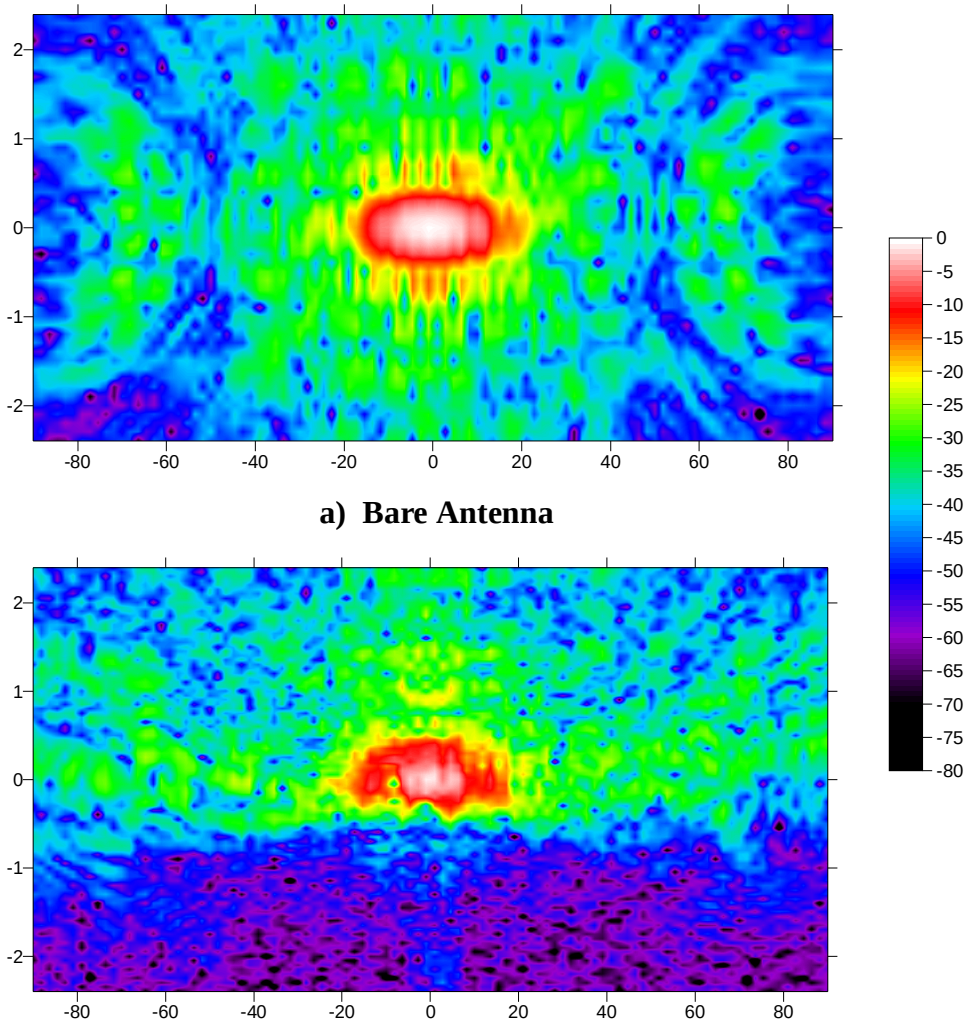

a) Bare Antenna

b) Antenna Plus Helicopter

Figure 14 Sample Measured Near Field Data

4.6 Far Field Data

The transformation from near field to far field is carried out using the FFT processing contained within the NSI2000 software. Figure 15 shows typical grey scale plots of the far field amplitude for the two near fields plotted in Figure 14. Here the data is plotted in terms of pattern azimuth angle ($\pm 90^{o}$) and elevation angle ($\pm 60^{o}$). This data is stored as .txt files and can therefore be further analysed using a variety of commercially available software.

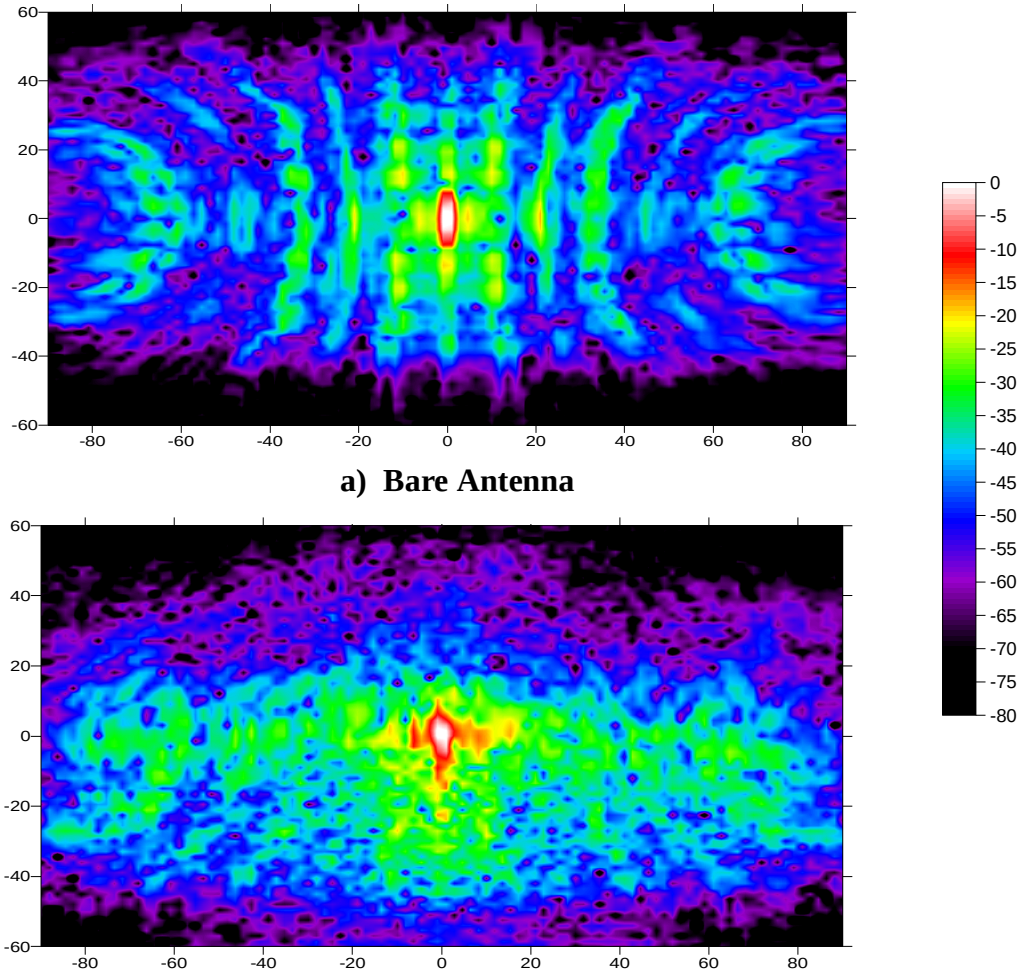

a) Bare Antenna

b) Antenna Plus Helicopter

Figure 15 Sample Transformed Far Field Data

Note that the far field data is plotted in Helicopter axes and not Test Site axes and therefore the plots are inverted when compared to the near field.

5 Predictions and Comparisons

5.1 Config 1 – Antenna and Radome only

As stated above, the antenna and radome characteristics are usually controlled by specifications which do not take into account the effects of the helicopter. Comparisons have therefore been carried out for the simple configuration of the antenna and radome combination in isolation. Figures 16 to 19 show the measured and predicted elevation patterns for a range of antenna elevation angles. Because of the relatively flat bottom to the radome, there is a well defined reflection lobe in the elevation plane. The variations in these reflection lobes are clearly seen in both measurement and prediction plots. Precise lobe detail in the computer model is very dependent on the accuracy of the antenna distribution in terms of amplitude and phase.

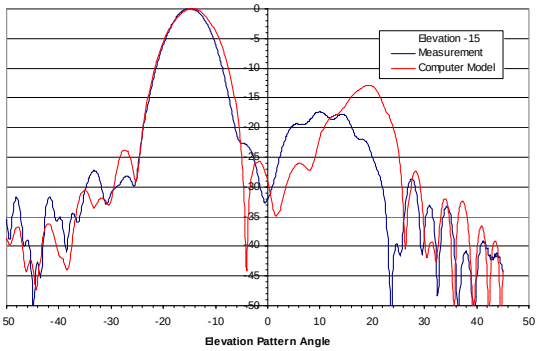

Figure 16 Elevation Set at -15^{o}

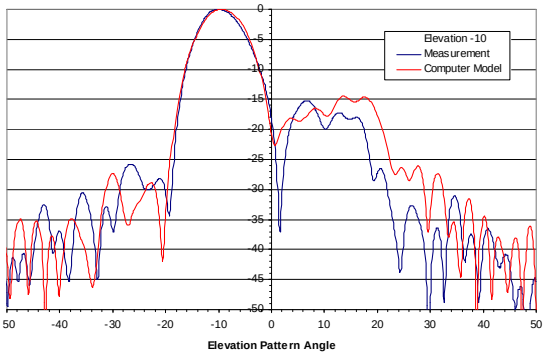

Figure 17 Elevation Set at -10^{o}

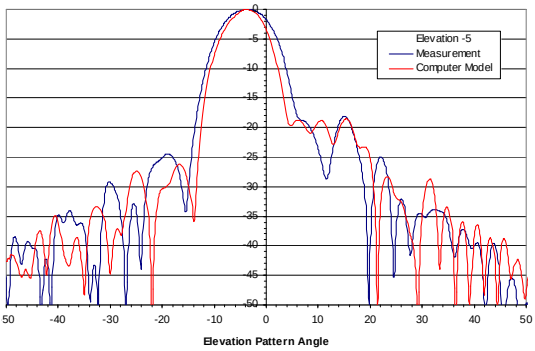

Figure 18 Elevation Set at -5^{o}

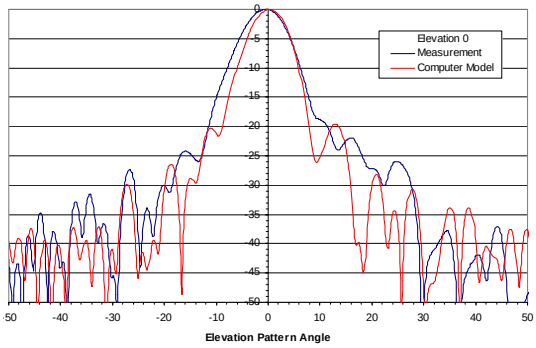

Figure 19 Elevation Set at 0^{o}

The differences in the azimuth plane plots are more difficult to distinguish and there is very little variation with elevation angle. Figures 20 and 21 show the azimuth

plane patterns and, as expected because of the shape of the radome, there is very little evidence of a reflection lobe in this plane.

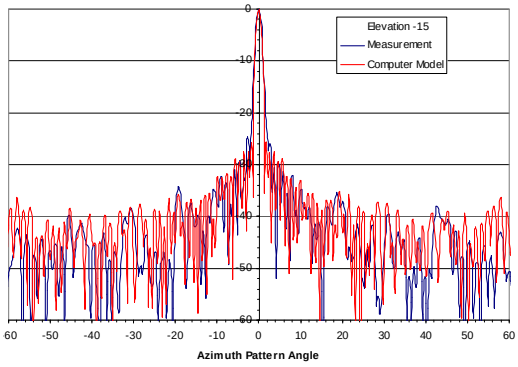

Figure 20 Elevation Set at -15^{o}

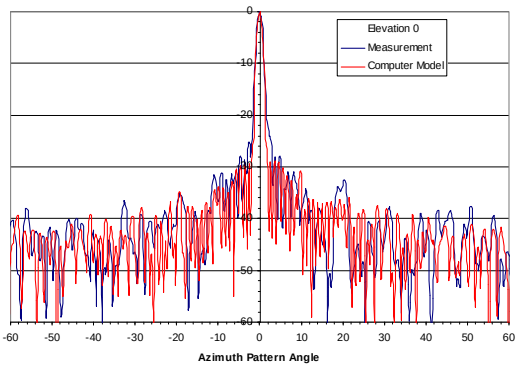

Figure 21 Elevation Set at 0^{o}

5.2 Config 2 – Helicopter and Radome (Pitch Angle Effects)

This configuration consists of the helicopter body plus the radar antenna and radome with the antenna looking towards the rear of the helicopter. In effect, for this configuration, the bottom of the helicopter acts as very large reflector in close proximity to the top edge of the antenna. The influence of the helicopter varies enormously with elevation scan angle (aircraft pitch) in terms of beam peak position, system gain and pattern distortion. Fig 22 to 24 are examples of the major elevation plane patterns from the measured data compared with the computer model for the rearward looking antenna. Figure 25 plots the variation in directivity of the antenna with elevation set of the antenna with respect to the helicopter. The computer model predicted significant beam shape distortion and boresight shift in all cases due to the presence of the helicopter (when compared with the bare antenna pattern) and these effects are confirmed by the measurement results.

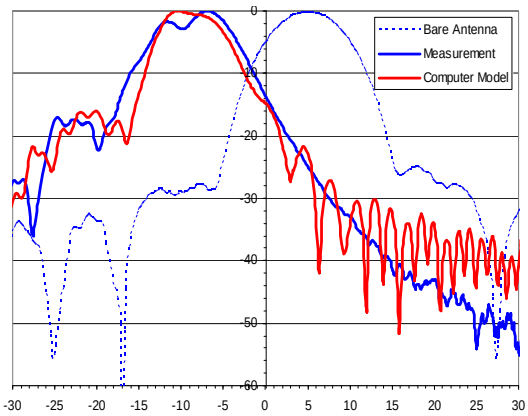

Figure 22 Elevation Set at 5^{o}

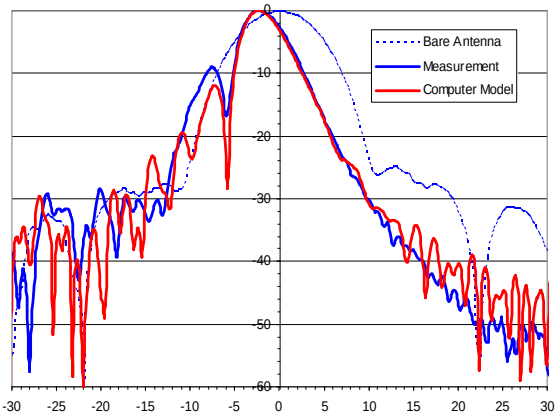

Figure 23 Elevation Set at 0^{o}

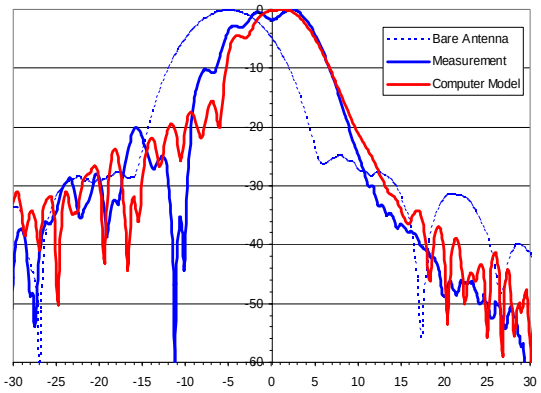

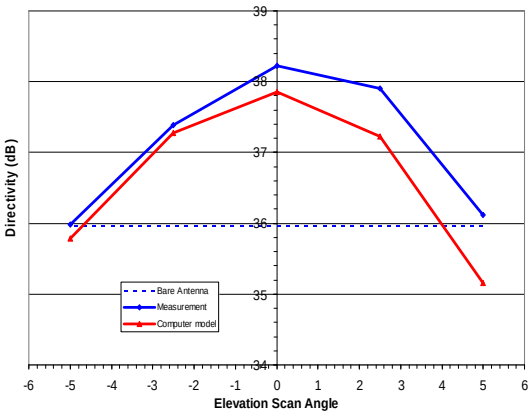

Figure 24 Elevation Set at -5^{o} **Figure 25 Directivity v Elevation**

5.3 Config 3 – Helicopter and Radome (Bank Angle Effects)

This configuration consists of the helicopter body plus the radar antenna and radome with the radar antenna looking towards the side of the helicopter (90^{o} Azimuth). The variation in directivity with elevation at 90^{o} azimuth is shown in Fig 26 with reasonable agreement between the computer model and the measurements.

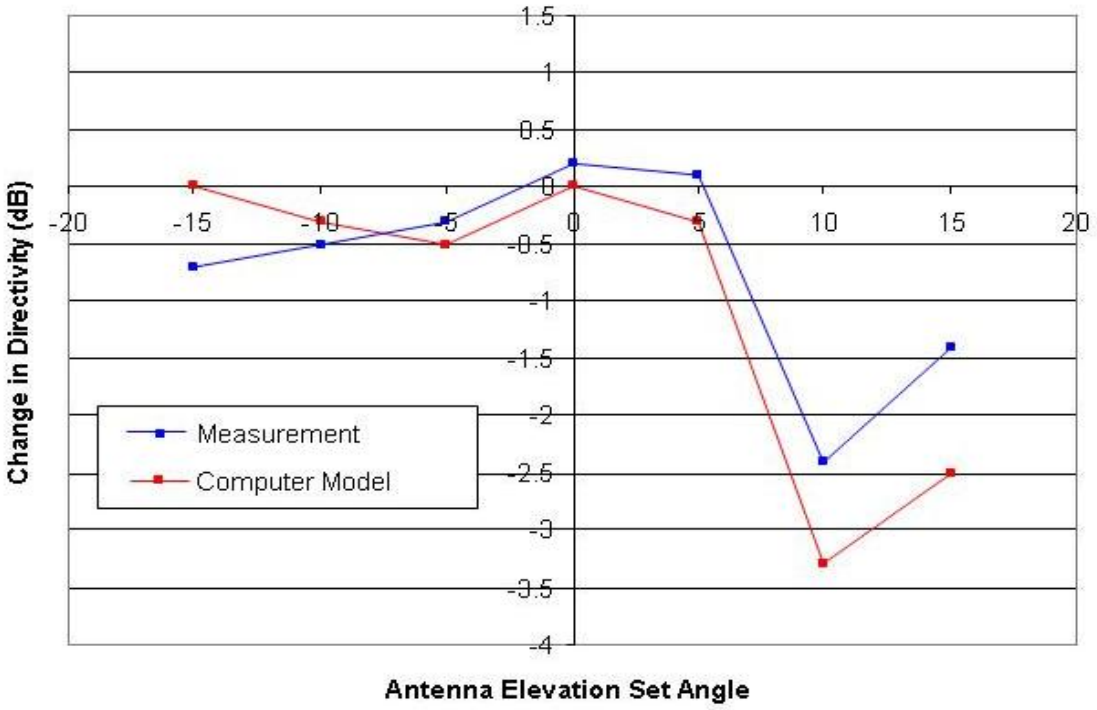

Figure 26 Directivity v Elevation (Bank Angle – Azimuth = 90^{o})

Figures 27 to 31 are the major elevation plane patterns for a range of elevation set angles of –15° to +5° and all at 90° azimuth. The Model predicts the elevation patterns quite well for the negative elevation set angles but the predictions become less accurate as the antenna scans up and looks into the belly of the helicopter although the general trends can be seen.

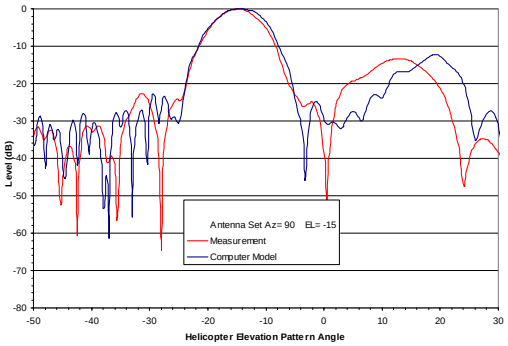

Figure 27 Az 90° El -15°

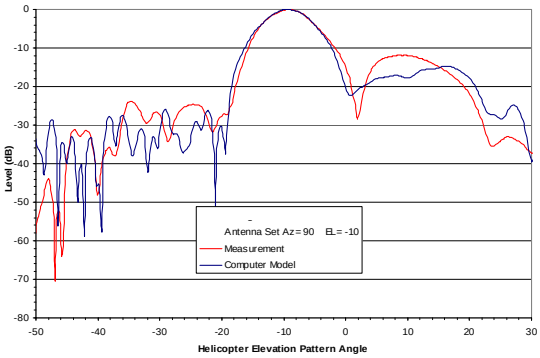

Figure 28 Az 90° El -10°

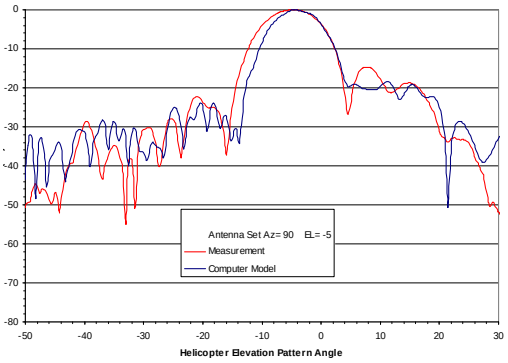

Figure 29 Az 90° El -5°

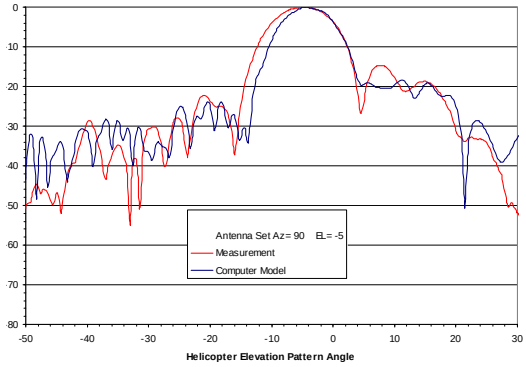

Figure 30 Az 90° El 0°

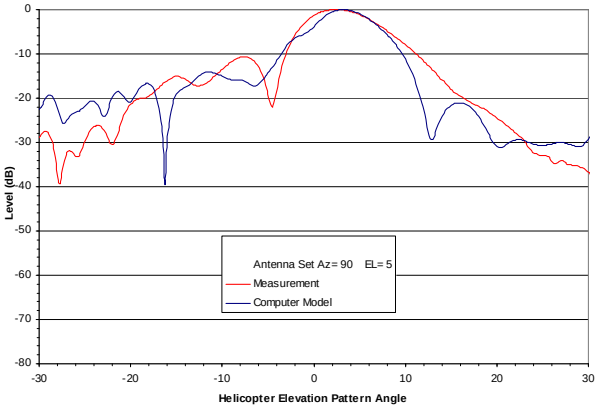

Figure 31 Az 90° El 5°

6. Conclusions

The effects of the helicopter and the obstacles mounted on the underside have been assessed using the FORAM computer modelling software developed by Cobham Advanced Composites. The major effects are the reflections and blockage caused by the helicopter structure. Comparisons have been made with the measurements carried out on a 'mock-up of the helicopter body and there is reasonable agreement between the two methods of assessment. Reflection lobes, both from the radome and the helicopter, are reasonably well predicted in both angular position and level. However the complexity level of the computer model was insufficient to provide precise low level sidelobe structure. The beam shift and distortion are predicted well and generally the change in the directivity of the antenna is predicted with similar curve shapes to the measurements carried out on the full scale mock up. These modelling techniques could be used to give better accuracy, at the expense of computational time, by increasing the detail of the modelled structures.

7. Acknowledgements

The author would like to thank Peter McNair for the bulk of the FORAM coding and for his extensive support during the use of the codes and Billy Dixon for his valued help during the testing programme.

8. References

[1] P. McNair, "Electromagnetic Modelling of Radomes in a Commercial Environment: a building Block Approach", Presented at the ICEAA-EESC Conference, Turin, Italy.

THE RF CUTTLEFISH: OVERVIEW OF BIOLOGICALLY INSPIRED CONCEPTS FOR SMART SKINS AND RECONFIGURABLE ANTENNAS

Gregory H. Huff, Sean Goldberger, and S. Andrew Long
Electromagnetics and Microwave Laboratory
Department of Electrical and Computer Engineering
Texas A&M University
College Station, TX 77843-3128

Abstract: Biological mechanisms have inspired a wide variety of multifunctional operational concepts. The adaptation or translations of these systems can provide an effective means of addressing many current and emerging challenges. The dynamic control and reconfiguration of electromagnetic (EM) boundary conditions represents one such area where novel concepts can provide a large impact. This is especially true for devices operating within or on the skin of polymorphic (shape-shifting) structures. Radio frequency micro/nano electromechanical systems (RF MEMS/NEMS) and solid-state devices are the predominant agility-enabling technologies for these platforms. However, providing stealth, cloaking, mimicry and other capabilities such as EM windowing to these platforms presents many challenges as their operational role changes and size or weight constraints become more stringent. The complexity arising from the biasing or control networks for a large number of devices and the introduction of nonlinear effects of some solid state components can eventually limit their effectiveness. This work examines the EM and structural reconfiguration mechanisms of the cuttlefish as an alternative to these technologies; a polymorphic biological system with synergistic goals that uses nano-scale materials in electronically/neurally controlled mechanisms to facilitate one of the most reconfigurable smart skins found in nature. This work will discuss the material systems and mechanisms of the cuttlefish and present a brief overview of the devices and concepts that have been inspired by its biological functionality.

1. Introduction

Bio-inspired systems stem from the desire to obtain a new or enhanced degree of physical insight into a complex system or emerging technological challenges. A bio-system that shares synergistic goals with this complex system must be identified during this process and the role of the bio-mechanisms that enable this behavior must be understood. In many cases the direct translation of these mechanisms can be challenging since this bio functionality has undergone many years of ‘evolutionarily fine-tuning’ and/or rapid mutations to address a specific challenge. Thus, the functional translation of bio-mechanisms into a bio-inspired mechanisms practical embodiment requires a certain degree of finesse to avoid layering additional complexity into the system.

The bio-inspired concepts for reconfigurable antennas and multifunctional smart skins in this work are based on the very unique blending of structural shape-shifting and rapid EM reconfiguration found only in the cuttlefish [1-6]. Examples of this behavior are shown in Fig. 1 (from [6]). There are approximately two-hundred independently controlled chromatophores, iridophores, and leucophores each per square-millimeter (their specific functionality will be discussed later). Conceptually, these resemble overlapping pixels in a deformable screen that the cuttlefish uses for mimicry, deception, communication, and camouflage (to name a few). The cuttlefish's neural control of these structurally integrated EM reconfiguration mechanisms results in very fast response times, and its highly creative uses of these mechanisms have earned this species the nickname "kings of camouflage" [6]. It can pulsate, flash, and alter very complex patterns with vivid colors in mere fractions of a second (different from hormonally controlled camouflage mechanisms that require much longer time scales – like cell signaling in chameleons [7]). As one of the first creatures to inhabit prehistoric oceans, these capabilities have evolved over hundreds of thousands of years to enhance the survivability of the cuttlefish, but have remained functionally unchanged (outlasting global climate changes, catastrophic events, and a myriad of evolving predators and food sources). While it might not seem intuitive at first glance, these enabling mechanisms and the adaptive properties of the cuttlefish's smart skin share many synergistic goals and currently desired capabilities of reconfigurable antennas and multifunctional smart skins. Therefore, they are examined in this paper as a means to rapidly facilitate reconfiguration, adaptation, and compensation.

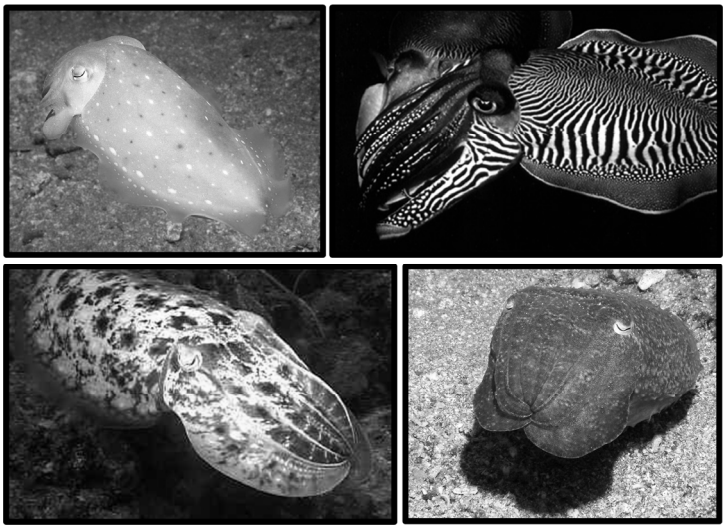

Fig. 1: Snapshots of the cuttlefish (from [6]) – the biological inspiration of this proposal – showing its ability to alter the optical properties of its skin.

This work uses the cuttlefish biological enabling mechanisms of as the basis for bio-inspired concepts in reconfigurable antennas and multifunctional smart skins. The enabling mechanisms of the cuttlefish and their functionality are discussed first. Once identified, a brief discussion on bio-inspired mechanisms will be used to discuss the operational concepts that translate this functionally from optical frequencies to the RF/microwave domain of the EM spectrum. A host of new concepts based on these bio-inspired mechanisms will then be provided for reconfigurable antennas and elements of multifunctional smart skins; this will include measured, modeled, and simulated results. This paper concludes with a short summary and discussion on future and ongoing work.

2. Translating the Cuttlefish's Enabling Mechanisms

2.1. Biological Mechanisms and Operation

At the core of the cuttlefish's adaptive behavior are numerous opaque, elastic pigment sacs called chromatophores that are radially surrounded by a set of neurally-controlled muscular cords (Fig. 2). When electrical signals from the brain contract these muscles the sacs are stretched out into highly visible flat discs of dense pigment; when the muscles relax, these sacs fold down and compress into small dots of less visible pigment enveloped in opaque muscle tissue. This layer of chromatophores resides above a layer of iridophores – small strings of translucent, interconnected platelets – that can also be controlled independently to refract and polarize light by adjusting their spacing (an optical grating). The iridophores reside above yet another layer of similar, but more opaque, strings of platelets called leucophores that reflect light like deformable mirrors. The pigment sacs produce the orange to red, brown to black and yellow colors of the skin, the refracting cells vary their periodicity to create blue and green hues, and the reflecting platelets contract to form white spots (total reflection). Hence – the cuttlefish uses electronically controlled microfluidic elements containing colloidal materials and periodic gratings in multilayer configurations to manipulate the optical boundary conditions of its skin and rapidly reflect, refract, polarize, and re-transmit light – *a truly unique, remarkably concept to inspire a "smart" skin!*

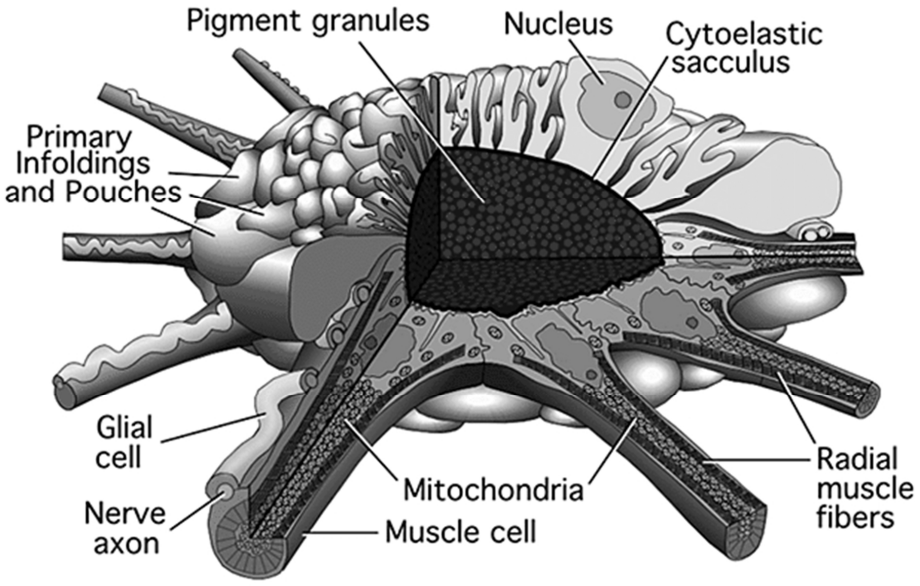

Fig. 2: Diagram [6] of the cuttlefish's chromatophore.

2.2. Bio-Inspired Material System

Electromagnetically functionalized colloidal dispersions (*EFCDs*) [8-17] with tailored dielectric, magnetic, and/or conductive properties are used as the material system inspired by the different colored pigment in the chromatophores. Several different nomenclatures based on the phases of the constituent materials (e.g., solid, liquid, or gas) can describe a colloidal dispersion, but solid-liquid dispersions are referred to as sols. *EFCDs* are thus

sols that result from the homogeneous dispersion of solid colloidal materials (spherical, magnetodielectric, low-loss particles with a diameter ranging form 1 to 1000 nm) into a low-loss liquid. Fig. 3 shows a conceptual illustration of the *EFCDs* and mixing rules (e.g., Maxwell Garnett formula shown (1) [18]) for a nominal set of materials flowing inside of a capillary structure or fluid channel. Magnetodielectric compositions of colloidal materials are selected for use in *EFCDs* based on their ability to alter the local constitutive parameters in a device or microfluidic impedance transformer and provide a high degree of electromagnetic agility. The effective (mixed) *EFCD* material parameter s_{eff} in (1) provides an intuitive understanding into how the liquid s_1 and volume fraction ϑ of colloidal material s_2 contribute to the *EFCD* properties; s has been used to independently represent the complex properties $s = s(1 - j\tan\delta)$ (ε or μ).

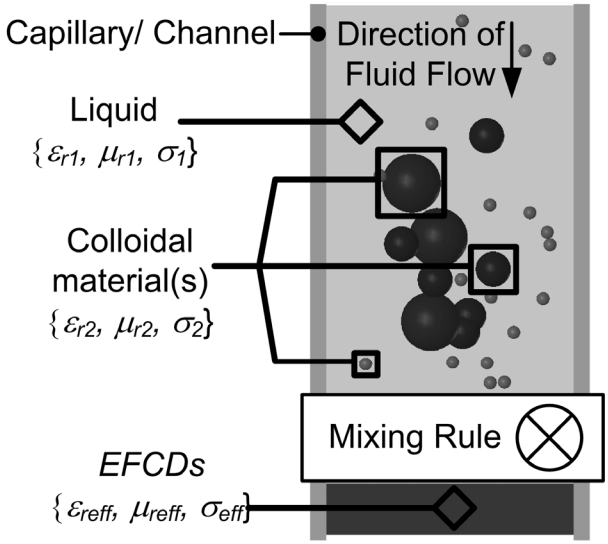

Fig. 3. Illustration of the dynamic material system and the application of mixing rules for colloids dispersed into a liquid (*EFCDs*) that are flowing down a capillary or fluid channel.

$$s_{eff} = s_1 + 3s_1\vartheta\frac{s_2 - s_1}{s_2 + 2s_1 - \vartheta(s_2 - s_1)} \qquad \textbf{(1)}$$

The *EFCDs* are electromagnetically functionalized by considering the reduction of loss mechanisms and the ability to maintain low viscosities while still using high volume fractions of colloidal material. Very low-loss colloidal materials are readily available but the maximum volume fraction of a monodispersed system ($\vartheta_{MDS}^{\max}$) (e.g., all colloids being the same size and spherical shape) is approximately 0.74, or 74% colloidal material by volume. As a point of reference, this is commonly referred to as the 'stacked cannonball' limit since closely-packed spheres resembles the pyramidal stacking seen in the pictures of pyramids of stacked cannon balls. Polydispersed systems (e.g., all colloids being different sizes but still spherical in shape) can be created up to 99% colloidal material ($\vartheta_{PDS}^{\max}$) by volume, so this represents a way to increase the contribution of these materials. However, achieving high volume fractions would not be possible without surfactants. Ionic dispersants are used in this work to electrostatically stabilize the colloids (e.g., coat them in like-charged, repulsive 'shells'). Referred to as the *electrical double layer*, this shell mitigates many of the inter-particle forces (van der Walls, etc.) and surface chemistry to avoid aggregation and clotting. However, their ionic nature introduces conductive losses. In lieu of this need to create highly mobile, highly concentrated dispersions it is important to illuminate the impact of these loss mechanisms.

2.3. Bio-Inspired Techniques for Electromagnetic Agility

The concept of electromagnetic visibility plays a very important role within the skin of the cuttlefish. Albeit at optical frequencies, the radial expansion of the chromatophore in the cuttlefish is used to independently reconfigure the RCS of each pigment sac. Hence, when it is stretched in a flat disc (e.g., the surrounding muscles are contracted) the lossy muscular sac surrounding chromatophore becomes stretched very thin. This thin layer of muscle has little effect on the RCS but and the flat disc of colloidal pigment material becomes very visible to incoming light. Conversely, when the lossy muscular sac is folded in on itself (e.g., the surrounding muscles are relaxed) it becomes very opaque and blends in with its surrounding tissues. In this case the chromatophore resembles a sphere of colloidal material coated in a lossy material and the RCS becomes very small in comparison to the disc shape. The visibility of these two structures can then be rapidly controlled through the electrical signals delivered by the nerve axons (neurally controlled) into the muscular chords. When the operation of leucophores and iridophores are integrated into its operation, this becomes a very complex system. However, it illuminates the need to study mechanisms that can be used to alter the electromagnetic visibility of *EFCDs* in reconfigurable antennas and multifunctional smart skins that can be used to enhance electromagnetic agility.

2.3.1. Distributed or Lumped Element Structures

When used throughout the volume of a device, the *EFCDs* can be used to vary the transmission line properties of distributed structures and the equivalent circuit parameters of lumped elements. Fig. 4 shows the basic lossy transmission line of length *dl* with complex propagation constant γ and complex characteristic impedance Z_0 loaded with a nominal complex termination Z_T. Fig. 4 also shows the equivalent circuit (telegrapher) representation for a differential length *dl* of this transmission line with per unit length parameters *R'*, *L'*, *G'*, and *C'* and a parallel RLC-circuit with R_T, C_T, and L_T in place of Z_T. *EFCDs* are shown flowing through all of these elements to notionally illustrate the impact of changing ϑ in (1). At this point, determining Z_0 and γ only require the transverse cross-section of the physical transmission line and, similarly, the geometry of the load termination to find Z_T. In this basic configuration, changing ϑ within the termination and/or transmission line enables the ability to dynamically transform the load impedance seen at the input to this line (Z_{in}) – all parameters *R'*, *L'*, *G'*, *C'*, R_T, C_T, and L_T are a function of

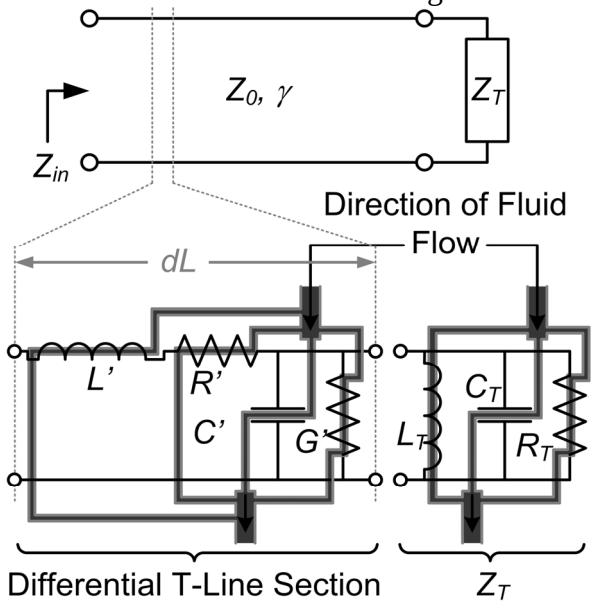

Fig. 4. Notional illustrations demonstrating the use of *EFCDs* in transmission lines and circuits.

ϑ and the ε or μ of both liquid and colloids. As a final stipulation the topology must be a closed geometry to allow fluid-flow. *In this general context, this concept resembles the reflective role of leucophores and iridophores in the cuttlefish's skin.*

2.3.2. Vascular Networks and Perturbations

EFCDs can also be used to locally alter the constitutive parameters and alter the loading or resonant behavior within a structure. For these situations, the material is assumed to be flowing down a capillary or channel that is significantly smaller than a wavelength in more than one dimension. These structures share the main goal of altering the local frequency response so their role resembles the chromatophore. Perturbation techniques provide significant insight into the placement and operation of these capillaries, but also allude to some interesting limitations and and/or requirements for the *EFCDs*. The left side of (3) [19] has been included to show a simplified perturbation expression for this basic behavior, specifically the shift in resonant frequency for a small dielectric perturbation. This is a very well known result, but given the ability to manipulate the constitutive material properties it can be re-examined to understand the limitations of a given perturbation as a function of the volume fraction ϑ of colloidal material in the *EFCD*. This maximum effect, or minimum resonant frequency, is indicated in the right side of (3) by lumping the integral terms into a single function $\Theta(\vartheta)$ and taking the limit of this expression as $\vartheta \to 1$ for high-contrast materials with $s_2 \gg s_1$ in (1). Using (3) it is possible to investigate the maximum electromagnetic visibility from a number of candidate capillary orientations and similar perturbations.

$$\frac{\omega-\omega_0}{\omega_0} = -\frac{\iiint \Delta\varepsilon \vec{E}_{\text{int}} \cdot \vec{E}_0 d\tau}{2\iiint \varepsilon \left|\vec{E}_0\right|^2 d\tau} = \Theta(\vartheta) \to \omega_{\min} = \lim_{\vartheta \to 1}\left[\omega_0\left(1-\Theta(\vartheta)\right)\right] \qquad \textbf{(2)}$$

3. Examples of Bio-Inspired Mechanisms

3.1. Functional Translation of Leucophores and Iridophores

The first step in translating the reflection and phase-shifting properties of the leucophores and iridophores resides in the development of a microfluidic reconfiguration mechanism. The coaxial stub microfluidic impedance transformer (*COSMIX*) shown in Fig. 5 has been considered for this. The *COSMIX* is a modified version of a two-port coaxial measurement cell, with one end capped-off and a small gap *d* left between the center-conductor and metallic end-cap. This 1-port device [8-10] provides a very capable enabling mechanism that also provides many opportunities to examine the interplay within the coupled physical systems (microfluidic, colloidal chemistry, and electromagnetics). Most notably, its reactive impedance can be tuned continuously from inductive to capacitive by altering the composition of *EFCDs* that flow through it. This represents a key component in the design and operation of a reactively controlled directive array [20] (and many other applications) which is very similar concept to the cuttlefish's use of the suns incident energy.

The *COSMIX's* equivalent circuit can also be seen in Fig. 5. The design equations (4) and (5) show how the EFCDs impact the transmission line properties of the coaxial structure and its termination. The CAD model ([8-9]) shows the inlet and outlet for fluid flow down the length of the *COSMIX*. These can be modeled as circular waveguides connected in parallel at their location on the coaxial line. The field structure of the coaxial line and their orientation will excite a *TM*-mode. The inlet/outlet diameter *t* and effective material properties of the *EFCDs* are chosen so these delivery systems remain well below cut-off so no guided modes develop in these structures. As such, they can be modeled as parallel loads with values given by their reactive impedance in cut-off (e.g., very large capacitors in parallel a t- line) and negligible within the frequencies and materials consider here.

$$R' = 0.5R_s\pi^{-1}\left(a^{-1}+b^{-1}\right) \quad G' = \left(\pi\sigma_{eff}\left(\vartheta\right)\right)\Big/\ln a/b$$
$$L' = 0.5\mu_{eff}\left(\vartheta\right)\pi^{-1}\ln a/b \quad C' = \left(\pi\varepsilon_{eff}\left(\vartheta\right)\right)\Big/\ln a/b \qquad \textbf{(3)}$$

$$X_T^{Cap}\left(\vartheta\right) = Z_0\left(\vartheta\right)\left(\frac{4a\sqrt{\varepsilon_{r,eff}\left(\vartheta\right)\mu_{r,eff}\left(\vartheta\right)}}{\lambda_0}\ln\frac{b}{a}\right)\left(\frac{\pi}{4}\frac{a}{d}+\ln\frac{b-a}{d}\right) \qquad \textbf{(4)}$$

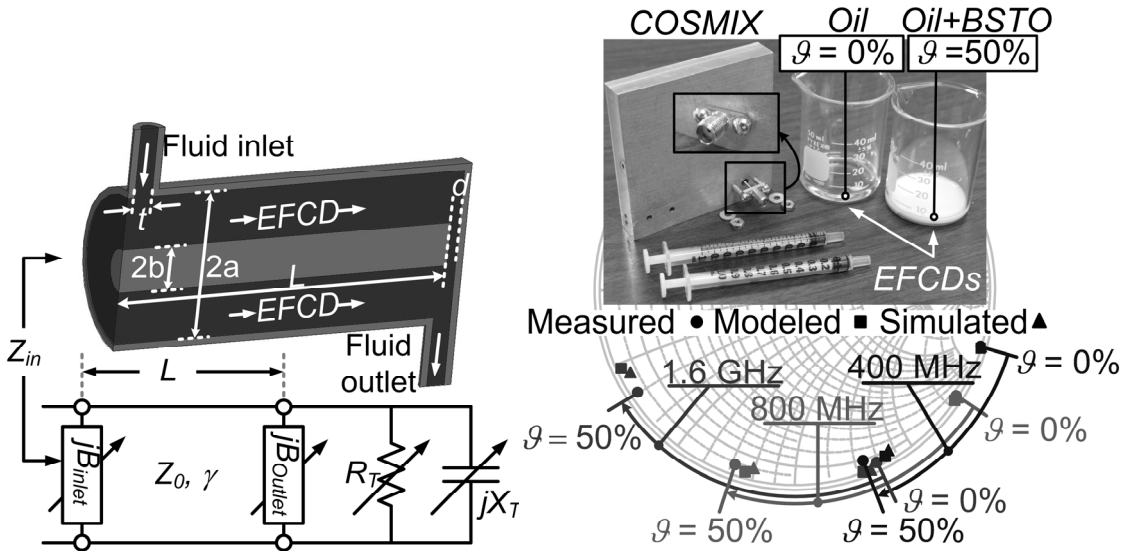

Fig. 5: The CAD model and equivalent circuit of the coaxial stub microfluidic impedance transformer (COSMIX) (right) and measured, modeled, and simulated .

Colloidal Barium Strontium Titanate (*BSTO*) (ε_{r2} ~ 1000 and *tan* δ_2 ~ 0.01) was treated with Nanosperse [18] surfactant (ε_r ~ 8 and *tan* δ ~ 0.11), and then dispersed into low-loss petroleum distillate oil (ε_{r1} ~ 2.1 and δ_1 ~ 0) at two different volume fractions ϑ = {0 and 0.50} to achieve *EFCDs* with ε_{eff} ~ {2.1 and 8.3} and *tan* δ_2 ~ {0 and 0.03}, respectively. These mixtures were vortexed (vigorously shaken and stirred) for 15 min. and sonicated (degassed and sifted) for 30 min. to create a homogeneous sol. Since the overall ϑ of surfactant was small (< 2.5%) this material was not included into the calculations of effective material properties. Fig 4 shows the fabricated structure, beakers

of the *EFCDs* and the measured, modeled, and simulated results at 400 MHz, 800 MHz, and 1.6 GHz. The smith chart was chosen for its ability to demonstrate the reactive loading of the *COSMIX* [1]-[2] as well as the effects from losses. This plot illustrates the significant tunability that can be achieved from fluidic devices that use dynamic material systems. Modeled and analytical results provide a full loop around the smith chart (tuning from inductive to capacitive) but were not included since measured results for those volume fractions were not available, but the agreement between measurement, theory, and simulations are in excellent agreement.

A microstrip patch antenna has been integrated with a COSMIX to demonstrate the bio-inspired ability to ability to alter the reflected fields of an incoming wave. The CAD model in Fig. 6 shows integration of the two structures for a 3 GHz antenna on a foam substrate. The patch has a width w = 50mm, length L = 47.5 mm, and resides on a Rochelle foam substrate with a height h = 3.0 mm and permittivity $\varepsilon_r \sim 1$; this material was chosen to isolate the effects of the COSMIX from other dielectric mechanisms (diffraction of surface waves, etc.) that might contribute to the overall performance. At present, the COSMIX resides at the location of the impedance match for a 50 Ω SMA probe. This will obviously have a significant impact on the performance of the device and is a reference point for future work.

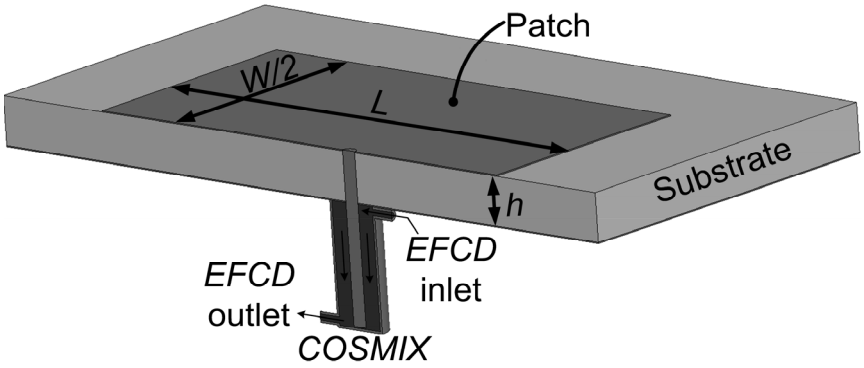

Fig. 6: The CAD model of a COSMIX attached to a microstrip patch antenna.

Simulated results for the COSMIX at 3 GHz can be seen in Fig. 7; simulations using the previously discussed EFCD dispersions are shown to illustrate the full scope of reactive loading possible. Measured results were not available for these systems due to limitations in the synthesis of these systems and the amount of data points desired to show the continuous level of tuning available. However, earlier measurements provide some validation to these results. Fig. 7 shows the limits for a monodispersed system and the continuation for a polydispersed system as well as the loading required to facilitate 360 of phase shift in the reflectarray element. Fig. 8 shows the simulated results of the element shown in Fig. 6. These results were obtained by simulation this integrated antenna in a waveguide configuration, and based on this study a volume fraction of at least $\vartheta = 0.78$ is required for the necessary phase shift which alludes to the use of different materials of a polydispersed system.

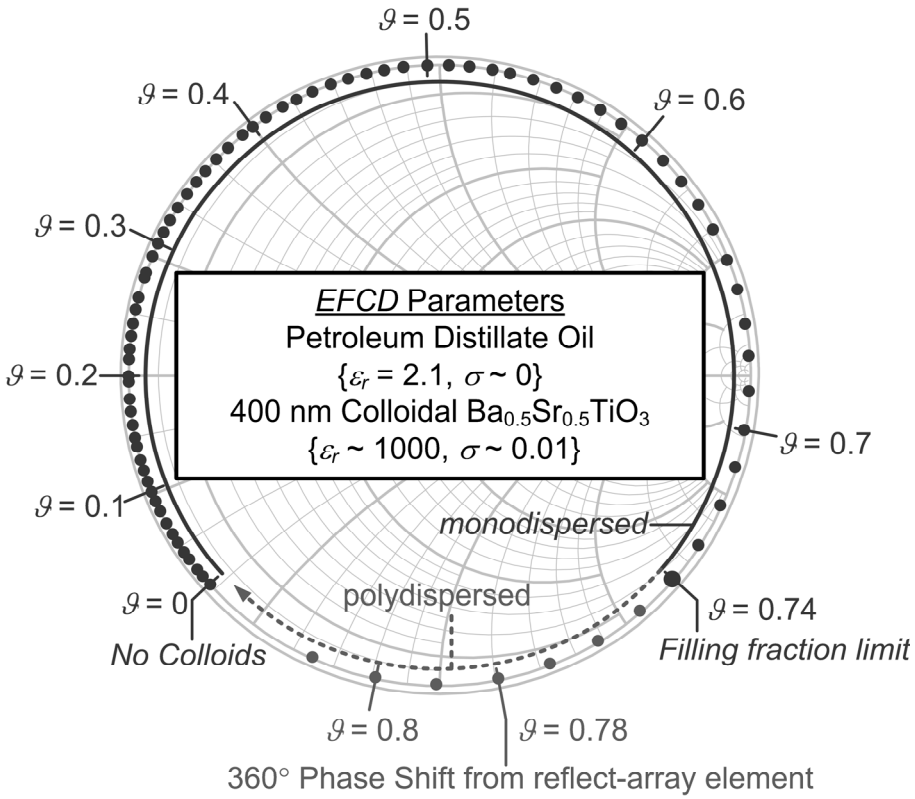

Fig. 7: Reactive impedance of the COSMIX at 3 GHz for BSTO dispersed into oil, including the filling fraction limit for monodispersed systems and the continuation to a polydispersed system.

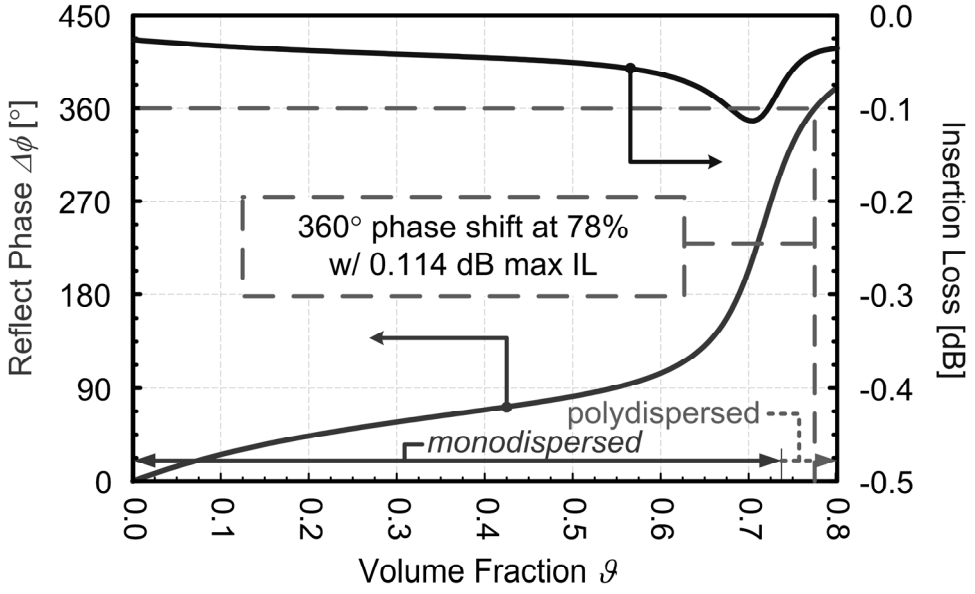

Fig. 8: Resulting phase shift from the reflectarray element in Fig. 5 including the filling fraction limit for monodispersed systems and the continuation to a polydispersed system.

3.2 Functional Translation of Chromatophores

The frequency reconfigurable patch antenna in Fig. 9 [8] provides an excellent means of studying the capabilities and limits of EFCD-based perturbation mechanisms. The cavity model of the structure is used first to identify the regions of EM visibility for a given EFCD. Perturbation theory then quantifies the effects from a small, properly placed, capillary perturbation and guides the integration of capillary-driven EFCDs into the center for magnetic materials and the edges for dielectric materials (both with respect to the resonant direction of the patch antenna). This generalizes the structure for both dielectric and magnetic materials. The same material system was used in this section as in Sect. 3.1 for three different volume fractions ϑ = {0, 0.25 and 0.50} to achieve *EFCDs* with ε_{eff} ~ {2.1, 4.1, and 8.3} and *tan* δ_2 ~ {0, 0.012 and 0.03}, respectively. In this configuration, where the fields of the patch are normal to the axis of the EFCD cylinder, the perturbation experiences a limit in the attainable frequency shift. This will be discussed in more detail during the presentation of this material but the measured results (Fig. 10) of these dispersions and deionized water (DI water) have been included to show the non-linear behavior and limit as EFCDs flow through the two outer capillaries.

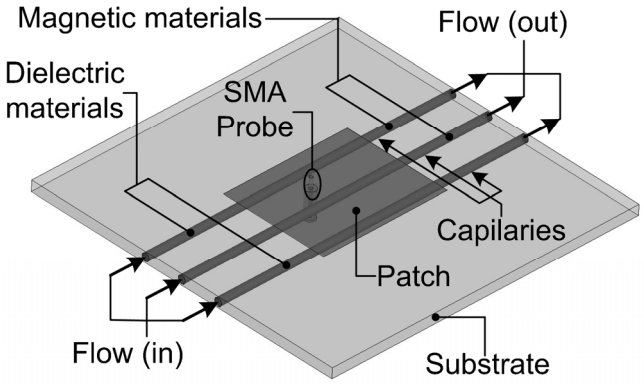

Fig. 9. Microstrip patch with substrate-embedded capillaries that flow EFCDs.

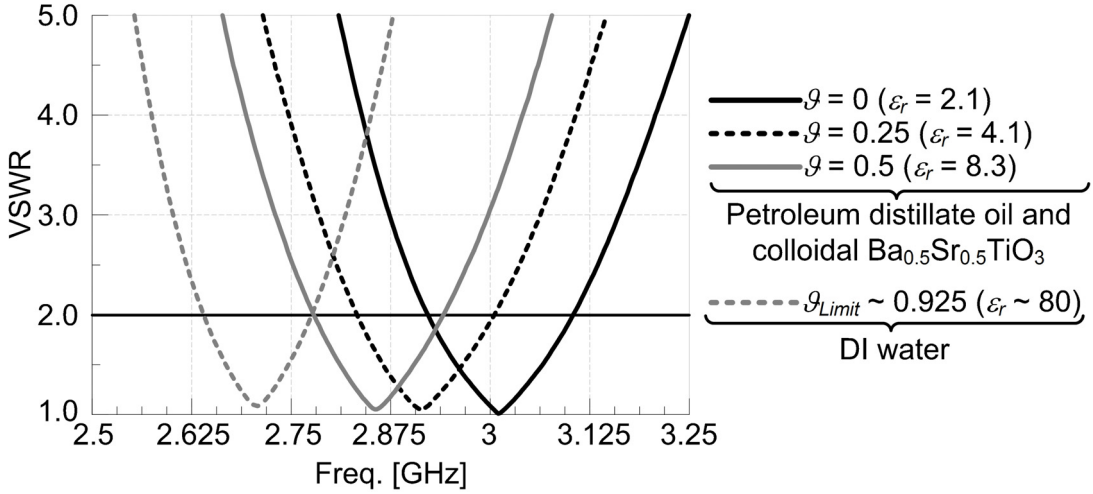

Fig. 10. Measured results for the structure shown in Fig. 8.

The concepts used to reconfigure the microstrip patch antenna can also be applied to antennas and other structures that operate within smart skins and/or within polymorphic systems. The structure in Fig. 11 has been used to evaluate the abilities of biologically inspired mechanisms from the first thrust as a cognitive (self-stimulating) and non-cognitive (externally stimulated) mechanism to stabilize (e.g., compensate) the *EM* performance of antennas that are subject to structural deformations. This section is related to active (e.g., transport) reconfiguration mechanisms, but distinctly important since the extreme flexing or bending of an antenna can create severe detuning (or even complete failure) [21]. This can be conceptualized by considering the antennas on a morphing wing aircraft or on the flailing arms of a space-walking astronaut in distress. Without circuitry to monitor and correct its performance, this antenna failure can lead to devastating problems should the antenna provide critical functions (radio for help, etc.), but this adds undesired complexity**.**

Fig. 11 shows a probe-fed, linearly polarized microstrip patch antenna designed for 3 GHz that has been used to demonstrate the potential of ongoing work for cognitive, capillary-based compensation mechanisms. The linearly polarized microstrip patch antenna which has a rigid bend along a single axis represents a conformally integrated antenna in this work that undergoes morphing. Although many possibilities exist, the physical deformation shown in Fig. 11 represents an initial investigation into the development of more rigorous compensation techniques. The bend occurs at the center of the patch along the resonant length *L*, and downward pivots at the ground plane about an axis coincident to the width direction. This detunes the antenna to a lower resonant frequency and alters the location where the probe must reside to maintain an impedance match. This indicates that a properly designed *and* placed mechanism (that can locally alter the electrical length) will mitigate this behavior.

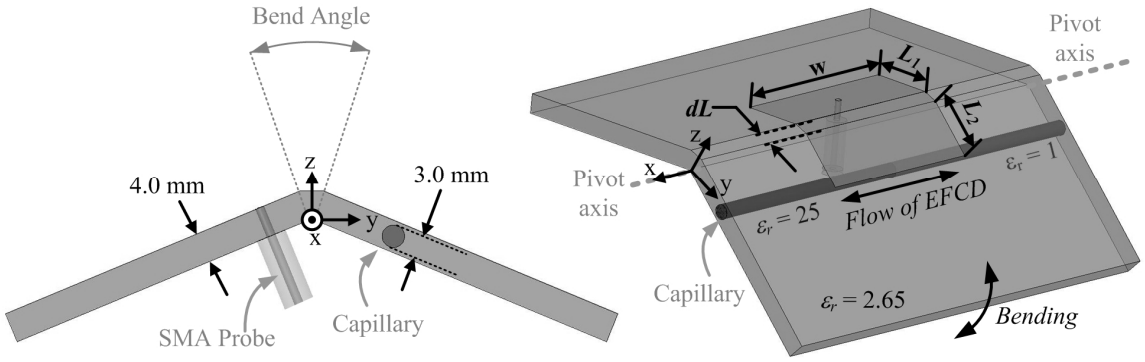

Fig. 11. A capillary compensation mechanism that corrects the antenna's detuning through the displacement of *EFCDs*.

The bend-assisted displacement of electromagnetically functionalized colloidal dispersions (EFCDs) in a capillary structure has been chosen as a novel means to compensate the effects of bending. This represents a different mechanism than the reconfigurable antenna (which alters the volume fraction of colloids in the EFCD). It can

be designed as a reactionary measure that operates similar to a fire billow or accordion; displacing appropriately engineered EFCDs into/out of local reservoirs as morphing occurs. The cavity model of the microstrip patch antenna, perturbation theory for materials, and the lengthening effect from bending all motivate the placement of a single, substrate-embedded capillary structure and the composition of the EFCDs it will transport. The EFCDs, assumed immiscible with respect to one another, operate in a high-low configuration. The design of the unbent patch shortens its resonant length to include the capillary with a high-permittivity EFCD. As the patch bends, the low-permittivity EFCD displaces the high-permittivity EFCD, maintaining the impedance match. Simulated and measured results for this operation can be seen in Figs. 12 and 13.

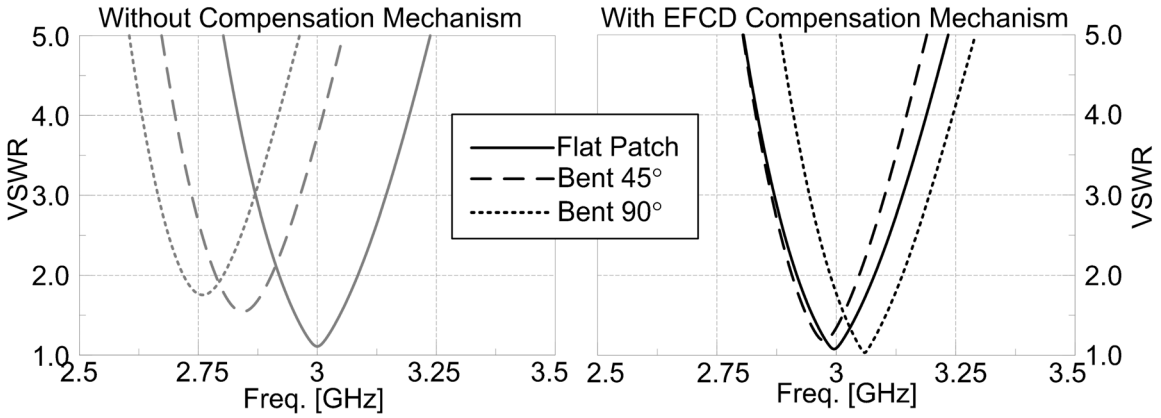

Fig. 12. Simulated VSWR for a patch antenna with (right) and without (left) the EFCD compensation mechanism and bending at 0°, 45°, and 90°.

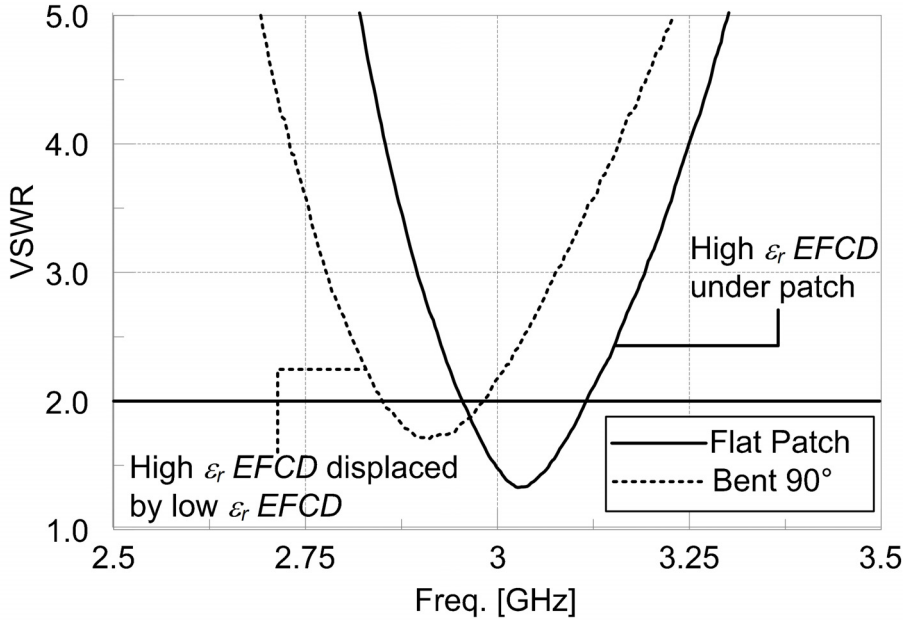

Fig. 13. Measured VSWR for a patch antenna with the EFCD compensation mechanism bending at 0° and 90°.

Comparison of the two plots in Fig. 12 shows the effects from bending. With no mechanism (left side), the patch has completely detuned from its original impedance bandwidth by the time it bends to 45°. In contrast, the patch with a compensation mechanism and the same 45° deformation maintains a majority its impedance bandwidth. Validating the effectiveness of this technique, the 90° bend overcompensates and shifts the bandwidth upward (this can be resolved by altering the EFCD composition and capillary diameter). In total, this provides as overlapping bandwidth of 59 MHz throughout the entire deformation process. The EFCDs used for measurements (Fig. 13) were identical to the previous studies, in which the 50% volume fraction (ε_r = 8.3) did not provide the necessary value of permittivity (ε_r = 25) to shift the impedance back to its desired state. A more detailed discussion on this mechanisms and its equivalent circuit model will be provided during the presentation of this material.

Simulated gain patterns at 3 GHz have been included in Fig. 14 to illustrate the effects of bending on radiation. These patterns are spatially aligned to the coordinate system shown in Fig. 10, where the patch bends around the x-axis. Though the design mitigates the impedance effects of deformation, the radiation pattern remains comparable to the unmodified patch – both show a broadening of co-polar, E-plane (yz-plane) radiation patterns which decreases the directivity. However, the control and compensated antennas' response to the deformation differs. The control patch has little cross-polarization when flat but experiences an increase as it bends, while the modified patch shows the opposite trend (also recovering symmetry in the ϕ = 90° plane).

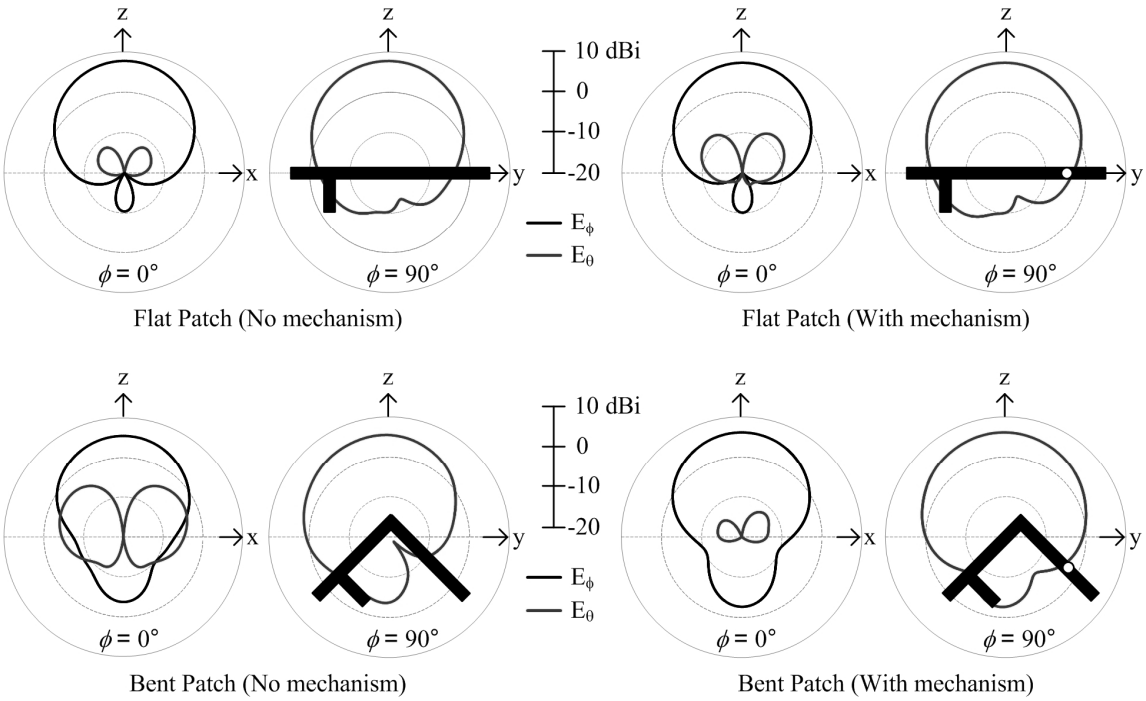

Fig. 14. Elevation radiation patterns for the patch antenna with (right) and without (left) a compensation mechanism for a flat patch and patch bent to 90°.

4. Summary

This manuscript has provided a summary of biologically inspired mechanisms currently under investigation for applications in multifunctional smart skins and reconfigurable antennas. Specifically, the adaptive skin behavior of the cuttlefish (chromatophores, iridophores, and leucophores) has been used to inspire microfluidic reconfiguration and compensation mechanisms that transport, mix, and/or displace electromagnetically functionalized colloidal dispersions (EFCDs). Theory and measurements have been used where possible to illuminate the current state of this concept, and simulated results have been used to extend these concepts where measurements were not readily available. Ongoing work will developing these concepts and apply then to more complex systems where they can work in tandem to support polymorphic systems and smart structures.

5. Bibliography

[1] N. J. Marshall, J. B. Messenger, "Colour-blind camflouge," *Nature*, vol. 382, August 1996, pp. 408 – 409.

[2] P. K. Loi, R. G. Saunders, D. C. Young, and N. J. Tublitz, "Peptidergic regulation of chromatophore function in the European cuttlefish Sepia Officinalis," *The Journal of Experimental Biology*, vol. 199, pp. 1177–1187, January, 1996.

[3] N. Shashar, D. T. Borst, S. A. Ament, W. M. Saidel, R. M. Smolowitz, and R. T. Hanlon," Polarization reflecting Iridophores in the arms of the squid Loligo pealeii," *The Biological Bulletin*, vol. 201 October 2001, pp. 267 – 268.

[4] A. Barbosa, L. M. Mäthger, C. Chubb, C. Florio, C. C. Chiao, and R. T. Hanlon, "Disruptive coloration in cuttlefish: a visual perception mechanism that regulates ontogenetic adjustment of skin patterning," Journal of Experimental Biology, vol. 210, pp. 1139 – 1147, 2007.

[5] L. M. Mathger and R. T. Hanlon, "Anatomical basis for camouflaged polarized light communication in squid," *Biology Letters*, vol. 2, September 2006, pp. 494 – 496.

[6] Nova, Public Broadcasting Services (PBS), "Kings of camouflage," April 2007, http://www.pbs.org/wgbh/nova/camo/.

[7] D. Stuart-Fox, A. Moussalli, and M J. Whiting, "Natural Selection on Social Signals: Signal Efficacy and the Evolution of Chameleon Display Coloration," *Am Nat*, Vol. 170, pp. 916–930, Dec., 2007.

[8] G. H. Huff, P. Bahukudumbi, W. N. Everett, A. Beskok, M. A. Bevan, D. Lagoudas, Z. Ounaies, "Microfluidic Reconfiguration of Antennas," in proc. 2007 *Antenna Applications Symposium*, Allerton Park, Monticello, Illinois, September 2007, p. 241 – 258.

[9] G. H. Huff and S. Goldberger, “A Coaxial Stub Microfluidic Impedance Transformer (*COSMIX*),” *IEEE Microwave and Wireless Components Letters*, to be submitted Aug. 2008.
[10] G. H. Huff, “Electromagnetically Functionalized Colloidal Dispersions and Microfluidic Reconfiguration Mechanisms for Phase-Reconfigurable Reflectarray Elements,” in proc. *2008 URSI General Assembly*, Chicago, IL, Aug. 2008.
[11] Sean Goldberger and G. H. Huff, “Frequency Reconfiguration of a Microstrip Patch Antenna Enabled by Colloidal Dispersions,” in proc. *2008 URSI North American Radio Science Meeting*, Boulder, CO, Jan. 2008.
[12] G. H. Huff and S. Goldberger, “Integration of colloidal materials in enabled vascular reconfiguration mechanisms in a microstrip patch antenna,” in review *IEEE Antennas and Wireless Propagation Letters*, to be submitted Aug. 2008.
[13] S. A. Long and G. H. Huff, “A Study of Microfluidic Compensation Mechanisms for Deformable Antennas,” in proc. *2008 URSI General Assembly*, Chicago, IL, Aug. 2008.
[14] S. Andrew Long and G. H. Huff, “Colloidal-Based Cognitive Compensation Mechanisms for Microstrip Antennas,” in review for 2009 16th SPIE Conf. Smart Structures/NDE.
[15] P. Bahukudumbi, W. N. Everett, A. Beskok, M. A. Bevan, G. H. Huff, D. Lagoudas, and Z. Ounaies, “Colloidal microstructures, transport, and impedance properties within interfacial microelectrodes,” *Applied Physics Letters*, vol. 90, 224102, May 2007.
[16] J. McDonald and G. H. Huff, “Microfluidic Mechanisms for Reconfigurable Dielectric Resonator Antennas,” in proc. *2008 URSI General Assembly*, Chicago, IL, Aug. 2008.

[17] G. H. Huff, P. Bahukudumbi, W. N. Everett, A. Beskok, M. A. Bevan, D. Lagoudas, Z. Ounaies, “Electromagnetically Tunable Fluids for Microfluidic Reconfiguration of Antennas,” in proc. *2007 URSI North American Radio Science Meeting*, Ottawa, ON, Canada, July 2007.

[18] A. Sihvola, Electromagnetic Mixing Formulas and Applications. Padstow, Cornwall, TJ International, 1999.

[19] N. Marcuvitz, Waveguide Handbook. New York, NY: McGraw-Hill Book Company, 1951.

[20] R. Harrington, “Reactively controlled directive arrays,” IEEE Transactions on Antennas and Propagation, vol. 26, pp. 390 – 395, May 1978.

[21] S. Koulouridis, G. Kiziltas, Y. Zhou, D. J. Hansford, and J. L. Volakis, "Polymer–Ceramic Composites for Microwave Applications: Fabrication and Performance Assessment," *Microwave Theory and Techniques, IEEE Transactions on*, vol. 54, pp. 4202-4208, 2006.

INVESTIGATION OF THE NULL STEERING CAPABILITY OF YAGI-UDA ARRAYS WITH VARIABLE REACTIVE LOADS

David F. Kelley
Department of Electrical Engineering
Bucknell University
Lewisburg, PA 17837
(570) 577-1313, dkelley@bucknell.edu

and

Timothy J. Destan
previously with:
Department of Computer Science
Bucknell University
Lewisburg, PA 17837
currently with:
High Performance Technologies, Inc.
4121 Wilson Boulevard, Suite 200
Arlington, VA 22203-1839
(703) 682-5382, tdestan@hpti.com

Abstract

The classic Yagi-Uda array is a static antenna in the sense that its radiation pattern is fixed except for the possibility of mechanical rotation. Although very high gain can be achieved using a simple physical structure, the side and back lobe levels can be relatively high, and the nulls can be relatively shallow. However, there are occasions in which it is desirable to steer a deep null toward a direction off the main beam in order to reduce interference in reception mode or to avoid interfering with a nearby user of the spectrum in transmission mode. If the array has a sufficiently large number of elements, this can be accomplished via adjustment of variable reactive loads connected to one or more of the outermost director elements. This paper presents the results of a preliminary study to investigate the null depths that can be achieved using controlled reactive loading and its influence on the gain and input impedance of the array. It is shown that effective null steering can be realized in most directions without significantly reducing the gain or seriously degrading the return loss at the feed point.

1. Introduction

Yagi-Uda array antennas (hereafter referred to as "yagis") consist of a single "driven" dipole element, nominally 0.5λ in length and connected directly to a receiver or RF signal source, and several additional parallel dipole elements that have no physical RF connections but that interact with the driven element and each other via mutual coupling. The latter are called *parasitic* elements. All of the elements are usually mounted at their centers along a support structure called a *boom*. A plan view of a typical yagi array is shown in Figure 1. By adjusting the lengths of the parasitic elements and the inter-element spacings, the array can be made to radiate in the end-fire direction. There is usually only one parasitic element, called the *reflector*, located behind the driven element. The remaining elements on the radiating side of the driven element are called *directors*. A common element notation scheme is included in Figure 1.

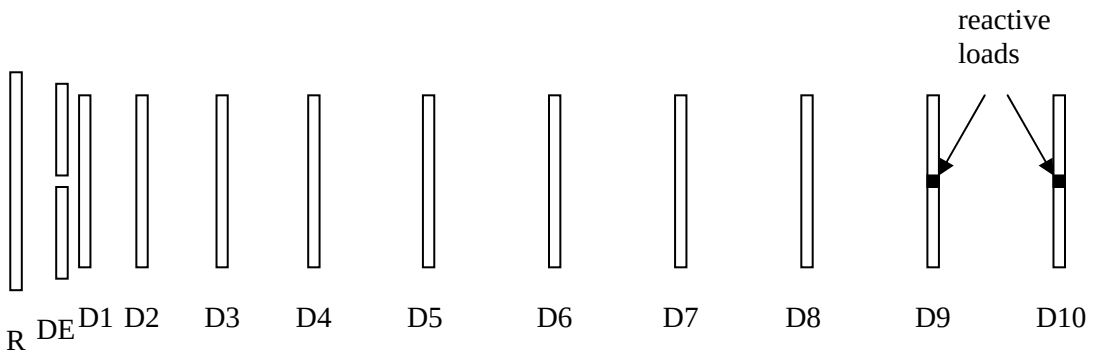

Figure 1. Plan view of a 12-element yagi array. The element labeling scheme used here is: R = reflector, DE = driven element, and D = director. The proposed reactive loads would be located at the centers of the directors at or near the front end of the array.

A key advantage of the yagi is that it exhibits relatively high gain using a mechanically simple structure. Although the sidelobe performance is not usually as good as that of other arrays of comparable size, yagis are widely used in the HF through lower microwave regions. Nevertheless, there are situations in which better rejection of signals in specific directions outside the main beam might be desirable. For example, a co-user of the spectrum might begin transmitting nearby, or it might be necessary to minimize interference to that user. A jammer, a strong noise source, or an inadvertent generator of in-band intermodulation products might appear. In these cases, the signal-to-interference ratio might be degraded enough to compromise the communication channel. One solution is to rotate the antenna (if it is rotatable) enough so that one of the nulls points

toward the offending source; however, this might move the desired signal well outside the main beam.

The solution proposed here is to load one or more of the parasitic elements with variable reactive loads (capacitors, inductors, transmission line stubs, or various combinations) that can alter the relative phases of the element currents in such a way to create a null in the direction of the interfering signal. If only a few elements are adjusted in this way, the shape and strength of the main beam should not be affected significantly, and the gain of the array should remain close to its nominal value. The input impedance should also change very little. Thus, the signal-to-interference ratio would be improved with little cost to other important performance parameters.

It is not usually possible to determine directly the reactive load values required to steer a null to a specified direction. Therefore, an optimization procedure of some kind must be employed to determine the appropriate load settings, or an adaptive algorithm must be used to control the settings. In either case, it would be useful to know *a priori* how much improvement in the signal-to-interference ratio (SIR) can reasonably be expected. The purpose of this paper is to apply a stepped range of reactive load values to the elements of a test bed yagi array in a numerical simulation and record the best null depths that can be achieved in various directions in the sidelobe region of the radiation pattern. The increment between reactance values is comparable to the tolerance typically obtained with realistic components. For the cases considered it will be shown that improvements in SIR of 20 dB or more can be obtained in most directions. Details of the methodology used are described in Section 2.

The proposed approach involves the evaluation of hundreds or even thousands of load configurations, each of which requires the calculation of a unique radiation pattern. If a full-wave analysis approach such as the method of moments, the finite element method, or the finite difference time domain method were used to find each pattern, the computation time could be quite lengthy. However, because only the element loads are changed and the array geometry remains constant, a faster approach that makes use of the embedded element patterns of the array can be used. (Embedded element patterns are also sometimes called active element patterns or collectively called the array manifold.) Once the embedded element patterns have been determined (a relatively fast process), the radiation pattern can be found quickly and efficiently for each new set of reactive loads. Details of this procedure are presented in Section 3.

The results of numerical simulations in which all possible reactance value combinations within reasonable limits are systematically applied to two test bed arrays are presented in Section 4. The data confirm many of the anticipated results outlined above, but some unexpected outcomes are also noted. Concluding remarks are presented in Section 5.

2. Methodology

In order to minimize gain deterioration and departure from the nominal input impedance of the array, the smallest number of reactive loads necessary to achieve the desired null depth should be used. Thus, *Matlab* m-files were written to calculate radiation patterns for the cases in which only one or two array elements are loaded with reactances. In each case, the loads may be applied to any element(s) desired. When only one element is loaded, the reactance value is allowed to vary from −1000 Ω to 1000 Ω in 20-Ω steps (a total of 101 values). It is assumed that reactances outside this range would amount to an open circuit, effectively removing the element from the array. The same reactance range and increment are used in the two-load case, resulting in $101^2 = 10{,}201$ possible combinations. For both the one-load and the two-load configurations, the null depths are calculated across the sidelobe region in five-degree increments for each set of reactance values, and the best null depths obtained in each direction are stored. Because the gain changes as loads are applied, the maximum and minimum gain values obtained over the range of applied reactance values are saved. The input impedance corresponding to each set of reactance values is also stored. The reactance values that lead to the best null depths in each direction are saved as well.

The act of adding a variable reactive load to a yagi element has the same effect as changing its length, which in turn is likely to affect the gain, input impedance, sidelobe level, and null direction(s) of the array. Of course, the last item in the list is the point of the exercise. The effect on sidelobe level is assumed not to be critical in this case, since the objective is to focus on only one azimuth in the sidelobe region, that is, the direction of a jammer or a legitimate sharer of the spectrum. Presumably, the sidelobe levels in the other directions would be of less importance. One of the expectations at the outset of this investigation was that gain and input impedance would be least affected if the reactive loads were located on the director elements farthest away from the driven element, since those elements typically support the weakest currents in the array and are the most weakly coupled to the driven element. This same line of reasoning leads to the second expectation that deterioration of gain and input impedance should decrease with increasing array length. With these ideas in mind, a 12-element array was chosen as the primary test bed antenna for this investigation. This number of elements represents a good compromise between sufficient length to avoid detuning effects and reasonable computation time. A six-element array is also briefly examined in order to confirm that shorter arrays are indeed more sensitive to element detuning.

There is a wide variety of yagi designs in the professional and amateur literature from which to choose. A guiding principle in the selection process was to find a design that exhibits stable performance over a relatively wide bandwidth. An input impedance of 50 Ω, if available, would also be desirable. The assumption was that such an array might have greater immunity to the detuning effects of reactive loading. The evolution of yagi array design has benefited greatly from the availability of modern computational analysis software. The arrays that serve as the starting points for the investigation presented here

are based on the optimized wideband antenna (OWA) design approach first proposed by Breakall [1]. A striking characteristic of OWA yagis is that the first director is located very close to the driven element. The spacing is typically much less than 0.1λ and is often close to 0.05λ. OWA yagis exhibit very wide impedance matching bandwidths (frequently approaching 10%) and gain and sidelobe level bandwidths that are nearly as wide for modest element diameters. In fact, for a given diameter, OWA yagis seem to exhibit much wider bandwidths than any other known designs. This exceptional bandwidth performance comes at the cost of a modest reduction in gain (usually 0.5-1.0 dB) compared to other arrays of the same boom length.

While several different OWA yagis have been built successfully, there appears to be little theoretical background on the design technique available in the literature. Recently, Cebik performed a series of detailed empirical investigations aimed at determining the critical design parameters of OWA yagis [2, 3]. The result of his analysis is a family of yagi designs ranging from six to 20 elements for several of the VHF and UHF amateur radio bands. Common to all of the designs is a nominal input impedance of 50 Ω. One of them, a 12-element array for the amateur radio "two-meter" band (144-148 MHz) serves as the main test bed antenna here [3]. The six-element OWA yagi designed by Cebik for the same band is also used. Both arrays have element diameters of 3/16 inch (4.7625 mm) and use non-conducting booms. Other dimensional details are given in Section 4. Both yagis were optimized at a frequency of 146 MHz, but their operational bandwidths extend well beyond the 144-148 MHz band.

3. Efficient Pattern Calculation

As mentioned earlier, hundreds or thousands of radiation patterns must be calculated in order to determine the potential null steering performance of a loaded array. Consequently, the use of traditional full-wave analysis techniques would lead to an impractically time-consuming algorithm. This section describes an alternative approach that makes use of the embedded element pattern data and mutual impedance matrix of the array. The basic method was first presented by Harrington [4] and was later elaborated upon by Kelley [5, 6] and other investigators. A summary of the approach is presented here for convenience.

As shown in [5, 6], the principle of superposition allows the total radiated field $\mathbf{E}(\theta,\phi)$ of an array, whether it consists of active or parasitic elements (or a combination), to be expressed by

$$\mathbf{E}(\theta,\phi) = \sum_{n=1}^{N} V_n \mathbf{f}_{sc,n}(\theta,\phi)\,, \tag{1}$$

where N is the total number of elements in the array, V_n is the voltage measured at the terminals of the n^{th} element (as shown in Figure 2 below), and $\mathbf{f}_{sc,n}(\theta,\phi)$ is the *short-circuit embedded element pattern* of the n^{th} element. Boldface type is used here to indicate vector quantities. The embedded element pattern is the electric field radiated by the entire array when the terminal voltage of the n^{th} element is forced to have a value of unity at zero phase and the terminals of all of the other elements are short-circuited. An embedded element pattern generally consists of both magnitude and phase data (or, equivalently, in-phase and quadrature data). Of course, for a standard (unloaded) yagi array, there is only one non-trivial embedded element pattern, since none of the other elements have loads connected to them across which voltages can appear.

Note that in previous publications by Kelley, embedded element patterns have been represented by the variable **g**. It has finally dawned on him that a reader could easily confuse this with the *gain* pattern of the array and that the use of the variable **f** is a much better choice for representing the *field* pattern. Thus, the variable **f** (or *f* in the case of scalar data for one polarization) will be used throughout this paper.

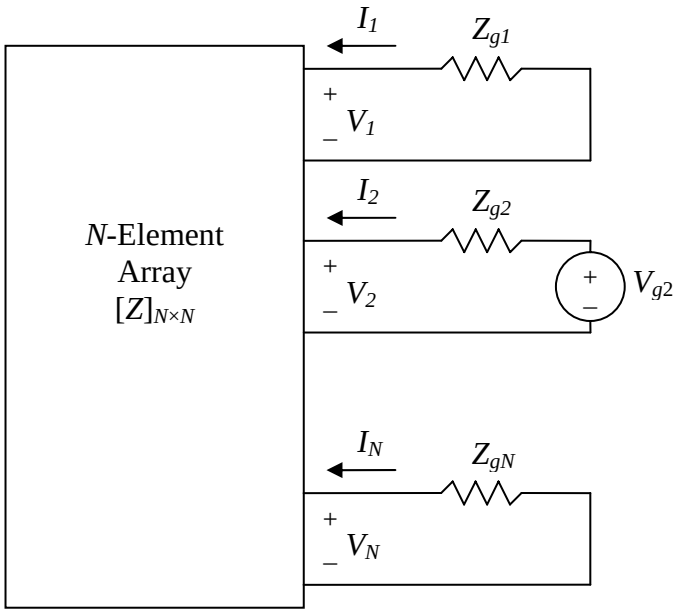

Figure 2. Network representation of an *N*-element yagi array. Although resistor symbols are used here, the loads are reactive (have purely imaginary values) in the ideal case and are complex-valued in practice. Port #2 is usually assigned to the driven element.

If there are only M discrete angular directions for which pattern data must be computed, then the expansion given in (1) can be expressed in matrix form as

$$[E] = [f_{sc}][V], \tag{2}$$

where $[E]$ is an $M \times 1$ vector containing the radiated electric field, $[f_{sc}]$ is an $M \times N$ matrix containing the embedded element pattern data, and $[V]$ is an $N \times 1$ vector containing the terminal voltages. The $[f_{sc}]$ matrix is formed by filling the n^{th} column with the pattern data for the n^{th} element. Each column is subdivided according to the polarization components of interest. For example, the upper half of $[f_{sc}]$ might contain data for the θ-component, and the lower half the ϕ-component. The vector would consist of only one component type if the other component type were of no interest. The data in the $[E]$ vector is decomposed in a similar manner. All quantities in (2) are complex valued.

A loaded yagi array can be considered to be an N-port network with up to $N-1$ loads connected to the parasitic elements and an RF signal source connected to the driven element. A graphical depiction of the network representation is shown in Figure 2. Non-zero voltages appear across the terminals due to the effects of mutual coupling between the various elements if loads are present. If the generator voltage V_{g2} connected to the driven element is known, the voltages across the reactive loads can be found via

$$[V] = [Z]\{[Z] + [Z_g]\}^{-1}[V_g], \tag{3}$$

where $[V_g]$ is an $N \times 1$ vector that contains a non-zero value in the second position and zeros elsewhere; $[Z]$ is the $N \times N$ mutual impedance matrix that relates the terminal voltages to the terminal currents; and $[Z_g]$ is an $N \times N$ diagonal matrix that holds the values of the reactive loads. If desired, the generator impedance Z_{g2} can be included in $[Z_g]$; however, its value has no effect on gain calculations, and its corresponding entry in the matrix is usually set to zero. The $[Z_g]$ matrix for an array with loads connected to the last two directors would have the structure

$$[Z_g] = \begin{bmatrix} 0 & \cdots & & 0 \\ & 0 & & \\ \vdots & \ddots & & \vdots \\ & & jX_1 & \\ 0 & \cdots & & jX_2 \end{bmatrix}. \tag{4}$$

If it is necessary to model realistic effects such as component losses or stray reactances, complex impedances could fill the appropriate entries in the $[Z_g]$ matrix.

Substitution of (3) into (2) yields the matrix expression

$$[E] = [f_{sc}][Z]\{[Z] + [Z_g]\}^{-1}[V_g], \tag{5}$$

which can be used to calculate the radiation pattern of a loaded yagi array very quickly. Since the matrices $[f_{sc}]$ and $[Z]$ depend only on the array geometry and not on the applied loads or sources, they can be computed *a priori* and stored for use by the Matlab algorithm described in Section 2. For each new set of reactive load values, it is necessary only to fill the appropriate entries on the main diagonal of $[Z_g]$, add it to $[Z]$, invert the sum, and finally perform the matrix multiplication in (5). Because the size of $[Z] + [Z_g]$ is equal to the number of array elements rather than the much larger number of segments in the moment method model, the algorithm is very efficient.

The input impedance Z_{in} of the array is given by

$$Z_{in} = \frac{V_2}{I_2}, \tag{6}$$

where V_2 is the voltage across the terminals of the driven element, and I_2 is the corresponding input current. These quantities can be extracted from the terminal voltage vector, which can be found using (3), and the current vector, which can be found using the network form of Ohm's law, $[I] = [Z]^{-1}[V]$.

The gain of the array in any given direction (θ, ϕ) for a particular polarization is found using

$$G(\theta,\phi) = \frac{4\pi r^2 |E(\theta,\phi)|^2}{\eta P_{in}}, \tag{7}$$

where r is the distance at which the embedded element pattern data are calculated; η is the intrinsic impedance of free space (377 Ω); and P_{in} is the input power to the array. The last quantity can be found via $P_{in} = |I_2|^2 \, \mathrm{Re}\{Z_{in}\}$, where it is assumed that the input current I_2 is expressed in rms units.

4. Examples and Results

Two test bed arrays based on OWA yagi designs by Cebik [3] are used to illustrate the potential null steering capability of reactive loading. The mutual impedance matrices and embedded element patterns required for the pattern calculation approach described in Section 3 were generated using *EZNEC* [7], a commercial implementation of the moment method-based software suite *NEC*-2. H-plane patterns were used here instead of E-plane patterns in order to remove the potentially beneficial effect of the element pattern null 90° from the direction of the main beam in the latter.

The algorithms used to generate the radiation pattern data for the various load reactance configurations were implemented in *Matlab*. The algorithms read in the raw embedded element pattern and element current data generated by *EZNEC*, organize those data into the embedded element pattern and mutual impedance matrices, and then calculate using (5) and (7) the radiation patterns for load reactance values ranging from −1000 Ω to 1000 Ω in 20-Ω steps. Typical elapsed times to cycle through the whole range of values for one loaded element are less than one second using a late model laptop computer with an Intel 2.16 GHz Core2 Duo processor running the Windows XP Pro operating system. For two loads the elapsed time is less than four seconds. The *Matlab* m-files are available upon request from the authors.

4.1 12-Element Array

The dimensions of the 12-element test bed array are given in Table 1, and a plan view that provides a visual depiction of the lengths and spacings of the elements relative to each other is shown in Figure 3. The extremely close spacing between the driven element and the first director that characterizes OWA designs is evident, in this case only 0.057λ.

Initially, only one array element was loaded with a variable reactance, beginning with Director #10, the one furthest from the driven element. As described in Section 2, the radiation pattern was computed for every load reactance value from −1000 Ω to 1000 Ω, and the best null depths obtained, along with the reactance values that led to them in each direction, were stored. The results for Director #10 (Element #12) are presented in Figure 4 and Table 2. The solid line in Figure 4 shows the extent to which radiation can be minimized in any given direction by varying the load attached to the last director. For example, at 140° from the main beam a null of approximately 40 dB below the peak gain can be produced using a load reactance of −60 Ω. All other reactances within the allowable range produce field strengths greater than or equal to that level in that direction. The dashed line shows the sidelobe region of the original (unloaded) array. The use of a single reactive load at Element #12 can improve the signal-to-interference ratio (SIR) by up to 15 dB or so, but only in a few narrow angular ranges. In many directions, no significant improvement is possible.

Table 1. Element lengths and spacings of a 12-element OWA yagi array designed by Cebik [3]. The diameter of each element is 3/16 inch (4.7625 mm). A non-conducting boom is assumed.

Element	Length (mm)	Space from Reflector (mm)
Reflector	1038	--
Driven Element	1000	223
Director 1	940	340
Director 2	922	645
Director 3	924	1034
Director 4	920	1559
Director 5	894	2197
Director 6	872	2946
Director 7	854	3724
Director 8	836	4531
Director 9	818	5334
Director 10	792	6045

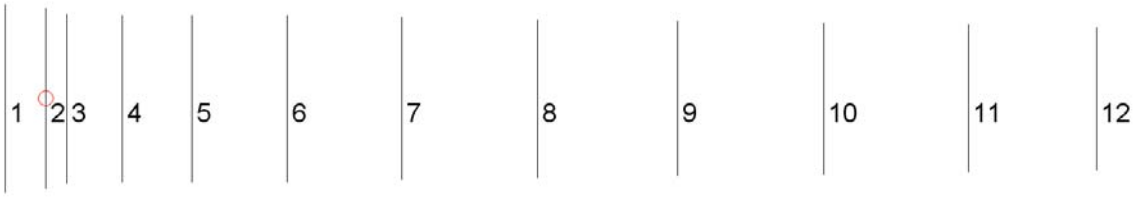

Figure 3. Plan view of a 12-element OWA yagi designed by Cebik. The circle in the middle of Element #2 indicates the feed point.

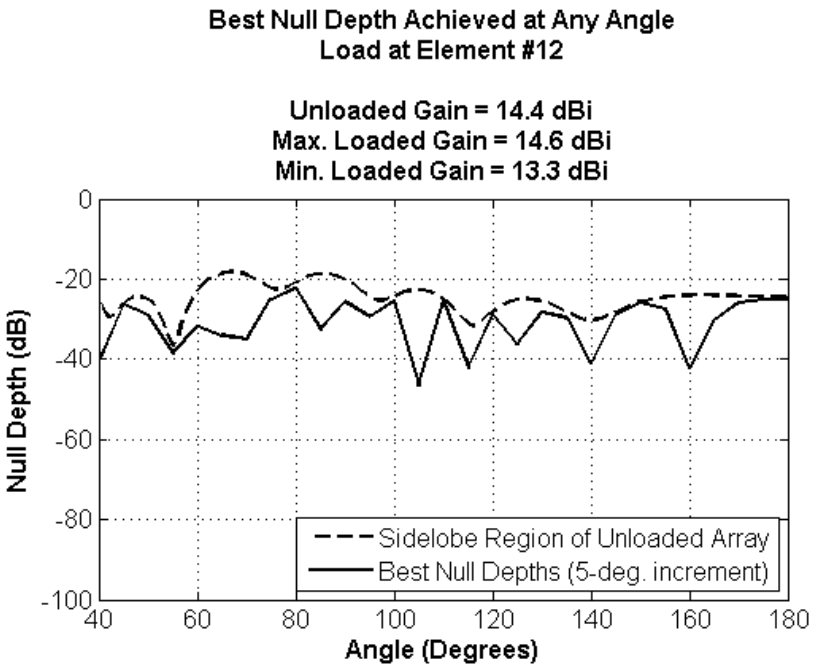

Figure 4. Null depth performance obtained with a single reactive load placed at Element #12, the outermost director.

Table 2. Reactance values that generate the best null depths in each direction of interest in the sidelobe region when the load is connected to Element #12.

Angle (deg.)	El. #12 *X* Value for Best Null (Ω)	Angle (deg.)	El. #12 *X* Value for Best Null (Ω)	Angle (deg.)	El. #12 *X* Value for Best Null (Ω)
40	100	90	140	140	60
45	60	95	100	145	40
50	100	100	-340	150	-60
55	40	105	300	155	660
60	360	110	-20	160	300
65	200	115	80	165	340
70	140	120	-100	170	1000
75	80	125	420	175	-240
80	-1000	130	440	180	-140
85	100	135	60	140	60

The gain of the unmodified array is 14.4 dBi, but Figure 4 shows that the gain obtained in the loaded case varies from a low of 13.3 dBi to a high of 14.6 dBi. Thus, at most only 1.1 dB is sacrificed in order to obtain null-steering capability, and for some reactance values the gain is actually enhanced.

Another interesting result is that there appears to be no correlation between the direction of an enhanced null and the reactance value that generates it. That is, the reactances given in Table 2 do not increase or decrease monotonically, but rather seem to vary in an almost random fashion. A partial reason for this is that as one null moves away from a given direction in response to a variation in the reactance, another one moves closer. The reactance values seem to "hand off" null-steering duties from one to another.

Besides the effect of reactive loads on gain, the other major concern is the change in input impedance. Figure 5 depicts the input reflection coefficients obtained for all 101 reactance values. Note that all fall within the VSWR = 2 (−10 dB return loss) circle. Thus, the impedance match is not seriously impaired for any reactive load value. Interestingly, the locus of data points forms a circle; this result bears further investigation!

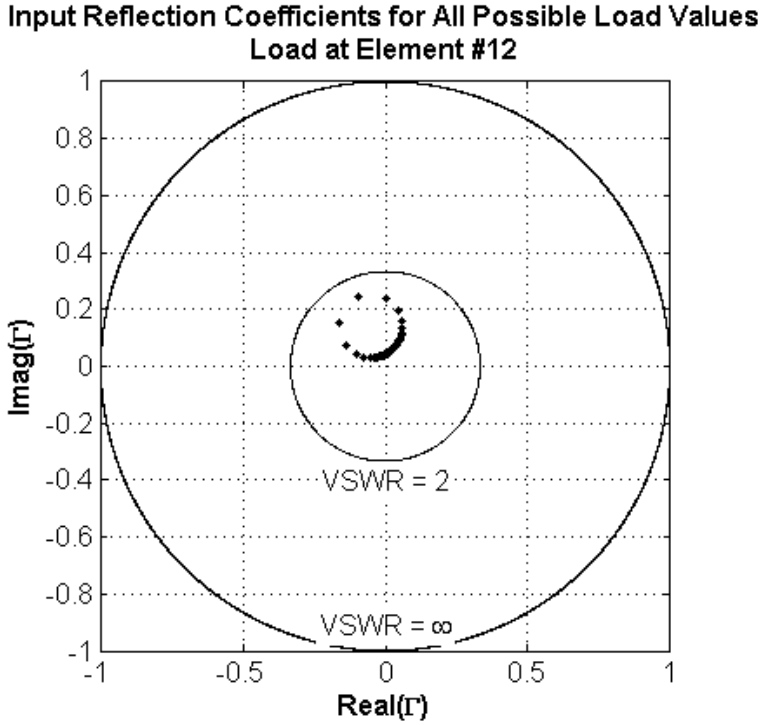

Figure 5. Impedance matching performance for a single load at Element #12.

Null depth performance was also investigated for the cases when one of the other elements was loaded. In almost all cases the performance is no better than when Element #12 is loaded. That is, significant improvement in SIR is not obtained for most angles. However, as shown in Figure 6, a slight improvement is obtained when Element #7 is loaded. Unfortunately, the improved performance comes at the cost of potentially lower gain and a degraded impedance match, as indicated in Figure 7. The curious circular pattern of data points appears again; in fact, the pattern appears no matter which element is loaded. Clearly, the improvement in SIR is marginal at best if only one reactive load is used with this particular array.

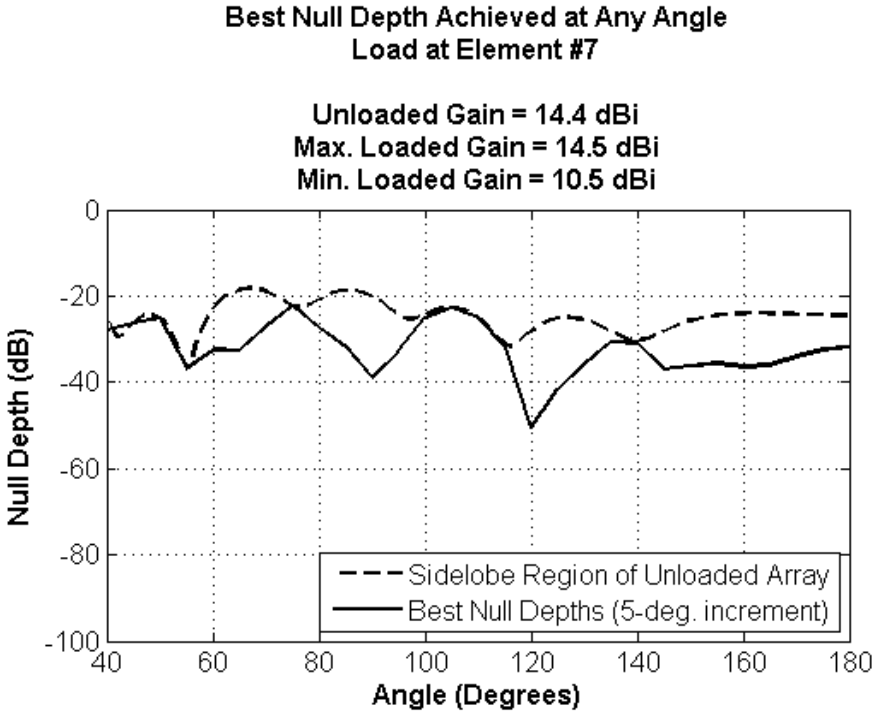

Figure 6. Null depth performance obtained with a single reactive load placed at Element #7.

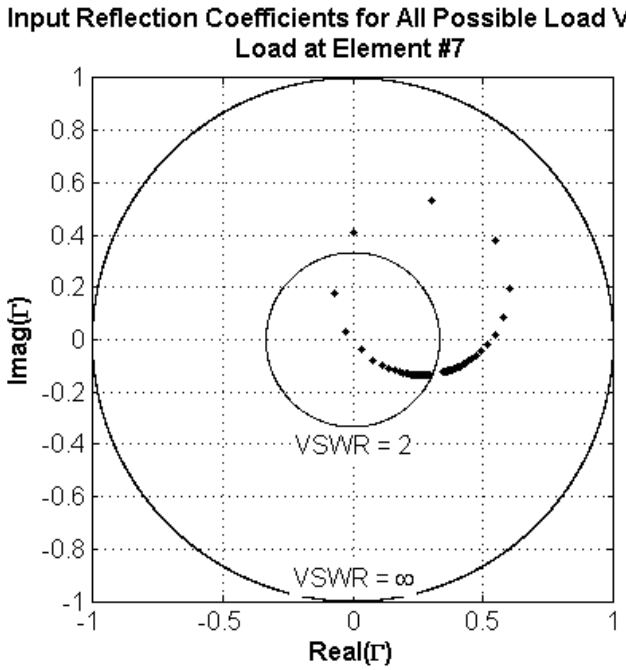

Figure 7. Impedance matching performance for a single load at Element #7.

Next, the performance obtained with two reactive loads was investigated. The first case considered was the loading of Elements #11 and #12 each with values ranging from –1000 Ω to 1000 Ω in 20-Ω steps, which results in 10,201 possible combinations. The null depth performance is shown in Figure 8 and the reflection coefficient data in Figure 9. Although the reactance values that produce the best nulls are not shown here, the data exhibit the same seemingly random variation depicted in Table 2 for the single-load case. The improvement in SIR that can be obtained with two loads is significant. In most directions the SIR can be increased by at least 15-20 dB with little or no reduction in gain, and most load combinations do not severely impair the impedance match at the feed point.

Results for loads placed at Elements #10 and #12 are shown in Figures 10 and 11. Although the null depth performance is not significantly different, the collection of input impedances might be viewed as better than that for the Element #11-12 case. However, the reduction in gain could be excessive.

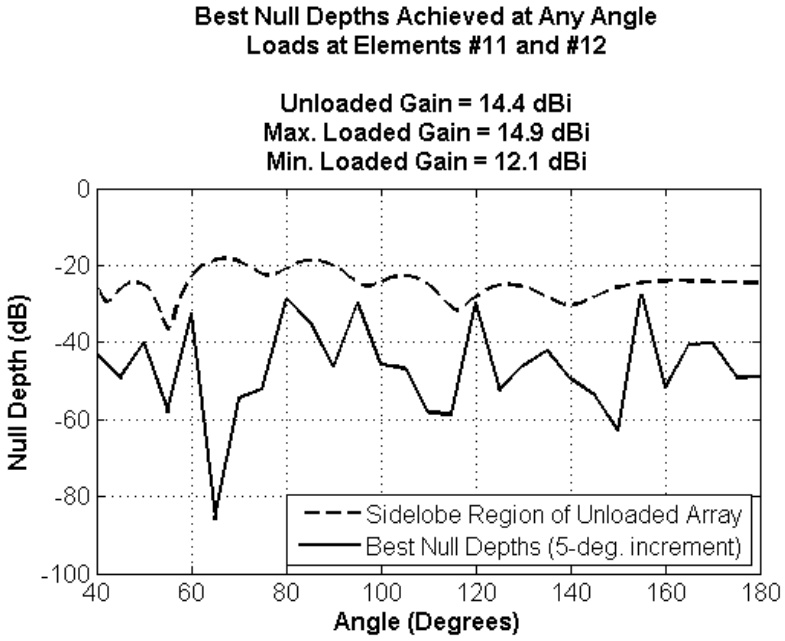

Figure 8. Null depth performance obtained with reactive loads placed at Elements #11 and #12.

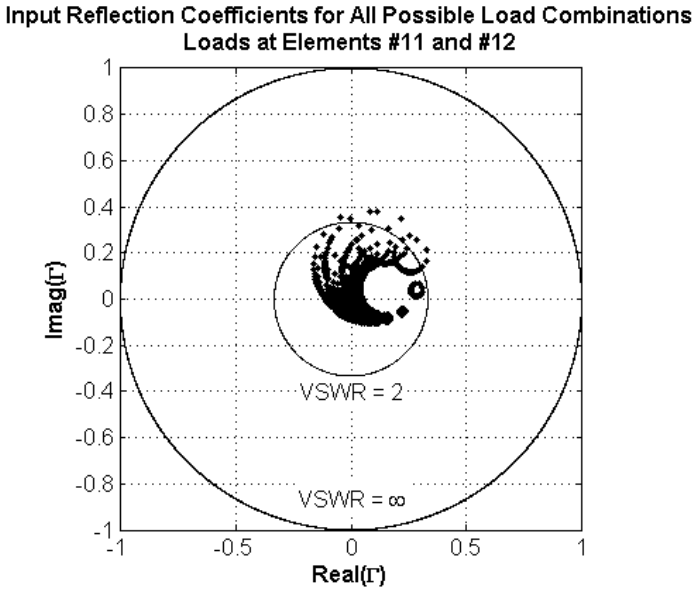

Figure 9. Impedance matching performance for reactive loads placed at Elements #11 and #12.

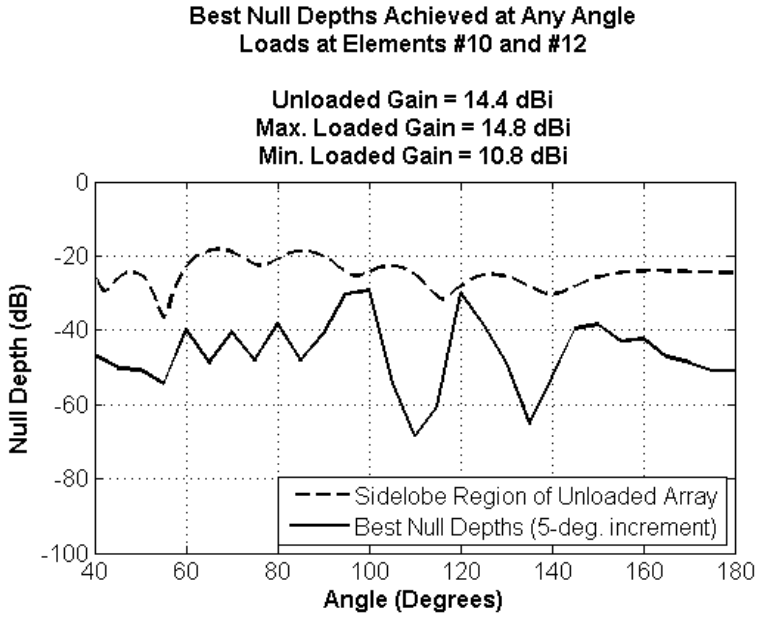

Figure 10. Null depth performance obtained with reactive loads placed at Elements #10 and #12.

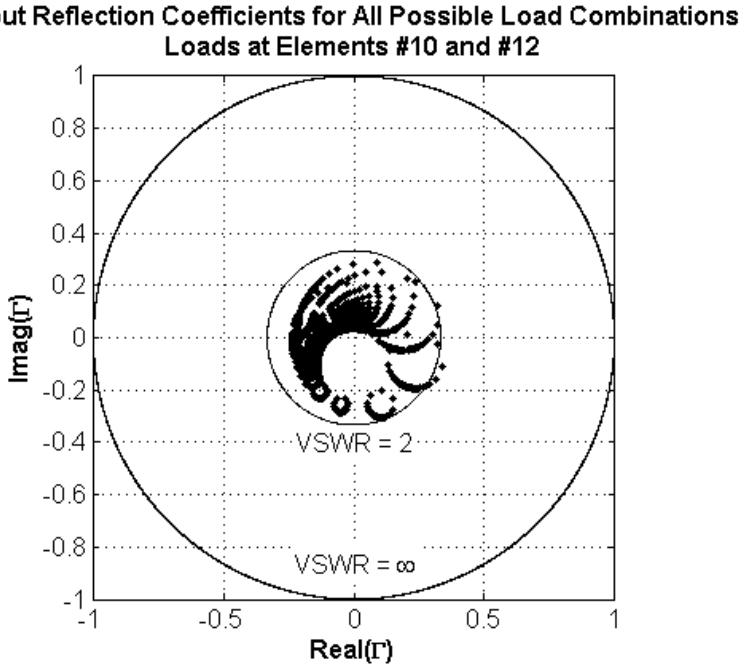

Figure 11. Impedance matching performance for reactive loads placed at Elements #10 and #12.

Similar results are obtained when other pairs of elements are loaded, although, as expected, the impedance match suffers significantly when a load is placed at one or more elements near the driven element. For this particular 12-element array, it was found that placing a load on any element closer than #9 gave a high probability of a poor impedance match. To be safe, only Elements #10 through #12 should be considered.

The ultimate improvement in null depth does not seem to depend greatly on which two elements are loaded, as long as both are near the front end of the array. In all cases the SIR can be improved by 15-20 dB in most directions and more so in a few directions. There are always a small number of directions for which the SIR cannot be improved significantly. Moving the locations of loads changes only the few directions in which improvement is marginal or spectacular, but in all cases the overall ultimate performance is roughly the same and much better than that available using only one loaded element.

4.2 6-Element Array

While the null-steering approach described here would normally be applied to medium-sized yagis or larger, it is instructive to investigate the results obtained for shorter arrays. Shown in Table 3 are the dimensions for a six-element yagi designed by Cebik using the OWA approach [3]. The plan view is given in Figure 12.

Figure 13 shows that the improvement in SIR obtained when a single load is placed at the outermost director is insignificant and that the gain can fall by as much as 2.1 dB. Although not shown here, the impedance match suffers greatly as well. When two elements are loaded, the gain and input impedance vary to such a large extent that the array can be considered to be unusable.

Table 3. Element lengths and spacings of a six-element OWA yagi array designed by Cebik [3]. The diameter of each element is 3/16 inch (4.7625 mm). A non-conducting boom is assumed.

Element	Length (mm)	Space from Reflector (mm)
Reflector	1029	--
Driven Element	1015	257
Director 1	949	364
Director 2	922	659
Director 3	922	947
Director 4	888	1377

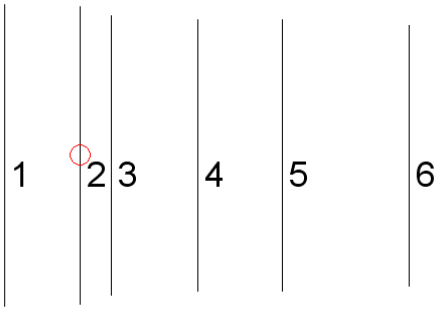

Figure 12. Plan view of a six-element OWA yagi designed by Cebik. The circle in the middle of Element #2 indicates the feed point.

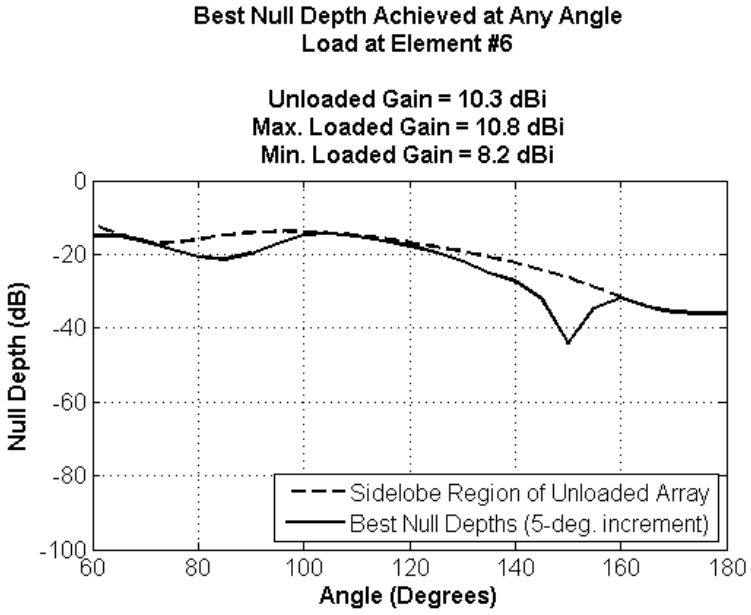

Figure 13. Null depth performance obtained with a single reactive load placed at Element #6 (outermost director) of the six-element OWA yagi.

5. Conclusion

This paper has presented an investigation of the potential for dynamically improving the SIR performance of a yagi array by loading a subset of the parasitic elements with lumped reactances. SIR improvements of up to 20 dB in directions ranging over most of the sidelobe region can be obtained with only modest changes in the gain and input impedance, provided that the array is of medium length or greater. This level of performance can be expected regardless of which element or set of elements is loaded; however, all loaded elements should be far from the driven element.

The work presented here represents the preliminary stages of a full investigation into the utility of dynamically controlled yagi arrays. An important consideration is the method used to produce variable reactances at each array element. Both positive and negative reactance values are typically required, and this implies that a combination of inductors and capacitors would be needed. The former can be difficult to vary and usually have considerable loss. An alternative approach might be to lengthen the loaded elements, effectively making them inductive, so that only capacitive reactances would be needed. Capacitive loads might take the form of varactors or switched banks of capacitors with binary-related values. Another possibility is to use transmission line stubs of appropriate lengths loaded with capacitors at one end.

Bandwidth issues were not considered here but are certainly important. The SIR improvement obtained at the center frequency of the array for a given set of reactance values must also be present over most of the operational bandwidth if dynamic control is to be useful. The bandwidth performance is likely to depend heavily on the reactive loading scheme employed.

6. References

[1] J. Breakall, "The Optimized Wideband Antenna (OWA) and Its Applications," *Proc. 12th Annual Review of Progress in Applied Computational Electromagnetics*, vol. 1, March 18-22, 1996, pp. 33-39.

[2] L. B. Cebik, "Notes on the OWA Yagi," *QEX*, July 2002, pp. 22-32.

[3] L. B. Cebik, "An OWA Family of 2-Meter Yagis From 6 to 12 Elements. Part 1: A Comparison of 12-Element Yagi Designs," posted August 2, 2002, www.cebik.com, accessed August 20, 2008.

[4] R. Harrington, "Reactively Controlled Directive Arrays," *IEEE Trans. Antennas Propagat.*, vol. AP-26, no. 3, May 1978, pp. 390-395.

[5] D. Kelley, “Relationships Between Active Element Patterns and Mutual Impedance Matrices in Phased Array Antennas,” *Proc. IEEE Antennas Propagat. Soc. Int. Symp.*, vol. I, June 2002, pp. 524-527.

[6] D. Kelley and S. D. Reier, “Efficient Pattern and Impedance Bandwidth Analysis of Reactively Steered Arrays,” *Proc. 2004 Antenna Applications Symposium*, Monticello, IL, Sept. 2004, pp. 99-116.

[7] R. Lewallen, *EZNEC Pro 4.0*, Beaverton, OR, http://www.eznec.com.

NON-FOSTER MATCHING OF ELECTRICALLY-SMALL ANTENNAS TO TRANSMITTERS

STEPHEN E. SUSSMAN-FORT
EDO Corporation, Antenna Products and Technologies, Bohemia, Long Island, NY 11716 USA stephen.sussman-fort@itt.com
and
Department of Electrical And Computer Engineering, State University of New York, Stony Brook, NY 11794 USA

RON M. RUDISH
EDO Corporation, Antenna Products and Technologies, Bohemia, Long Island, NY 11716 USA ronald.rudish@itt.com

ABSTRACT

It is difficult to transfer RF power from a transmitter to an electrically-small antenna, and consequently one must use transmitters of great power to radiate a relatively small amount of signal. The power efficiency, defined as the RF power radiated by the antenna divided by the DC power required by the transmitter and associated circuitry, is typically a few percent. This is a consequence of the gain-bandwidth theorem, which predicts narrow bandwidths and/or poor gain with such antennas.

Non-Foster matching employs *negative* inductors and capacitors, realized using negative impedance converters (NICs), and thus *bypasses* the restrictions of the gain-bandwidth theorem. As compared to passive matching, non-Foster provides superior transmission gain and allows the use of a lower-power transmitter to obtain the same radiated RF power over a given bandwidth. Even with the DC bias requirements of the NICs, non-Foster can achieve significantly greater power efficiency than the best passive match.

We give experimental results showing a factor-of-two improvement in power efficiency for non-Foster over passive matching to an electrically-small monopole-antenna model (Q=250 at 20 MHz) with 5% bandwidth about 20 MHz and an average signal power of 1W to the radiation resistance. We give a method for handling the high voltages at the antenna terminals. We expect greater power, bandwidth, and efficiency in the future.

1. Introduction

Electrically-small monopole and dipole antennas present high-Q impedances characterized by large parasitic reactances and small radiation resistances. For such antennas, the effectiveness of passive matching is severely limited by the gain-bandwidth theorem, which predicts narrow bandwidths and/or poor gain. The problem with passive matching is so pronounced that using no matching at all is actually a viable alternative. In receivers, the inability to resolve this impedance mismatch results in poor received signal-to-noise ratio as compared to using a full-size antenna. In transmitters, the impedance mismatch makes it difficult to transfer RF power to an electrically-small antenna, and consequently one must use transmitters of great power to radiate a relatively small amount of signal. Power efficiencies of a few percent or less are typical. (We define efficiency η here as the RF power radiated by the antenna divided by the total DC power required by the transmitter and associated circuitry.)

In many applications, however, full-size antennas are impractical, and a means is required to effectively match their electrically-small counterparts. The technique of *non-Foster matching* employs networks of *negative* capacitors and inductors, realized via special active circuits called negative impedance converters (NICs), and thus *bypasses* the theoretical restrictions of the gain-bandwidth theorem. The benefits of non-Foster matching are particularly striking for electrically-small antennas, where wide matching bandwidths and order-of-magnitude gain improvement now become possible. With receivers, this translates into broadband order-of-magnitude improvement in received S/N, as compared to the best possible passive match. We present details of the approach, as well as extensive experimental results, in references [1] – [3].

In non-Foster *transmit* matching, we can achieve a significant advantage in transmission gain (S_{21}) over passive matching to a given electrically-small antenna. The challenge is to achieve this advantage in S_{21} with an accompanying increase in power efficiency η for a specified power delivered to the antenna over a selected bandwidth. We must also deal with the fact that even moderate levels of radiated power will produce large RF voltages and currents at the terminals of an electrically-small antenna. The transistors of the NICs used in a non-Foster matching circuit would be vulnerable to damage unless precautions are taken. Our earlier work [3], [4] has laid the foundation for non-Foster transmit matching. In the design of low-power circuits delivering a few milliwatts to an electrically small antenna, we developed class A and class B NICs which included a strategy for the mitigation of the high-voltage problem. However, these circuits did not achieve the required improvement in power efficiency as compared to the best passive match.

In what follows, we present the development of higher-power NICs and non-Foster networks. We give experimental results for a non-Foster matching circuit that achieves a factor-of-two improvement in power efficiency over the best passive match to an

electrically-small antenna model (Q≈250 at 20MHz) with 5% bandwidth and an average signal power of over 1W to the radiation resistance.

2. Basics of Non-Foster Impedance Matching

The canonical approach to non-Foster impedance matching begins with modeling the antenna and then canceling its parasitics in a stepwise process. Starting with a model of an electrically-small monopole (Fig. 1a), for example, we cancel the positive elements L, C, and C' by introducing the negative elements –L, –C, and –C'. This transforms the original antenna impedance to its frequency-dependent radiation resistance (Fig. 1b). This impedance is transformed in turn to 50 Ω via an inductive-T dualizer with positive and negative elements L_o and $-L_o$, respectively (Fig. 1c).

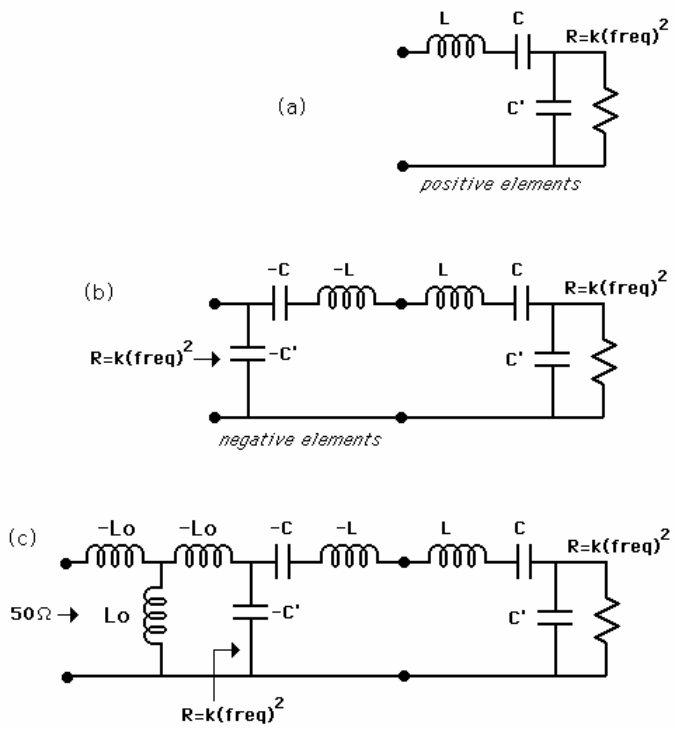

Fig. 1: Canonical Non-Foster impedance matching

As discussed in [3], the negative elements themselves are realized by terminating a two-port called a *negative impedance converter* (NIC) in the corresponding positive element (Fig. 2). Any network containing NICs is conditionally stable, but appropriate design techniques can yield a predictably stable result. This task is simplified by the fact that we may use a reduced model for the antenna which includes only its dominant parasitic capacitance C. Non-Foster matching then involves using a single negative capacitor as

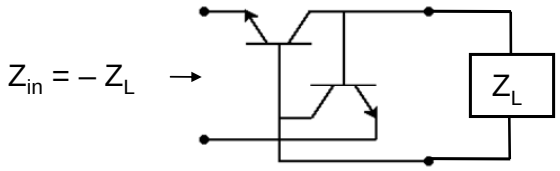

Fig. 2: Negative Impedance Converter (floating input terminals)

shown in Fig. 3. In fact, all research to date has been for this case, with no further effort (as yet) to match to 50 ohms. Using this approach in receive matching has yielded 10dB or more improvement in transmission gain and S/N over a frequency band of two or more octaves [1]-[3]. Our development of transmit matching will continue in this same vein.

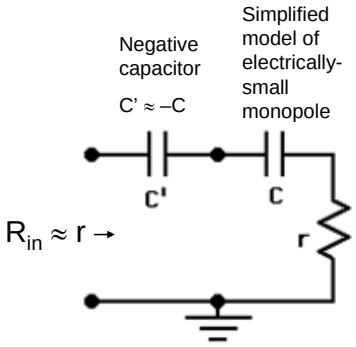

Fig. 3: Practical Non-Foster impedance matching

3. Transmit Matching and the High Voltage Problem

Regardless of the matching scheme, be it non-Foster or passive, electrically-small antennas require high terminal voltages and currents in order to radiate even moderate power levels because of *voltage division action.* In Fig. 4, we show a simplified model of an electrically-small monopole. (We shall focus on the monopole for the remainder of this paper.)

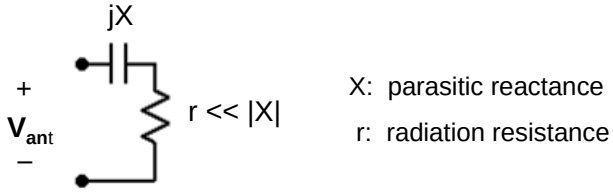

Fig. 4: Simplified model of electrically-small monopole

The voltage applied to the antenna terminals is divided between the parasitic capacitance C [X = –1/(ωC)] and the radiation resistance r. With r << |X|, as is the case in electrically-small antennas, only a small fraction of the applied voltage reaches the radiation resistance. Hence a large voltage must exist at the antenna terminals for any significant power delivered.

Our strategy to managing this high voltage is embodied in the negative-LC matching arrangement of Fig. 5. We simply resonate C of the antenna with a passive inductor L, and then we cancel *both* C and this added L with a *negative* series-LC circuit realized via an NIC. With *each* L selected to resonate with its corresponding C in the middle of a chosen frequency band, the voltage V_{LC} at the NIC input —and, consequently, the voltages across the transistors of the NIC— are kept at a reasonable level over some band about resonance.

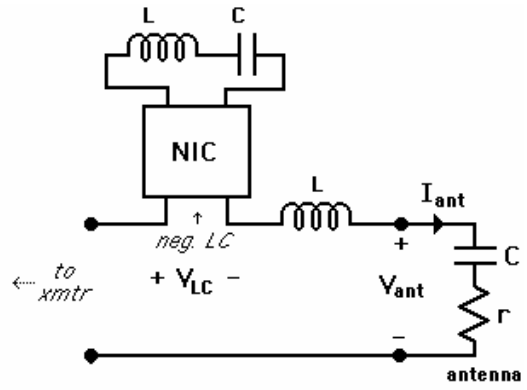

Fig. 5: Negative-LC matching

As a specific example, consider a two-foot vertical antenna with a Q of approximately 250 at 20 MHz. A simple circuit model for this antenna has parasitic capacitance C=33pF and radiation resistance r=1 Ω in Fig. 5. For a resonance at ≈20 MHz, L=1.8μH. If *100mW* is to be delivered to r, then the voltage V_{LC} can easily be determined and is plotted in Fig. 6. Also plotted is V_{LC} when both inductors L are omitted in Fig. 5.

The approach described above offers the significant benefit of mitigating the high-voltage problem over a relatively small (e.g. 5%) "voltage bandwidth" about the LC resonant frequency. This is quite different from non-Foster matching in *receivers*, where multi-octave bandwidths are intrinsic to the process. The high voltages of transmit matching force us (1) to divide a given *broad* passband into channels, and then (2) to design individual matching networks for each such channel. Our work here can be thought of as being for the first such channel centered near 20 MHz. We will compare the performance of non-Foster transmit matching to the best passive match for that

channel. Future research will consider ways of switching in different inductor pairs in Fig. 5 to matching over other sub-bands.

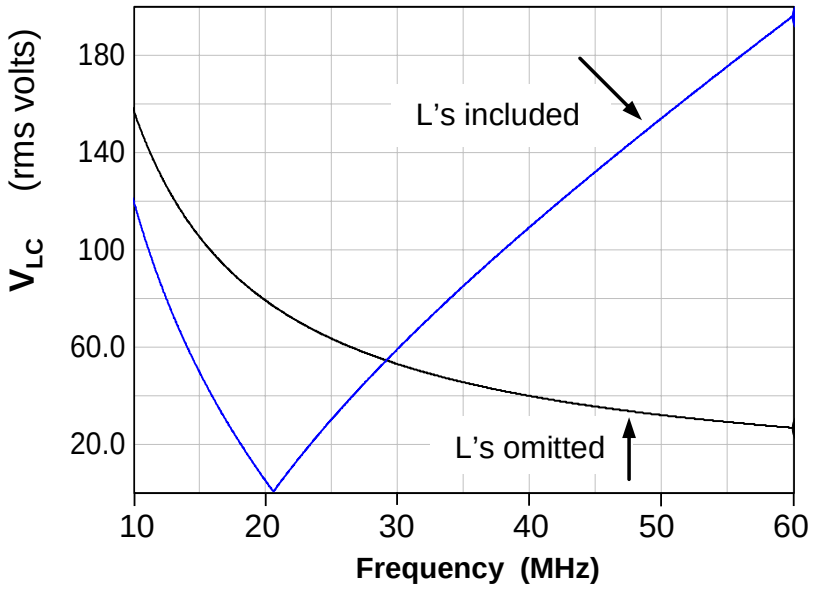

Fig. 6: V_{LC} (rms) at NIC input in Fig. 5 with r=1Ω, C=33pF, and 100 mW delivered to r.

4. Evaluating the power efficiency of non-Foster matching

Non-Foster matching to an electrically-small monopole achieves a large advantage in transducer gain S_{21} because this technique bypasses the constraints of the gain-bandwidth theorem, which applies only to passive networks. This means that for the same RF power delivered to the antenna over a given bandwidth, passive matching will require a much larger transmitter than non-Foster. On the other hand, non-Foster matching requires DC bias power for the transistors of the NICs. To compare non-Foster to passive matching, we must evaluate the power efficiency η for each case.

Consider the scenario of Fig. 7 in which non-Foster matching is symbolically contrasted with the best possible passive match. We may refer to non-Foster matching as active matching, to emphasize the DC bias requirements of the circuit. In the active match, we have included a matching transformer at the input, since it improved the overall performance in our experiments. The best possible passive match may comprise inductors, capacitors, and transformers.

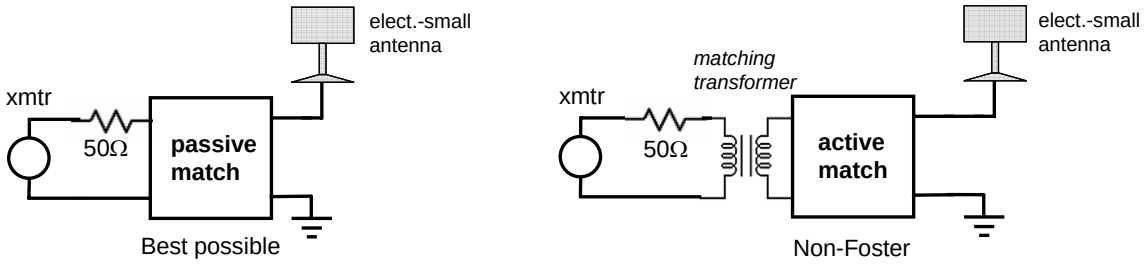

Fig. 7: Calculation of power efficiency of best possible passive match and non-Foster match

We evaluate a given non-Foster active matching circuit vs. the best possible passive match to the specified antenna in terms of the power efficiency η of each circuit:

$$\eta = \text{output signal power / required DC power}$$

In both cases, we calculate η for the same output signal power to the antenna over the same bandwidth.

Hence for **the non-Foster circuit**, we first set the available input power from the transmitter, $\mathbf{P_{in\text{-}active}}$ to a suitable level. Next, we measure the signal power delivered to the antenna, $\mathbf{P_{ant}}$, by monitoring the actual voltage waveform across r in the antenna model of Fig. 4. Over a selected bandwidth **B**, we compute $\mathbf{P_{ant}}$ as the average value of the signal power delivered to the antenna over a discrete number of frequencies. The total DC power needed, $\mathbf{P_{DC\text{-}active}}$, is the sum of (1) the NIC bias power plus (2) the DC power necessary for the transmitter, which we estimate as twice $\mathbf{P_{in\text{-}active}}$. The efficiency of the non-Foster circuit is then

$$\mathbf{\eta_{active} = P_{ant} / P_{DC\text{-}active}}.$$

Next, we design the **best possible passive circuit** between the antenna model and the transmitter over the same bandwidth **B**. (Our own matching network design software [5] is an excellent tool in this regard.) The average transmission gain achieved will be less than that obtained with non-Foster, and to get the same power $\mathbf{P_{ant}}$ delivered to the antenna, we need to *increase the transmitter power* by the appropriate scale factor to the value $\mathbf{P_{in\text{-}passive}}$. The total DC power needed, $\mathbf{P_{DC\text{-}passive}}$, is that needed for the transmitter, which we estimate as twice $\mathbf{P_{in\text{-}passive}}$. The efficiency of the passive circuit is then

$$\mathbf{\eta_{passive} = P_{ant} / P_{DC\text{-}passive}}.$$

Clearly, we want η_{active} to be much larger than $\eta_{passive}$. We know the transmission gain of non-Foster to be much better than that for the best passive matching network, ***so the key is to minimize the bias power needed for the NICs of the non-Foster matching network.***

5. Evolution of non-Foster transmit matching – 100mW class circuits

The first NICs investigated by us were biased class A, and this is quite appropriate for receiver applications, where an important non-Foster design goal is to improve signal-to-noise ratio. In transmit matching, class A NICs require a large DC bias power, and this leads to poor power efficiency in the non-Foster approach. This is so even though, as discussed above, we would need a much smaller transmitter than in the passive case to deliver a specified RF signal level to a given electrically-small antenna. We have designed class A NICs that are ≈50% *less* efficient than a comparable passive match, and class B and C NICs that possess about the *same* efficiency as a passive match, all at ≈100 mW signal power levels to the antenna. We briefly describe these circuits as an entrée to our 1W, factor-of-two efficiency improvement circuit to be discussed later.

5.1 Voltage inversion NICs

An initial step in improving the power efficiency of non-Foster matching is simply to use a single-transistor version of the NIC. Linvill's original paper [6] illustrated the use of the circuit of Fig. 8a but discussed achieving the required phase inversion via a transformer as in Fig. 8b.

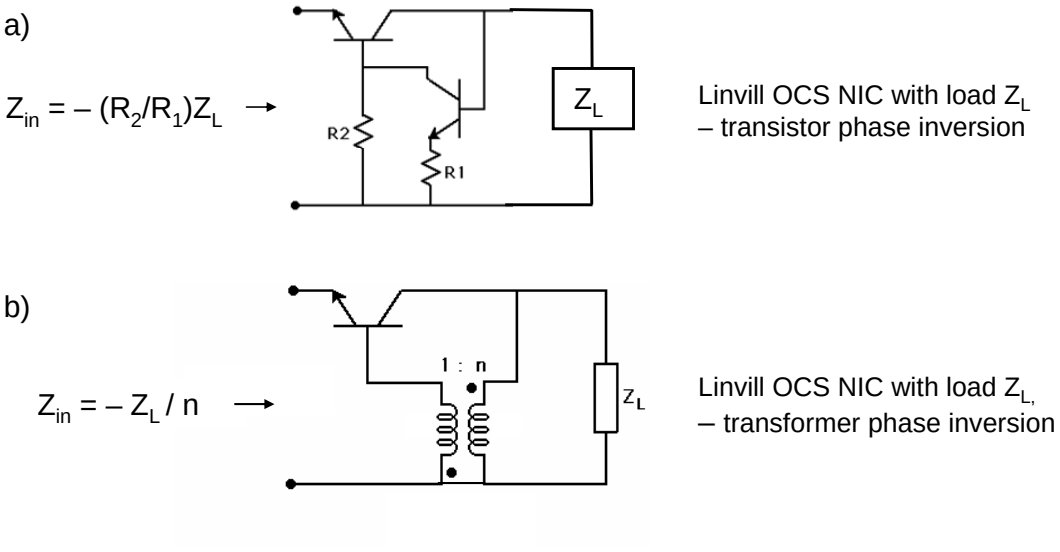

Fig. 8: Voltage Inversion NICs (common-terminal)

Note that these circuits are common-terminal between the load impedance and the input with the phase inversion required for NIC operation obtained by the common-emitter transistor and transformer, respectively. (The floating NIC of Fig. 2 achieves the phase inversion by effectively crossing the wires between the load and the input.) The actual non-Foster matching circuit evaluated is the one shown in Fig. 9. Although not shown in the schematic, a transformer was used at the input to make the effective value of R_{source}, as seen by the matching circuit, to be 12.5Ω.

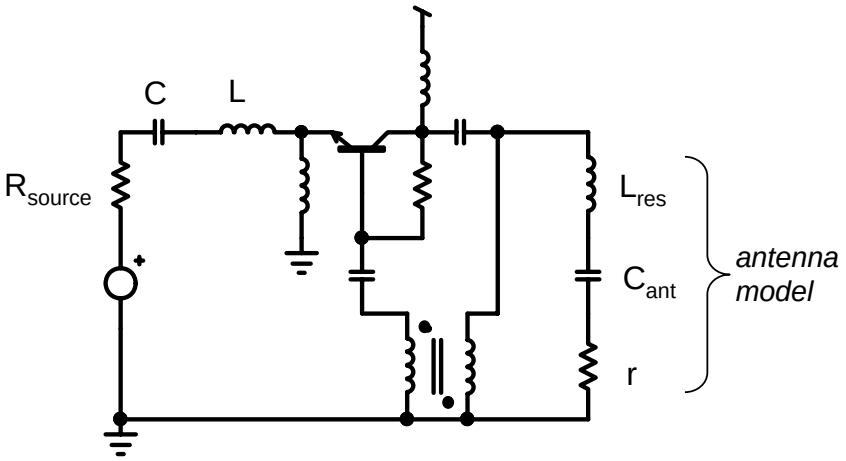

Fig. 9: Non-Foster matching

In order to use the common-terminal NIC above, we negate not only the antenna's parasitic capacitance C_{ant} and the voltage-managing resonating inductor L_{res}, but the radiation resistance r. The idea is cancel the negated L_{res} and C_{ant} with C and L on the left, respectively. The negated r is absorbed by the much larger source resistance R_{source} and does affect operation of the circuit.

5.2 Experimental results for a class A circuit

We built the circuit of Fig. 9 using the electrically-small monopole antenna model described in Sec. 3 with C_{ant} =33pF, L_{res} =1.8μH and r=1 Ω. With the circuit biased class A, we measured the power efficiency of the circuit over 17-23 MHz for two different bipolar devices (2n3553 and MRF340) and compared it to that of the best possible passive match as calculated by the software CiAO [5]. In the passive simulation, component Qs of the Ls and Cs were matched to those of the active network. The results are summarized in the table below.

Table 1:

Efficiency comparison of class A non-Foster match to passive

Device	BW	$P_{ant\text{-}avg}$	η
2n3553	17-23 MHz	106 mW	**1.73%**
Passive circuit	17-23	106	**2.52%**
MRF340	17-23	79.1	**1.63%**
Passive circuit	17-23	79.1	**2.50%**

Clearly, the class A biasing has prevented any power efficiency advantage of the non-Foster match in this case. However, we gained valuable experience with this kind of circuit that motivated us to the class B and class C circuits discussed below. Shown below is the plot of S_{21} from R_{source} to r for the non-Foster match, which shows the great gain advantage over passive matching for the passband of 17-23 MHz.

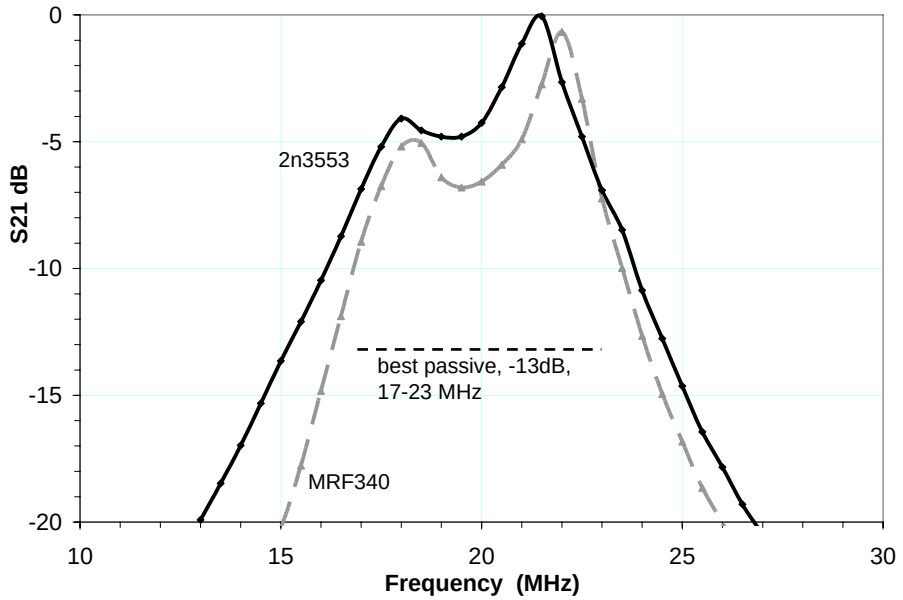

Fig. 10: Measured transducer gain S_{21} for two class A non-Foster circuits compared to simulated best passive matching result over 17-23 MHz.

5.3 Experimental results for a class B circuit

In an effort to improve power efficiency, we developed the class B non-Foster matching circuit of Fig. 11. As in class B *amplifiers*, the input signal is split up into positive- and negative-going sinusoidal halves, and the transistors are biased near cutoff. Unlike class B amplifiers, where the load current is taken from the power supply, the load current in the matching circuit is derived from the input signal as processed by the NIC circuitry.

Inasmuch as we cannot usefully ascribe the concept of impedance to the nonlinear waveforms internal to the class B arrangement, only a waveform interpretation of the circuit operation is, in fact, possible. For brevity we omit this here, but we will explain the waveform behavior of a *class C* NIC in a subsequent section.

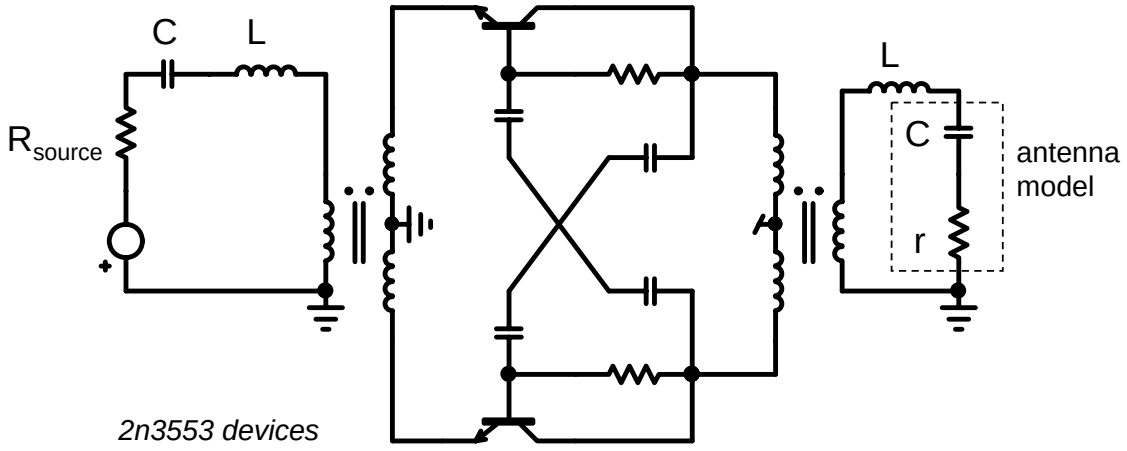

Fig. 11: Class B Non-Foster matching circuit

We built the above circuit, and the measured efficiency results are shown in Table 2. We note that for the first time in our experiments the non-Foster power efficiency is better than that for the passive circuit (albeit only incrementally).

Table 2:

Efficiency comparison of class B non-Foster match to passive

Circuit	BW	$P_{ant\text{-}avg}$	η
Class B	20-23.5 MHz	65 mW	**3.55%**
Passive	20-23.5	65	**3.16%**

The improvement in efficiency of the class B circuit over the class A is a direct consequence of the fact that the class B circuit needs only a low-level idling current for bias, while the class A circuit must be biased much more in the middle of the operating voltages and current.

S_{21} is plotted in Fig. 12. The non-Foster gain advantage is substantial over the selected bandwidth. For comparison, S_{21} of the class A circuit is also shown. The bandwidth is reduced in class B because the input signal must be large enough to turn on the transistors. This is easiest at the resonance of L and C; as we move away from

resonance, the impedance of the series connection of L and C lowers the signal current and brings the transistors back towards cutoff. The bandwidth would presumably increase if the input signal level were augmented, but care must be taken not to exceed device ratings. In normal operation, the circuit generates large voltage and current transients as the transistors turn on and off.

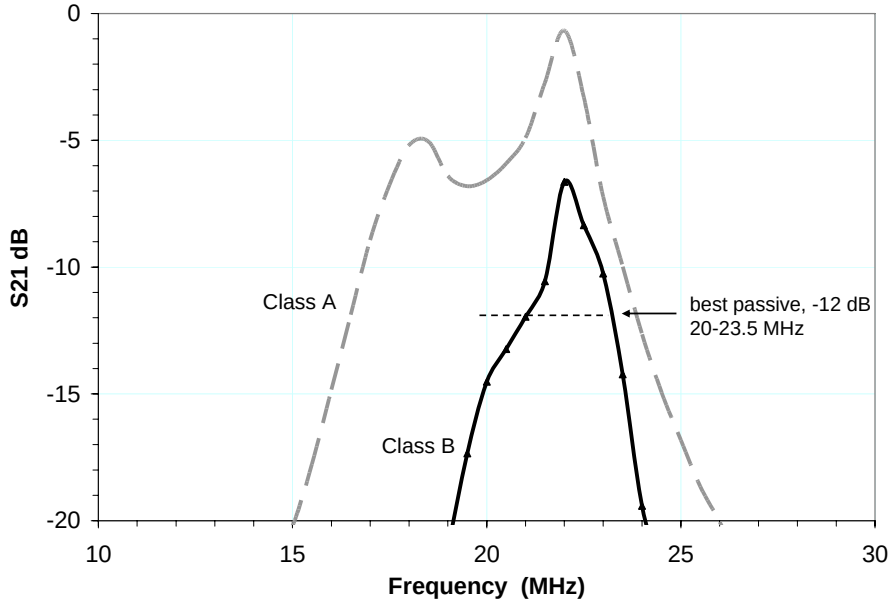

Fig. 10: Measured transducer gain S_{21} for class B non-Foster circuit compared to simulated best passive matching result over 20-23.5 MHz.

6. Class C non-Foster matching circuits

6.1 Fundamental issues of NIC design for transmit matching

Non-Foster transmit matching is a complex design task. We seek greatly improved power efficiency (as compared to optimal passive matching) while maintaining circuit stability and high transmission gain. Of the many network structures available for NICs, one must choose those which lend themselves directly to improved power efficiency. The class B circuit was the first step in this direction, but a single-transistor class C arrangement will be seen to be superior. We note further that the NIC of Fig. 9 allows a large signal current to flow through the emitter-collector path to the antenna; certain other NIC topologies [7] would not permit this because the input is to the *base* of a transistor.

There are many practical problems that arise in designing NICs capable of handle signal power levels of 1W and beyond. For example, how does one choose power transistors for use in NICs? Simulations models often do not exist for power transistors, and when they do, they seldom give meaningful computer-simulation result for NICs. (The models do work, for the most part, in *amplifier* designs.) We must also consider the problems of selecting components that work well at higher current levels (e.g. high-current, low-loss inductors). Even device heatsinking is an issue, particularly because we have found that the heatsinks used in power NICs need to be isolated from ground.

6.2 Behavior of a Class C NIC:

The concept of impedance usually connotes linear circuits, although sometimes "large-signal" impedances are associated with power amplifiers. Nevertheless, one can make an impedance-like interpretation of NICs operating in a nonlinear mode by resorting to a waveform interpretation, similar to that first given by Linvill in 1953. Consider the NICs of Fig. 12. The transistors are assumed biased at cutoff (class C). We do not explicitly show the biasing networks.

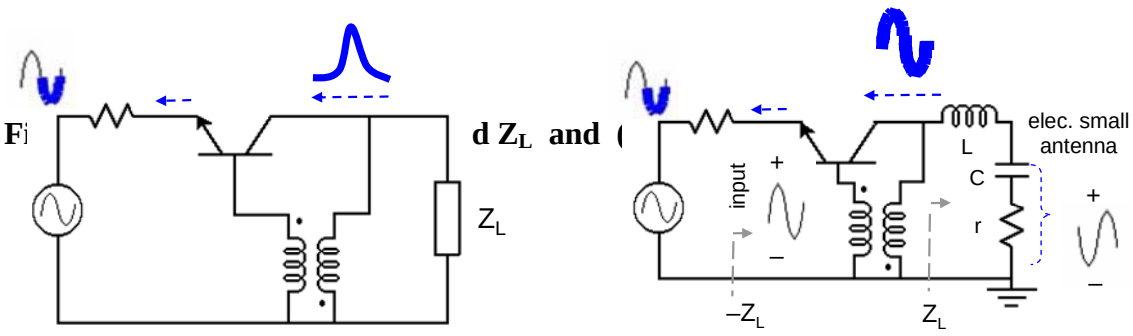

a) Linvill NIC with load Z_L **b)** Linvill NIC with resonated load

Fig. 12: Linvill NIC with load a Z_L and a resonated load

In Fig. 12a, a sufficiently large input signal will turn the transistor on. A large current pulse will then flow through the transistor and the load Z_L The current through the transformer (1:1 turns ratio) will be small since it will be equal in magnitude to the base current.

In Fig. 12b, we have the same situation but the load is assumed to be a series-LC circuit resonant near the signal frequency. (This models the resonated electrically-small antenna as discussed in Sec. 3.) In this case, the load will filter the current pulse so that only the *fundamental frequency* remains. The resulting sinusoidal load voltage – inverted by the transformer – appears at the base and then appears (in Linvill's words) "practically

undiminished" at the input. The effective "large signal" input impedance is the ***negative of*** $\mathbf{Z_L}$, since the current through the input and Z_L is the same, but the voltages are inverted. The circuit of Fig. 12b is almost certainly unstable, as we normally need a compensating positive series-LC circuit at the input as in Fig. 9. The series-LC networks provide high voltage mitigation around the resonance. But they limit bandwidth, just as in the class B case.

6.3 Comparison to conventional class C amplifiers

At this point, the following question must come to mind: why not use a conventional class C amplifier to drive an electrically-small antenna? In attempting this, we would still have to deal with the high-voltage problem, so the circuit realization would have to be of the form shown in Fig. 13.

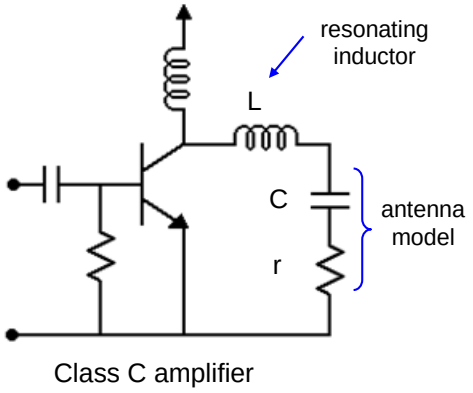

Fig. 13: Class C amplifier with an electrically-small antenna

With the antenna resonated with the inductance L to minimize voltage excursion in a passband, the resulting small resistance (≈1Ω at resonance) will cause the amplifier to be *unstable.* (Stability-circle analyses of various devices have confirmed this.) For stability, power transistors in conventional amplifier topologies often require resistive terminations at *all* frequencies as well as additional stabilizing lossy circuit components. These constraints are incompatible with electrically-small antennas.

The non-Foster network of Fig. 9 may be regarded as the class C solution to the matching of electrically-small antennas. The circuit includes both impedance matching *and* amplification, with stability.

6.4 Experimental results for a class C circuit

We have constructed several class C non-Foster matching circuits of the type shown in Fig. 9 using the electrically-small monopole antenna model described in Sec. 3 with C_{ant} =33pF, L_{res} =1.8μH and r=1 Ω. The antenna Q is approximately 250 at 20 MHz. We used high-quality components, particularly for the resonating inductors (custom air-wound).

We describe the results of a representative experiment in which we used a 2sc1969 BJT. With the circuit biased class C, we measured the power efficiency over a 1.2MHz bandwidth (21 – 22.2 MHz) and compared it to that of the best possible passive match as calculated by the software CiAO [5]. In the simulation, we modeled the components to be at the same high-level of quality as used in the non-Foster network.

Circuit	BW	$P_{ant\text{-}avg}$	η
2sc1969	21 – 22.2 MHz	1.3 W	21.1%
Passive circuit	21 – 22.2 MHz	1.3 W	9.46%

Table 3: Efficiency comparison of class C non-Foster match to passive

The non-Foster circuit with the 2sc1969 device achieves a power efficiency advantage of **2.2** (= 22.1 / 9.46).

We plot, in Fig. 14, S_{21} of the non-Foster circuit and show the calculated performance of the best possible passive circuit over the indicated bandwidth. Also plotted, in Fig. 15, is the power delivered to that radiation-resistance load r in Fig. 9. Note the large gain advantage of the non-Foster match over passive as well as the high signal power (peaking at 5 W) delivered to the antenna model.

7. Conclusions

We have demonstrated that non-Foster matching for transmit applications has achieved a 2:1 power efficiency advantage over the best passive match to an electrically-small antenna over a 1.2 MHz bandwidth about 20 MHz. We achieved a 1.2W average power level over this bandwidth, with a peak power to the antenna of 5W. Work is ongoing to increase bandwidth and efficiency.

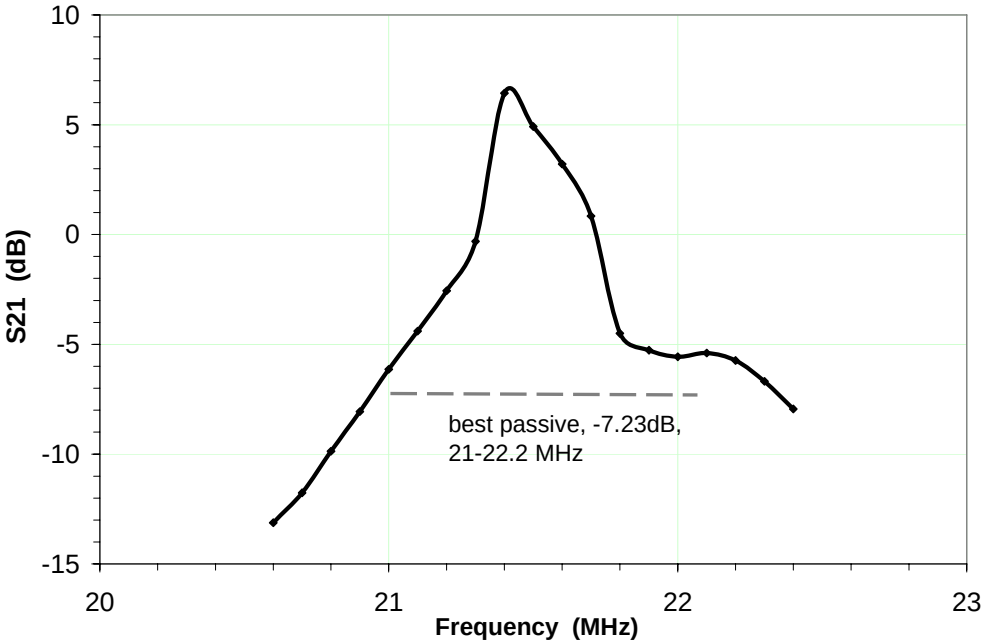

Fig. 14: Measured transducer gain S_{21} for class C non-Foster circuit compared to simulated best passive matching result over 21-22.2 MHz.

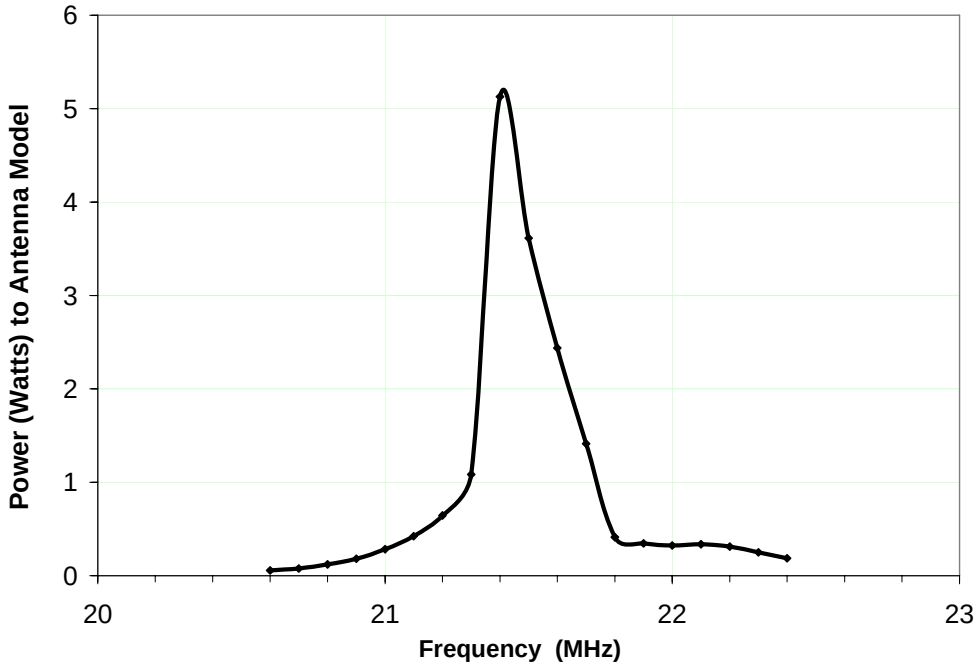

Fig. 15: Measured power delivered to antenna model for class C non-Foster circuit

8. References:

[1] Stephen E. Sussman-Fort and Ronald M. Rudish , “Non-Foster Impedance Matching of a Lossy, Electrically-Small Antenna over an Extended Frequency Range”, *2007 Antenna Applications Symposium,* Allerton Park, IL, Sept. 18-20, 2007.
[2] Stephen E. Sussman-Fort, “Matching Network Design Using Non-Foster Impedances,” *International Journal of RF and Microwave Computer-Aided Engineering*, vol. 16, issue 2, pp. 135-142, March 2006.
[3] Stephen E. Sussman-Fort and Ronald M. Rudish, “Progress In Use Of Non-Foster Impedances To Match Electrically-Small Antennas And Arrays”, *Twenty-Ninth Antenna Applications Symposium,* Allerton Park, IL, Sept. 21-23, 2005.
[4] Stephen E. Sussman-Fort and Ronald M. Rudish, Non-Foster Impedance Matching for Transmit Applications, *2006 IEEE International Workshop on Antenna Technology: Small Antennas and Novel Metamaterials,*White Plains, NY, March 6-8, 2006.
[5] Stephen E. Sussman-Fort, "Computer-Aided Matching Network Synthesis," *International Journal of Microwave and Millimeter Wave Computer Aided Engineering*, vol. 1, no. 3, pp. 288-305, July 1991.
[6] J. G. Linvill, “Transistor negative impedance converters,” *Proc. IRE,* vol. 41, pp. 725-729, June 1953.
[7] C. K. Kuo and K. L. Su, “Some New Four Terminal NIC Circuits,” IEEE Proc. Circuit Theory, pp. 379-381, August 1969.

USING SERIES RESONATORS IN PARALLEL TO ACHIEVE BROADBAND PERFORMANCE IN INDUCTIVELY LOADED ANTENNAS

Paul E. Mayes, Paul W. Klock and Suhail Barot
Electromagnetics Laboratory
University of Illinois at Urbana-Champaign
p.mayes@comcast.com, p.klock@illinois.edu, sbarot@uiuc.edu

Abstract: In previous papers we have discussed the use of parallel resonators in series as a way to increase the match bandwidth of a radiating system. In this paper, the dual situation is addressed: the use of series resonators in parallel. This leads to more familiar radiating resonators (linear dipoles and monopoles), but apparently increases the effects of coupling. Electromagnetic coupling among linear elements has already been analyzed. Here, it is shown how the effect of coupling can be used in the design of broadband and multi-band systems.

The dimensions of radiating resonators can be reduced by introducing interior inductive loading. By placing a series inductor near the end(s) of a dipole or monopole, not only is the resonant length decreased, but the current distribution can be made nearly uniform at resonance. It is demonstrated that such a uniform distribution can be beneficially used in extending the match bandwidth. If needed, additional bandwidth can be obtained by introducing multiple resonances. Results from several different computer codes and conventional circuit analysis are reported.

1. Introduction and previous work

Electrically small antennas, those that are significantly smaller than one-half wavelength at the operating frequency, are usually characterized as having small radiation resistance and small operating bandwidth. These characteristics can be ameliorated by (a) using an offset feed and (b) introducing multiple radiating resonators having different resonant frequencies.

The principles of operation of broadband, electrically small antennas were introduced using wide-angle cones as the radiating resonators [1]. The size of the cones was reduced by placing inductors across the apertures. In the vicinity of the resonant frequency of each of this type of radiating resonator, the input impedance goes from inductive to capacitive. Similar behavior is obtained from a parallel combination of an inductor and a capacitor. Losses in such a circuit can be represented by a resistor in parallel with the inductor and capacitor. At zero frequency, the losses of radiation are zero and the input impedance is likewise zero. The locus of the input impedance versus frequency produces a trace on the Smith Chart that starts at zero for zero frequency, goes through increasingly larger values of inductive reactance until reaching the resistive value, R, at the frequency of resonance, and continues on the capacitive side of the chart for higher frequencies. Thus, the only possibility for approximate matching to a real value of impedance is near

the resonant frequency. The bandwidth of approximate match is determined by the value of R.

However, the match bandwidth can be greatly expanded by allowing the additional complication of multiple resonances, properly spaced. The possibilities are illustrated by consideration of a circuit composed of several tank circuits connected in series, such as depicted in Figure 1 [2]. At zero frequency, in the system of Figure 1, all of the capacitors are open and all of the inductors are shorts so that the input impedance is zero. As frequency increases, the net input impedance is inductive reactance until the lowest frequency at which resonance occurs. Suppose the resonators are arranged in order of increasing resonant frequency, ($\omega_1<\omega_2<...\omega_n...<\omega_N$). When the operating frequency, ω, is equal to ω_n, then all of the tanks with resonant frequency ω_0 such that $\omega_0<\omega_n$ will have impedance which is inductive and the others will have impedance which is capacitive. As a result, there will be a series resonance between two adjacent parallel resonances. When taken together, all resonances form an alternating set of parallel and series resonances. For lossless systems, the resulting input impedance will trace the rim of the Smith Chart. When losses are present, the impedance locus will fall in an area that is inside the chart. A similar argument can be applied to the circuit of Figure 2, a system comprising series-type resonators connected in parallel.

2. Realization of series resonators

Since the impedance of dipoles has a behavior that is similar to that of a series RLC circuit, it is expected that the impedance of combinations of dipoles should also be similar to that of combinations of series RLC circuits. However, there are two major sources of differences. The effective resistance of a combination of dipoles is probably not independent of frequency. While it may be possible to devise a frequency-dependent resistance for a system of series RLC circuits, it is not apparent how this should be done in an optimum fashion. For electrically small antennas, the variation in resistance over the pertinent frequency band is apt to be negligibly small so that a constant resistance is a reasonable approximation. In addition., the input impedance of a collection of dipoles may be greatly dependent upon the field coupling that will exist between the various dipoles in the combination. While it may be possible, once again, to devise a system of coupling between circuits so that the input impedance of the combined circuits is very close to that of the combination of dipoles, there is no simple way to know how to do this. Nevertheless, the concept of approximate equivalent circuits representing the behavior of a radiating system will prove to be useful.

It was pointed out previously that a combination of series RLC circuits in parallel could be made to produce nearly coincident loops on the Smith Chart. This provides some hope that similar results can be obtained by combining dipoles in parallel. Some requirements on the circuits are apparent in order to make such a combination of dipoles have practical importance. If the locus of input impedance can be made to have the form of coincident loops on the Smith Chart, and if these loops can be placed near the center of the chart, then the reflection coefficient magnitude will remain nearly constant over the bandwidth encompassed by the loops. If, furthermore, this can be accomplished by using radiating resonators that are small compared to the wavelength for all frequencies in this

band, then the realization of an electrically small antenna with wideband match is possible.

Realization of size reduction of a linear element has long been obtained by placing an inductive element in series with the element (dipole or monopole). Figure 3 depicts one analysis model that was modified from FERM (Finite Element Radiation Model) [3] to compute the electrical properties of inductively loaded dipoles. The correspondence between the data for such flat dipoles and those with circular cross section is given in [4]. Figure 4 gives a set of results computed using FERM and LFMoM for the input impedance of a blade dipole with different load inductors. The impedance of the same antenna produced the results shown in Figure 5 when using HFSS. The blade dipole is center fed and the loads were placed near the ends (as shown in Figure 3); the double half-size patches denoting the presence of a lumped element at the junction between the patches. When there is no load, the impedance locus agrees with the textbook results [5]. As the value of the inductors is increased, the resonant frequency, resonant resistance, and the bandwidth decrease in the manner shown by the SWR plots of Figure 6.

The importance of location of the inductor is illustrated by the current plot in Figure 9. Note that the value of 191 nH produces a nearly constant current between the loads. The benefit gained by placing the load inductor near the ends of the dipole is illustrated by comparing the results shown in Figure 7 with those shown in Figure 6 The progression of decreasing input resistance at resonance is seen to be much slower in Figure 6 than in Figure 7. As a result, a small dipole loaded near the end has a higher value of resonant resistance than one for which the load is closer to the midpoint of the dipole.

Some of these results have been verified experimentally using the device shown in Figure 9. The physical realization of a blade dipole is narrow strip of thin copper (0.5 cm x 7.5 cm) which is fed as a monopole above a 43.5-in copper ground plane. The chip inductor has a nominal value of 82 nH and was placed at various distances from the center. The input impedance was measured by an Agilent E8363B network analyzer. The measured values are shown in Figure 10 and are found to be in good agreement with the expectations.

3. Multiple series resonators (dipoles) in parallel

Since there is no assurance that the input impedance of a parallel connection of radiating elements will have the same form as that of a parallel connection of circuit resonators of series connection, a knowledge of the behavior of other examples is useful. For many years it has been common practice to obtain wideband performance from a log-periodic array of dipoles by transposing the feeder between adjacent elements. Hence, it was deemed appropriate to try a transposed connection between dipoles of a multi-resonant system even though the objective was to achieve only a near-constant magnitude of the impedance, not simultaneously near-constant radiation pattern as well as impedance. A system of multiple loaded dipoles connected by a short feeder with or without a transposition of the feed conductors involves a great many variables. It is most likely that the best system devised by trial and error methods will fall short of optimum. Nevertheless, some examples are presented that demonstrate that certain desirable aspects of the performance are within reach.

The construction of most of the examples is illustrated in Figure 11 In one example, two dipoles made from thin conducting material, 0.5 cm in width, are cut to lengths of 9 and 15 cm. The dipoles are connected to a transposed feed-line made from two strips of the same material, separated by 0.125 cm and of 0.75 cm width. The system is excited, for purpose of analysis, by a voltage generator at the base of the shorter dipole. The existence of a loop on the Smith Chart plot of the input impedance of the system shown in Figure 11 has been demonstrated for an array of two dipoles having the following dimensions:

H_1 = 4.5 cm, H_2 = 7.5 cm, $w_1 = w_2$ = 0.5 cm, width of flat feedline conductors = 0.75 cm, separation between feedline conductors = 0.25 cm, length of feedline = 0.5 cm

The computed input impedance is shown in Figure 13. Provision was made in the code for placing loading elements on the second patch from each end of the dipole. Input impedance was computed again for increasing values of inductive load. The impedance band encompassed by the loop moves down in frequency as the inductance is increased. Thus, the match band can be obtained continuously as the load is varied.

As stated before, there are many parameters in this structure and this leads to numerous ways to affect the performance. Figure 14 shows how the shape and position of the loop are changed by a change in the separation between the planes of elements. Figure 15 shows how the inevitable reduction in the average real impedance of the points within the loop can be matched by a change in the feedline impedance. Finally, Figure 16 shows the influence of the transposition in the feeder. The transposed feeder appears to be leading to a broadband loop. The non-transposed feeder is producing a two-band match.

4. Future work

Although the general principles of design of small antennas with significant impedance bandwidth have been established with this work, there are still many unanswered questions about the performance. In particular, the search for an optimum design is yet to be started. This search will undoubtedly be facilitated by a better understanding of the role of coupling between the elements. Fortunately, much previous work has been done on the mutual impedance between linear elements. Also, since the feed structure is physically smaller than the system, circuit analysis of that part of the system should be straightforward. Hence, analytical tools other than computer simulation offer an alternative to collecting knowledge about system performance.

For some applications, a multi-band match is more important than a broadband one. Investigation of the parameters that govern the two types of performance are in the very early stages and should be continued.

There have been some indications that some of the systems described herein may be sensitive to variations in parameters. This aspect of their performance deserves more attention. In particular, if some parameters lead to reduction in sensitivity, knowledge of those would be very important.

5. References

[1] Y. T. Lo and S. W. Lee, Antenna Handbook, pp.4-94, 6-9, 9-59, New York: Van Nostrand Reinhold, 1988.

[2] P. E. Mayes and W. Gee, "Using Multiple Resonant Radiators for Increasing the Impedance Bandwidth of Electrically Small Antennas," *Proc.24th Annual Antenna Applications Symposium,* Allerton Park, Illinois, September 2000.

[3] J. M. Bowen, "A Study of Techniques to Solve the Disparate Mesh Size Problem with an Application to Sinuous Antennas," Thesis, University of Illinois at Urbana-Champaign, 1999.

[4] E. C. Jordan and K. G. Balmain, "*Electromagnetic Waves and Radiating Systems,*" p.563, Prentice-Hall, Englewood Cliffs, N. J., 1968.

[5] R. W. P. King, "*The Theory of Linear Antennas*," pp. 141 – 227, Harvard University Press, Cambridge, Massachusetts, 1956.

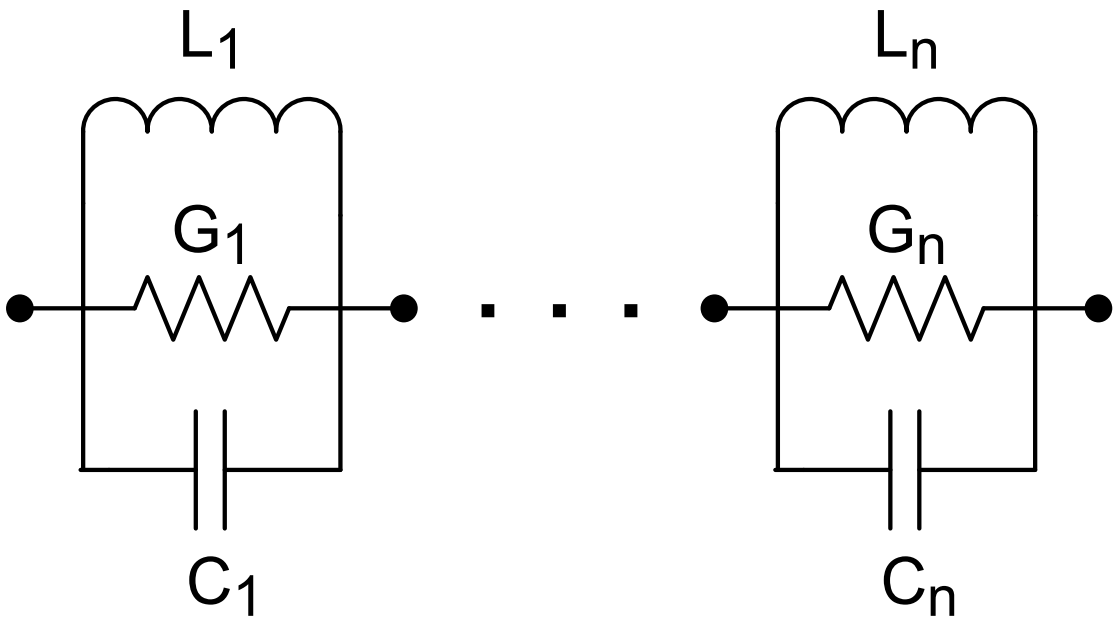

Figure 1. Circuit of series-connected tanks: G, L, and C elements connected in parallel.

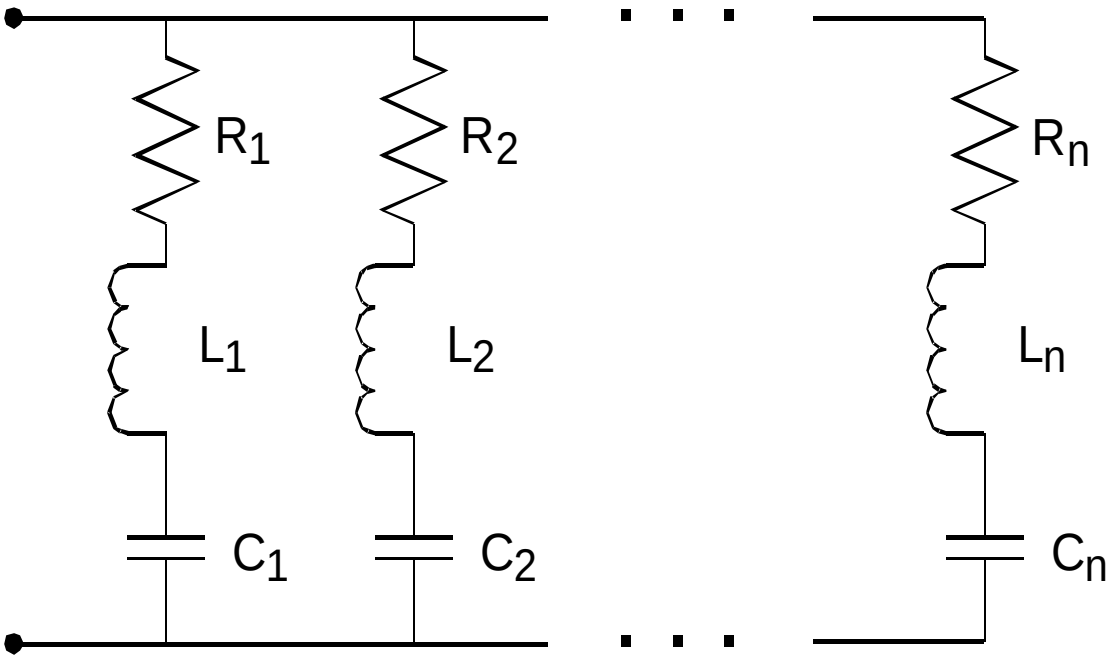

Figure 2. Circuit of parallel-connected series R, L, and C elements.

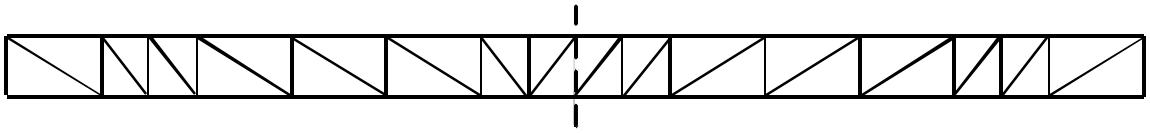

Figure 3. Set of patches used in FERM/LFMoM analysis of a blade dipole. The double half-patches in the center indicate the presence of a source and those near the ends indicate the presence of a load.

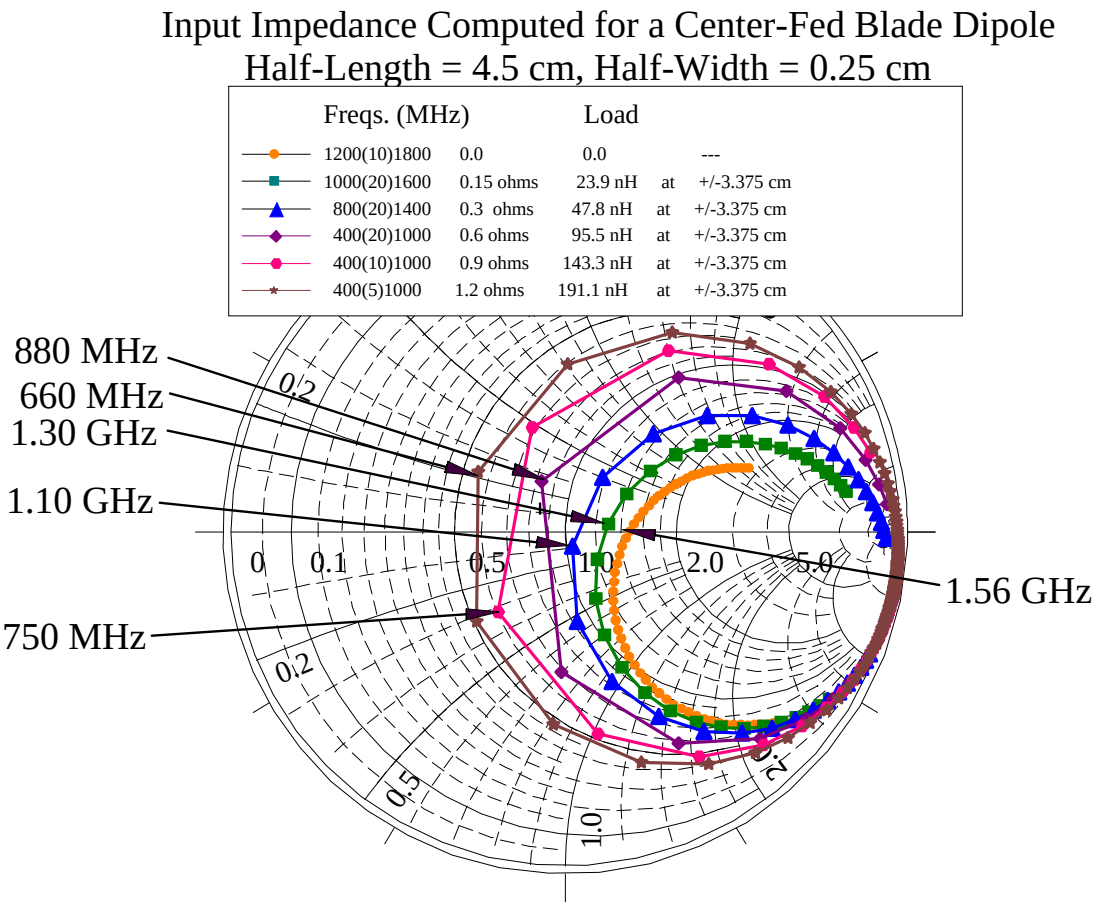

Figure 4. Computer simulations (FERM/LFMoM) of 9.0-cm dipole with various inductive loads.

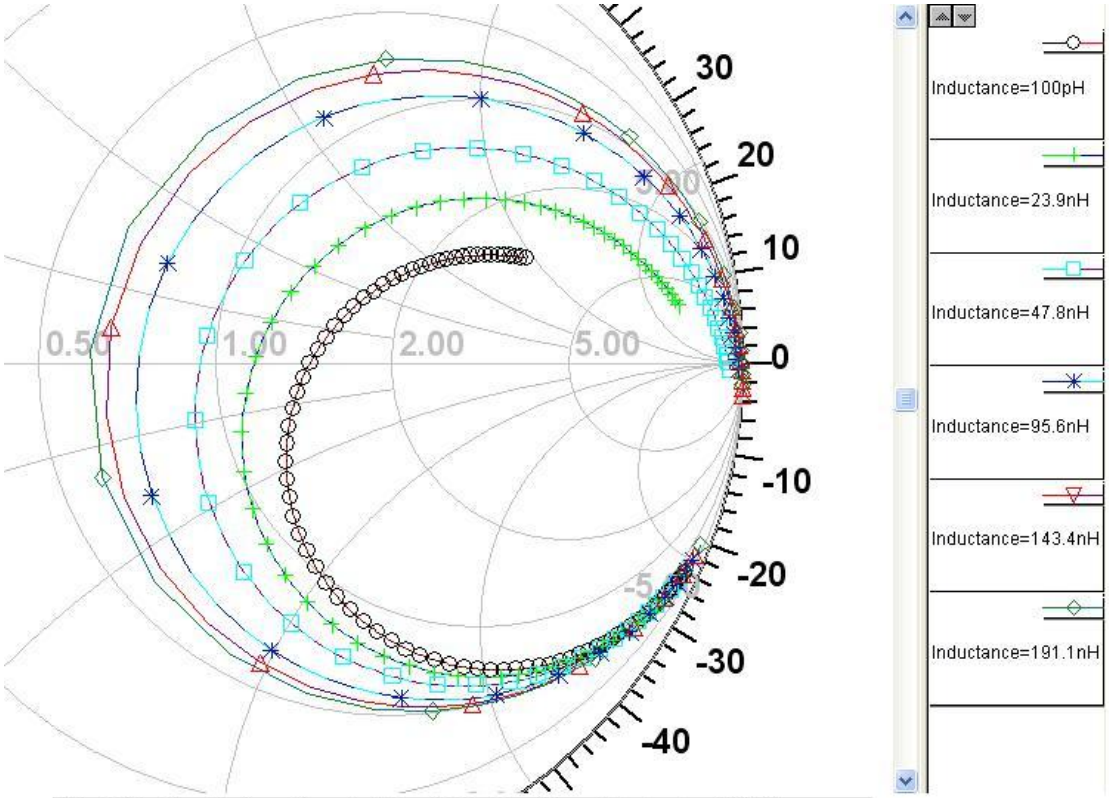

Simulation Results for a 45mm half length dipole with variable loads at 33.75mm

Load	f_{RES}	R_{RES}
0.1nH	1.528GHz	71.40
23.9nH	1.292 GHz	57.75
47.8nH	1.108 GHz	47.65
95.6nH	0.866 GHz	37.25
143.4nH	0.720 GHz	33.20
191.1nH	0.632 GHz	30.80

Figure 5. Computer simulations (HFSS) with various loads at 3.375 cm from center of 9.0-cm dipole .

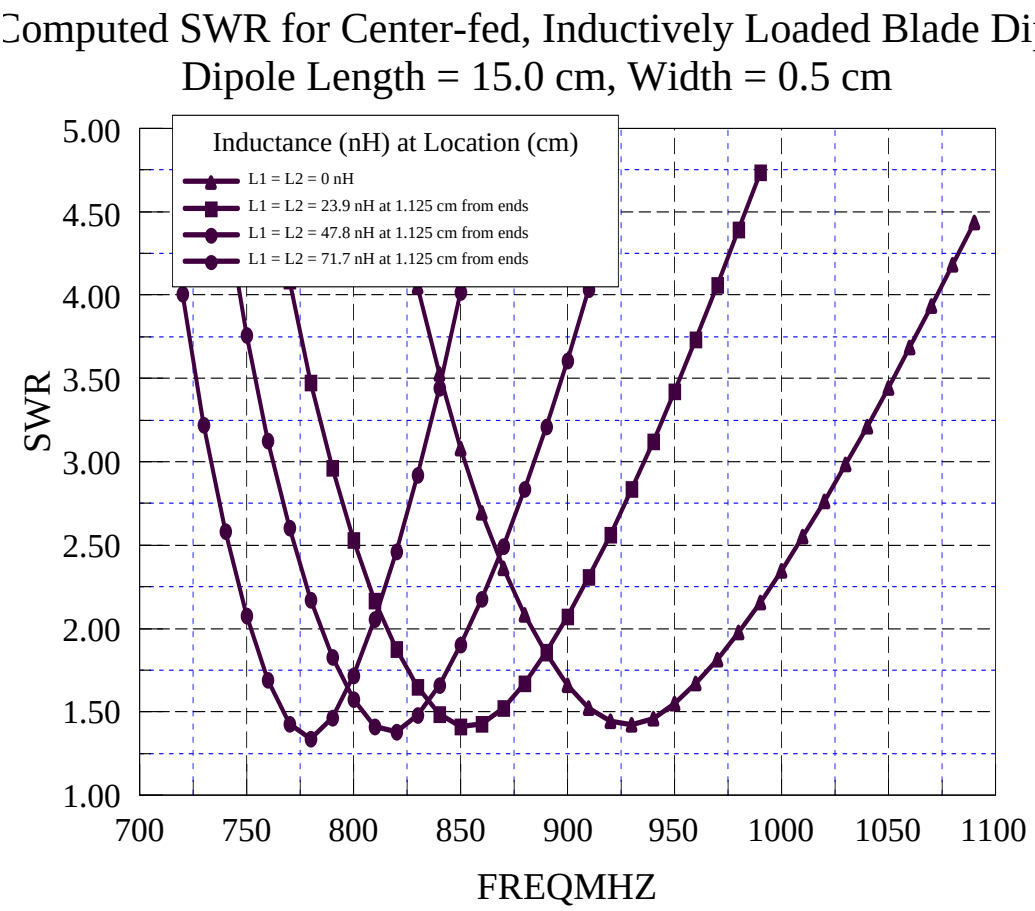

Figure 6. Computed SWR of the blade dipole when loaded by various inductors near the ends.

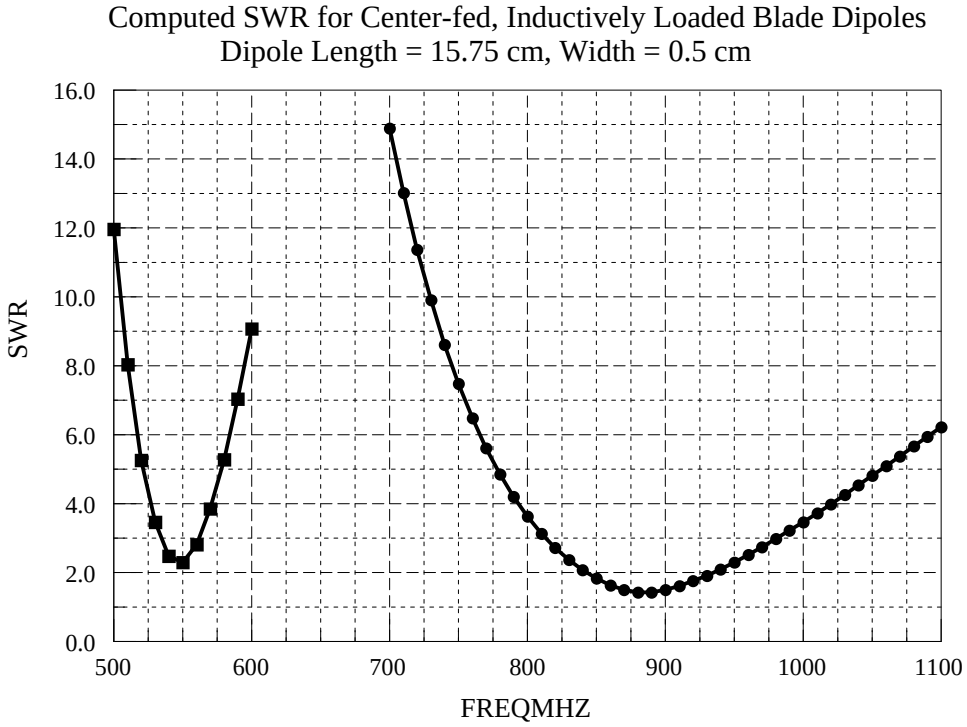

Figure 7. Computed SWR of the blade dipole when loaded by inductors near the feedpoint. Only the cases for L = 0 and L = 47.8 nH are shown.

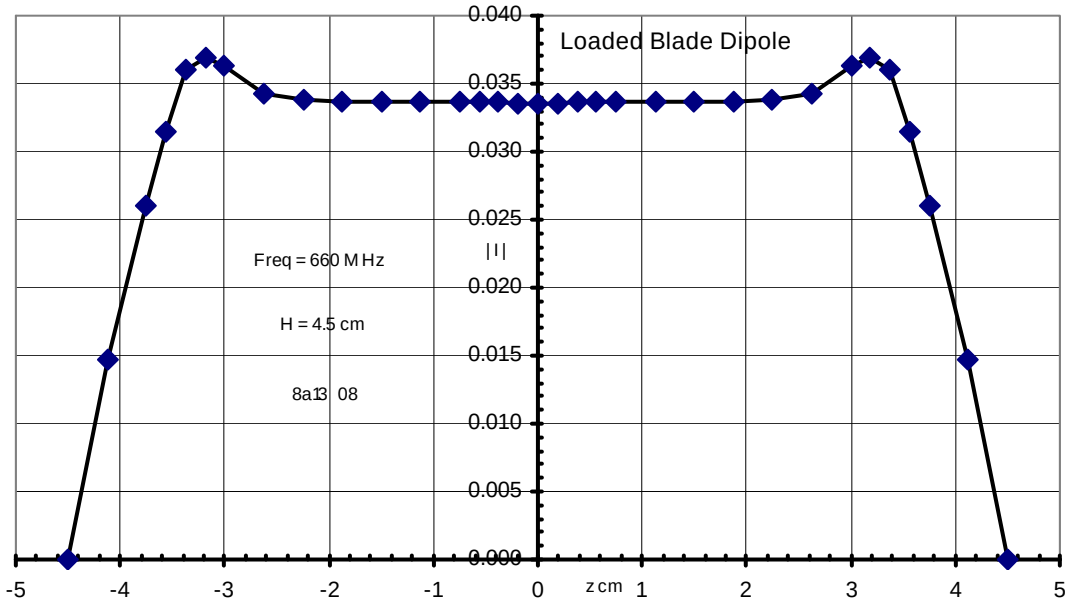

Figure 8. Current distribution on blade dipole loaded with 191 nH inductors at z = +/- 3.375 cm.

Figure 9. Photograph of blade dipole used for measurements.

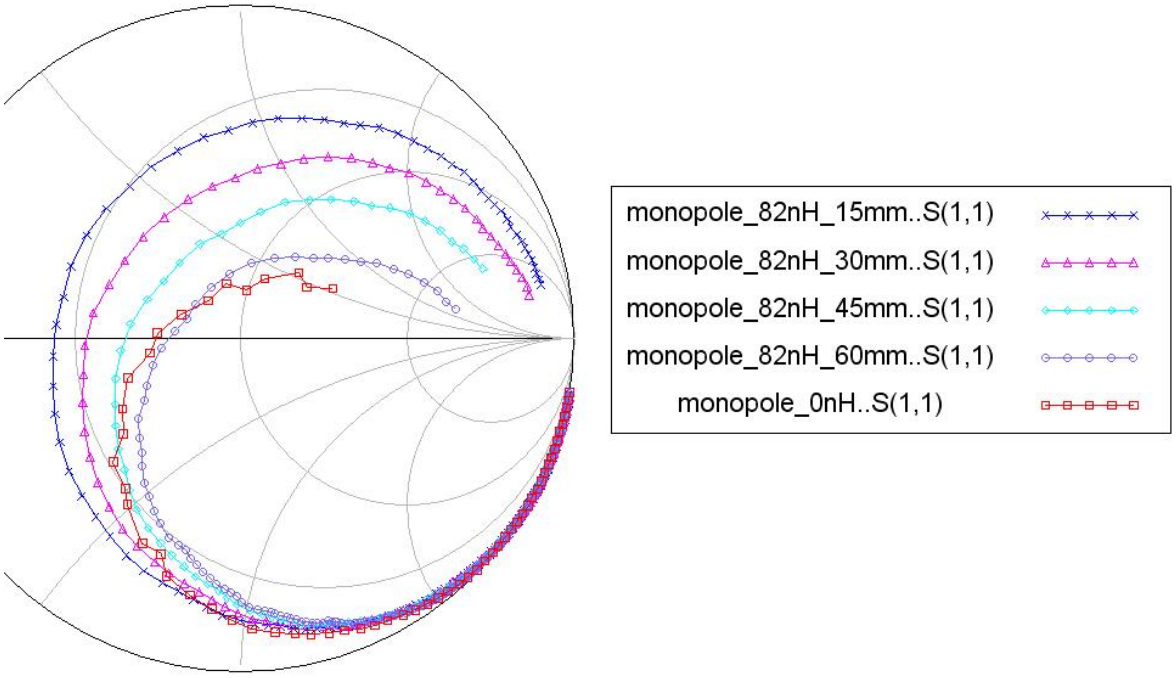

Figure 10. Measured values of the input impedance of an 82-nH inductor at various locations on a monopole of 7.5 cm height.

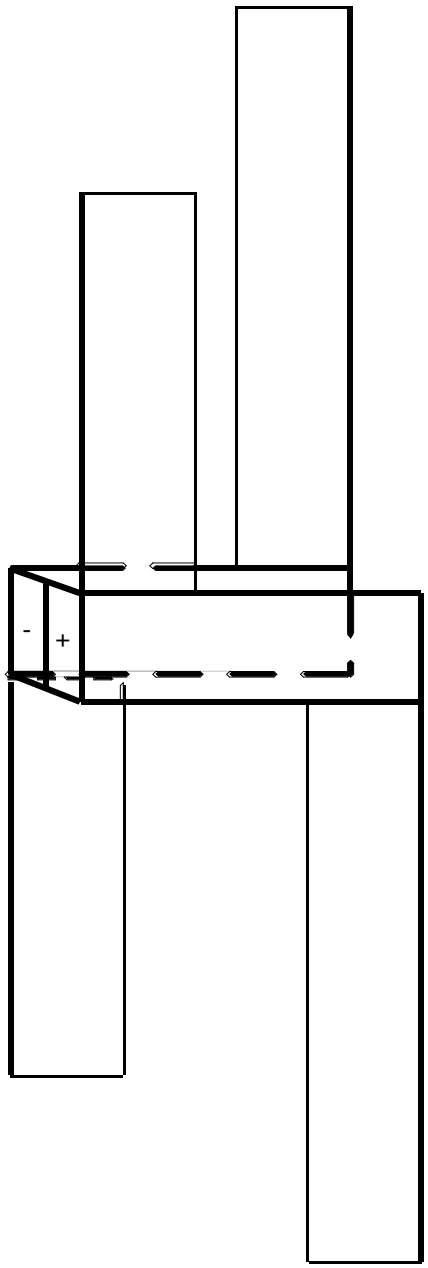

Figure 11. Line drawing of two-element array of dipoles showing the feed used in the computer analysis.

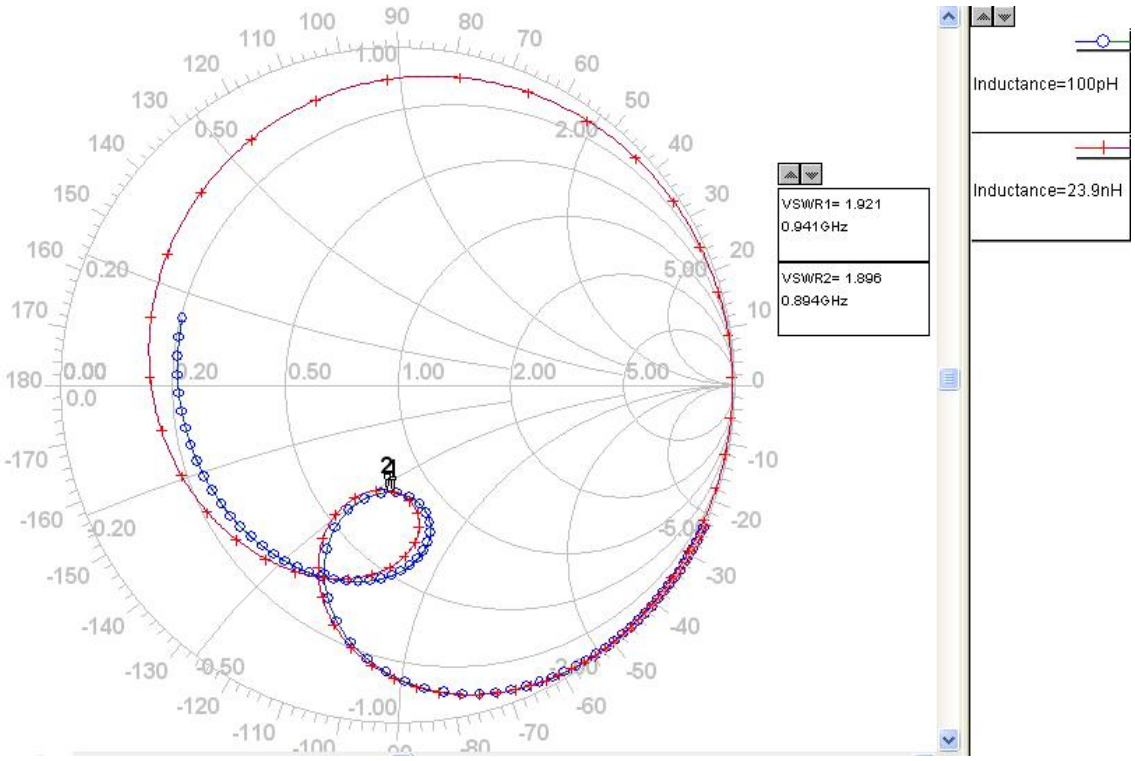

Figure 12. Computer simulations of unloaded and lightly loaded two-element dipole arrays connected in the manner of Figure 10. These results were obtained by using HFSS and compare favorably with those that were obtained by using FERM/LFMoM on the same structure.

Calculated Input Impedance: Two-Element Array of Parallel Blade Dipoles
Center-fed with 180-degrees Added Between Elements (Crossed Feeder)
Dipole 2 Length = 15.0 cm, Dipole Widths=0.5 cm, Dist. btwn Center-lines=1 cm

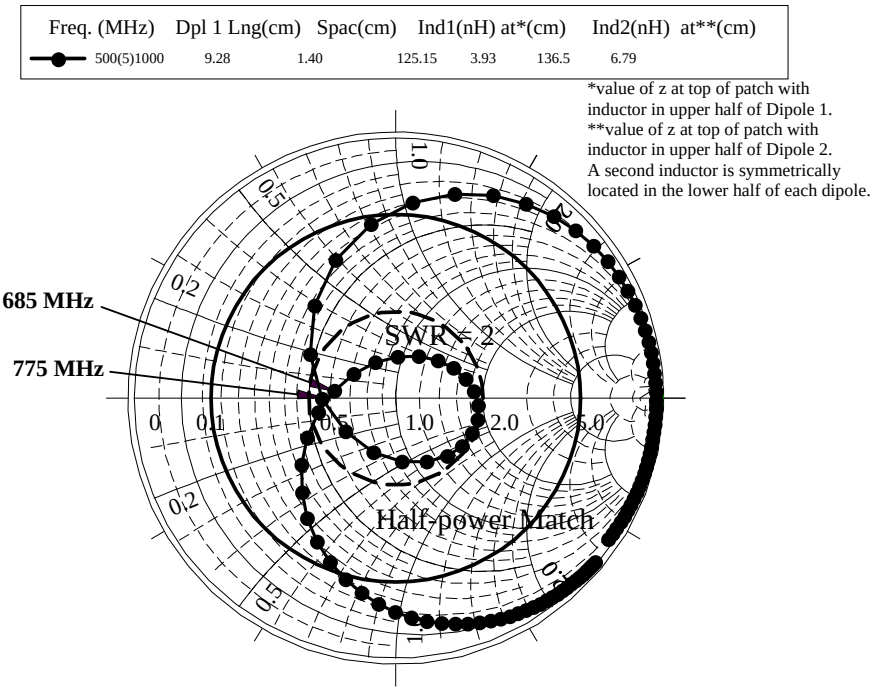

Figure 13. Input impedance of two-element array with transposed feeder adjusted to give a loop in the impedance locus (computed using FERM/LFMoM).

Calculated Input Impedance: Two-Element Arrays of Parallel Blade Dipoles
Center-fed with 180-degrees Added Between Elements (Crossed Feeder)
Dipole 2 Length = 15.0 cm, Dipole Widths=0.5 cm, Dist. btwn Center-lines=1 cm

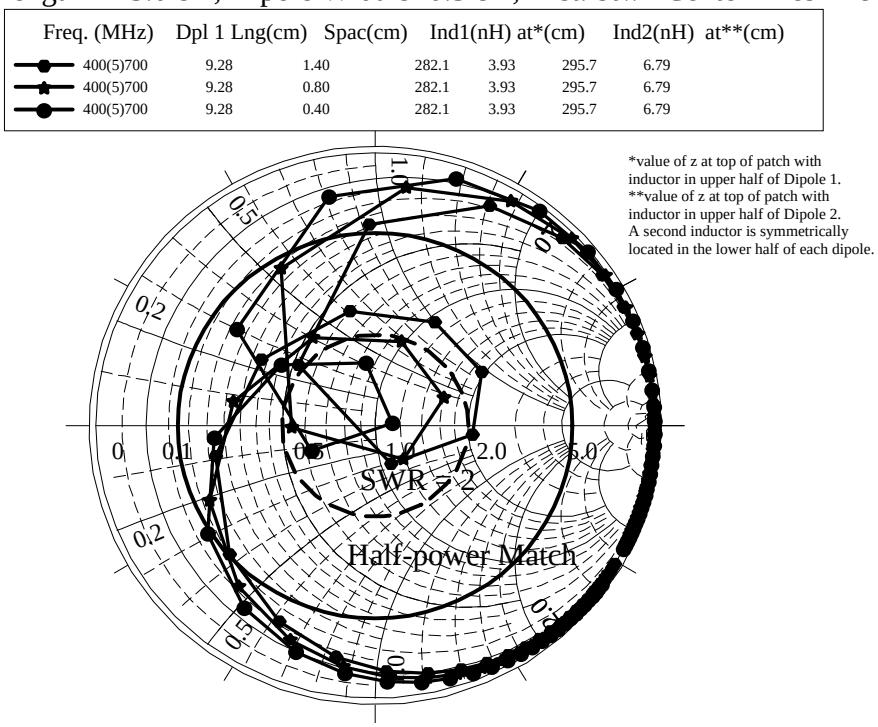

Figure 14. Input impedance for a two-element array of dissimilar dipoles as a function of the separation between the two planes of elements (computed using FERM/LFMoM).

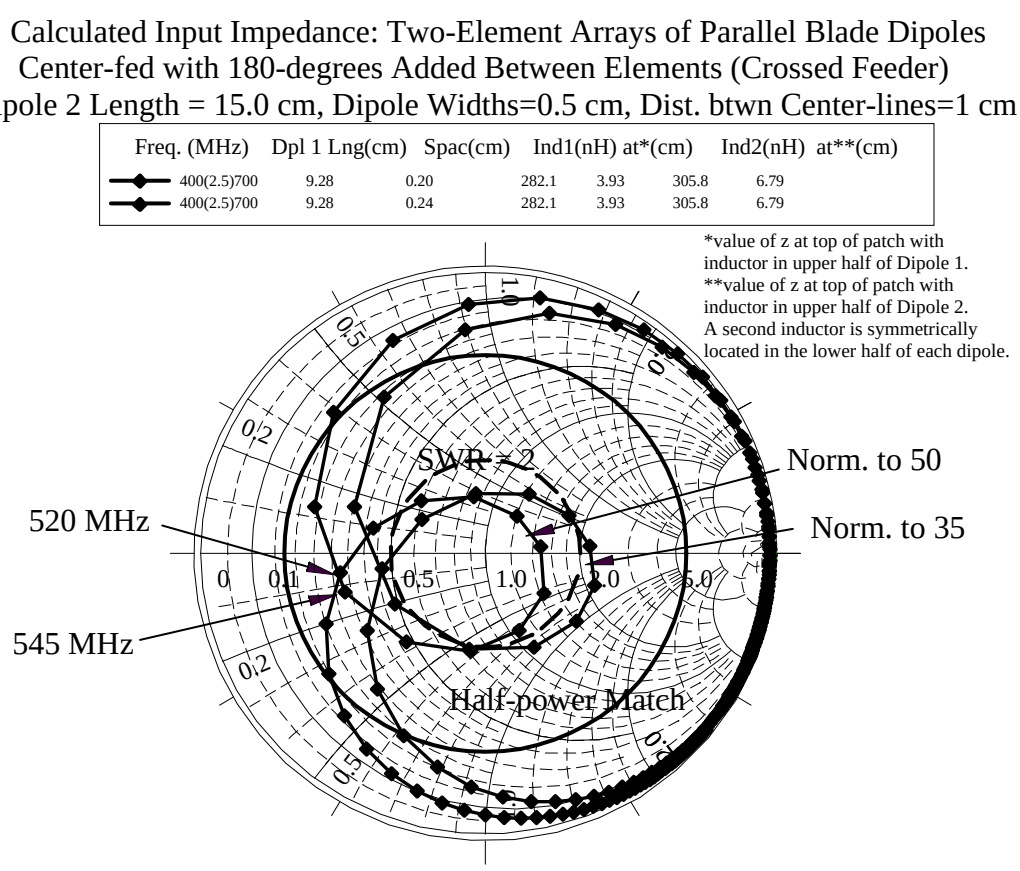

Figure 15. Input impedance of two-element array of dissimilar loaded dipoles showing the reduction in SWR that can be achieved by feeding the array with a feeder of lower impedance (computed using FERM/LFMoM).

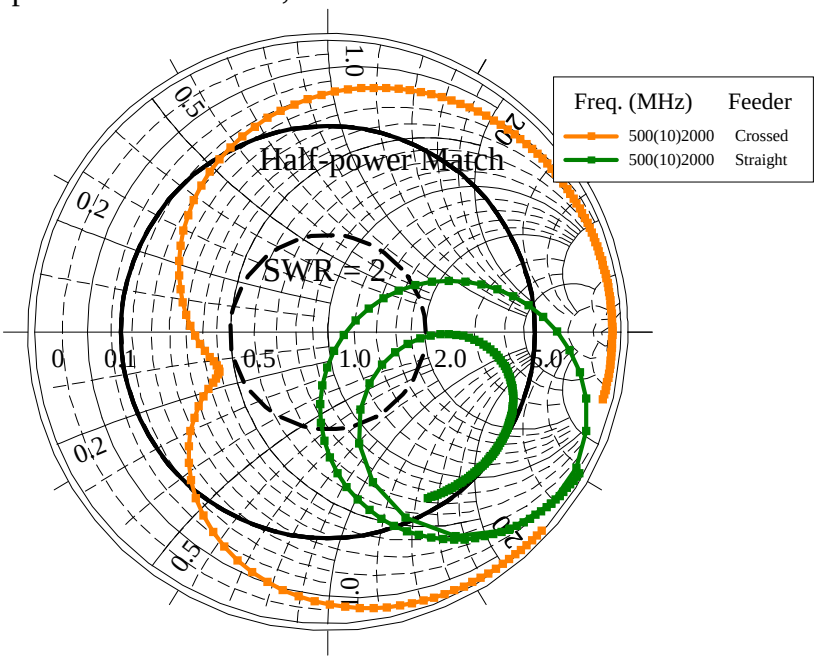

Figure 16. Comparison of computed input impedance for a two-element array that is fed by (a) a transposed feeder and (b) by a feeder that is not transposed. In this example, the transposed feeder gives an impedance locus with a dimple, a precursor to the loop of the broadband case whereas the locus for the non-transposed feeder passes through the match region twice, indicative of multiband performance.

Design and Limitations of Ku/Ka Band Compact Feeds Employing Dielectric Loaded Corrugated Horns

J.P. Creticos and D.H. Schaubert

Center for Advanced Sensor and Communication Antennas
Department of Electrical and Computer Engineering
University of Massachusetts, Amherst, MA 01003
jcretico@ecs.umass.edu and schaubert@ecs.umass.edu

This paper presents the design guidelines for, and the capabilities of, compact Ku/Ka band feeds consisting of a corrugated horn coaxially loaded with a tapered dielectric rod embedded in a foam sleeve. Independent control of the radiation pattern and phase center at each band allows feeds that are capable of meeting a variety of performance criteria. It is found that maximum feed directivity is primarily limited by the foam sleeve's capabilities while minimum feed directivity is primarily limited by the minimum aperture size achievable with the corrugated horn that does not significantly affect foam sleeve operation. Additionally, we show that a minimum frequency separation between upper and lower band frequencies is required to avoid situations where the dielectric rod significantly affects lower band operation. To demonstrate these capabilities and limits, two remote sensing reflector antennas using this feed geometry are discussed. In the first design, the feed fully illuminates the reflector at both bands so that diffraction limited gain is achieved from the reflector. The second design fully illuminates the reflector at Ku band and under-illuminates the reflector at Ka band to achieve matched half-power secondary beamwidths at Ku and Ka bands.

1. Introduction

Developments in computational power, retrieval algorithms, and microwave devices allow more complex and functionally diverse radar systems. These radars require single aperture antennas capable of simultaneously supporting multiple frequencies, polarizations, and incidence angles. Because of their efficiency, reflector antennas with multi-functional feeds are frequently used. Two such radars are the High-Altitude Wind and Rain Airborne Profiler (HIWRAP) and the Dual-Wavelength Precipitation Radar (DPR) ground based sensor network. These radars motivated the antenna studies reported here.

1.1 HIWRAP Antenna Overview

HIWRAP, being developed by NASA Goddard Space Flight Center, is to be flown on the Global Hawk UAV and will measure the tropospheric winds by collecting multi-look Doppler profiles from cloud volume backscattering measurements. By operating at Ku

and Ka bands, HIWRAP is significantly more sensitive to cloud particles than lower frequency radars enabling it to measure the mean cloud particle velocity and thus map the 3D tropospheric winds. Additionally, its dual-wavelength operation enables it to map the full atmospheric boundary layer winds from Doppler-precipitation backscatter measurements, derive information about the drop-size distribution of the precipitation and estimate the ocean surface wind field using ocean wind scatterometry techniques [1]. The small payload bay of the Global Hawk and the need for a lightweight and rugged antenna system puts strenuous demands on the antenna design. In particular the HIWRAP antenna has the following requirements:

- The antenna must fit in a cylindrical volume 18″ in height and 40″ in diameter so that it can be mechanically scanned while in the Global Hawk payload bay.
- The antenna must support 13.91 GHz (Ku) and 35.56 GHz (Ka) beams at 30° incidence and 13.47 GHz (Ku) and 33.72 (Ka) beams at 40° incidence. The bands are selected based on the ability to penetrate cloud cover and measured surface winds (Ku band) and for increased sensitivity (Ka band). Specific frequencies are selected to be near the operating frequencies of other NASA instruments. Multiple incidence angles allow the retrieval of horizontal wind components using Doppler measurements and also allow ocean scatterometry at Ku band. 30° and 40° incidence were specifically chosen after a thorough investigation of the wind retrieval benefits of different look angles [2].
- All beams should have aperture limited gain.
- The 30° incidence beam should be horizontally polarized and the 40° beam should be vertically polarized. Use of orthogonal polarizations reduces wind direction ambiguity associated with ocean scatterometry [3].
- The antenna must have a return loss of at least 18 dB over a 100 MHz bandwidth at 13.91 GHz and 35.56 GHz for the inner beam and 13.47 GHz and 33.72 GHz for the outer beam. High return loss requirements reduce the need for additional isolation and filtering in the radar frontend resulting in a lower radar noise figure.
- Nadir sidelobes must be at least 22 dB below the main lobe peak, particularly at Ku band which measures precipitation down to the ocean surface. High nadir sidelobes will result in corruption of the lowest range gate data due to significant ocean surface scattering.

1.2 DPR Antenna Overview

The DPR sensor network, being developed by Remote Sensing Solutions for NASA, is a low cost, rugged sensor network that will be used to develop and validate retrieval algorithms. Like HIWRAP, DPR is a Ku/Ka band radar that additionally requires low integrated cross-polarization and matched Ku and Ka band radiation patterns. Specifically, the requirements for DPR are:

- The antenna must support one Ku band (13.91 GHz) and one Ka band (35.56 GHz) frequency. These frequencies are chosen to be the same as the upper Ku and

Ka band HIWRAP channels so significant portions of the HIWRAP radar design can be reused for DPR.

- The antenna must support one boresited beam with horizontal and vertical polarizations at both frequencies. Polarization diversity provides information on the shape and orientation of radar targets [4].
- The antenna must have a return loss of at least 18 dB over a 100 MHz bandwidth for each polarization at each frequency so a low radar noise figure can be achieved.
- The antenna must have at least 25 dB integrated cross-polarization isolation with a goal of 30 dB. High polarization purity allows accurate measurement of low level depolarization due to variations in raindrop shape.
- The one-way 3 dB beamwidths should be approximately 1° and must be matched at Ku and Ka bands to within 10%. Matching Ku and Ka band radiation patterns ensures the same volume is measured at both bands.
- The antenna sidelobes must be at least 25 dB below the main beam level with a goal of 30 dB. Low sidelobes reduce the noise due to precipitation outside the cell of interest.

1.3 Paper Overview

Both the HIWRAP and DPR antennas use reflector antenna geometries to meet high performance antenna requirements. Key to meeting the HIWRAP and DPR antenna requirements was the development of the dual-band feed that makes use of a corrugated horn for lower frequencies and a foam sleeve antenna for upper frequencies.

Section 2 of this paper discusses the design of these multi-band compact feeds. The effects of both the dielectric rod and foam sleeve on lower band performance are characterized so that effective designs can quickly be realized. The foam sleeve antenna, which was first shown to work in such feeds at this symposium last year [5], is briefly discussed. To demonstrate the effectiveness of these compact feeds, measured results for the complete HIWRAP antenna where such feeds were used are presented in Section 3. In Section 4, the feed design and measurements for the DPR antenna are presented and further limitations on the feed technology are discussed in Section 5.

2. Compact Feed Antennas

The schematic of a typical HIWRAP feed which uses a corrugated horn loaded with a foam sleeve corrected dielectric rod is shown in Figure 1. To allow independent optimization and tuning of the feed at both Ku and Ka bands, the feed is designed such that the dielectric rod and foam sleeve primarily control Ka band behavior while the outer waveguide walls and corrugated horn primarily control Ku band. Here the dielectric rod is constructed from Rexolite 1422 (ε_r=2.53) and the foam sleeve is constructed from 10 lb/ft^3 Emerson and Cuming ECCOSTOCK SH (ε_r=1.16). The feed is divided into two primary sections, the backend and frontend. In this paper we focus on the frontend section of the feed and assume the feed backend efficiently couples the Ka band signal to

the HE_{11} surface wave mode on the dielectric rod and the Ku band signal to the HE_{11} mode of the partially filled circular waveguide.

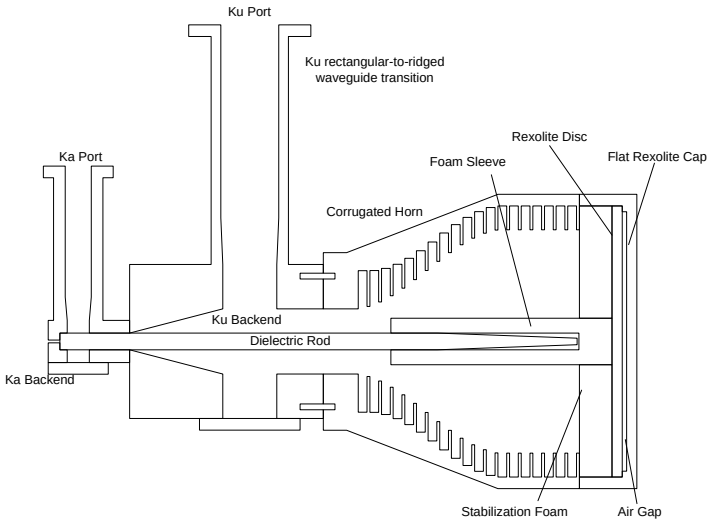

Figure 1: Schematic of typical HIWRAP feed.

Within certain limits, the Ku and Ka band portions of the feed frontend can be made to operate independently. The purpose of this section is to establish these limits and quantify some of the effects that the dielectric rod and foam sleeve have on corrugated horn operation. Additionally, because the operation of the foam sleeve antenna has not been previously described in literature, its operation is briefly discussed.

2.1 Dielectric Rod Effects on Corrugated Horn Performance

Dielectric loading affects corrugated horn performance by altering the horn's dispersion characteristics and field distribution. Changes in horn dispersion primarily alter throat design where the HE_{11} mode of the smooth wall waveguide is transformed into the HE_{11} mode of the corrugated horn. Changes in the horn's aperture distribution affect both beamwidth and radiated cross-pol. To analyze these effects, modal analysis in conjunction with a surface admittance approximation for the corrugations is used to analyze a constant diameter, loaded, corrugated waveguide as shown in Figure 2. The development of the analysis is not included here but may be found in [6]. Modeling the horn as a cascaded series of constant diameter waveguides allows the axially varying horn diameter to be accounted for. The analysis is similar to that used by Clarricoats in [7] for the analysis of an air-filled corrugated horn.

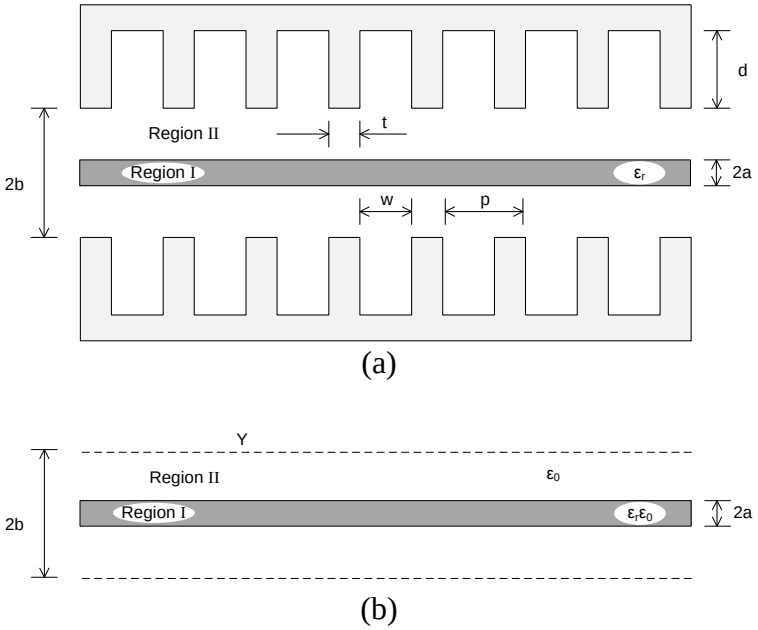

Figure 2: (a) Dielectric loaded corrugated waveguide and (b) approximation of dielectric loaded corrugated waveguide using surface admittance approximation.

The attractive feature of the modal analysis with a surface admittance approximation is the simplicity and intuition preserved by the analysis. Unfortunately, this understanding and ease of implementation comes at the cost of reduced accuracy, particularly in feed cross-pol predictions. For this reason the cross-pol effects of dielectrically loading a corrugated horn are not discussed.

Throat Matching Considerations

The first application of the loaded corrugated horn analysis is throat section design. A good throat section makes a smooth transition from the HE_{11} mode in the partially filled smooth wall waveguide to the desired HE_{11} mode in the corrugated horn. The smoothness of the transition is analyzed by observing the propagation constant throughout the transition – any large discontinuities in propagation constant will result in high reflection and, possibly, higher order mode excitation. The corrugated horn is analyzed as a cascade of constant diameter corrugated waveguides. At the junction of each waveguide section only the HE_{11} mode of each section is considered and reflection coefficient magnitude due to the junction is approximated by,

$$|\Gamma| = \left|\frac{\lambda_{g2} - \lambda_{g1}}{\lambda_{g2} + \lambda_{g1}}\right|. \tag{1}$$

To determine the accuracy of the modal analysis with a surface admittance approximation, the normalized guide wavelength for an air-filled guide is compared with

the more accurate space harmonic results from [7]. Figure 3 shows the surface admittance approximation predicts trends well with exact values typically within 5%. In the region of interest – when the corrugation depth is near $\lambda_0/2$ – the difference between the surface admittance and space harmonic analysis results is negligible.

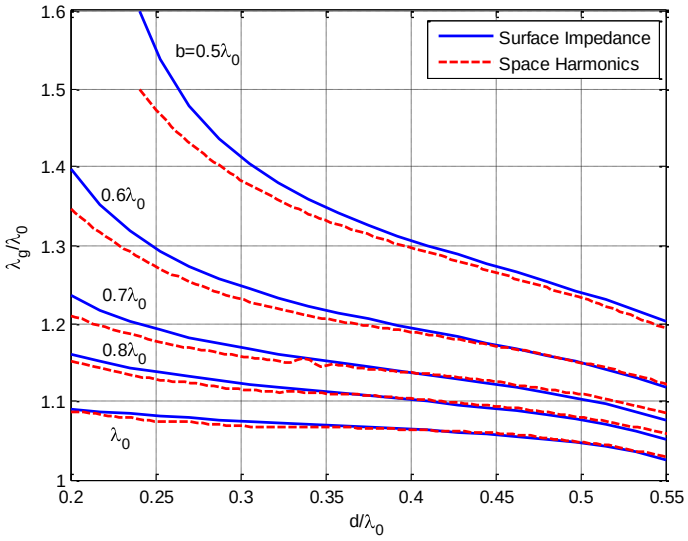

Figure 3: Comparison of normalized guide wavelength of air filled waveguide obtained using surface impedance and space harmonic approaches. Parameter is b/λ_0.

Figure 4 shows the dispersion of various combinations of the parameters *b*, *d*, and *a* defined in Figure 2a. Using the charts of Figure 4 for ε_r=2.53 or similar charts for other ε, the feed designer can choose combinations of *b* and *d* that provide a smooth transition from the propagation constant in the smooth wall waveguide to the propagation constant at the horn aperture.

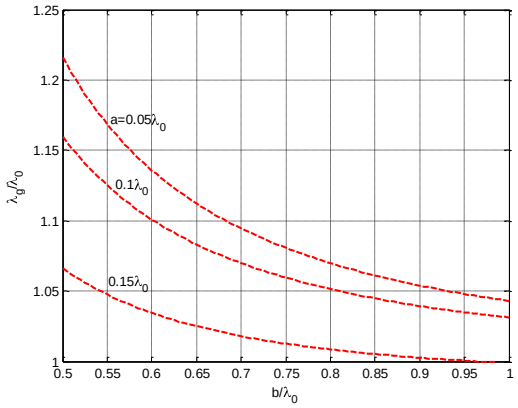

(a)

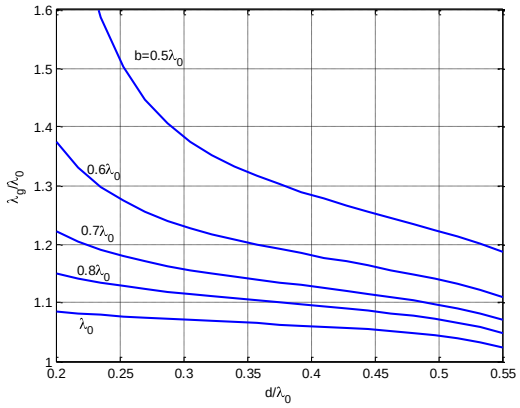

(b)

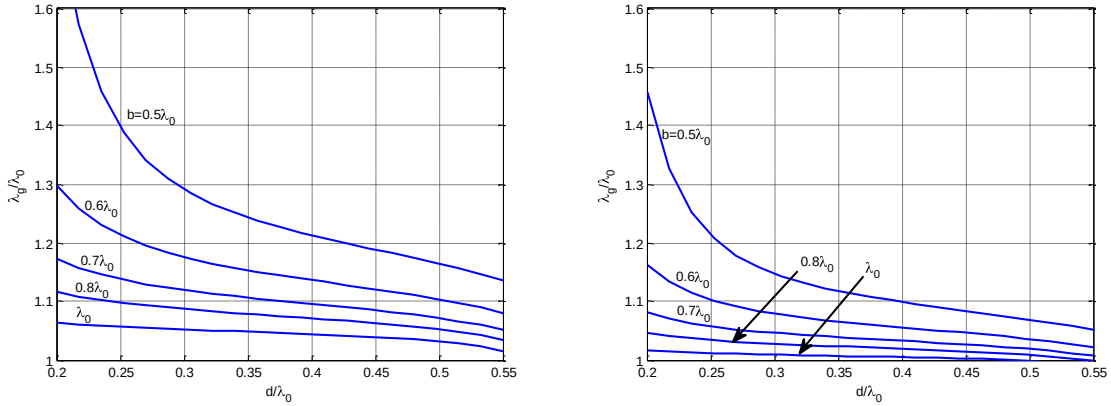

Figure 4: Normalized guided wavelength in circular dielectric loaded (a) smooth wall waveguide and corrugated waveguides with (b) a=0.05λ_0, (c) a=0.1λ_0, and (d) a=0.15λ_0. ε_r=2.53.

Field Distribution Considerations

If the dielectric is too large or ε_r too high, dielectric loading will greatly affect horn operation. Either of these scenarios will cause the energy to be bound to the rod rendering the corrugations ineffective and will make the radiation aperture smaller, resulting in a broader main beam. To quantify these effects, Figures 5-7 show, dispersion, integrated power density, and field distributions for a few typical cases.

Figure 5 shows that the dispersion of the partially filled waveguide is nearly the same as the dispersion of the dielectric rod alone except at small radii when the permittivity is moderately high. Figure 6 shows similar behavior for the fractional power carried inside the dielectric. Both figures indicate increasing ε_r reduces the diameter at which the energy becomes bound to the rod. The loaded corrugated waveguide field distributions for two dielectric diameters and permittivities, seen in Figure 7, show how the aperture distribution shrinks when the dielectric becomes the guiding mechanism. Higher permittivities display a large jump in E-plane due to the boundary condition on the electric flux density.

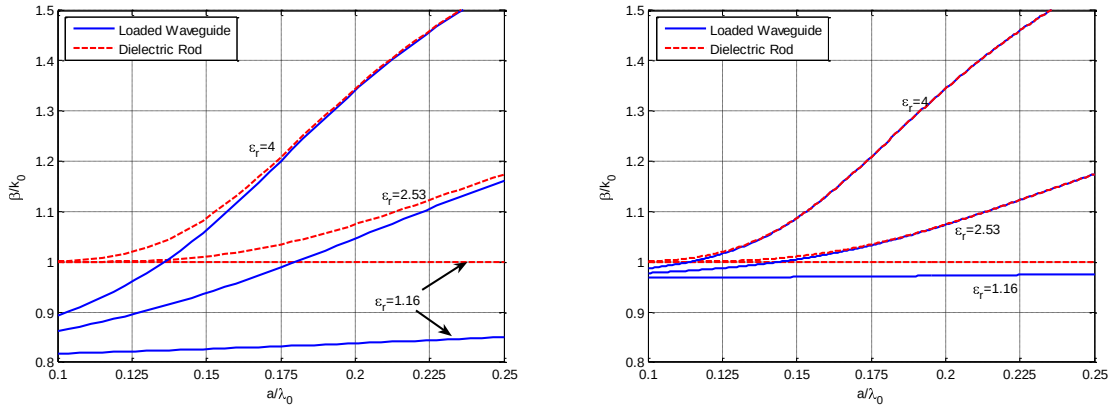

(a) (b)

Figure 5: Comparisons of β/k_0 for (a) loaded smooth wall waveguide with b=0.5λ_0 and dielectric waveguide alone and (b) loaded corrugated waveguide with b=1.5λ_0, d=0.25λ_0, and w/p=0.667 and dielectric waveguide alone.

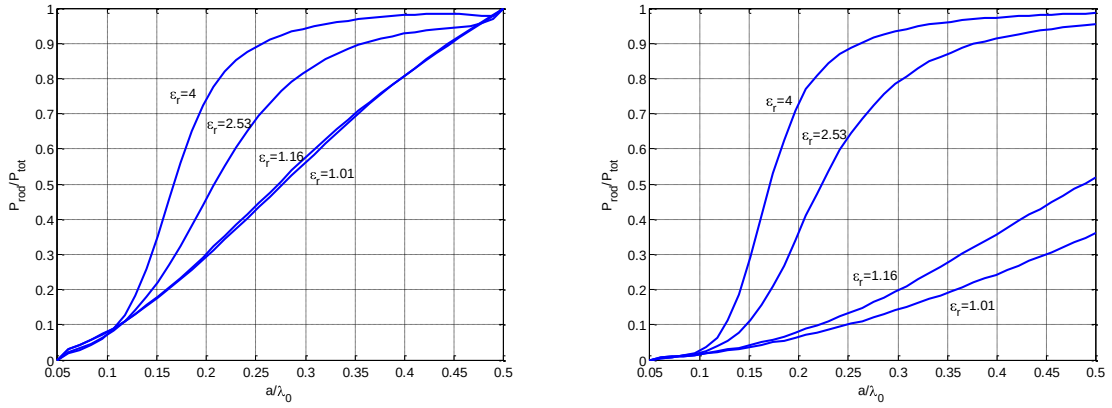

(a) (b)

Figure 6: Relative power carried within the dielectric rod of (a) a loaded smooth wall waveguide with b=0.5λ_0 and (b) a corrugated waveguide, b=1.5λ0, d=0.25λ0, and w/p=0.667.

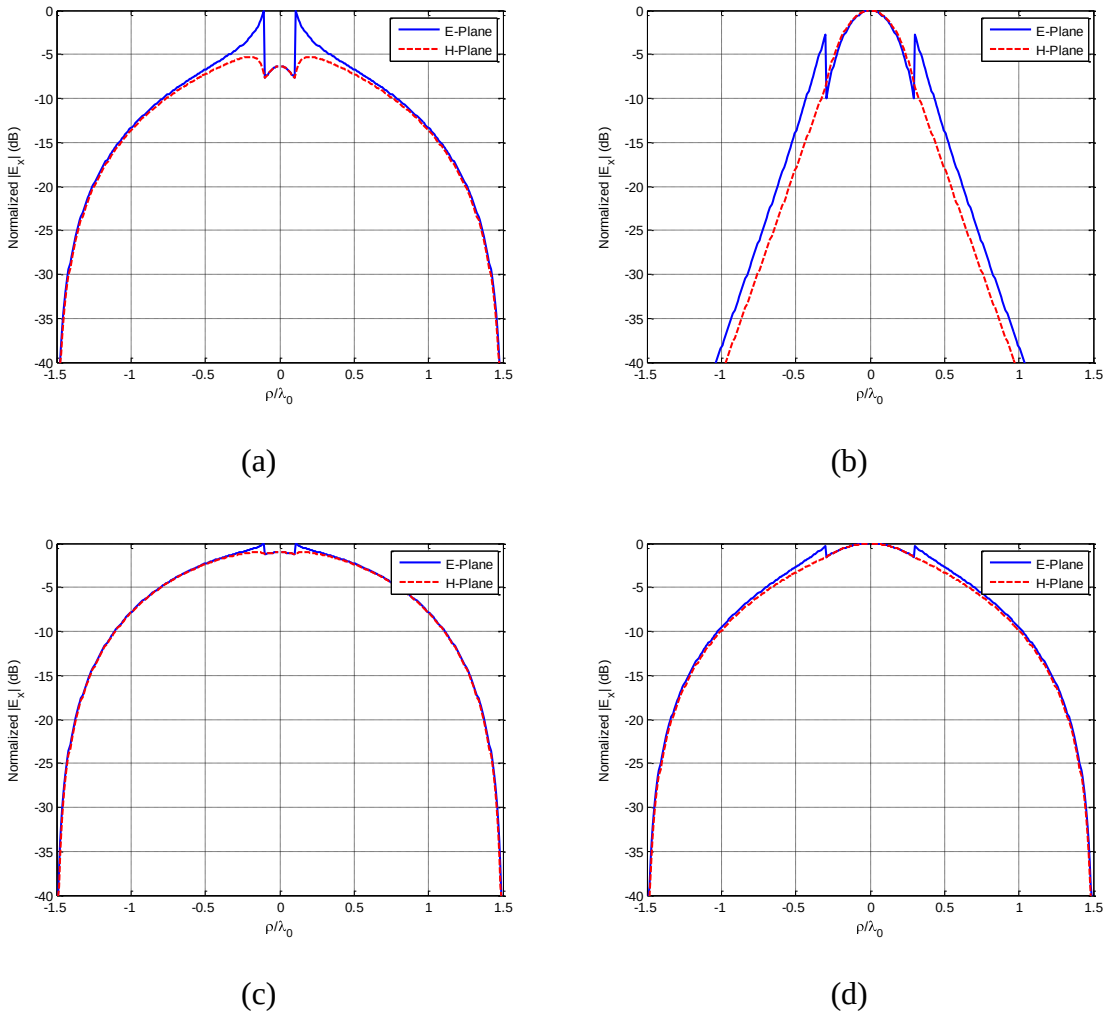

Figure 7: Comparison of Ex (co-pol field component) in loaded corrugated waveguide aperture with (a) a=0.1λ_0, ε_r=2.53, (b) a=0.3λ_0, ε_r=2.53, (c) a=0.1λ_0, ε_r=1.16, and (d) a=0.3λ_0, ε_r=1.16. w/p=0.76.

Minimum Frequency Separation

The studies of dielectric rod effects on corrugated horn operation naturally lead to the question of the minimum allowable frequency ratio between upper and lower bands. The complex expressions required to accurately model the fields and propagation constant within the feed, and the number of variables that must be considered, make it difficult to arrive at a single expression. However, two specific concerns must be addressed in all cases when designing such feeds:

1. The dielectric rod must not act as the primary energy guiding mechanism at the lower band.
2. The lower band waveguides must not affect upper band signals carried by the

dielectric rod.

The first concern is addressed by Figures 3-6. In order for the corrugated horn and metal waveguide walls to act as the primary guiding mechanism at the lower band, the majority of the guided energy must stay outside the rod. There is no clear point at which the guiding mechanism transitions from the outer waveguide to the dielectric rod. However, from Figure 6, it is clear that using a dielectric rod with $a=0.25\lambda_0$ and $\varepsilon_r=2.53$ will result in the dielectric rod carrying the majority of the energy while using a rod with $a=0.1\lambda_0$ and $\varepsilon_r=2.53$ will allow the outer waveguide to dominate lower band performance. In between these points, such as when $a=0.15\lambda_0$ and $\varepsilon_r=2.53$, Figures 3-6 indicate the corrugations still have a significant effect on lower band operation but care must be taken as the dielectric rod is also strongly influencing lower band dispersion and field distribution.

The second concern can be addressed by investigating the change in propagation constant of a partially filled waveguide at the upper band while the outer waveguide size is adjusted [8]. Figure 8 shows typical curves depicting the change in propagation constant with variation in b for $\varepsilon_r=2.53$. As the outer waveguide size increases, its influence on propagation constant diminishes until changes in the outer waveguide radius lead to negligible changes in propagation constant. At this point it can be assumed that discontinuities in the outer waveguide – such as corrugations – will not severely influence lower band operation and a minimum frequency ratio has been satisfied to ensure upper band behavior will not be significantly affected by lower band feed components. While considering the effects of dielectric rod size on upper band operation, the cutoff radius of the TE_{01} and TM_{01} modes should be kept in mind and the rod should generally be made small enough so that only the HE_{11} mode propagates on the dielectric rod waveguide. For Rexolite, this implies keeping $a<0.306\lambda_0$ [9].

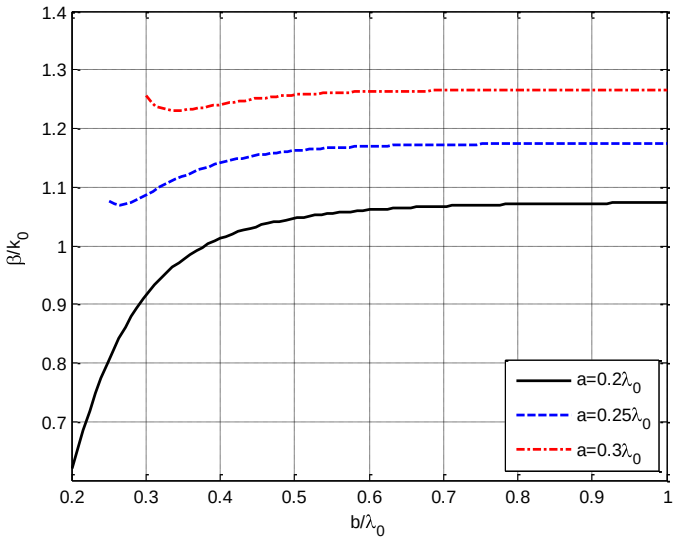

Figure 8: Variation in normalized upper band propagation constant, β/k_0, with outer waveguide diameter for different rod diamaters. Note λ_0 is the free space wavelength at the upper band in this case.

2.2 Foam Sleeve Antenna Operation

Key to satisfying the high performance requirements of both the HIWRAP and DPR antennas is the use of a foam sleeve to achieve reduced beamwidths at Ka band while maintaining independent control over feed radiation at Ku and Ka bands. Literature reviews produced a similar antenna patented by Krall and Syeles [10] which is an ε_r=84 embedded in ε_r=81 surrounding medium. Such an antenna cannot be used in a loaded corrugated horn design because it will significantly influence lower band operation.

The foam sleeve antenna is a type of surface wave antenna and, referring to Figure 9, the antenna is divided into three sections. From z=-∞ to z=z_1, the dielectric rod is constant diameter and guides an incident surface wave travelling in the +z direction. In the feed section, which is between the z=z_1 and z=z_2 planes, the dielectric rod is tapered transferring the majority of the guided energy to the foam sleeve. From the z=z_2 to z=z_3 planes, the foam sleeve acts as a surface waveguide until it is terminated at the z=z_3 plane. The primary sources of radiation are the discontinuities at the z_1, z_2, and z_3 planes and the taper section of the dielectric rod in the feed section. Radiation due to the discontinuities at the z_1 and z_2 planes and due to the taper in the feed section is undesirable feed radiation which typically has a broader pattern than radiation due to the foam sleeve termination. An approximation due to Zucker for the normalized termination radiation pattern of a surface wave antenna is

$$F(\theta) = \frac{\beta - k_0}{\beta - k_0 \cos\theta} \qquad (2)$$

where β is the propagation constant of the surface waveguide. As $\beta \rightarrow k_0$, the fields become loosely bound to the waveguide causing the illuminated aperture at $z=z_3$ to become very large and, as predicted by (2), the termination radiation pattern beamwidth goes to zero.

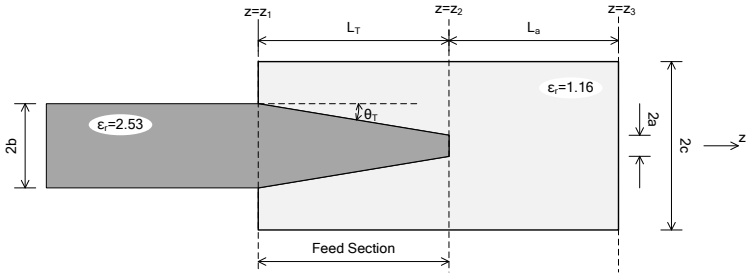

Figure 9: Schematic drawing of foam sleeve antenna.

Feed radiation, which is less directive, is not negligible and must be accounted for in the foam sleeve antenna design. Since the foam sleeve antenna is a surface wave antenna, methods developed by Zucker for achieving optimal directivity by adjusting the relative phase between feed and termination radiation can be used to narrow the main beam at the cost of high sidelobes. Here we try to avoid such methods because the increased sidelobe levels reduce reflector illumination efficiency.

Figure 10 shows increased foam sleeve diameters allow higher directivity and comparable sidelobes to smaller diameter cases. Additionally, smaller taper angles, θ_T, and tip radii, a, reduce sidelobe levels and increase directivity. In all these cases higher directivity is achieved because feed efficiency – defined here as the percent power transferred from the dielectric rod to the guided HE_{11} surface wave mode on the foam sleeve – is improved by using larger diameter sleeves, more gradual tapers, and smaller tip radii. Foam sleeves that extend further beyond the end of the dielectric rod have both higher directivity and sidelobes because the phase relation between feed and termination radiation is approaching the optimal directivity case.

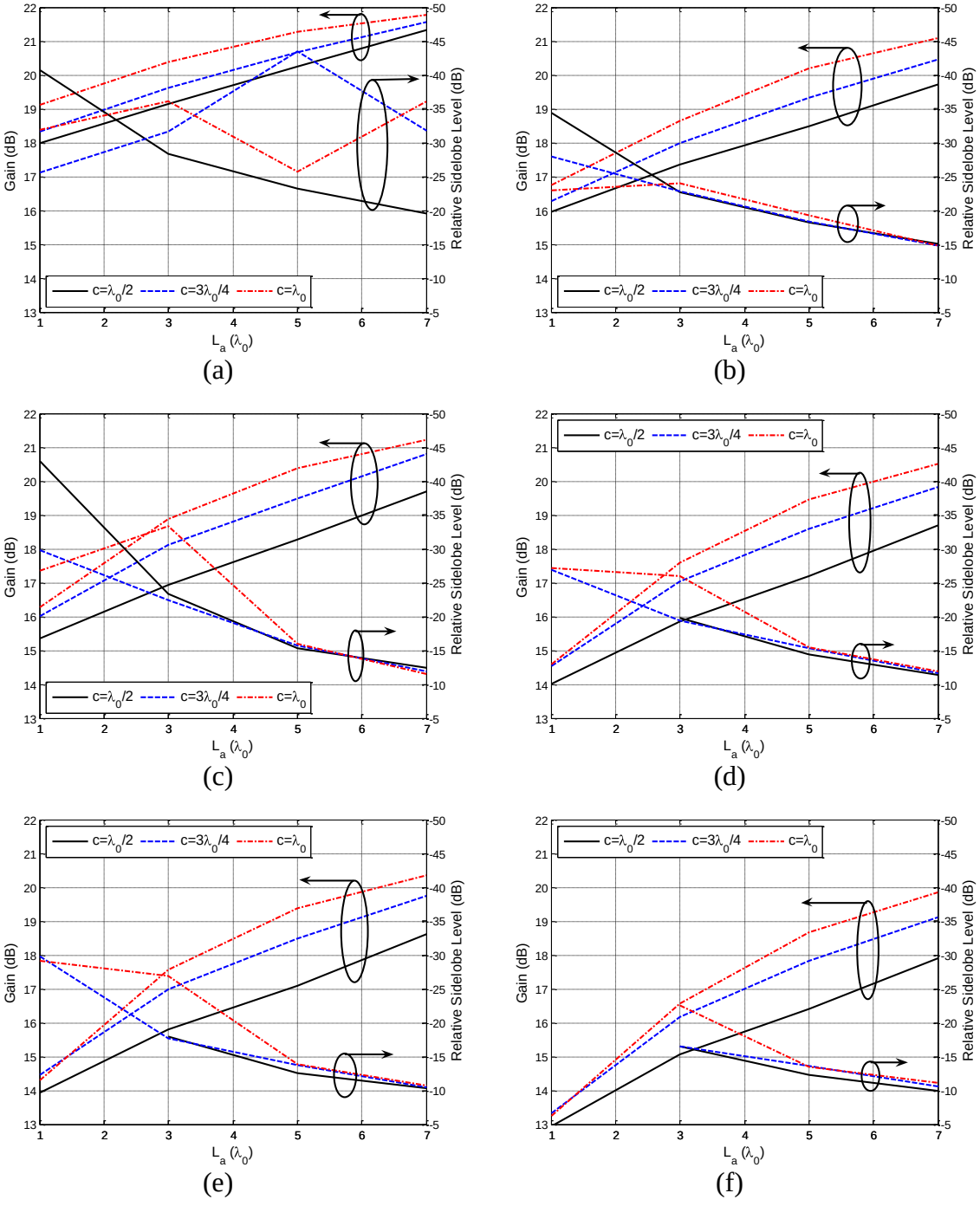

Figure 10: Directivity and sidelobe of foam sleeve antenna for (a) θ_T=1°, a=0.1λ_0, (b) θ_T=1°, a=0.15λ_0, (c) θ_T=3°, a=0.1λ_0, (d) θ_T=3°, a=0.15λ_0, (e) θ_T=5°, a=0.1λ_0, (f) θ_T=5°, a=0.15λ_0.

3. HIWRAP Antenna

The first feeds based on the compact feed geometry presented here are the feeds used in the HIWRAP antenna. In this case the feeds are used to fully illuminate an offset fed, prime focus reflector for maximum gain. The reflector has an 18.750″ focal length and 19.924″ projected aperture diameter. Since the HIWRAP antenna is an offset reflector, the f/D is computed based on the parent parabola from which the reflector is cut. In this case the parent parabola diameter is 51.848″ and f/D=0.36. The small f/D is required to effectively use the volume of the Global Hawk payload bay and this requirement, combined with the need to scan more than 5 beamwidths at Ka band, makes the antenna sensitive to the Ku and Ka band phase centers not being accurately co-located at the designed feed positions. Because the foam sleeve and corrugated horn sections of the antenna operate independently, the compact feed presented in this paper is ideally suited for these requirements.

To reduce feed size, the HIWRAP feeds use profiled corrugated horns with a constant diameter corrugated waveguide section added to the end of the profile to move the phase center toward the horn aperture. The feed for the beam at 30° incidence uses a 1.23″ diameter horn and the feed for the beam at 40° incidence uses a 1.20″ diameter horn. Both horns have a 1.5″ long profile. To support Ka band operation, the 30° feed uses a 0.180″ diameter dielectric rod that is linearly tapered to 0.070″ diameter over 1.475″. The 40° feed uses a 0.190″ diameter dielectric rod that is linearly tapered to 0.070″ diameter over 1.500″. The 30°and 40°feed foam sleeve diameters are 0.440″ and 0.500″, respectively, and each foam sleeve extends 0.375″ beyond the end of the dielectric rod. One of the feeds is shown in Figure 11 and the entire HIWRAP antenna is shown in Figure 12.

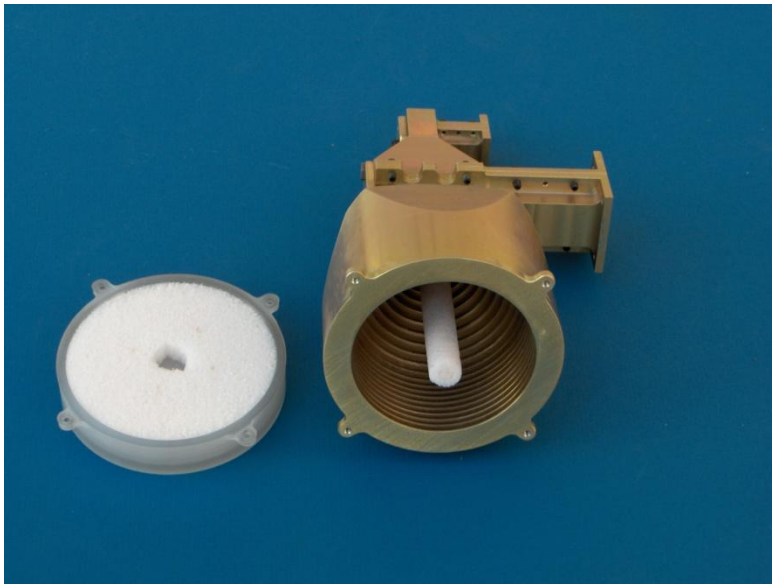

Figure 11: Compact feed for use in the HIWRAP antenna with radome removed.

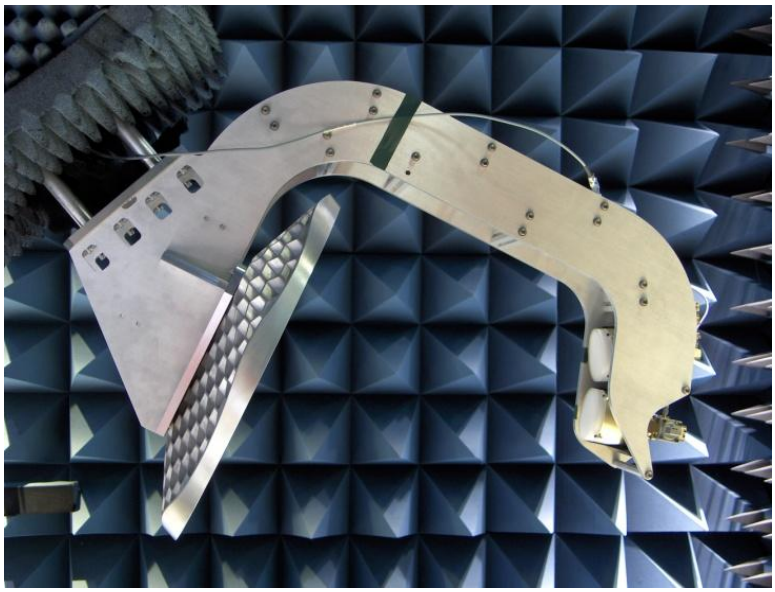

Figure 12: HIWRAP antenna inside anechoic chamber as it will be oriented while in flight.

The HIWRAP feeds were characterized using planar near-field measurements in the University of Massachusetts, Amherst near-field range and show good agreement with Ansoft HFSS simulations (Figure 13). The integrated HIWRAP antenna was measured in the compact range at NASA Goddard Space Flight Center and was found to have 35.92 dBi and 39.59 dBi gain for the 30° beam at Ku and Ka bands and 35.56 dBi and 39.53 dBi gain for the 40°beam at Ku and Ka bands (Figures 14 and 15). The reflector is aligned so its boresight direction corresponds to 33° incidence. The 7° scan required to achieve the 40° beam caused the coma lobe to be absorbed into the main lobe creating a shouler at -11.20 dB at Ka band. This shoulder is significantly absorbed into the main beam and the first distinct nadir sidelobe for both beams at both bands is well below the -22 dB requirement.

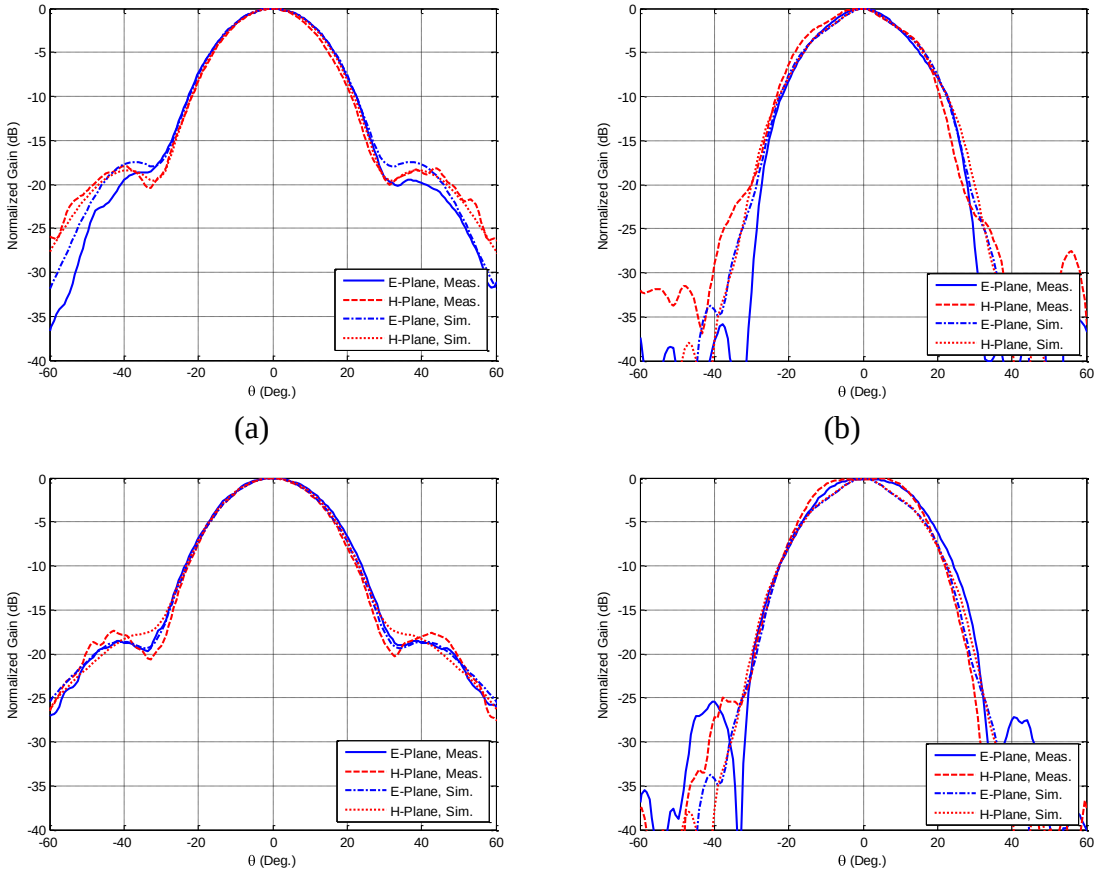

Figure 13: 30° feed radiation patterns at (a) Ku and (b) Ka bands and 40° feed radiation patterns at (c) Ku and (d) Ka bands.

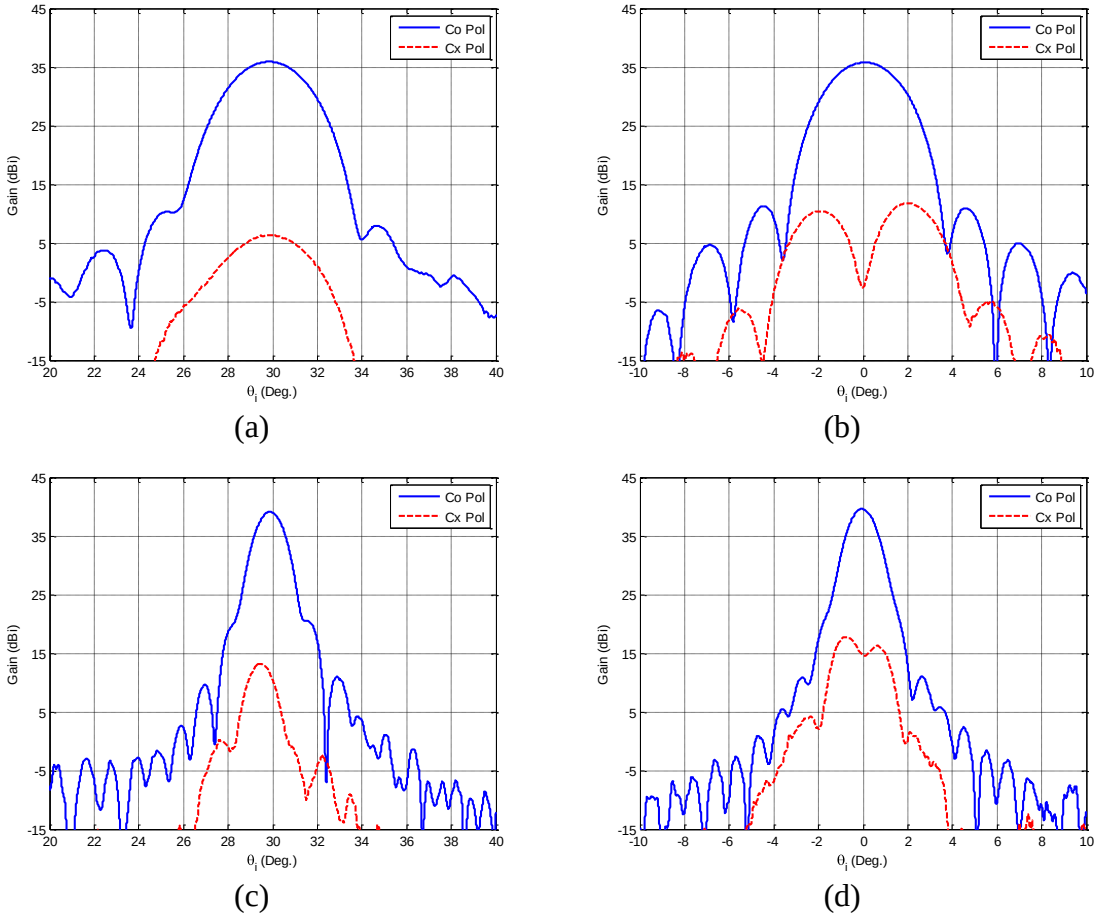

Figure 14: Measured HIWRAP antenna radiation patterns due to 30° feed at Ku band in the (a) elevation and (b) azimuth planes and at Ka band in the (c) elevation and (d) azimuth planes.

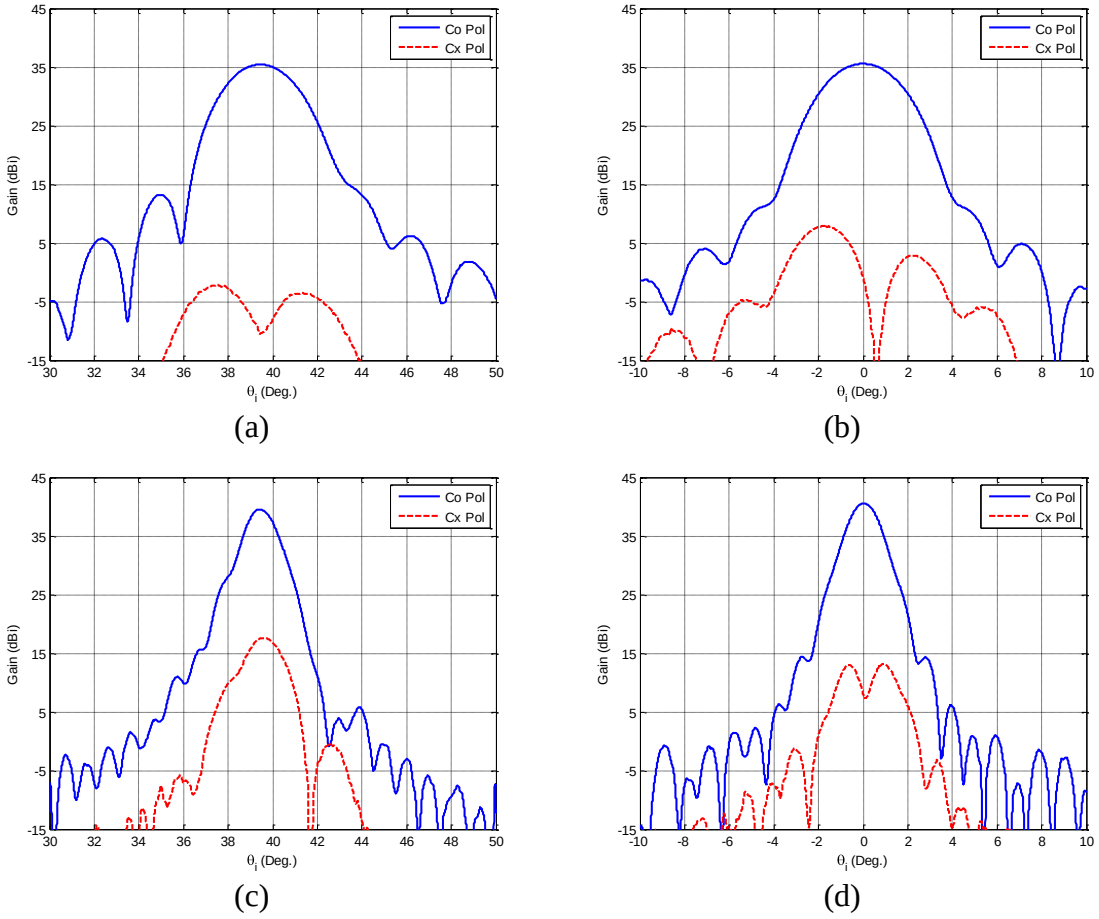

Figure 15: Measured HIWRAP antenna radiation patterns due to 40° feed at Ku band in the (a) elevation and (b) azimuth planes and at Ka band in the (c) elevation and (d) azimuth planes.

4. DPR Antenna

The second application of the compact feed discussed here is the DPR reflector antenna. The DPR reflector is a dual-offset Gregorian antenna that satisfies the Mizugutchi condition, [11]. Satisfaction of the Mizugutchi condition gives the reflector inherently low cross-pol and the dual-offset design eliminates aperture blockage that would increase sidelobe levels. Approximately matched reflector secondary Ku and Ka band beamwidths can be achieved when the relation $D_{Ku}f_{Ku}=D_{Ka}f_{Ka}$ is satisfied where D_{Ku} and D_{Ka} are the illuminated diameters of the reflector at frequencies f_{Ku} and f_{Ka} bands, respectively.

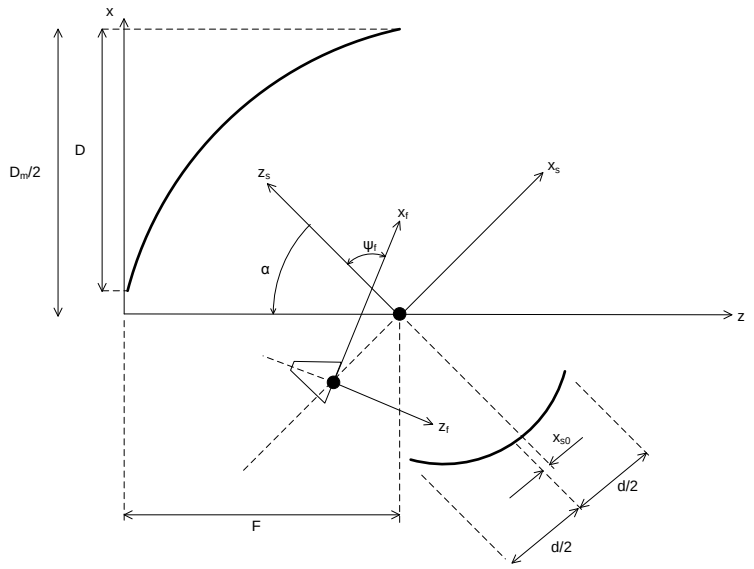

Figure 16: Schematic of the DPR offset Gregorian antenna.

To achieve approximately 1° half power beamwidth secondary reflector patterns at both bands in combination with better than -25 dB sidelobes and low cross-pol can be obtained with the reflector values listed in Table 1. Using Gaussian patterns as approximations to the Ku and Ka band feed patterns, the desired matched beam condition is met and the integrated cross-pol, calculated as

$$I_{cx} = \frac{\iint \{|E_{cx}|^4 + |E_{co}E_{cx}|^2\} du\, dv}{\iint |E_{co}|^4 du\, dv} \approx \frac{\iint |E_{co}E_{cx}|^2 du\, dv}{\iint |E_{co}|^4 du\, dv} \tag{2}$$

where E_{co} is the co-pol field pattern, E_{cx} is the cross-pol field pattern, and the integrals are evaluated over the main beam, is found to be -37.09 dB at Ku band and -35.75 dB at Ka band. This satisfies both the -30 dB goal and -25 dB requirement but only accounts for the cross-pol of the reflector and ignores feed cross-pol contributions.

Table 1: Design values for the DPR reflector based on Figure 16. *e* is the sub-reflector eccentricity.

d	0.42 m	α	45.42°
x_{s0}	-0.09 m	ψ_f	79.44°
e	0.33	f	0.6 m
$2c$	0.17 m	D	1.6 m
D_m	3.344 m		

The greatest challenge in designing the DPR feed is supporting significantly different beamwidths at Ku and Ka bands. The feed is limited by the minimum beamwidth that can

be achieved at Ka band with the foam sleeve while maintaining low sidelobes. The final feed design uses a 0.180″ diameter dielectric rod with a 1.500″ taper that is embedded in a foam sleeve of 0.600″ diameter that extends 0.500″ beyond the end of the rod. The corrugated horn, used to support Ku band radiation, has a diameter of 1.200″ and a $\lambda_{Ku}/4$ groove is cut into the face of the horn to reduce the edge diffraction effects typically seen with small aperture corrugated horns.

A prototype DPR feed, shown in Figure 17, was fabricated and tested. The feed has two orthogonal waveguide sidearms at each band with each sidearm responsible for one polarization. At both Ku and Ka bands, the sidearm port further from the front of the feed is considered to be Port 1 and the port closer to the front of the feed is Port 2. Feed patterns, shown in Figure 18, were measured using the University of Massachusetts, Amherst near-field range's spherical measurement capabilities. Ku band patterns show good symmetry but have high peak cross-pol levels in the diagonal plane due to the horn's small aperture size. The Ka band patterns have -25 dB sidelobes that are captured by the reflector. These sidelobes are a result of needing to extend the foam a fair distance beyond the end of the dielectric rod to achieve minimum beamwidth. Narrower Ka band feed patterns are achieveable at the expense of higher sidelobes while wider Ka band feed patterns would require extremely wide Ku band feed patterns and a correspondingly small aperture horn.

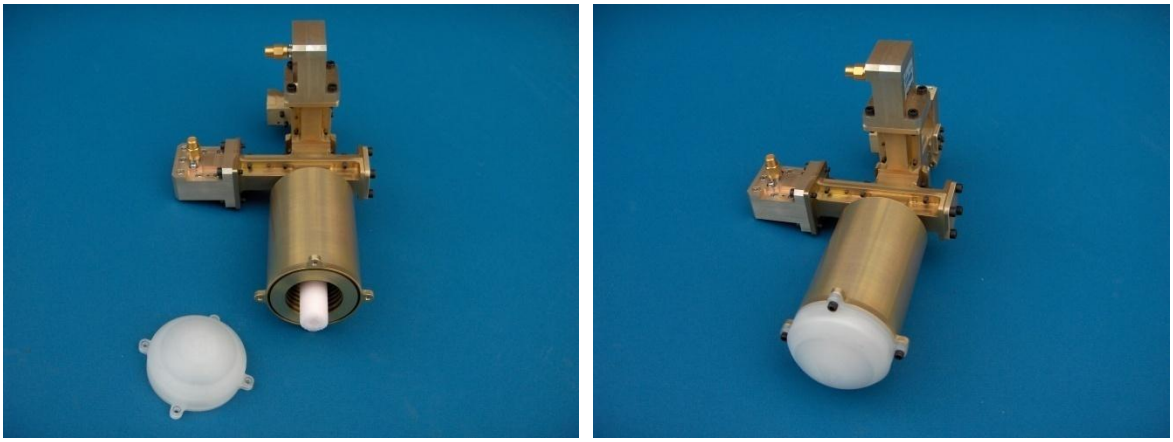

(a) (b)

Figure 17: Pictures of prototype DPR feed (a) with cover removed and (b) with cover attached.

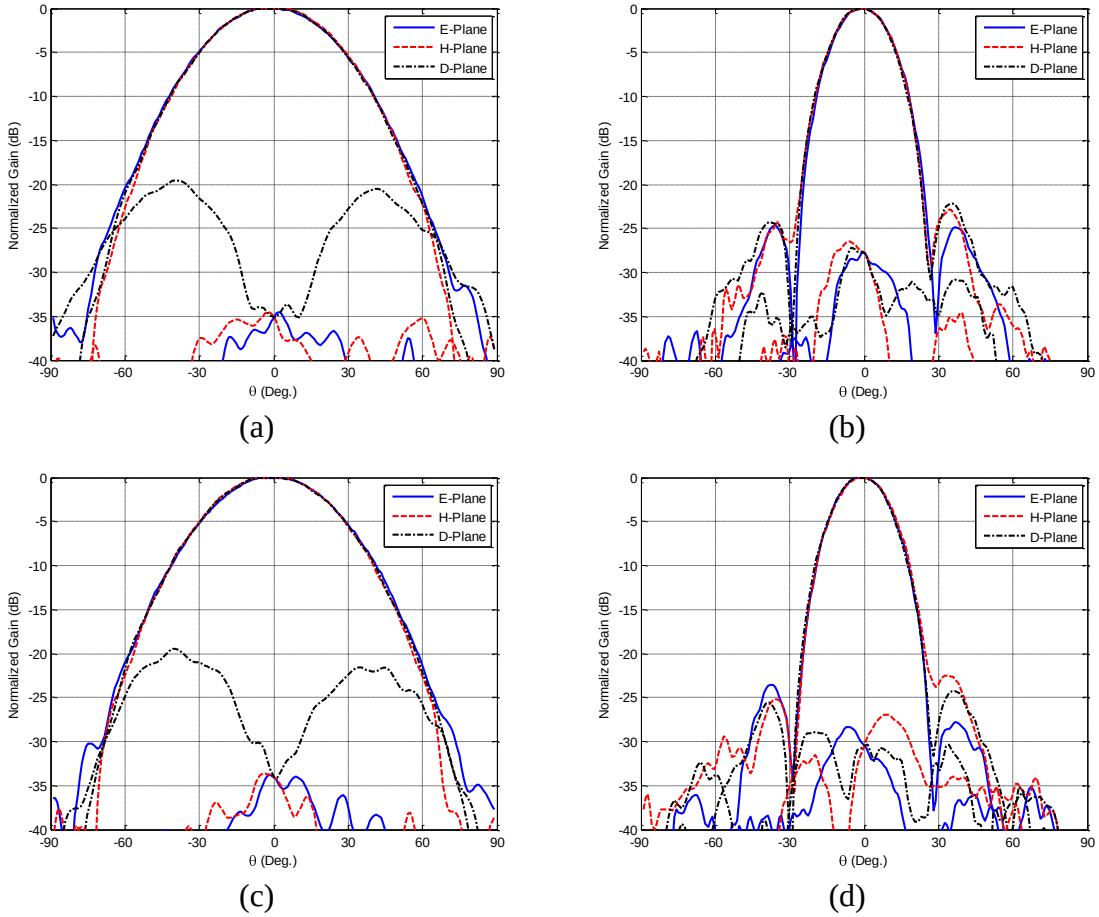

Figure 18: Measured feed patterns for (a) Port 1, Ku Band, (b) Port 2, Ku Band, (c) Port 1, Ka Band, and (d) Port 2, Ka Band.

To estimate the radiation pattern of the DPR antenna when fed with the prototype feed, FEKO was used to perform physical optics analysis with the measured feed patterns acting as a source. The actual DPR antenna system is too large for FEKO to mesh and solve at Ka band, so a smaller, equivalent single reflector was analyzed. The equivalent reflector has a focal length of 0.415 m and a diameter of 0.8 m, resulting in approximately 2° beamwidth instead of 1° beamwidth as expected from the actual 1.6 m DPR reflector.

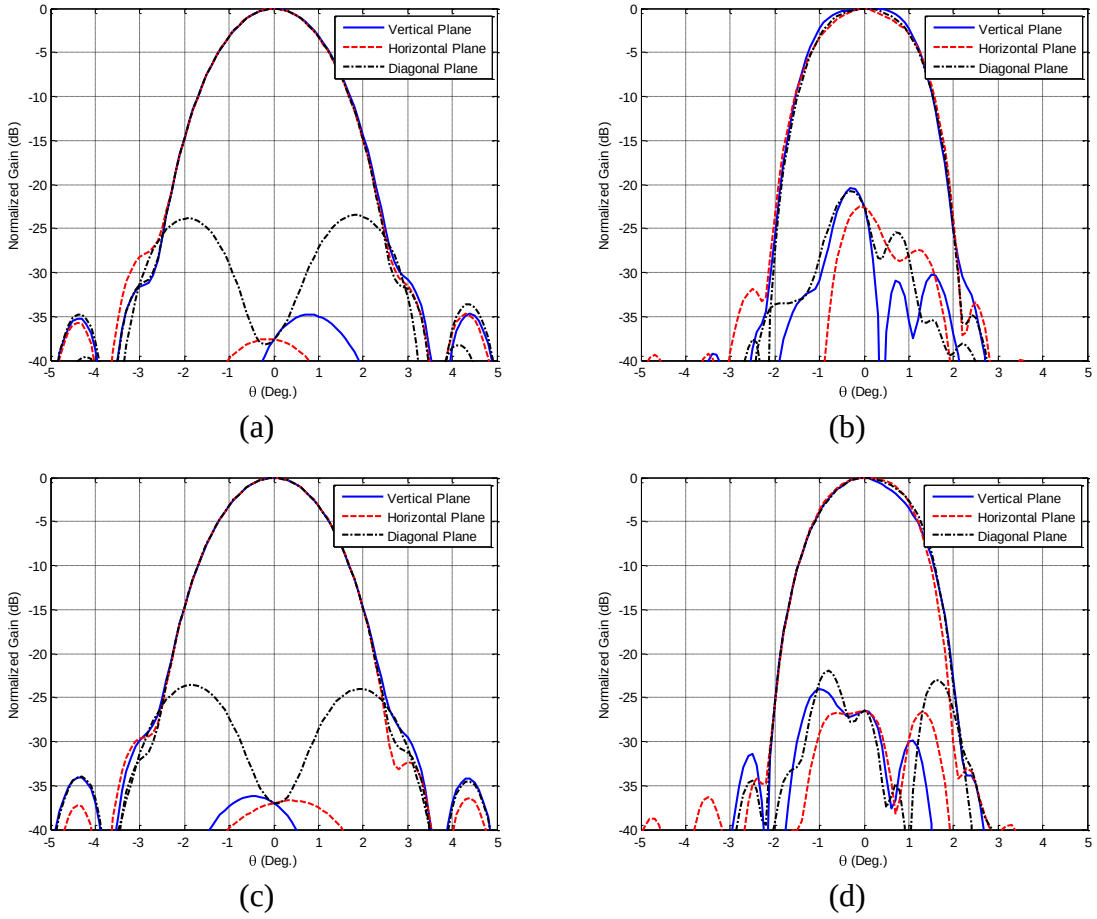

Figure 19: Predicted secondary reflector patterns for equivalent 2° beamwidth symmeric reflector (a) Port 1, Ku Band, (b) Port 2, Ku Band, (c) Port 1, Ka Bnad, and (d) Port 2, Ka Band.

Illuminating the equivalent reflector with the measured feed patterns results in the secondary patterns shown in Figure 19. Immediately apparent is the tendency toward a flat top shape at Ka band. This is because the -25 dB Ka band feed sidelobes are captured by the reflector. These sidelobes are out of the phase with the main beam and degrade the secondary reflector pattern near boresite. In the patterns shown in Figure 19 the feed has been moved 0.35 cm away from the reflector along the feed axis to reduce the feed sidelobe degradation effects. The average half power beamwidth of all the Ku and Ka beams is 1.970° and no individual planar cut varies from the average beamwidth by more than 10%. The average beamwidth for each beam is within 4% of 1.970°.

Defocusing the feed along the feed axis affects both Ku and Ka bands. Simulations indicated that defocusing the Ka band phase center alone a greater distance would allow the feed sidelobes to interact constructively with the feed main beam and eliminating the

flat top secondary pattern. Ideally this would be possible because the feed geometry is designed to allow independent tuning of Ku and Ka bands. However, the small diameter of the Ku band corrugated horn combined with the large diameter of the Ka band foam sleeve results in interaction between the Ku and Ka band performances. The DPR feed design represents a limit on the achievable feed performance with the current geometry because the phase centers of Ku and Ka band cannot be independently adjusted.

Using the secondary patterns in Figure 19 also allows prediction of the integrated cross-pol of the entire antenna to be anticipated. Since the symmetric reflector is expected have lower inherent integrated cross-pol than the offset Gregorian, the -37.09 dB and -35.75 dB cross-pol values contributed by the offset Gregorian are added to the results predicted for the equivalent reflector. Table 2 shows satisfaction of the -25 dB integrated cross-pol requirement at Ku band and slightly higher integrated cross-pol at Ka band. The high Ka band integrated cross-pol, like the flat top secondary patterns, is due to the Ka band feed sidelobes being captured by the reflector. The effects of the sidelobes may be overcome by using a dichroic subreflector that passes the Ka band feed sidelobe energy through without reflection. Studies indicate that such a subreflector would eliminate the flat top secondary pattern shape at Ka band and reduce the integrated cross-pol below the required levels [12].

Table 2: Measured integrated cross-pol of the DPR prototype feeds and the corresponding predicted integrated cross-pol of the DPR antenna.

	Feed I_{CX} (dB)	Sym. Reflector I_{CX} (dB)	Antenna I_{CX} (dB)
Port 1, Ku Band	-24.72	-27.98	-27.48
Port 2, Ku Band	-24.10	-28.11	-27.59
Port 1, Ka Band	-26.95	-24.40	-24.09
Port 2, Ka Band	-27.60	-25.14	-24.78

5. Feed Geometry Limitations

The DPR feed, and more specifically, the need to scale feed beamwidths with frequency, represents one of the present feed geometry's main limitations. Because of the small aperture size, the foam sleeve and corrugated horn no longer operate independently and the effects of Ka band feed sidelobes can only be mitigated by treating the reflector surface. Holding the Ka beamwidth and frequency constant (or more generally, holding the upper band frequency and feed beamwidth constant), shifting the lower frequency up or down does not significantly affect the required aperture size of the corrugated horn since the lower band feed beamwidth is aperture limited. Reducing the lower frequency will lead to a wider feed beamwidth but the required lower band reflector aperture size increases by the same factor since the final goal is matched secondary beams. However, much lower frequencies will suffer from the inability of a corrugated horn to perform well with an extremely small aperture [7] and from the need to use a small f/D reflector because the feed beamwidth is so wide at the lower band. Increasing the lower frequency will lead to better corrugated horn performance but isolation between the upper and lower

bands must be considered by addressing the concerns of Section 2.1.

In the more common situation, where a feed with approximately matched beamwidths at both bands is required, the HIWRAP feed shows that the present feed geometry is very effective. In such a case the minimum frequency separation requirement does not change from the frequency scaled beamwidth case above but the maximum frequency separation limit disappears since larger frequency separations will require a larger horn relative to the dielectric rod and foam sleeve diameters. The electrical size of the horn will remain large enough that it can be designed to operate efficiently and, since the feed beamwidth at both bands is now reasonable, the f/D for the reflector does not become prohibitively small.

6. Conclusion

This paper demonstrates the corrugated horn loaded with a dielectric rod embedded in a foam sleeve as an effective feed geometry for dual band feed designs. The foam sleeve allows a range of achievable beamwidths and maintains independence between the operation of the feed at both bands. This independence allows fine tuning of radiation patterns at both bands so that high performance reflector antennas can be realized.

To aid future designers, general guidelines for selecting dielectric rod and foam sleeve diameters are provided and the effects of the dielectric rod and foam sleeve on lower band operation are quantified using a surface admittance approximation to model dielectric loaded corrugated waveguide behavior.

The capabilities and limitations of these feeds are illustrated with two recently developed feeds. The first feed, used in NASA's HIWRAP antenna shows the capability of the feed geometry to fulfill the typical feed requirements of having approximately matched beams at two independent bands. The second feed, used in RSS's DPR antenna, produces matched beams out of a reflector by scaling the radiation at the two bands. This feed exhibits many of the limitations of the present feed geometry. These two feed examples, along with the presented design charts, allow quick selection and development of similar feeds by future designers.

7. Acknowledgements

Portions of this work were supported by NASA Goddard Space Flight Center grant number NNG05GQ52G and Remote Sensing Solutions of Barnstable, MA.

8. References

[1] G. Heymsfield, *et al.*, "Development of the high-altitude imaging wind and rain airborne profiler (HIWRAP)," *NASA Sci. Tech. Conf.*, 2007.

[2] J. Carswell, "Final report: A revolutionary wind and rain airborne profiler for unmanned aircraft vehicles," NASA STTR Final Report, Jan 2006, contract No. NNG05CA96C.

[3] J. Carswell *et al.*, "A high altitude wind mapping radar," *IEEE Aero. Conf.*, 2008

[4] J. Carswell, “Final report: A novel low-cost dual-wavelength precipitation radar sensor network,” NASA SBIR Final Report, Jul 2005, contract No. NNG05CA73C.
[5] J. Creticos and D.H. Schaubert, “A compact Ku/Ka band feed for airborne antenna applications,” 2007 Antenna Applications Symposium, pp. 169 – 180, 18-20 September, 2007.
[6] J. Creticos, “Development and design of dual-band, multi-function remote sensing antennas”, Ph.D. Dissertation, University of Massachusetts, Amherst, 2008.
[7] P. Clarricoats and A. Olver, *Corrugated Horns for Microwave Antennas*. Peter Peregrinus Ltd., 1984
[8] D. Mooradd, “Design development and construction of a dual-frequency, dual-polarized millimeter wave cloud profiling radar antenna,” Master’s Thesis, University of Massachusetts, Amherst, 1993.
[9] R. Collin, *Field Theory of Guided Waves*, 2nd ed. Wiley-IEEE Press, 2001.
[10] A. Krall and A. Syeles, “Embedded dielectric rod antenna,” U.S. Patent 4 274 097, Jun. 16, 1981.
[11] Y. Mizugutch *et al.*, “Offset dual reflector antenna,” *IEEE Antennas and Propag. Soc. Int. Symp.*, vol. 14, pp. 2-5, Oct. 1976.
[12] J. Creticos and D. Schaubert, “DPR antenna: Final report”, June 2008

A tunable dielectric patch antenna[1]

Eduardo M. A. Oliveira[1], Sergey N. Makarov[1], Colby Dill[2], and Reinhold Ludwig[1]

(1) ECE Department, Worcester Polytechnic Institute, Worcester, MA 01609
(2) Virtual Machines, Inc. 192 Church St., Holliston, MA 01746
emo@wpi.edu, makarov@wpi.edu, ludwig@wpi.edu, colbydill@comcast.net

Abstract: A study is conducted of a tunable dielectric patch antenna which uses a thick dielectric patch filled with a high-epsilon liquid dielectric instead of using a conventional metal patch. The tunability is achieved by changing the patch height and thereby adjusting the water level. The antenna belongs to the class of rectangular dielectric resonator (DR) antennas that are constructed above an insulated ground plane, although the present antenna may also use a thin dielectric patch. The antenna match to 50 Ω is preserved for different heights and for different resonance frequencies provided that transversal antenna size and probe feed position remain fixed. In this paper we describe the physical principle of achieving tunability; it is revealed that nearly constant electric field distributions exist in the cavity beneath the dielectric brick at different values of brick thicknesses. A tunability frequency bandwidth of 50% is demonstrated both numerically and experimentally. The measured and estimated antenna radiation efficiency varies from 20% to 40% in the L-band. Several potential applications are discussed, including direct antenna coupling to a biological medium.

Keywords: Dielectric waveguides, Dielectric resonators, Antennas, Microstrip antennas.

Content:

Introduction
I. Transmission line approach
II. Numerical simulations
III. Experimental validation
IV. Discussion
V. Conclusions
References

[1] An initial version of this paper was presented at *Antennas and Propagation IEEE Int. Sym.* APS-2008, San Diego, CA, July 2008.

Introduction

In this study, we investigate a class of rectangular dielectric resonator (DR) antennas [1]-[7] above an insulated ground plane. The insulation forms a cavity beneath the dielectric brick, which is critical for the subsequent analysis. Furthermore, the antenna must possess a high value of the relative dielectric constant. The rectangular dielectric brick is filled with a high-epsilon liquid dielectric such as distilled water. The present investigation will prove that such an antenna above an insulated ground plane is *tunable*, i.e. allows to adjust its resonant frequency by changing the antenna height (liquid level) while concomitantly maintaining good impedance match and keeping all other geometry parameters unchanged. An antenna match to 50 Ω is achieved for different heights and hence different resonant frequencies as long as the transversal antenna size and the probe feed position remain the same. An initial version of this paper [8] was presented at Antennas and Propagation IEEE Int. Sym. APS-2008, San Diego, CA .

The physical explanation of the tunability effect (Section I) is based on the transmission line (TL) approach or the so-called dielectric waveguide model (DWM) [2]-[5] for rectangular DR antennas. This approach treats the DR antenna as a half-wave resonator on the basis of an insulated dielectric image transmission line, or a dielectric image waveguide [9]-[12]. It is a natural extension of our familiar TL approach to rectangular metal patch antennas, which are also the half-wave open-open resonators, but on the base of a microstrip transmission line [13]. The major difference is that the metal patch is now replaced by a (thicker) dielectric patch and the conduction currents in the metal patch are replaced by volume polarization currents in the dielectric. Plus, the underlying transmission line type changes.

When the relative dielectric constant of the brick (or of the slab for the waveguide counterpart) is sufficiently high, nearly the same modal field distribution within the resonant cavity beneath the dielectric brick or beneath the metal patch may be observed (Sections I and II), irrespective of the height of the dielectric brick. Therefore, the feed position within the cavity, which is responsible for impedance matching, also remains the same for different dielectric heights. On the other hand, the varying height of the dielectric brick still controls the varying resonant frequency.

Similarity of the resonant fields within the cavity forces us to call this particular case of the DR antenna the "dielectric patch antenna" as compared to the standard metal patch antenna. An additional argument supporting this analogy is that the height of the dielectric brick may be even smaller than the thickness of the insulating substrate (Section II), as opposed to insulated DR antennas considered earlier [4], [5], [15], [16] where the dielectric height is at least four times the substrate thickness.

Section II provides the simulation data supporting the tunability hypothesis (an X/C-band antenna) and discusses the antenna radiation patterns. Section III presents the

experimental and simulation data on continuous tunability of an L-band antenna that uses distilled water. Section III then estimates antenna efficiency in the L band, which is affected by dielectric relaxation in water. Section IV discusses possible applications of the tunable dielectric patch antenna. Several potential applications are discussed, including a direct antenna coupling to a biological medium. Finally, Section V summarizes and concludes the paper.

I Transmission line approach

1.1. "Transmission line" point of view

In this section we will apply a meaningful transmission line approach or the dielectric waveguide model (DWM) [2]-[5] to an insulated rectangular dielectric resonator antenna with a high value of the relative dielectric constant. This approach relates the present antenna to the metal patch antenna and provides a possible explanation of the physical principle behind the antenna tunability. The conventional metal patch antenna is an open-open half wave resonator, on the basis of a (wide) microstrip transmission line [13]. The term "half-wave" implies one half of the guided wavelength λ_g. This situation is shown schematically in Fig. 1a. One could regard an insulated dielectric resonator antenna in a similar fashion, as an open-open half wave resonator, but on the basis of an insulated dielectric image line as shown in Fig. 1b. The insulated image line [9]-[12] is a particular case of a more general dielectric transmission line [12]. The line in Fig. 1b includes a metal ground plane, a substrate, and a dielectric slab that effectively replaces the metal strip for the printed microstrip transmission line. The dielectric slab may be either thicker or thinner than the substrate, but it must have a high value of the relative dielectric constant, as discussed further below.

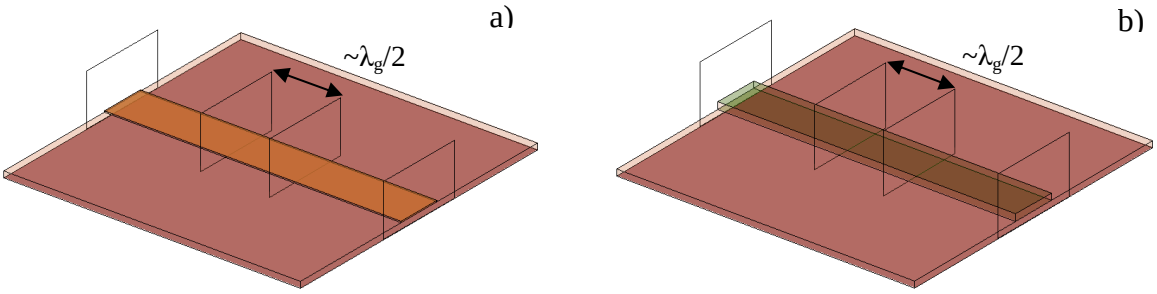

Fig. 1. a) – A metal patch antenna as a $\lambda_g/2$ open-open section of a microstrip transmission line that is cut out in the figure; b) - a "dielectric patch antenna" as a $\lambda_g/2$ open-open section of a dielectric image transmission line – the half-wave resonator is again cut out.

1.2. Fields of an insulated dielectric image waveguide

The dominant (hybrid electric, or HE_{11} [12]) waveguide mode is excited by a vertical electric field (or current) imposed in the substrate *between* the ground plane and the slab, similar to the microstrip excitation. However, it is not a TEM-type mode; it has a particular cutoff frequency. If the substrate were missing we would have the standard image line, which may be treated as a half of the rectangular dielectric waveguide. The method of images for a dominant HE mode allows us to remove the ground plane and replace it by another (image) waveguide half, and vice versa [12]. The image lines have been popular in the 1960s and 1970s, particularly for sub-millimeter waves as they have lower losses compared to the microstrips. In recent years, interests in these lines is again gaining momentum, particularly as applied to non-radiating dielectric waveguides (NRD), see for example [17] and the cited references. In this paper, we will investigate an insulated image line which implies the presence of a dielectric grounded substrate. The dielectric image line under study will have a very high dielectric constant of ε_r=81, which corresponds to distilled water. The line thickness (or height) is either slightly less than the thickness of the substrate or larger.

As a typical example, we consider an image transmission line of a dielectric slab with $\varepsilon_r = 81$ (distilled water), over a 25 mil Rogers 6010 laminate with $\varepsilon_r = 10.2$. The thickness of the dielectric slab varies from 20 to 40 mil, whereas the slab width is fixed at 177 mil (4.5mm). The cutoff frequency of the corresponding image waveguide found numerically (Ansoft HFSS) is approximately 10 GHz at 20 mil, 8 GHz at 30 mil, and 7 GHz at 40 mil thickness. Fig. 2 depicts the electric field magnitude distribution at 11 GHz (1 GHz above cutoff) for the trace with the smallest height of 20 mil (0.5mm). The observation planes are separated by $\lambda_g/4$ at 11 GHz.

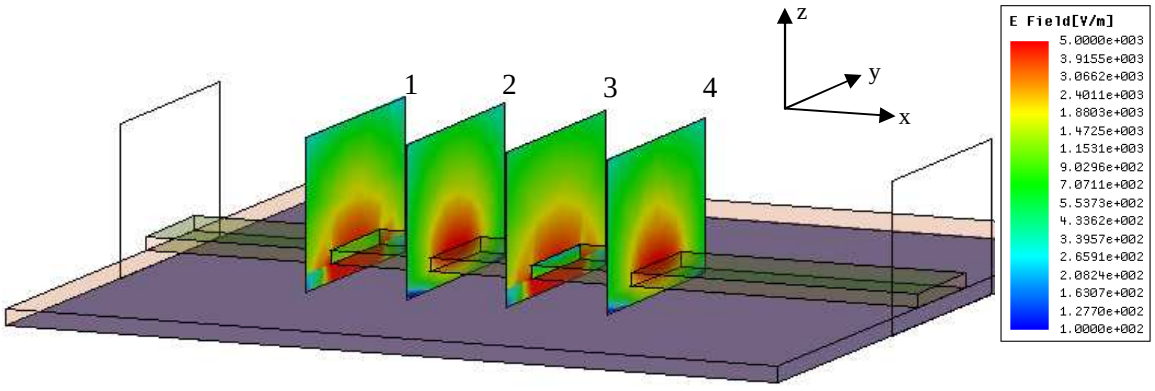

Fig. 2. Electric field magnitude distribution at 11 GHz for the trace with the slab height of 20 mil (0.5mm) over the 25 mil thick Rogers 6010 substrate. The observation planes are separated by $\lambda_g/4$ at 11 GHz (Ansoft HFSS TL model). The incident power per port is 1W.

One can see that the modal field of the dominant HE_{11} mode oscillates along the waveguide axis and has two distinct nodes: the node where the electric field is mostly concentrated beneath and outside the slab (nodes #1 and #3), and the node where the electric field is mostly concentrated within the slab (nodes #2 and #4). The waveguide Poynting vector indicates a similar behavior.

When a dielectric patch antenna is cut out, nodes #1 and #3 should be on its radiating edges, whereas node #2 is in the middle. Such a field behavior (no electric field beneath the patch in the middle and a field maximum close to the edges) is almost identical to that of the patch antenna resonator as discussed in the next subsection.

1.3. Fields of a dielectric resonator antenna

To establish the field distribution in the antenna's E-plane (Fig. 3a) we first look at the E-plane cut of the familiar probe-fed metal patch half-wave resonator shown in Fig. 3c. The required distribution of free surface charges, σ_M, and the required electric field distribution in Fig. 3c are achieved by virtue of a longitudinal metal surface conduction current density, $\bar{J}_M$. If the metal patch is replaced by a dielectric brick shown in Fig. 3b, the conduction currents and free charges no longer exist, at least for a low-loss dielectric material.

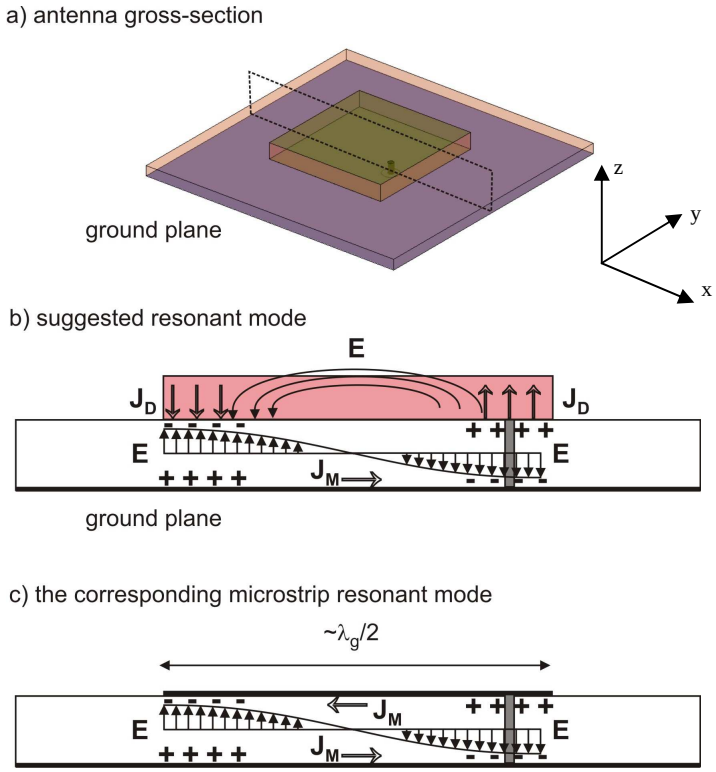

Fig. 3. a) – A cut of the dielectric patch antenna in the E-plane; b) - qualitative field distribution at a $\lambda_g/2$ resonance through the E-plane; c) - the same field distribution for the microstrip patch resonator. The feed is seen as a column on the right hand side.

However, a thicker dielectric brick may still support (vertical) volume polarization currents, $\vec{J}_D$, and a resulting bound surface charge density σ_D as shown in Fig. 3b. When the dielectric is relatively thick and its dielectric constant is *high*, both $\vec{J}_D$ and σ_D may attain large values. In particular, the volume polarization current is given by [14]

$$\vec{J}_D \equiv j\omega(\varepsilon_r - 1)\varepsilon_0 \vec{E}, \tag{1}$$

where ε_r is the relative dielectric constant of the brick dielectric and $\vec{E}$ is the applied electric field. Similarly, the bound surface charge density σ_D, from Gauss's law, [14]

$$\sigma_D \equiv (K_+ - K_-)D_\perp \tag{2}$$

where K_+ and K_- are the dielectric contrasts on both sides of the boundary and $D_\perp = \varepsilon_0 \varepsilon_r E_\perp$ is the continuous normal component of the total electric flux density on the boundary. The dielectric contrast is given by $K = (\varepsilon_r - 1)/\varepsilon_r$. One can see that both $\vec{J}_D$ and σ_D nearly linearly increase with increasing ε_r at a given electric field $\vec{E}$. Thus, once ε_r is large, the same resonant field distribution within the cavity may in principle be supported with the dielectric polarization currents and bounded charges, see Fig. 3b, at the half-wave resonance. We can therefore suggest that the patch antenna with a top dielectric brick should exist, and that it should behave very similarly to the metal patch antenna, at least within the cavity beneath the dielectric brick where the probe feed is located. However, there should also be some differences in both cases.

1.4. Antenna tunability

The preceding discussion is intended to support the concept of a tunable dielectric patch antenna. Tunability here implies that once the proper position of the probe feed is cast in hardware, the antenna match to 50 Ω should equally be achieved for different patch heights (and hence for different resonant frequencies) as long as the transversal antenna size remains fixed. This means that by simply filling a cavity in Plexiglas with water, we may be able to tune the antenna to different frequencies while ensuring a good impedance match at any resonant frequency.

The impedance match for the metal patch antenna is determined by the feed position within the resonant cavity that contains the dielectric substrate and does not change substantially when we increase the metal patch thickness, as seen by the numerical simulations given below. However, neither does the resonant frequency change. The impedance match for the dielectric patch antenna is also determined by the feed position within the resonant cavity that contains the dielectric substrate. This is achieved by the feed assembly, which does not penetrate into the dielectric brick, see Fig. 3 b). If we assume that the field in the cavity is always that of the half wave transmission line

resonator, see Fig. 3b), and remains nearly the *same* for different brick thicknesses, then the impedance match should not be affected (or weakly affected) by the brick thickness. However, the resonant frequency does change, since different thicknesses change the path of volume polarization currents in the dielectric itself. Although this contemplation is only qualitative, the next section will provide us with simulation and experimental evidence.

II Numerical simulations

2.1. Antenna's resonant frequency and feed position at different patch heights

To estimate the resonant frequency and investigate the antenna itself, we perform a number of numerical simulations with a commercial simulation tool (Ansoft HFSS v.11). As a dielectric patch, we choose a dielectric brick with $\varepsilon_D = 81$ and with the bulk conductivity of $\sigma = 0.0002$ S/m (distilled water). The supporting substrate is Rogers RT/duroid 6010 PTFE Ceramic Laminate, with $\varepsilon_S = 10.2$ and $\tan\delta = 0.0023$. The substrate's thickness is fixed at 25 mil and the brick's horizontal dimensions are also fixed at 4.5mm×4.5mm or 177mil×177mil (X-band). However, its thickness *h* varies from 0 mil to 100 mil in steps of 5 mil. Fig. 4 shows the corresponding setup for a probe-fed patch. The probe does not penetrate the patch, but only contacts it at the bottom.

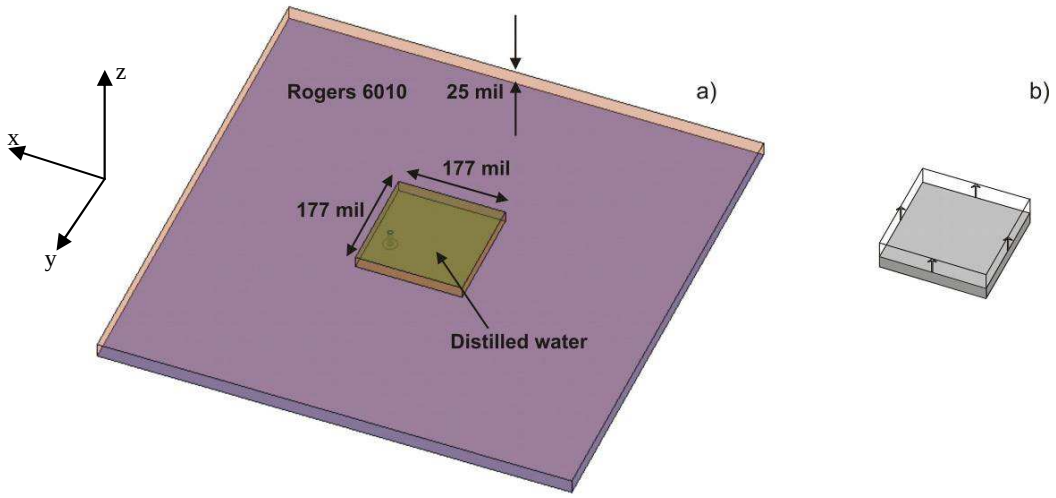

Fig. 4. a) - Patch antenna setup with a dielectric brick patch (X-band); b) - parametric sweep direction with respect to antenna height while keeping the longitudinal dimensions fixed.

A case for comparison will be the standard narrowband patch antenna with the same dielectric substrate (Rogers 6010), but with a metal patch (PEC approximation was used). The square metal patch has the same horizontal dimensions as the dielectric brick. The metal patch thickness also varies from 0 mil to 100 mil. By comparing these two cases we can establish some attractive properties of the proposed antenna compared to the equivalent metal patch antenna.

The feed offset from the patch center was varied for the dielectric antenna in order to achieve the best match to 50Ω. Then, the resonant frequency and impedance bandwidth were found, based on the RL ≤ -10 dB return loss criterion. Table 1 shows the data for the first (parallel) half-wave resonance. One can see that the dielectric patch antenna does exhibit the same parallel resonance when the patch thickness becomes sufficiently large. The resonant frequency becomes higher for thin patches and decreases for thick patches.

Table 1. Selected resonance frequencies f_{res} and bandwidth $B_{RL\text{-}10dB}$ data for two antennas (metal patch vs. dielectric patch) on a 25 mil-thick Rogers 6010 (ε_r=10.2) - numerical simulations. The longitudinal patch size is fixed at 4.5mm×4.5mm.

Patch thickness, mil	Metal patch		Dielectric patch		
	f_{res}, GHz	$B_{RL-10dB}$, %	f_{res}, GHz	$B_{RL-10dB}$, %	Feed offset from center, mm
0	9.79	0.92	-	-	
5	9.80	1.02	-	-	
10	9.80	1.12	-	-	
20	9.80	1.30	**12.40**	**2.66**	**1.4**
25	9.81	1.33	**11.55**	**2.34**	**1.4**
50	9.81	1.53	**9.27**	**1.94**	**1.3**
75	9.80	1.62	**8.05**	**1.86**	**1.3**
100	9.80	1.73	**7.20**	**1.81**	**1.4**

Interestingly, the impedance bandwidth of the dielectric antenna is larger for thin patches; it reaches twice that of the metal antenna at 20 mil thickness, but the normalized patch size is simultaneously 25% larger, for the same frequency. Finally, for a thick dielectric patch (50, 75, and 100 mil), the impedance bandwidth is also somewhat larger, but the equivalent patch size is *smaller* than that for the metal antenna, for the same center frequency. The theoretical antenna's efficiency for the dielectric patch is in excess of 97%.

Most importantly, the feed position for the best match to 50 Ω virtually does not change: it is 1.4mm offset from the antenna's center at 25 mil dielectric brick thickness; 1.3mm offset at 50 mil; 1.3mm offset at 75 mil, and again 1.4 mm offset at 100 mil thickness. This observation is critical for a possible reconfigurable design. For example, Table 1 predicts nearly 50% variation of the resonance frequency when the height (water level) changes from 20 mil to 100 mil. This variation covers the entire X-band and a part of the C-band. The total antenna height does not exceed 125 mil (3.2mm or 0.1λ) in the worst case, thus making it a good candidate for a low-profile antenna/array element.

2.2. Fields at different patch heights

Fig. 5a shows the numerically determined electric field distribution (magnitude of the field) of the dielectric patch antenna at the resonance in the E-plane for 20, 30, 40, and 50 mm patch thicknesses (from top to bottom). The resonance frequencies are 12.4, 10.9,

9.9, and 9.3 GHz. The antenna's E-plane includes the probe feed. While the field distribution in the dielectric brick considerably changes with increasing its thickness, the field distribution in the cavity beneath the patch remains nearly constant. Therefore, the feed position for the best match to 50 Ω also remains the same! For the sake of completeness, we also present the fields in two antenna's H-planes: one is drawn through the patch center (Fig. 5b); and another is drawn close to the patch edge (Fig. 5c). These fields are consistent with the longitudinal cut in Fig. 5a and with the corresponding waveguide fields in Fig. 2.

2.3. Estimation of the resonant frequency - the $\lambda_g/2$ rule

It is worth providing estimates of the resonant frequency of the dielectric patch antenna based on the half of guided wavelength rule, for the insulated image guide. If the patch length is *L*, then

$$L \approx d\frac{\lambda_g}{2} \Rightarrow f_{\text{res}} \approx d\frac{c_0}{2\sqrt{\varepsilon_{\text{eff}}}}, \tag{3}$$

where ε_{eff} is the effective dielectric constant of the waveguide for the dominant mode excited with the vertical electric field, and *d* is a fringing factor, similar to the metal patch antenna [19] . Table 2 gives the corresponding data obtained numerically. We have used $d = 1$ in Eq. (3). We can see that the present estimate is a useful first step for the square patches. We expect it to work even better for patches that are longer in the resonant direction.

Table 2. Resonance frequencies and their estimates based on Eq. (3). The longitudinal patch size is fixed at 4.5mm×4.5mm (the square patch).

Dielectric patch/Insulated image guide				
Patch thickness, mil	f_{res}, GHz simulated	Guide's ε_{eff}, simulated	f_{res}, GHz based on $\lambda_g/2$	Error percentage of the $\lambda_g/2$ rule
20	**12.40**	**5.4**	**14.35**	**-13.6%**
25	**11.55**	**8.2**	**11.65**	**-0.8%**
30	**10.87**	**10.9**	**10.33**	**+5.0%**
40	**9.93**	**16.2**	**8.47**	**+14.7%**
50	**9.27**	**20.6**	**7.35**	**+20.7%**
75	**8.05**	**26.1**	**6.53**	**+18.9%**

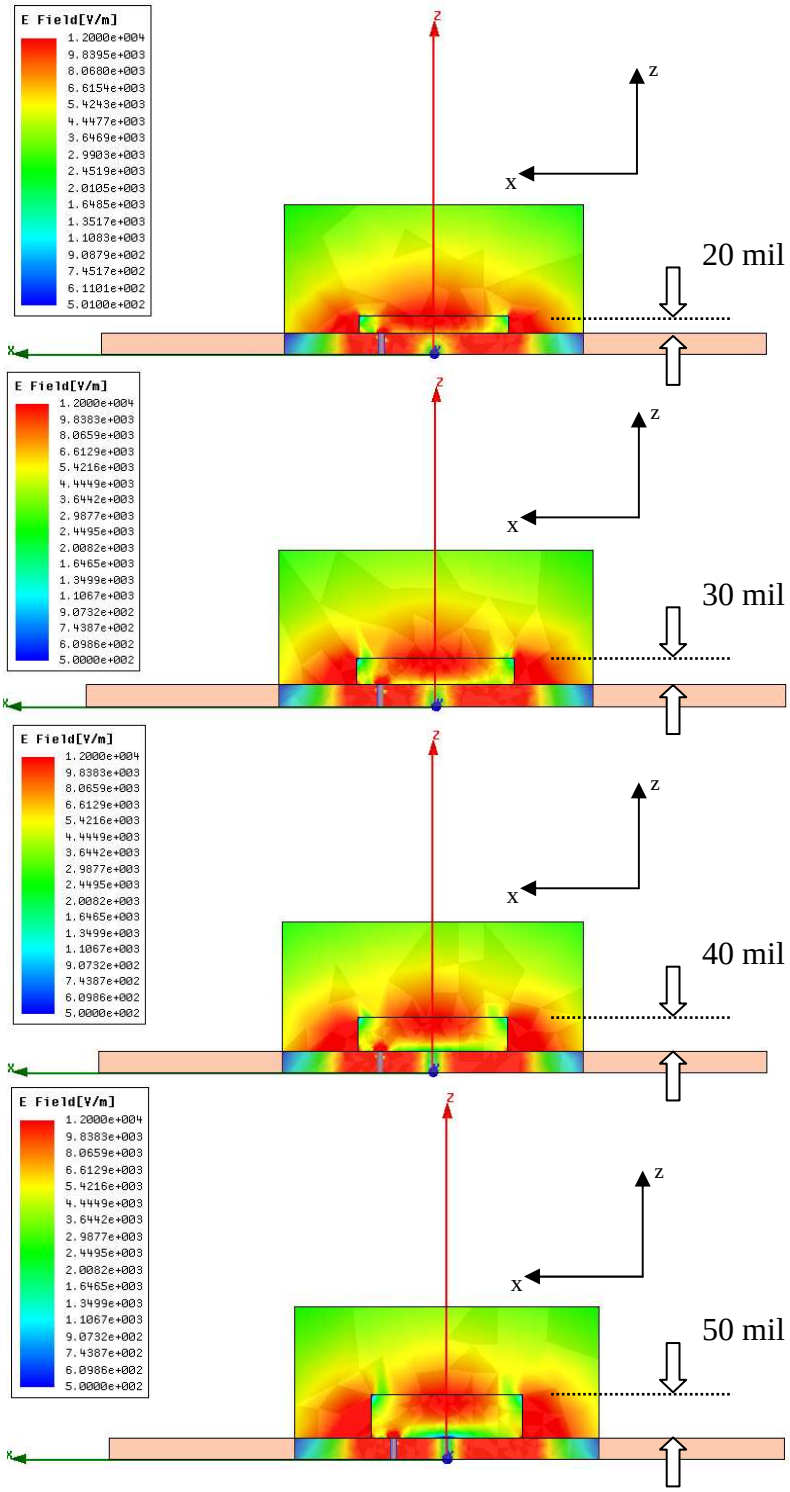

Fig. 5a. Electric field distribution (field magnitude) at the resonance in the E-pane for 20, 30, 40, and 50 mil patch thickness (from top to bottom). The resonant frequencies are 12.4, 10.9, 9.9, and 9.3 GHz. The input port power is 1W.

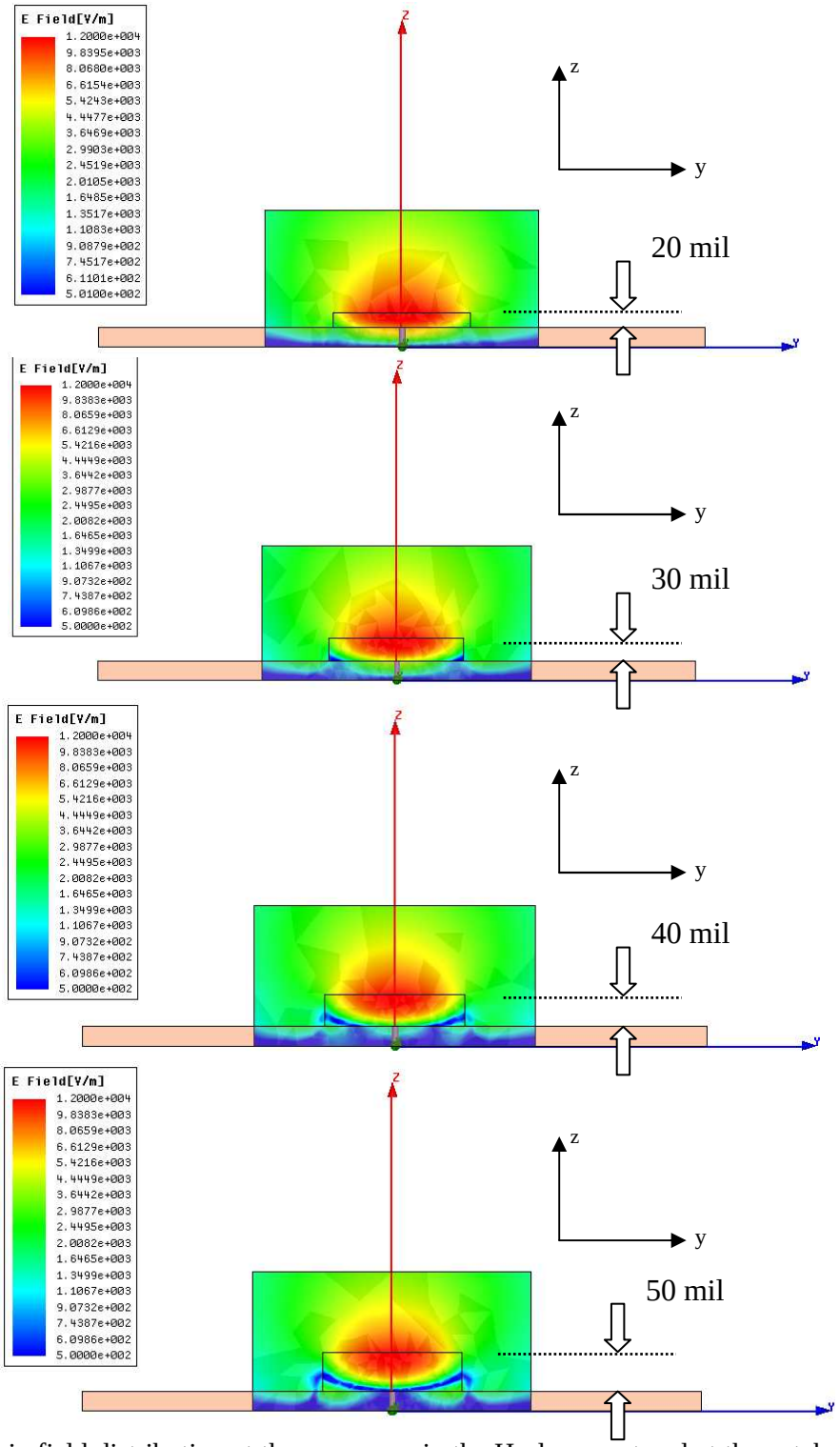

Fig. 5b. Electric field distribution at the resonance in the H-plane centered at the patch center for 20, 30, 40, and 50 mil patch thickness (from top to bottom). The resonant frequencies are 12.4, 10.9, 9.9, and 9.3 GHz. The input port power is 1W.

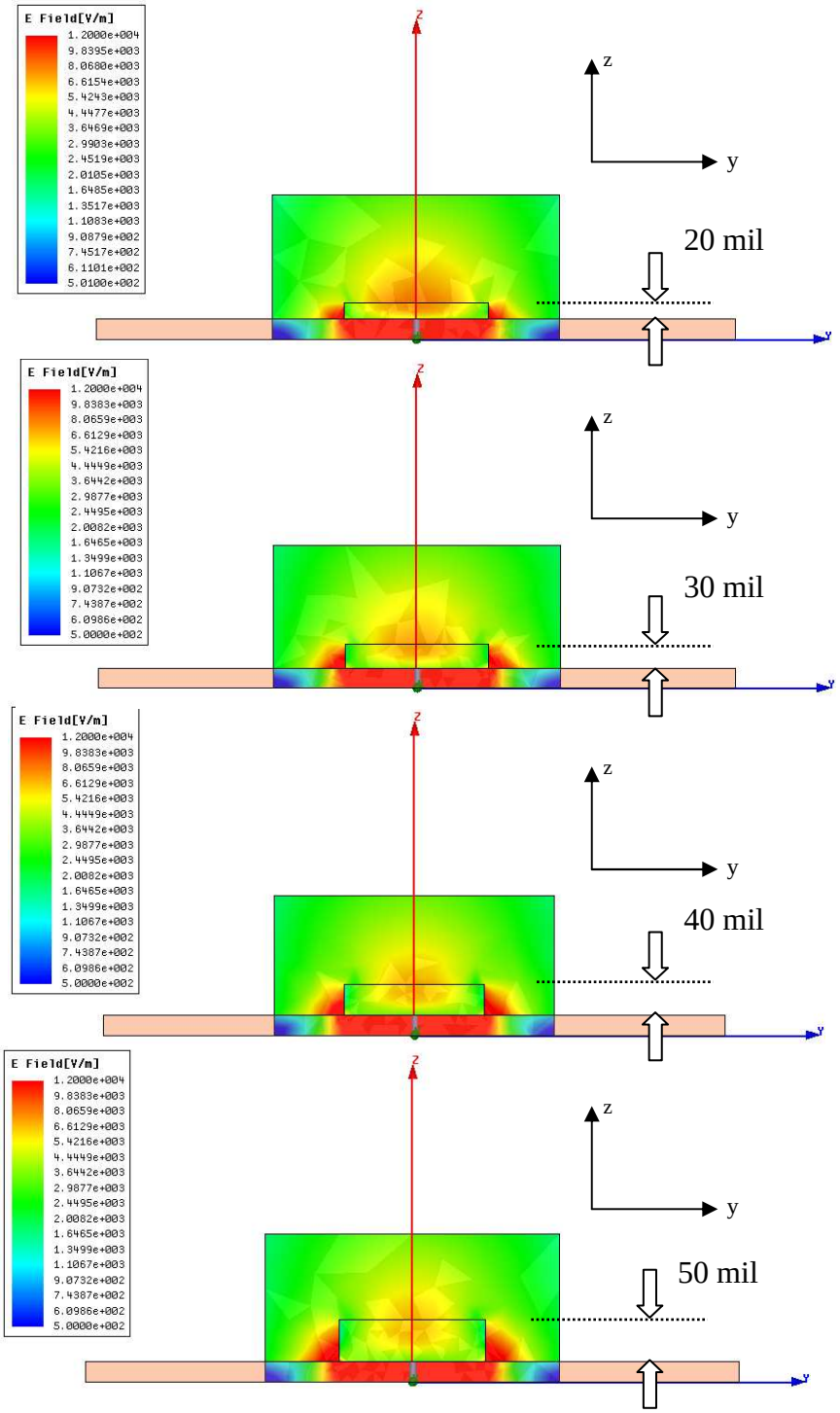

Fig. 5c. Electric field distribution at the resonance in the H-plane close to patch edge for 20, 30, 40, and 50 mil patch thickness (from top to bottom). The resonant frequencies are 12.4, 10.9, 9.9, and 9.3 GHz. The input port power is 1W.

2.4. Radiation patterns

Fig. 6 a) and b) show co-polar and cross-polar patterns at the resonance frequency of the two antennas (metal and dielectric) of 25 mil thickness each. One can see that there is no significant difference in radiation between the metal and dielectric patches, except for a slightly lower polarization isolation in the H-plane. A closer examination also reveals slightly higher variations of the co-polar gain in the E-plane. This observation confirms the suggestion that the same half-wave microstrip mode is excited in both cases. The antenna pattern does change significantly with increasing height of the dielectric patch, see Fig. 6 c), d). All patterns are very similar to those of the DR antennas above a ground plane excited in either TM or HEM mode [18].

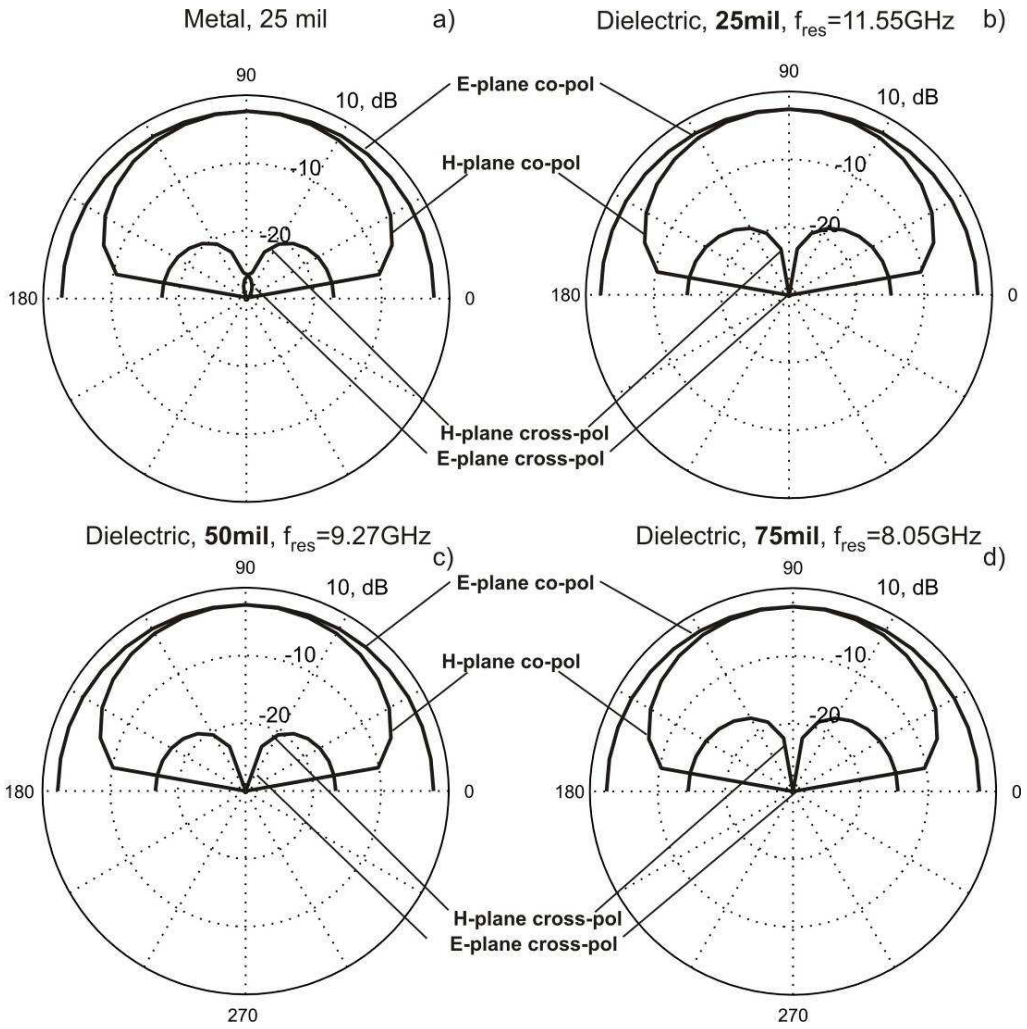

Fig. 6. Dominant polarization and cross-polarization gain patterns in the E- and H-planes for several antennas having the same patch size of 4.5mm×4.5mm. a) - Metal patch with patch thickness of 25 mil; b) - dielectric patch with patch thickness of 25 mil; c) - dielectric patch with patch thickness of 50 mil; d) - dielectric patch with patch thickness of 75 mil.

2.5. Broadbanding

In order to increase the antenna bandwidth, thickness of the dielectric substrate between the brick and the ground plane should be increased, and its dielectric constant should be lowered. To date, we have been able to obtain a bandwidth of about 7.5%, still keeping the same patch mode for the probe feed. However, a slot-fed dielectric-brick patch antenna might provide us with a higher bandwidth. The simulations reveal that the antenna with a thick dielectric patch and a long feed can easily be converted to a short monopole with a dielectric top hat as studied in Refs. [1], [25], [26].

III Experiment

3.1. Setup

An antenna prototype was built using a Rogers TMM10 hard ceramic with 150 mil (3.81 mm) thickness and ε_r =11.3 as a substrate. The active patch substance is distilled water. The water-filled cavity made out of Plexiglas has the size of 44 by 44 mm and with a depth of 13.2 mm. The probe feed is offset at 6.0 mm from the center. One antenna setup is shown in Fig. 7. It is important to emphasize that the probe feed is strictly conformal with the substrate surface and does not penetrate into the water volume, namely the probe tip only touches the bottom of the active water volume.

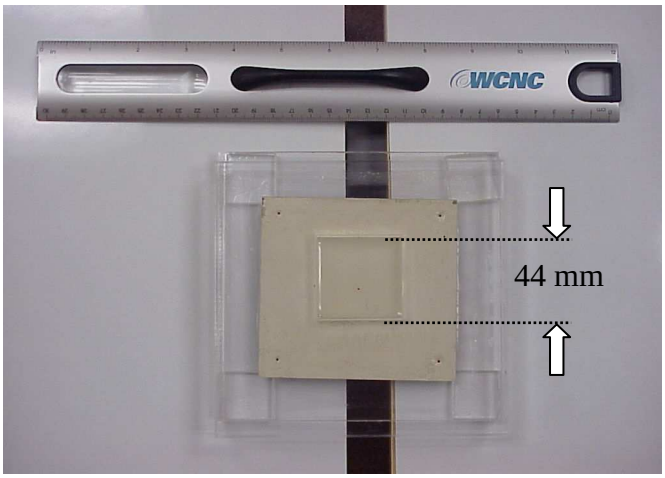

Fig. 7. Antenna setup at 1-2 GHz (L-band).

When partially or fully filled with distilled water, the antenna exhibits a well-defined, single resonance, which monotonically decreases with frequency as the water level increases. The feed position remains the same. The tunability range of the present antenna is from 2.1 to 1.35 GHz. The continuous antenna tunability for water levels from 5 to 13mm is documented in a short movie, see for instance Ref. [20]. Fig. 8 shows typical return losses at water levels of 6mm, 11mm, and 13 mm. The solid curve plots

the measured magnitude of the scattering parameter S11 after calibration, whereas the dashed curve gives the corresponding Ansoft HFSS simulations with build-in material parameters for distilled water.

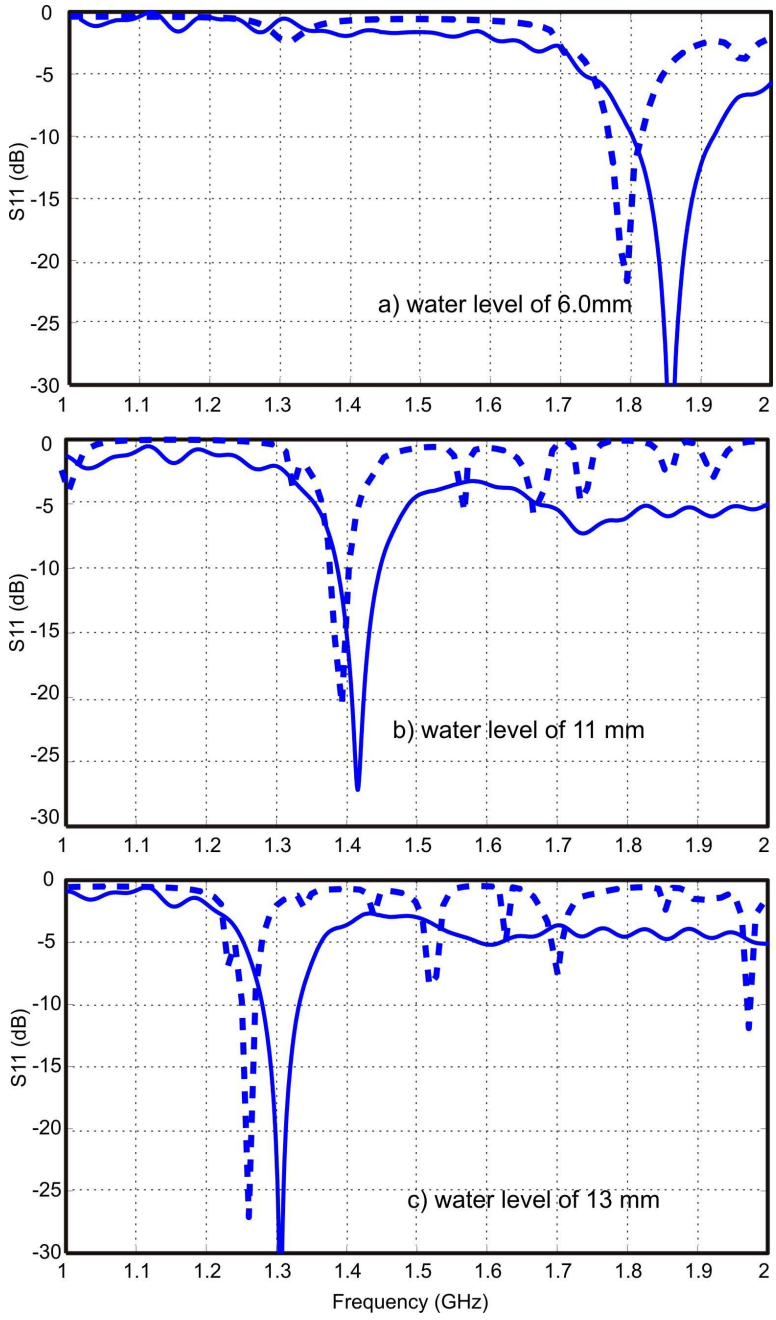

Fig. 8. Return loss of the dielectric patch antenna continuously tuned at different water levels. Solid curve -experiment; dashed curve - numerical simulations using a low-frequency water model.

3.2. Results

Although the resonant frequency agrees well in both experiment and simulations, the experimental antenna bandwidth in Fig. 8 is much wider than in the simulations. This observation points toward lower antenna efficiency and higher loss. It should be noted that Ansoft HFSS by default uses the simple (low-frequency) water model with conductivity of 0.0002 S/m for distilled water and relative dielectric constant of 81. To resolve bandwidth and antenna loss discrepancies, we would need to resort to the rather complicated behavior of RF absorption in water. In reality, water exhibits a high dielectric constant (approximately 81 at low frequencies) due to its large dipolar molecules. Following the well-known discussion in [21], and under the influence of an electromagnetic field, these dipolar molecules attempt to continuously reorient themselves by following the applied electric fields. As the frequency of the field is increased to the microwave range (>1 GHz), the molecules can no longer completely follow the field, which causes a phase lag that leads to energy loss which is usually observed as heat. This dielectric relaxation phenomenon [22] can be mathematically expressed via the concept of a complex permittivity. The following equation, known as the Debye equation [22], is commonly employed to express the response of the dielectric relaxation assuming ideal and non-interacting dipoles; it is a good approximation up to about 80 GHz [23]:

$$\varepsilon_r(f) = \varepsilon_r(\infty) + \frac{\varepsilon_r(0) - \varepsilon_r(\infty)}{1 + j2\pi f\tau} \tag{4}$$

Here $\varepsilon_r(\infty)$ is the permittivity at the high-frequency limit, $\varepsilon_r(0)$ is the permittivity at the low-frequency limit; and τ is the relaxation time. Ref. [21] fits Eq. (4) with experimental data and suggests the approximation (from 2 GHz) for the relative dielectric constant and conductivity

$$\begin{aligned} \varepsilon_r(f) &= 8.38287 + \frac{61.6171}{1 + 3.71028\times10^{-21} f^2} \\ \sigma(f) &= 1.24903 + \frac{2.08801\times10^{-19} f^2}{1 + 3.71028\times10^{-21} f^2} \end{aligned} \tag{5}$$

which gives $\varepsilon_r(f) = 69.1$, $\sigma(f) = 2.1\,\text{S/m}$ at about 2.0 GHz.

Experimentation with the above values for the case of a 6mm-high water patch (Fig 8a) resonating at 1.85 GHz indicated considerably higher bandwidth and a higher loss than the bandwidth and the loss observed in experiment. A more realistic value appears to be $\sigma(f) \approx 1\,\text{S/m}$. Fig. 9 shows the corresponding return loss data for the 6mm water level calculated for two different values of the relative dielectric constant. The experimental and the theoretical bandwidth are nearly the same, but the resonant frequency is still a bit

off. Although the resonant frequency slightly increases with further lowering the dielectric constant, the impedance match becomes worse.

When the closest value of $\sigma(f) \approx 1\,\mathrm{S/m}$ is employed, the estimated antenna efficiency is about 40% for 6 mm water height, and about 20% for 11 and 13 mm water heights. The antenna efficiency is estimated using the above conductivity value that gave the best fit for the experimental bandwidth, and then feeding this value into the numerical antenna solver. The efficiency slightly increases with increasing the relative dielectric constant.

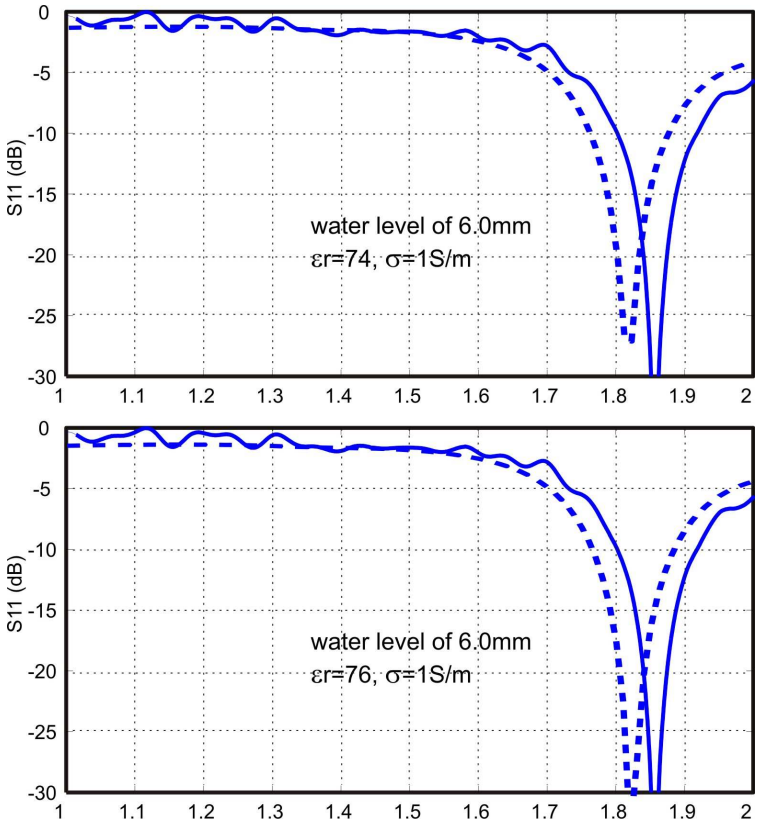

Fig. 9. Comparison of experimental and numerical data for $\sigma(f) \approx 1\,\mathrm{S/m}$. The estimated antenna efficiency at the resonance is 42%.

3.3. Other antennas that use fluidic dielectrics

A recent activity [27]-[32] should be mentioned, related to the use of fluidic dielectrics for pattern control of large reflectors and feed horns. In these references, the dielectric constant, ε_r, of a fluid changes in a certain fixed volume, which requires at least two distinct dielectric fluids.

IV Discussion

One speculative application of the present model to a reconfigurable antenna concept is straightforward: we pressurize water in a small closed rectangular plastic tank with a flexible upper cover, and thus increase its thickness, but still maintain fixed longitudinal dimensions. The pressure level could be varied by an external RF resonant controller. For example, Table 1 predicts nearly 50% variation of the resonant frequency when the height (water level) changes from 20 mil to 100 mil. This variation covers the entire X-band and a part of the C-band. The total antenna height does not exceed 125 mil (3.2mm, or 0.1λ) in the worst case, thus making it a good candidate for a low-cost, low-profile antenna/array element. Unfortunately, lower radiation efficiency of at most 42% and mechanical tunability are not appropriate for high-end applications. Another remarkable observation is the high sensitivity of the antenna's resonance characteristics to changes in water level, or to contaminants in the water such as an acid (ferric chloride) with small concentrations. Therefore, using the present antenna for a remote wireless sensor, for which the sensing element coincides with the antenna element itself, may be more promising.

In the present antenna setup, the resonance is controlled by a finite dielectric patch over an infinite ground plane. What if we "invert" the antenna, namely extend the dielectric patch body to infinity (e.g. use a large water volume, for instance biological tissue), but reduce the ground plane and the ceramic substrate size to a finite value in order to provide the same or similar control over the resonant frequency? A preliminary numerical study has shown that such an inverting setup as outlined in Fig. 10 will function, with the main beam directed mostly into dielectric.

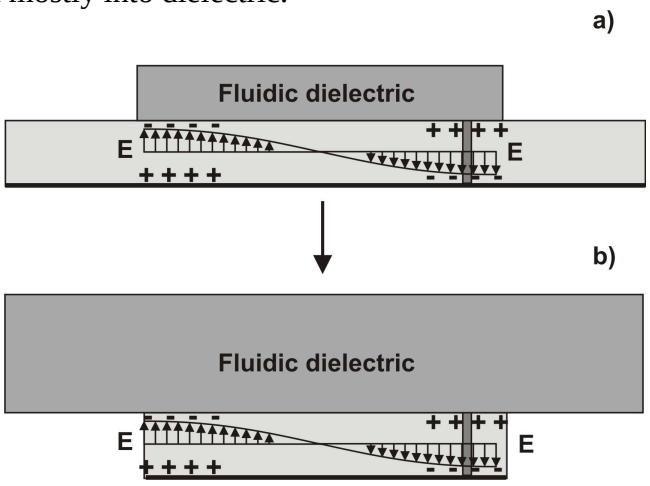

Fig. 10. a) - Dielectric patch antenna in the initial configuration; b) -"inverted" dielectric patch antenna.

At the same time, this setup might offer a practical advantage of natural coupling to a dielectric medium. It is known that coupling of the traditional antenna (patch, slot, or a printed dipole) to breast tissue is an important problem in microwave imaging for breast cancer detection - see [33]-[39]. Recent approaches to microwave imaging tend to employ a coupling medium between an imaged object (the breast) and the antenna [34]. In this case, both the antenna and the breast are immersed in a coupling medium. Such an approach may require a special and rather expensive setup. It has been shown very recently [38] that a DR antenna may provide good matching with the tissue is without adding any matching materials or lumped loads. We note that the antenna from Ref. [38] still has three distinct coupling elements whereas this present arrangement exhibits only one, see Fig. 8. This very interesting research is beyond the scope of the present study and will be considered separately.

V Conclusions

In this study, we propose and describe a tunable dielectric patch antenna which uses a finite-thickness dielectric patch filled with a high-epsilon dielectric (distilled water) instead of the metal patch. The tunability is achieved by changing the patch height by adjusting the water level. We have described the physical principle for tunability: it is essentially the same electric field distribution in the cavity beneath the dielectric brick (with a very high value of the relative dielectric constant) at different values of the brick thickness. A tunability range of 50% bandwidth is demonstrated, both numerically and experimentally. The antenna height may be as small as the substrate height. The antenna's radiation efficiency is from 20% to 40% in the L-band. Several potential applications have been discussed; among them a direct antenna coupling to a biological medium.

Acknowledgements

The authors wish to thank Prof. Leo C. Kempel of Michigan State University, Prof Juraj Bartolic, University of Zagreb, Croatia, and Mr. Angelo Puzella of Raytheon Company, Sudbury, MA for useful discussions. This paper was prepared when one of the authors (SNM) was on sabbatical leave with Lawrence Livermore National Laboratory, Livermore, CA.

References

[1] M. W. McAllister, S. A. Long, and G. L. Conway, “Rectangular dielectric resonator antenna,” *Electronic Lett.*, vol. 19, no 6, March 1983, pp. 218-219.

[2] R. K. Mongia, “Theoretical and experimental resonant frequencies of rectangular dielectric resonators,” *Proc. Inst. Elect. Eng.*, vol. 139, pt. H, pp. 98–104, Feb. 1992.

[3] R. K. Mongia and A. Ittipiboon, "Theoretical and experimental investigations on rectangular dielectric resonator antennas," *IEEE Trans. Antennas Propagation*, vol. 45, no 9, Sep. 1997, pp. 1348-1356.

[4] B. Li and K. Wa Leung, "On the differentially fed rectangular dielectric resonator antenna," *IEEE Trans. Antennas Propagation*, vol. 56, no 2, Feb. 2008, pp. 353-359.

[5] Chee-Parng Chua, P. A. Pavovich, R. M. Dragos, and Mook-Seng Leong, "A compact and wideband rectangular dielectric resonator antenna," *2005 IEEE Electronics Packaging Technology Conference*, pp. 313-316.

[6] S. Kulkarni, S. Uy, R. Lemdiasov, R. Ludwig, and S. Makarov, “MoM VIE solution for an isolated metal-dielectric resonator with the zeroth-order edge-based basis functions,” *IEEE Trans. Antennas and Propagation*, vol. AP-53, no. 4, pp. 1566-1571, April 2005.

[7] S. Kulkarni and S. Makarov, "The effect of numerical integration on MoM VIE solution for some isolated dielectric resonators," *IEEE/ACES International Conference on Wireless Communications and Applied Computational Electromagnetics*, 3-7 April 2005, pp. 313 - 316.

[8] S. Makarov and V. Iyer, "A narrowband patch antenna with a dielectric patch," *2008 IEEE Int. Antennas and Propagation Sym.*, San Diego, CA, July 2008, #IF527.6.

[9] R. M. Knox, “Dielectric waveguide microwave integrated circuits,” *IEEE Trans. Microwave Theory Tech.*, vol. MTT-24, no. 11, Nov. 1976, pp. 806-814.

[10] K. Ogusu, “Numerical analysis of the rectangular dielectric waveguide and its modifications,” *IEEE Trans. Microwave Theory Tech.*, vol. MTT-25, no. 11, Nov. 1977, pp. 874-885.

[11] W. V. McLevige, T. Itoh, and R. Mittra, "New waveguide structures for millimeter-wave and optical integrated circuits," *IEEE Trans. Microwave Theory Tech.*, vol. MTT-23, no 12, Oct. 1975, pp. 788-794.

[12] R. V. Lowman and R. N. Simons, “Transmission lines and waveguides,” in: *Antenna Engineering Handbook*, John L. Volakis, Ed., Mc Graw Hill, 2007, fourth edition, pp. 51-3 to 51-54.

[13] D. M. Pozar, *Microwave Engineering*, Wiley, New York, 2005, 3rd edition.

[14] C. A. Balanis, *Advanced Engineering Electromagnetics*, Wiley, New York, 1989.

[15] A. A. Kishk and M. R. Zunoubi, “Analysis of the dielectric disc antennas above a grounded dielectric substrate,” in *IEEE AP-S Int. Symp.*, 1992, vol. 4, pp. 2171-2174.

[16] A. A. Kishk, M.R. Zunoubi, and D. Kajfez, "A numerical study of a dielectric disk antenna above grounded dielectric substrate," *IEEE Trans. Antennas Propagation*, vol. 41, no 6, June 1993, pp. 813-821.

[17] F. Kuroki, R. Tamaru, and K. Miyamoto, "Experimental study of transmission line characteristics of high permittivity tape transmission line at millimeter-wave

frequencies," *Proceedings of the 37th European Microwave Conference*, Oct. 2007, pp. 957-960.
[18] A. A. Kishk, "Dielectric resonator antennas," in: *Antenna Engineering Handbook*, John L. Volakis, Ed., Mc Graw Hill, 2007, fourth edition, pp. 17-1 to 17-24.
[19] K. Carver and J. Mink, "Microstrip antenna technology," *IEEE Trans. Antennas Propagation*, vol. 29, no 1, Jan. 1981, pp. 2-24.
[20] http://ece.wpi.edu/ant/00_dielectric_patch_project/exp01
[21] C.-H. Chen and D Peroulis, "Liquid RF MEMS wideband reflective and absorptive switches," *IEEE Trans. Microwave Theory Tech.*, vol. 55, no 12, Dec. 2007, pp. 2919-2929.
[22] C. H. Hamann, A. Hamnett, and W. Vielstich, *Electrochemistry*, Wiley-VCH, Weinheim, 2007, 531 p.
[23] R. Buchner *et al.*, "The dielectric relaxation of water between 0 C and 35 C," *Chem. Phys. Lett.*, vol. 306, no. 1–2, pp. 57–63, Jun. 1999.
[24] C. A. Balanis, *Antenna Theory. Analysis and Design*, Wiley, New York, 2005, 3rd ed.
[25] N. Yu. Bliznyuk and A.I. Nosich, "Radiation efficiency of imperfect circular disk antennas," *MIKON-2000*, vol.1, May 2000, pp. 163–165.
[26] A. I. Nosich and N. Y. Bliznyuk, "Simulating axisymmetrically excited resistive and thin-dielectric disk antennas with increased efficiency and bandwidth," *31st European Microwave Conference Proc.*, Oct. 2001, pp. 1–4.
[27] J. J. Rawnick and S. B. Brown, "Taper adjustment on reflector and sub-reflector using fluidic dielectrics," *US Patent #6,873,305*, March 29, 2005.
[28] S. B. Brown and J. J. Rawnick, "Dynamically changing operational band of an electromagnetic horn antenna using dielectric loading," *US Patent #6,879,29*, April 12, 2005.
[29] J. J. Rawnick and S. B. Brown, "Antenna with dynamically variable operating band," *US Patent #6,891,501*, May 10, 2005.
[30] J. J. Rawnick and S. B. Brown, "Taper control of reflectors and sub-reflectors using fluidic dielectrics," *US Patent #6,909,404*, June 21, 2005.
[31] J. J. Rawnick and S. B. Brown, "Reflector and sub-reflector adjustment using fluidic dielectrics," *US Patent #6,930,653*, August 16, 2005.
[32] S. B. Brown and J. J. Rawnick, "Horn antenna with dynamically variable geometry," *US Patent #6,972,728*, December 6, 2005.
[33] Jack E. Bridges, "Breast cancer detection, imaging, and screening by electromagnetic millimeter waves," *US Patent #5,807,257*, Sep. 15, 1998.
[34] A. Abbosh, M. Bialkowski, and S. Crozier, "Investigation into optimum characteristics for the coupling medium in UWB breast cancer image systems," *2008 IEEE Int. Antennas and Propagation Sym.*, San Diego, CA, July 2008, #IF416.2.
[35] A. Abbosh, M. Bialkowski, and S. Crozier, "A simple model for electromagnetic scattering due to breast tumor," *2008 IEEE Int. Antennas and Propagation Sym.*, San Diego, CA, July 2008, #IF416.3.

[36] Y. Lee, J. Kim, J. M. Lee, S. J. Jeon, T.M. Grzegorczyk, and P. M. Meaney, "Microwave tomography technology test-bed system for study breast cancer detection technology based on electromagnetic field," *2008 IEEE Int. Antennas and Propagation Sym.*, San Diego, CA, July 2008, #IF416.3.

[37] M. Klemm, I. Craddock, J. J. Leendertz, and A. Preece, "Experimental and clinical results of breast cancer detection using UWB microwave radar," *2008 IEEE Int. Antennas and Propagation Sym.*, San Diego, CA, July 2008, #IF416.6.

[38] Wei Huang and Ahmed A. Kishk, „Preliminary study of a two-element DRA sensor array for microwave breast cancer detection," *2008 IEEE Int. Antennas and Propagation Sym.*, San Diego, CA, July 2008, #IF416.8.

[39] S. P. Poplack, Tor D. Tosteson, W. A. Wells, B. W. Pogue, P. M. Meaney, A. Hartov, C. A. Kogel, S. K. Soho, J. J. Gibson, and K. D. Paulsen, "Electromagnetic Breast Imaging: Results of a Pilot Study in Women with Abnormal Mammograms," *Radiology*, vol. 243, no. 2, May 2007, pp. 35-359.

Investigation of a Reconfigurable Stacked Patch with Beamsteering Capabilities

J. E. Ruyle* and J.T. Bernhard
Electromagnetics Laboratory
Department of Electrical and Computer Engineering
University of Illinois at Urbana-Champaign, Urbana, IL 61801
http:\\antennas.ece.uiuc.edu
E-mail: jruyle2@illinois.edu; jbernhar@illinois.edu

Abstract: Reconfigurable antennas can improve the performance of a wireless network in many ways, such as steering the beam of an antenna away from noise sources and increasing the capacity of a multiple-input multiple-output network. This paper discusses two methods of analysis of the behavior of a pattern reconfigurable stacked patch antenna. First, a parametric study is pursued to determine the effect of each variable in the antenna structure. Second, an in-depth analysis of the electric field behavior is discussed. Each method offers insight into the mechanism of beamsteering in the antenna structure.

1 Introduction

Antennas with beamsteering capabilities can increase the signal-to-noise ratio (SNR) of a system by directing the beam of the antenna away from noise sources. They have also been shown to increase the capacity of a multiple-input multiple-output (MIMO) network [1, 2]. However, phased arrays, the traditional structures used for achieving beamsteering, are expensive and bulky, especially at commercial wireless frequencies. Reconfigurable antennas offer the possibility of beamsteering without the expense and bulk of phased arrays.

This paper starts with a discussion describing the structure and behavior of a stacked patch pattern reconfigurable antenna. Then it presents two methods of analysis of the behavior of the antenna. First, a parametric study is pursued to determine the effect of each variable in the antenna structure. Second, an in-depth analysis of the electric field behavior is discussed. Each method offers insight into the mechanism of beamsteering in the antenna structure.

2 Antenna Structure and Behavior

The antenna design investigated is a probe-fed stacked patch with a driven bottom patch and a parasitic top patch. The antenna's dimensions are shown in Fig. 1. The height of both the top and bottom substrates is 0.3175 cm. The top substrate is RT Duroid 6010 with a relative permittivity of 2.94. The bottom substrate is RT Duroid

5880 with a relative permittivity of 2.2. The antenna operates as a pattern reconfigurable antenna in a band centered at 2.365 GHz spanning from approximately 2.3 to 2.4 GHz.

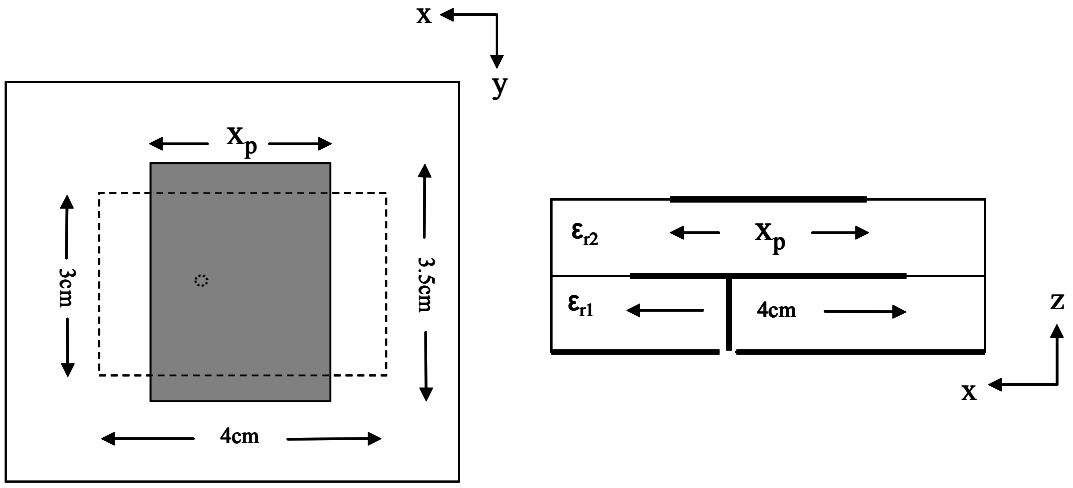

Figure 1: Structure of antenna. (a) Top view of antenna (bottom patch shown as a dashed line). (b) Side view.

An analysis of the antenna was performed in simulation. The antenna shown in Fig. 1 was simulated in Ansoft HFSS [3]. The length of the top patch, x_p, was varied symmetrically from the antenna's center from 3.35 cm to 3.65 cm. The resulting E-plane patterns are shown in Fig. 3. With these changes in x_p, the co-polarized beam changes direction from broadside to either +35° or -30°. The patterns in Fig. 2 have been individually normalized.

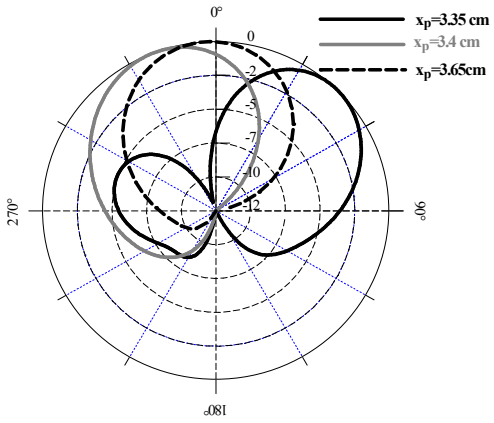

Figure 2: E-plane co-polarized patterns normalized in dB for different lengths of top patch at frequency 2.3625 GHz.

The simulated impedance behavior for the antenna with x_p= 3.35 cm is shown in Fig. 3. As depicted in Fig. 3, the antenna is resonant at 2.225 GHz and 2.2725 GHz. However, as illustrated in Fig. 3, the band of frequencies at which beamsteering behavior is observed is above this: 2.32-2.42 GHz. This band varies slightly with feed point,

which will be discussed in Section 3.4. The impedance changes very little with top patch length, as shown in Fig. 4, except for the longest top patch length.

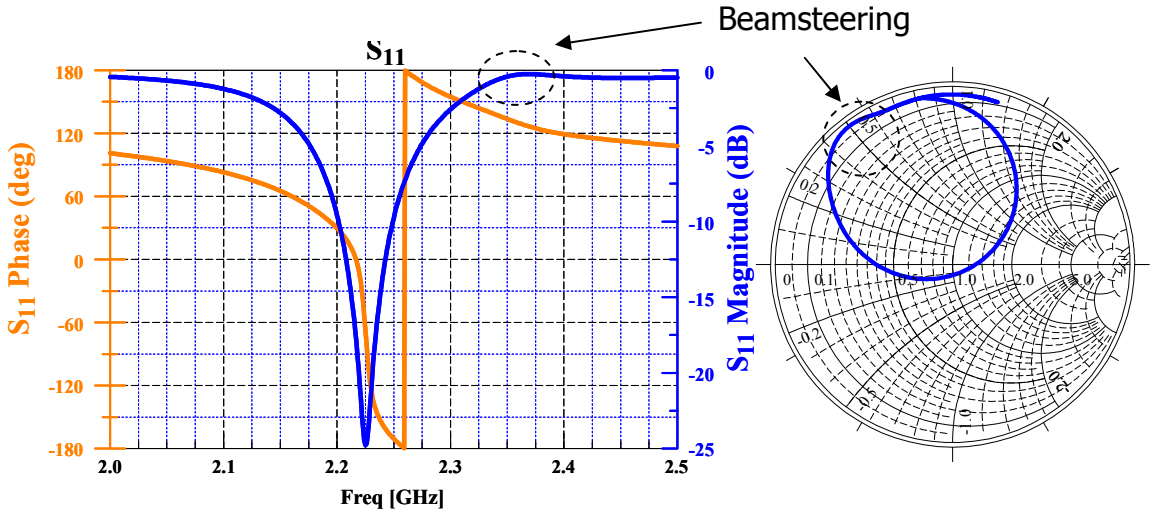

Figure 3: Simulated impedance data of antenna for a feed point 0.55 cm from the center of the patch.

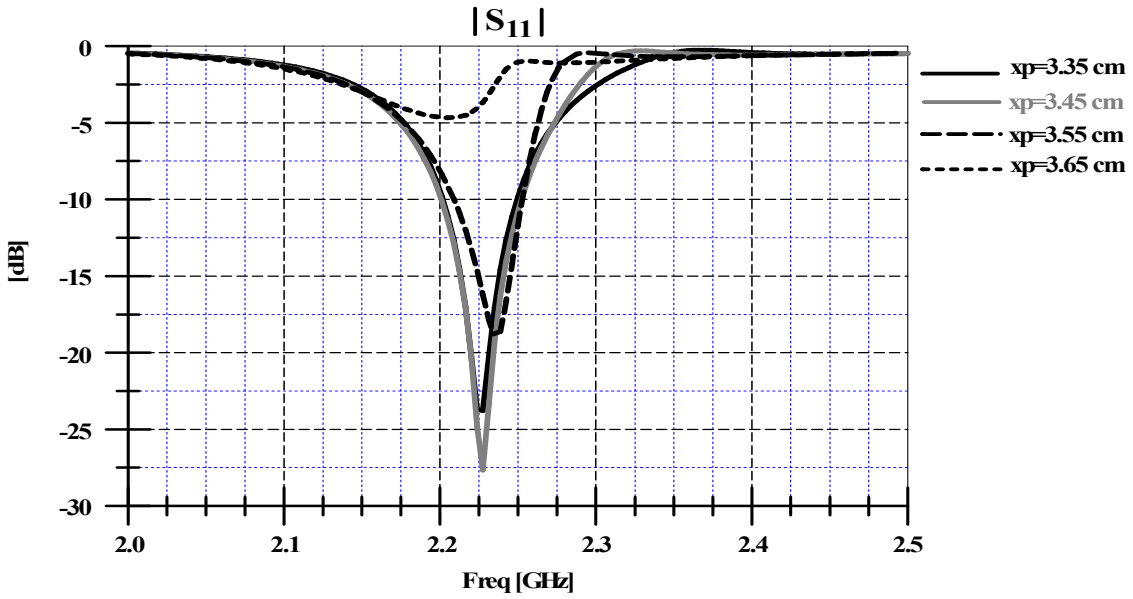

Figure 4: Simulated impedance data for change in top patch length.

The beam pattern for this antenna also changes with frequency. The simulated data for this length is shown in Fig. 5. The feed point is different for this data; it is 1 cm from the center of the patch for both the simulated and measured data. The reason for this change will be discussed in Section 3.4. The measured data is shown in Fig. 6 for a slightly different set of frequencies. These patterns have been normalized at each

frequency. A 90-MHz frequency shift between simulations and measurements was observed for all performance parameters, so the patterns shown in Fig. 6 are for frequencies 90-MHz higher than the simulated patterns. Comparing Figs. 5 and 6, the measured behavior is consistent with the results from simulation.

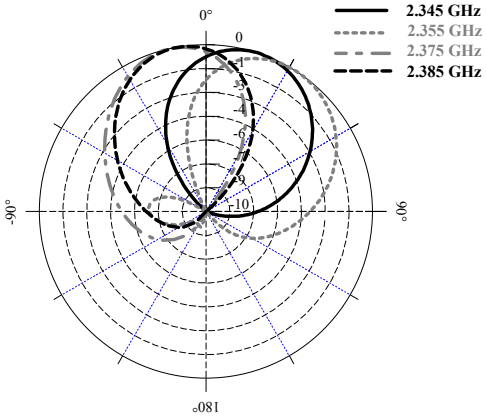

Figure 6: Simulated E-plane co-polarized patterns normalized in dB for different frequencies for x_p=3.35 cm.

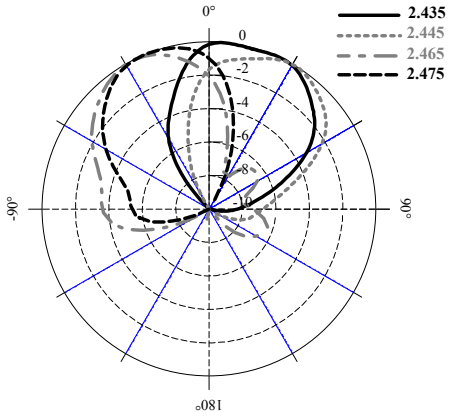

Figure 5: Measured E-plane co-polarized patterns normalized in dB for different frequencies for x_p=3.35 cm.

3 Parametric Studies

In an attempt to determine the effects of various dimensions on the behavior of the antenna, many parametric studies were pursued in simulation. The results of the studies that seemed to offer insight into the behavior of the antenna are provided in the following sections. For all studies only one parameter was varied at a time. Unless specified as the variable for a particular study, the dimensions are as shown in Fig. 1 with an x_p value of 3.35 cm. These dimensions are 4 cm for the length of the bottom patch and its width is 3 cm. The length of the top patch (x_p) is 3.35 cm and the width is 3.5 cm. The height of the top and bottom substrate is 0.3175 cm.

3.1 Top Substrate Height

The height of the top substrate was varied from 0.0127 to 0.8 cm in steps of 0.0127 cm. The behavior of the antenna with increasing top substrate height can be broken into six groups based on frequency band and top substrate heights greater than or less than 0.35 cm. In the lowest frequency band and for top substrate heights less than 0.35 cm, the beam angle starts negative and trends toward zero with the most negative beam angles being observed for a frequency of 2.0 GHz and the least negative beam angles for 2.2 GHz. The beam angles in between occur for successive increases in frequency. Above 0.35 cm, the beam angles are fairly static and near broadside. The middle frequency band (2.23- 2.325 GHz) shows a dramatic increase in beam angle with

top substrate heights greater than approximately 0.35 cm with fairly static behavior before this height. The frequency with the least beam angle is 2.23 GHz and the frequency with the greatest beam angle is 2.325 GHz. The beam angle increases with frequency throughout the entire middle frequency band. It is quite unexpected that the beam angles would increase with an increasing substrate height since this would normally imply a decrease in coupling between the patches. With a decrease in coupling, the parasitic top patch should have less effect on the behavior of the structure. Since the parasitic patch appears to have more effect with an increase in top substrate height, the coupling mechanism is probably more complicated than simple radiative coupling. In the highest frequency band and for top substrate heights less than 0.35 cm the beam angles produced exhibit an asymptotic behavior with increasing top substrate height. The asymptote for the largest top substrate height occurs for a frequency of 2.35 GHz and the asymptote for the smallest top substrate height occurs for a frequency of 2.5 GHz. Each asymptote for progressively smaller top substrate heights is for a successively higher frequency series.

The frequency with the minimum S_{11} value, the upper and lower frequencies for the impedance band, and frequency of maximum beam angle for the range of top substrate heights are shown in Fig. 7. The frequency band is defined as frequencies for an S_{11} value less than -5 dB. As shown in Fig. 7, the frequency with the maximum beam tilt remains constant for any top substrate height greater than 0.35 cm. The bandwidth of the antenna also remains fairly constant.

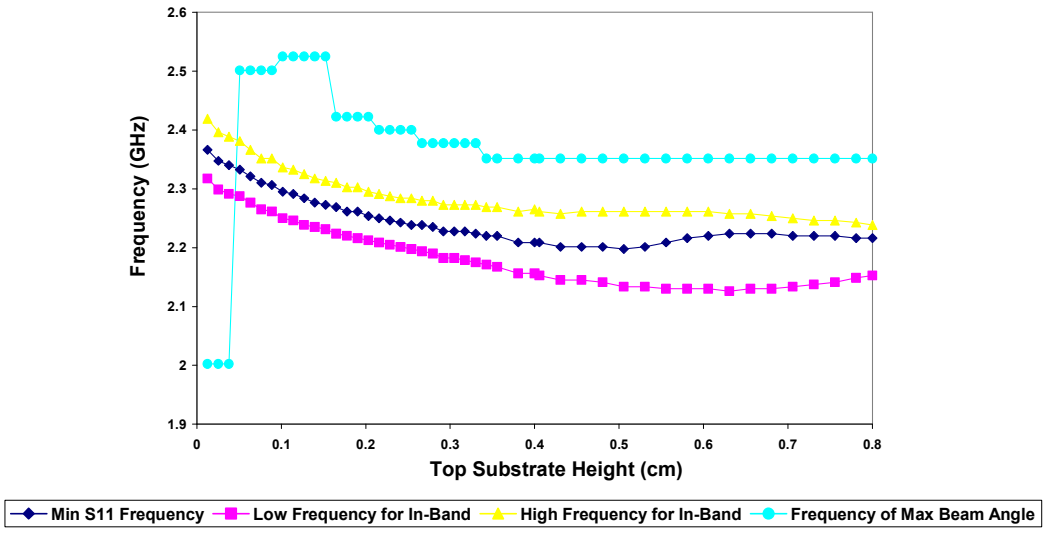

Figure 7: Matched impedance frequency band information along with the frequency of maximum beam angle for increasing top substrate height.

3.2 Top Patch Length

The length of the top patch was varied from 3 to 5 cm in steps of 0.5 mm. The antenna has multiple modes of behavior based on frequency and top patch length. For the low frequency band of 2.0 -2.13 GHz the beam angles produced are static and small for

top patch lengths less than approximately 3.85 cm. For this same frequency band and for top patch lengths greater than 3.85 cm, the beam angles produced become large and negative in a roll-off behavior. The lowest frequency (2.0 Hz) rolls off for the smallest top patch length (3.85 cm) and successive frequencies roll off for larger top patch lengths. The middle frequency band (2.15 - 2.23 GHz) has static beam angles at broadside for top patch lengths below 3.7 cm and above 4 cm. For top patch lengths in between 3.7 cm and 4 cm the middle frequency band has peaks of negative beam angles. The peak for the smallest top patch length occurs for the lowest frequency; the successive peaks for increasing top patch length correspond to successive increases in frequency. At and around 2.23 GHz little or no beamsteer is observed for all top patch lengths. This is unfortunate because the matched impedance band of the antenna for a 50-Ω system is centered around 2.23 GHz for all top patch lengths. For the high frequency band of 2.25-2.5 GHz the antenna has asymptotic beam behavior for top patch lengths less than 3.6 cm, static beam behavior for top patch length between 3.6 and 4 cm, and a gradual increase in beam angles in positive θ for top patch lengths greater than 4 cm. The asymptote for the smallest top patch length occurs for the highest frequency, 2.5 GHz, and vice versa with successive frequencies corresponding to the top patch lengths in between. For all frequency bands the beam angles return to nearly broadside for top patch lengths between 3.6 and 3.7 cm.

The frequency of minimum S_{11}, frequency band, and frequency of maximum beam tilt are shown in Fig. 8. As can be seen in the graph, there is nearly no matched impedance band for top patch lengths greater than 3.6 cm. As can also be seen in the graph, the frequency of maximum beam tilt is never within the matched impedance band of the antenna. The frequency of maximum beam tilt appears as if it should match with the matched impedance band of the antenna for top patch lengths of 3.6 to 3.7 cm. However, as discussed earlier, these are the top patch lengths that return the pattern almost completely to broadside.

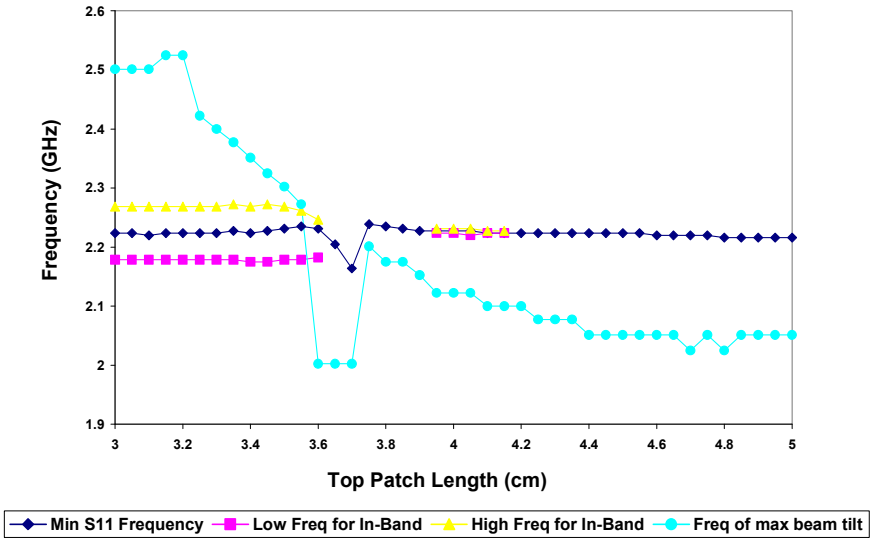

Figure 8: Matched impedance frequency band information along with the frequency of maximum beam angle for increasing top patch length.

3.3 Bottom Substrate Height

The height of the bottom substrate was varied from 0.0127 to 0.3429 cm. There are two modes of behavior for the antenna based on frequency. For the low frequency band, from 2.0 - 2.35 GHz, the increasing bottom substrate height produces lines with a positive slope when the beam angles are plotted against it. For the high frequency band, from 2.375 to 2.5 GHz increasing the bottom substrate height produces lines with a negative slope when the beam angles are plotted against it. The frequency with the largest positive beam angle is 2.35 GHz and the frequency with the largest negative angle is 2.375 GHz. The magnitude of the beam angles produced is less for frequencies successively smaller than 2.35 GHz and larger than 2.375 GHz. The data taken also suggests that a bottom substrate height greater than 0.15 cm is needed for useful beam angles (greater than 15°) to be produced by the stacked patch antenna.

The effect of the height change on the frequency of minimum S_{11}, the impedance matched frequency band, and the frequency of maximum beam tilt are shown in Fig. 9. As expected, the frequency band expands as the bottom substrate height increases. The frequency of maximum beam tilt is around 2.35 GHz for bottom substrate heights greater than 0.15 cm. The frequency of maximum beam tilt is 2 GHz for bottom substrate heights less than 0.15 cm but as discussed earlier these beam angles are close to broadside.

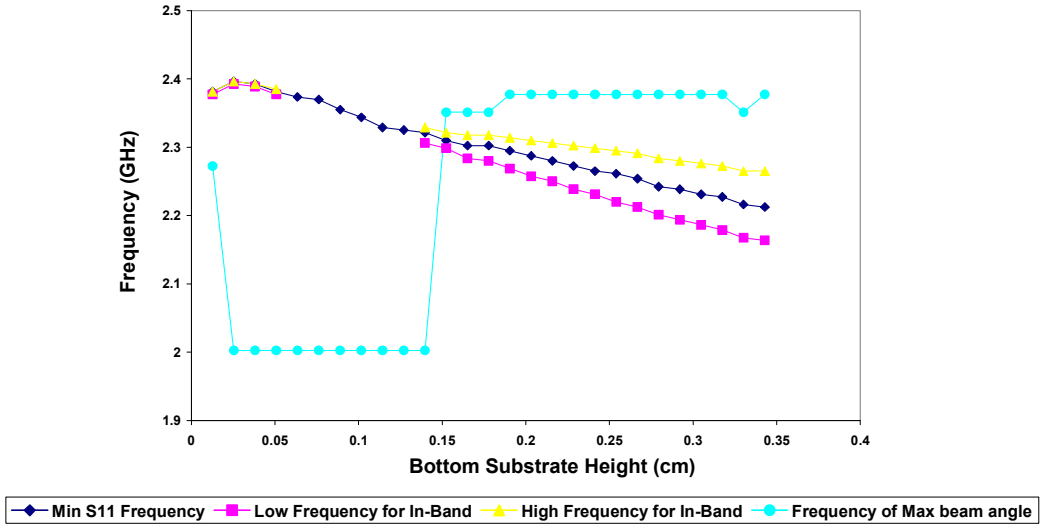

Figure 9: Matched impedance frequency band information along with the frequency of maximum beam angle for increasing bottom substrate height.

3.4 Feed Position

The feed position was varied from -1 to +1 cm in steps of 0.5 mm with respect to the center of the patch. The effect of feed position on beam angle is shown in Fig. 10. The effects of feed position on resonant frequency, frequency band, and frequency of maximum beam tilt are shown in Fig. 11. It is clear from Fig. 10 that the beam angle

increases as the feed point moves closer to the center of the patch. The beam angles are also inverted for mirrored feedpoints. Unlike the other parametric studies, all frequencies are affected by the change in feedpoint. At a center feed position, all frequencies have a large beam tilt. However, across all feed points the frequency of maximum beam tilt stays nearly constant around 2.35 GHz. This suggests that the feed position merely expands the band of frequencies for which beamsteer is observed. It does not generally shift this band. As can be seen in Fig. 11, the feed point in the center of the patch excited the TM_{020} mode of the patch instead of the dominant mode - TM_{010}. Interesting beam patterns are produced when the stacked patch is operating in this mode. After the first band of operation is understood, this band could offer even more degrees of reconfiguration. Moving the feedpoint out toward the edge of the patch moves the resonance to the left of the center of the Smith chart up in frequency. With a feedpoint of -1 cm or +1 cm this anti-resonance occurs in the middle of the band of beamsteer. So, the antenna can be made resonant in the middle of the band of beamsteering, around 2.35 GHz, for a feed point of -1 cm or +1 cm. However, the real part of the impedance at this point is always very small for all feed points.

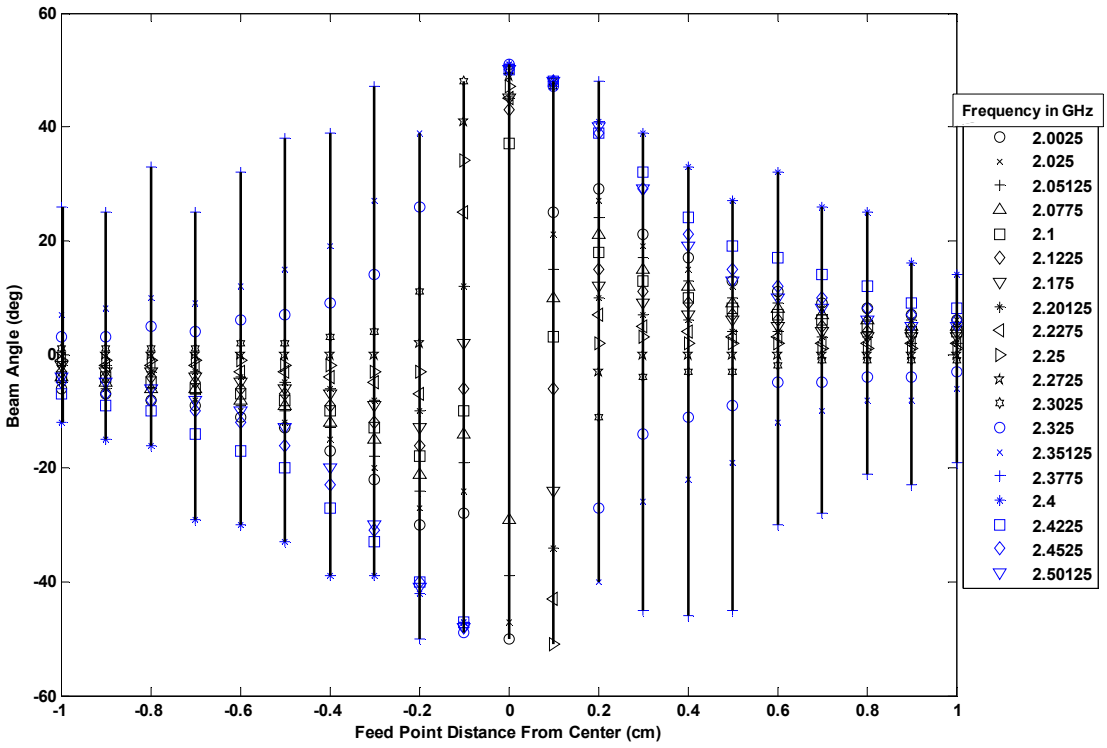

Figure 10: Beam angles produced for a frequency band of 2.0 – 2.5 GHz for a feed point ranging from -1 to +1 cm.

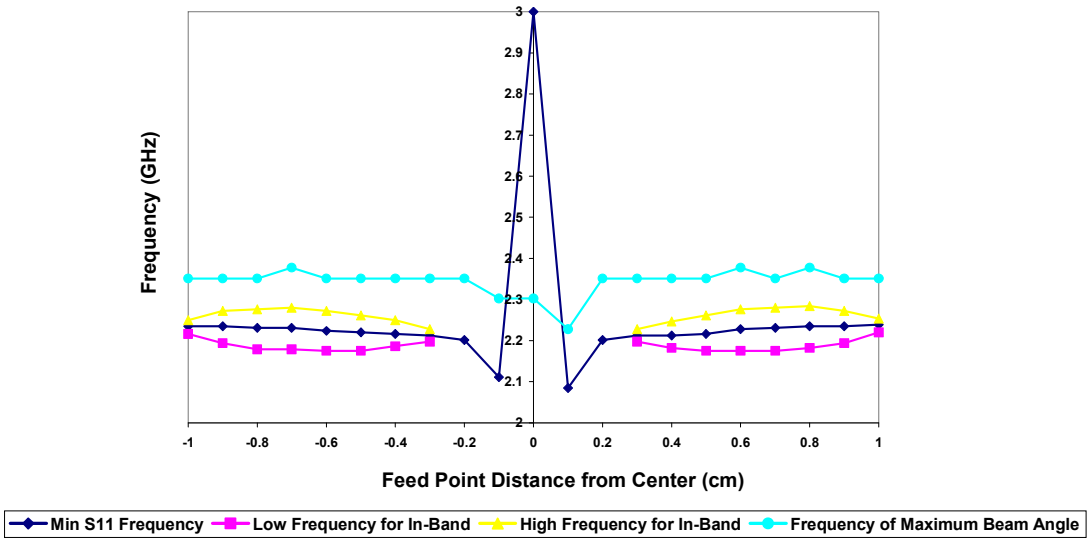

Figure 11: Matched impedance frequency band information along with the frequency of maximum beam angle for a feed point ranging from -1 to +1 cm.

3.5 Top Width Change

The width of the top patch was varied from 2.75 cm to 4 cm in steps of 0.5 mm. The width was found to have little effect on the amount of beam steering or on impedance behavior. The width of 3.5 cm was chosen because it had the greatest beamsteer for the frequency of 2.365 GHz. However, any width in the range of dimensions studied could be used if necessary without any deleterious effects on the beamsteering behavior of the antenna. The co-polarized data for the pattern in the H-plane was also taken and the width of the top patch has no effect on the beam angle in this plane. The pattern in the H-plane is always at broadside for all widths studied. The H-plane data was only taken for this study. It was assumed that changing the width of the top patch would change the patterns in the H-plane. However, no change was observed in beam pattern or in impedance behavior.

3.6 Dielectric Constant Ratio

A parametric study was pursued in which the ratio of the lower to upper dielectric constants was maintained relatively constant. The electrical lengths of both patches along with the electrical distance of the probe from the center of the patch were maintained. For these properties, an effective dielectric constant was found for the layered structure using the method from [4]. The electrical height of the substrates and the electrical widths of the patches were also kept constant. For these parameters the dielectric constant was used instead of an effective dielectric constant to maintain the electrical distances since they are needed to find the effective dielectric constant. Although an iterative process could have been used to make these parameters more accurate, the method used should be effective for the purposes of this study. Figure 12 shows that if the ratio of the dielectric constant of the bottom substrate to that of the top

substrate is maintained along with the electrical lengths of all parameters, then the behavior of the antenna remains relatively constant. When this study was performed, it was observed that by maintaining the ratio between the dielectric constants of the top and bottom substrates, the structure maintained its aspect ratio. Therefore, the relative positions of the top and bottom patches remained constant.

To determine whether the dielectric constant ratio or the relative positions of the top and bottom patches was the important factor in keeping the behavior of the antenna constant, the ratio of dielectric constant of the bottom substrate to that of the top was varied from 0.1 to 1. No significant pattern in behavior was noticed. The beam angles, gain, and impedance data were analyzed from 2.0 to 2.6 GHz. As can be seen in Fig. 13, all important frequencies change in no particular pattern for all ratios of dielectric constants studied. Therefore, it can be concluded from this study that the ratio between dielectric constants of the bottom and top substrate is not important; most likely, what matters is the aspect ration of the top and bottom patches.

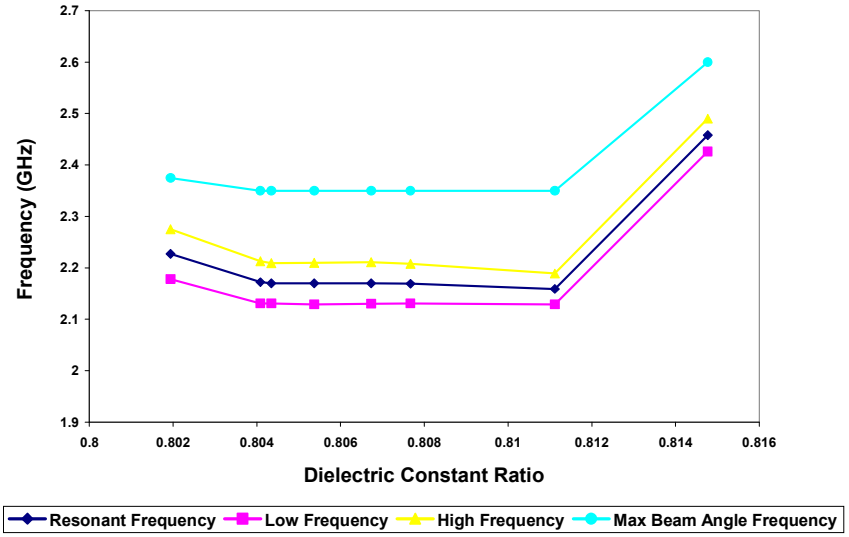

Figure 12: Matched impedance frequency band information along with the frequency of maximum beam angle for a relatively static ratio between the dielectric constants of the upper and lower substrates.

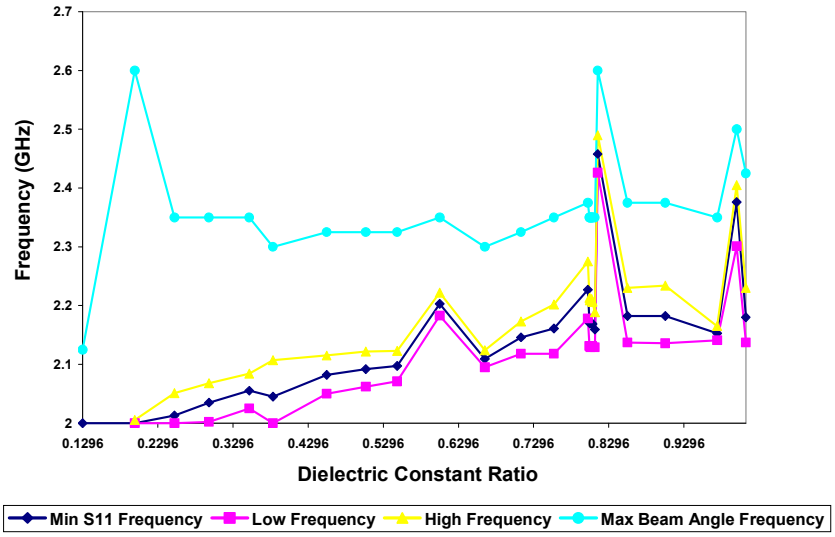

Figure 13: Matched impedance frequency band information along with the frequency of maximum beam angle for a dielectric constant ratio between the upper and lower substrates of 0.1 to 1.

3.7 Conclusions from Parametric Studies

From the parametric studies that were performed, it was found that the variables that affect antenna performance are the top and bottom substrate height, top patch length, feed position, and relative positions of the top and bottom patches. The variable that has little or no effect is the top patch width.

The results of the parametric studies, while providing some insight into the behavior of the antenna, did not provide the basis for a model of the antenna. The top substrate height had an unpredicted effect. The coupling between the top and bottom patches appeared to increase as the top substrate height increased. The top patch length had a large effect on the beam angle of the E-plane co-polarized radiation pattern. The feed position also affected the beam angle. As the feed point approaches the middle of the patch, more frequencies exhibit beamsteering behavior. The relative positions of the top and bottom patches were found to be important by varying the ratio of the top to the bottom dielectric constant. Based on these observations, a more in-depth study of the basic operation of the antenna is needed to understand how the antenna is providing beamsteer.

4 Electric Field Analysis

In the course of this research, it was observed that the electric fields in the top and bottom substrates of the antenna changed significantly when the frequency was varied. The electric fields were therefore extracted from HFSS in order to determine exactly how the fields were changing and the effect this change had on the beamsteering behavior of the antenna.

The fringing electric fields on the edges of the top and bottom patches of the stacked patch that represent the radiation from the structure, were extracted from HFSS over the frequency band of interest. The grey boxes in Fig. 14 show the area from which data was taken. Since the fringing fields are the dominant radiation mechanism, following the method of the cavity model [5], the patch antenna can be reduced to two slots in a ground plane with the fringing electric fields inside. The electric fields for each slot were summed in the z-direction and averaged in the y-direction to find an effective vector for each slot. A simplified diagram of the electric fields for a normal patch antenna operating in the first resonant mode is shown in Fig.15. The effective vectors found from the data are representative of the vectors circled in the diagram. For a normal patch antenna, in the far-field, the vertical components (E_z) of the left and right slots cancel at broadside. This leaves only the horizontal component (E_x) to affect the radiation pattern. These horizontal fields are in-phase and approximately one half-wavelength apart in space, producing a broadside radiation pattern.

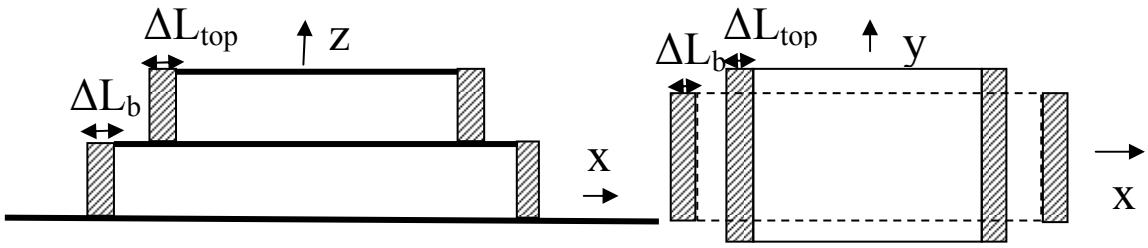

Figure 14: Diagram of stacked patch. Grey boxes represent area of data taken. (Left) Side view. (Right) Top view.

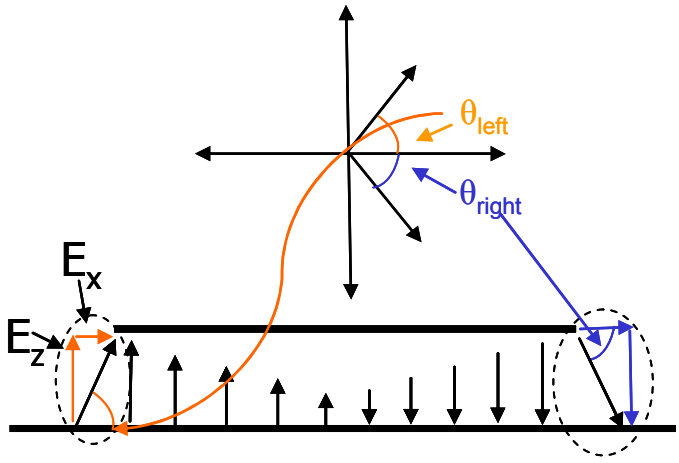

Figure 15: Electric field of regular patch antenna operating in the first mode with vector slot fields shown. These vectors are broken down into components and shown with representative phase angles.

The fields in the x and z-directions of all four radiating slots of the stacked patch antenna are shown in Figs. 20 and 21. The slots are referenced as left and right. The slot referenced as left is nearer to the probe. As shown in Fig. 16, the fields in the z-direction

invert for the top patch at 2.3 GHz and at 2.275 GHz for the bottom patch. The inversion is a polarity change. Therefore, the electric field lines that were pointing in the positive z-direction are pointing in the negative z-direction, and vice versa. As shown in Fig. 17, the x-directed fields in the top substrate are opposite to the x-directed fields in the bottom substrate. Figures 16 and 17 show that for the region of beamsteer the field structures in the top and bottom substrates are 180° out of phase with each other. There are also magnitude differences for the fields on the left and right in the region of beamsteer. For the bottom patch, the fields on the left are stronger, whereas, for the top patch the fields on the right are stronger.

An angle θ representing the phase of the vector field in the slots of a patch antenna can be found as shown in Fig. 18. The angle for each of the slots of the stacked patch structure is depicted in Fig. 18. These angles are used to find the effective electrical lengths of the top and bottom patches, shown in Fig. 19, using the relation

$$\theta_{patch} = 180 - (\theta_{right} + \theta_{left}).$$

We derived the above formula using the following logic. The phase angles of the fields of the right and left slots should be 180° out of phase if the patch is a half-wavelength long because the electric fields in the substrate of the patch should be completely symmetric in the E-plane about the middle of the patch. If they do not cancel, then the patch has an electrical length other than a half-wavelength. Following the above formula and using the extracted data, the bottom patch looks nearly electrically 180° long, with the following exceptions, a small frequency band where the fields of the bottom patch invert and the frequency band for which beamsteering is observed. The top patch, however, appears electrically shorter as frequency increases. The electrical length of the top patch changes from 180° to 160° across the frequency band studied.

The two left and right slot fields, from the patch and parasitic element, were added together to obtain an effective left and right slot. These fields are shown in Fig. 20. The fields invert for the total structure at 2.275 GHz. In general, the fields in the total left slot are much larger than those in the right slot. Using these fields, angles are found to represent the vector fields of each slot, shown in Fig. 21, and these angles are used to find an electrical length for the whole structure, shown in Fig. 22. There is a clear band shown in Figs. 21 and 22 matching with the band of frequencies for which maximum beamsteer is observed. As Fig. 22 shows, the angle of the vector representing the total right slot fields changes from negative to positive, bringing the vector from the fourth quadrant to the first. The graph presented in Fig. 22 shows a very interesting result; even though the structure is symmetric around the centerpoint (with the exception of the feed), the phases of the vectors on the ends of the representative total structure will be disparate for different frequencies within a fairly small band.

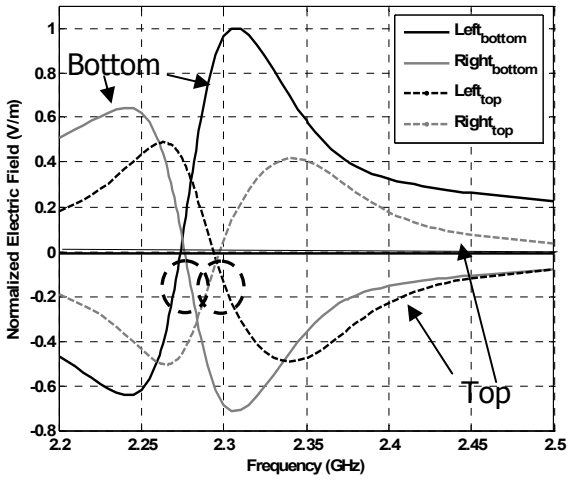

Figure 16: Electric field of slots in z-direction

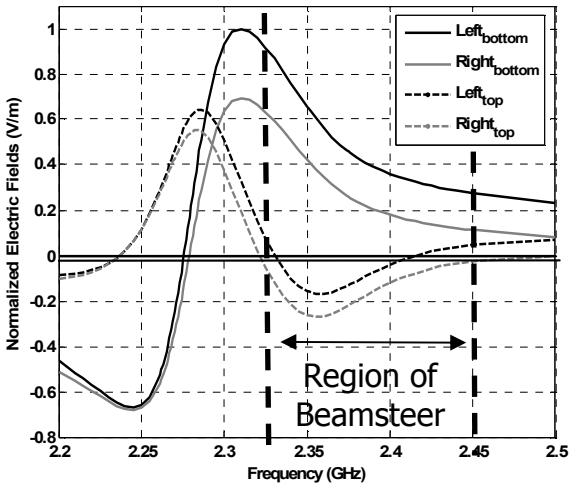

Figure 17: Electric fields of slots in x-direction

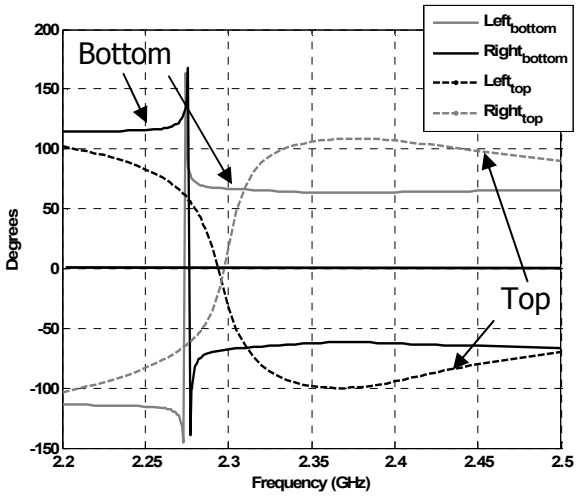

Figure 18: θ of slots using E-field information.

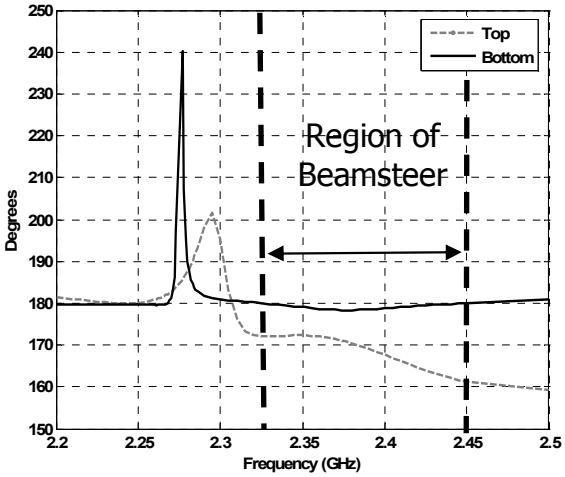

Figure 19: Electrical length of top and bottom patches using angle of slot fields

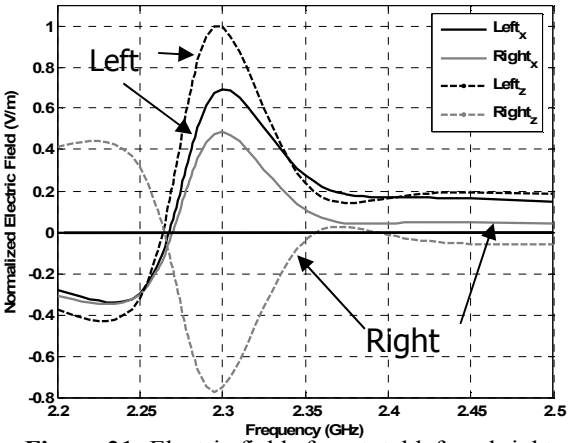

Figure 21: Electric fields for a total left and right slot

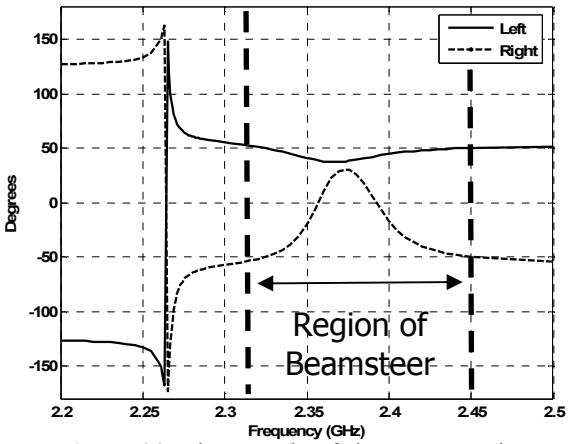

Figure 20: Phase angle of slots representing a composite left and right slot

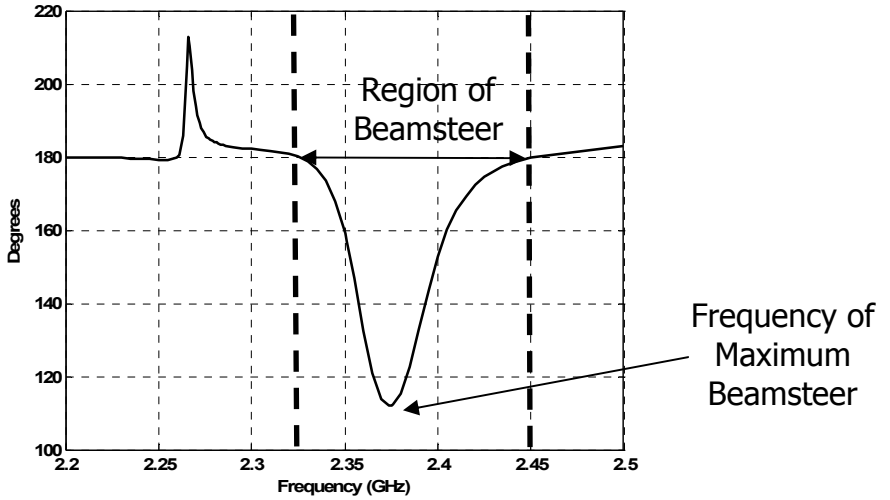

Figure 22: θ representing the electrical length of the total structure

The data presented in Fig. 25 clearly shows a band of frequencies for which the total structure's electrical length changes from its expected value. The electrical length should progressively increase as frequency is increased. However, for the band of frequencies 2.325-2.45 GHz, the structure looks electrically shorter than expected. This band matches up with the frequencies for which the patterns have beamsteering behavior. For the frequency at which maximum beamsteer is noticed, the total patch actually looks only 110° long when it should look longer than 180° long. This frequency of maximum beamsteer (f=2.365 GHz) matches up with the shortest electrical length found for the structure, as shown in Fig. 25.

5 Conclusions

Two methods of analysis were pursued to understand the behavior of a pattern reconfigurable stacked patch antenna. Many parametric studies were undertaken to find the effect of each dimension in the antenna structure. Some insight was gained with these studies. It was found that the width of the top patch had very little effect on the behavior of the antenna. However, in all other studies undertaken, the dimensions that changed had a large effect on the behavior of the antenna. The dimensions tested were: the bottom substrate height, top substrate height, length of the top patch, and feed point position.

An analysis was undertaken that studied the behavior of the electric field of the stacked patch antenna across a frequency band. These studies yielded some very interesting results. It was found that if the stacked patch antenna structure is observed as a whole, then the antenna looks electrically shorter than a half-wavelength in a frequency band when it should look electrically longer than a half-wavelength.

The antenna discussed shows promise as a reconfigurable antenna. However, more work must be done to understand its behavior. In future work, a model for the antenna will be developed and will be used to more fully understand the mechanisms

which cause beamsteering in the stacked patch antenna structure. We will use this insight to develop strategies to maintain the effects that cause beamsteering while improving the impedance match over the band.

6 Acknowledgments

This work was supported by the U.S. Army Research Office under Grant W911NF-06-0366. The dielectric substrate materials for this work were provided by Rogers Corporation.

7 References

[1] J. D. Boerman and J. T. Bernhard, "Performance study of pattern reconfigurable antennas in MIMO systems," *IEEE Trans. Antennas and Propag*., vol. 56, no. 1, pp. 231-236, Jan. 2008.

[2] D. Piazza and K. R. Dandekar, "Reconfigurable antenna solution for MIMO-OFDM systems," *Electron. Lett.,* vol. 42, no. 8, pp. 446-447, April 13, 2006.

[3] Ansoft HFSS, *Version 9*, Ansoft Corporation, Pittsburg, PA, 2006.

[4] J. T. Bernhard and C. J. Tousignant, "Resonant frequencies of rectangular microstrip antennas with flush and spaced dielectric superstrates," *IEEE Trans. Antennas and Prop.*, vol. 47, no. 2, pp. 302-308, Feb. 1999.

[5] C. A. Balanis, *Antenna Theory*, 3rd ed. Hoboken, NJ: Wiley, 2005.

A STRUCTURALLY-FUNCTIONALIZABLE ARCHIMEDEAN SPIRAL APERCHASSIS

Gregory H. Huff
Electromagnetics and Microwave Laboratory
Department of Electrical and Computer Engineering
Texas A&M University
College Station, TX 77843-3128

Abstract: Miniaturization and efficiency are often at odds in the design of broadband radiating structures. This relationship becomes even more complicated once the application-driven size and weight constraints are included into the design process. Structural integration (e.g., being load-bearing) and other dimensions of multifunctionality add additional complexity into this design-space. However, they also represent a means of finding alternative integration techniques for balancing the system-level objectives through the design of the radiating aperture. This work examines the role of an internally-fed Archimedean spiral antenna which makes use of the volumetric spaces created by the topology of an internalized stripline feed network; specifically as a means to reduce the footprint of peripheral systems such as sensors, radios, etc. by integrating them directly into the radiating structure. This inclusion of essential components into the structure is analogous to the concept of a chassis in automobiles (which typically includes the "running gear" and other essential components), and provides the motivation for concept of an aperchassis (a radiating structure with structural functionality and volumes/surfaces for internalized subsystems). The design, operation, and experimental results of the stripline-based dyson-style balun, broadband impedance transformer, and stripline-based high-impedance spiral aperchassis will be discussed in this work, and simulated results will also be discussed which extend the functionality of the structure.

1. Introduction

There are many challenges in overall design of UAV-based antennas that can provide instantaneous or reconfigurable coverage across HF, UHF, and VHF bands. In a general context, this requires strategies for spatial trade-offs to satisfy the application-based constraints from intended platforms The maximum size of these structures represents an area of primary concern, especially within the HF band since the wavelengths are at least an order of magnitude larger in size than the applications. Within the design of these antennas, the need for broadband baluns represents an embedded challenge that can quite often make the implementation of a candidate design very challenging. Spiral antennas [1-3], derivatives thereof [e.g., 4], and other complimentary/balanced structures have been examined extensively for this. Many innovative designs have been implemented [5-

9] that provide the differential excitation to the complimentary arms of the spiral, but the performance provided by the Dyson ("infinite") balun [1-3] is very desirable. However, this balun structure has traditionally been implemented using the coaxial line which can create difficulties within the context of monolithic fabrication techniques. This is especially difficult when conformal integration and/or structural functionality is required since typical reinforcing materials are composed of laminates and other materials that must be matched for thermal management, mechanical loading, and other requirements.

At the system integration level, these spatial and performance constraints can manifest themselves in many other ways. For example, the proper placement of sensors, electronics, cameras, and other sub-systems or payloads across a platform must be such that they do not interfere with the antenna's performance. Since these are the systems that facilitate multifunctionality, their integration into the platform represents a critical step in the design and performance of the structure. Thus, strategies [10] for volumetric spaces and surfaces must be in play for a given design so they do not interfere with the electromagnetic performance of the antenna or the balanced feed network.

This work examines such a strategy to mitigate the growing complexity arising from multifunctionality and antenna requirements in spatially constrained platforms. It begins by describing the motivation and nomenclature of the aperchassis – a radiating structure that supports system integration through internalization. Next, a summary of the design methodology outlines the process for developing a spiral structure based on a broadband antenna and stripline-based balun and antenna design with an internalized volume for electronics. A fabricated design example for an Archimedean spiral aperchassis then illustrates the basic performance of an externally-fed aperchassis and simulated results are given for an internalized design. The work concludes with a brief summary.

2. Origin of Aperchassis Nomenclature

The design, operation, and conformal integration of structurally functional antennas are receiving significantly more attention as multifunctional systems become more prevalent. However, the nomenclature used to describe these radiators depends greatly on the diverse roles they fill in a given application. For example, conformal load-bearing antenna structures (*CLAS*) have matured over the past decade for aerospace applications as either "bolt-in" systems or radiating components fabricated within the structural frame or skin of an aircraft. These antenna systems are therefore designed to operate as a structural functional aerosurface or skin. Similarly, aperstructures were initially considered for naval applications. Given the typical size of ocean/sea-going vessels the antennas are not required to have a significant structural role (albeit this may change or be changing) but they do act as a conformal radiating surface with some structural integrity. This integration into a larger structure lends the name aperstructure.

The antenna nomenclature in this work is based on the concept of a radiating chassis. This can be motivated by considering the evolving definition and operation of a chassis for several different platforms leading from the classical definition in mechanized device

up to a modern electronics. The automobile provides the first instance of a chassis, which includes the structural frame plus the "running gear." The running gear includes elements vital to the operation and includes the engine, transmission, driveshaft, differential, and suspension. It does not include the body or other elements usually not necessary for integrity of the structure. In a tank the chassis (or hull) is the bottom part of the tank and includes the tracks, power plant, driver's seat, and crew compartment. For basic electronic devices (televisions, radios, etc.) the chassis is typically a metal frame on which the circuit boards and other electronics are mounted; in the absence of a metal frame, the chassis refers to the circuit boards and components themselves, not the physical structure. Computers provide a step closer to this work, where the chassis refers to the rigid framework onto which the motherboard, memory, disk drives, and other equipment are mounted. Similar to the framed automobile, this chassis supports the shell-like case, or housing that protects vital internal equipment. Thus, the aperchassis can be defined as a radiating structure (aper-) that provides both the load-bearing structural support and the framework (-chassis) for internally- or surface-integrated components vital to the intended operation such as T/R-modules, filters, sensors, power plants and/or batteries.

3. Summary of Design Methodology

The aperchassis design strategy in this section can be applied to other structures, but for the spiral aperchassis in this work it requires three primary components: (1) the geometry of a gap-fed spiral antenna, where a finite-width and length have been assigned to the gap-feed voltage source, (2) a finite-ground stripline impedance transformer and transmission line that can be made conformal to a spiral topology, and (3) a stripline-based Dyson-style balun that provides the 1:1 impedance transformer and mode-conversion between the (combined) radiating slotline spiral modes that emerge from the center of the spiral and the guided stripline mode. The primary consideration in this design is that the input impedance of the spiral must match the characteristic impedance of the stripline, which has the same dimensions as the gap-feed. Items (1) and (2) must therefore be examined judiciously – and together – since the spiral properties and performance of the finite-ground stripline will have a shared relationship based around the Arm-Width Constant K (or slot-to-metal ratio) of the spiral. This parameter will impact the input impedance and radiated fields in the design of the spiral, but can also be treated as a degree of freedom in the design of the stripline. For the finite-ground stripline this parameter will impact the guiding properties by limiting the width of the center conductor, effectively creating a lower-bound on its characteristic impedance. However, by utilizing K to create a high impedance spiral (typically greater than 150 Ω) the center-conductor of the stripline can be narrowed to operate effectively between the finite grounds.

The conversion from the gap-fed spiral structure into an aperchassis-suitable topology can be seen in Fig. 1, and proceeds by first converting one arm of the two-arm spiral geometry into a three-conductor, finite-ground, stripline topology. Both grounds and the center conductor use the same spiral winding. The complimentary arm of the spiral

resides on the center-conductor layer in the stripline topology by extruding the center-conductor of the spiral-wound stripline through the center of the spiral (across the gap), then tapering and winding it into the complimentary geometry (e.g., the ground layer in the stripline structure). A Dyson-style balun structure can then be formed at the center of the spiral by adjusting the tapering and gap-distance at the center. In this configuration the stripline grounds will act to both the feed structure and as an arm of the spiral antenna. The impedance transformer can then be positioned along the stripline section to provide an internalized impedance match.

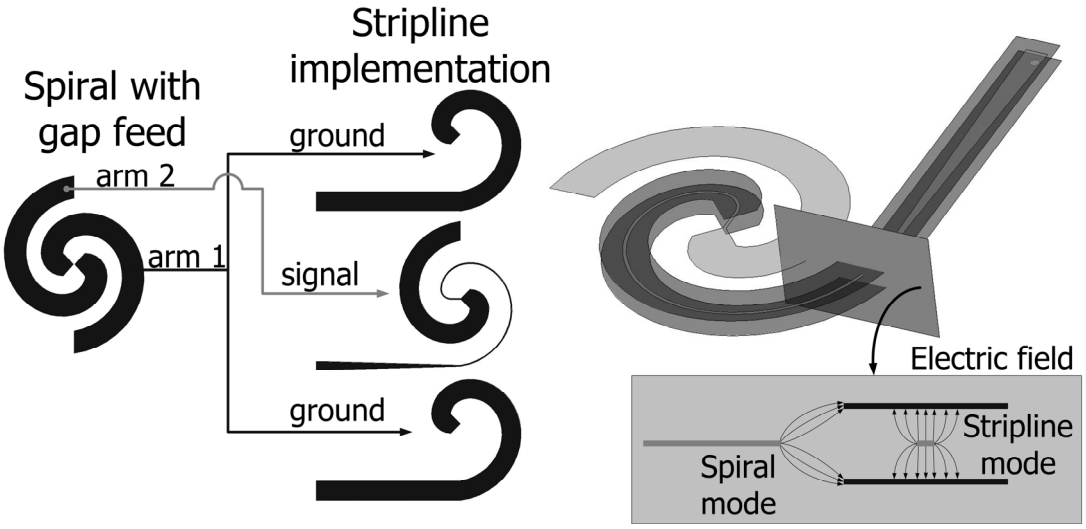

Fig. 1. Transformation of two-arm Archimedean spiral into the aperchassis with an external feed for measurements.

4. Example 1: Externally-Fed Archimedean Spiral Aperchassis

An externally-fed Archimedean spiral aperchassis (Fig. 1) with a slot-to-metal ratio of .75 (15 mm: 20 mm) and input impedance 150 Ω has been designed to demonstrate the antenna performance of the aperchassis concept. Rochelle Foam ($\varepsilon_r \sim 1$) substrates with a total height h = 7.6 mm (2×3.8 mm) were used to fabricate structure. The measured bandwidth spans 748 MHz (800 MHz using the 60 mm outer, resonant, osculating circular slot radius) to 4.121 GHz (3.4 GHz using the 14 mm inner, resonant, osculating circular slot radius taken at the end of the balun taper). Rochelle Foam was chosen as a substrate material that would allow dimensions suitable for mechanical milling and hand assembly (see Acknowledgements). Fig. 2 shows the base spiral geometry with its simulated [11] input impedance (left ordinate) and VSWR (right ordinate). These values were found with a gap source located at the center of the spiral; its input impedance $Z_{in} \sim$ 150 Ω determined by K, and its width w corresponding to a stripline center conductor width w = 1.6 mm ($Z_0 \sim$150Ω). The 50 Ω (w = 9 mm) to 150 Ω (w = 1.6 mm) impedance transformer has a length L = 120 mm and provides an external excitation of the antenna. The grounds and center conductor were formed by solder-tacked copper tape and the fabricated antenna can be seen in Fig. 3 with the measured and simulated VSWR

(stripline feed and SMA probe feed). A probe feed (r = 0.615 mm) through the bottom layer, with two pins (r = 0.615 mm) connecting the upper and lower grounds (parallel to the probe feed) has been used in this design to excite the 50 Ω stripline, and creates several impedance discontinuities.

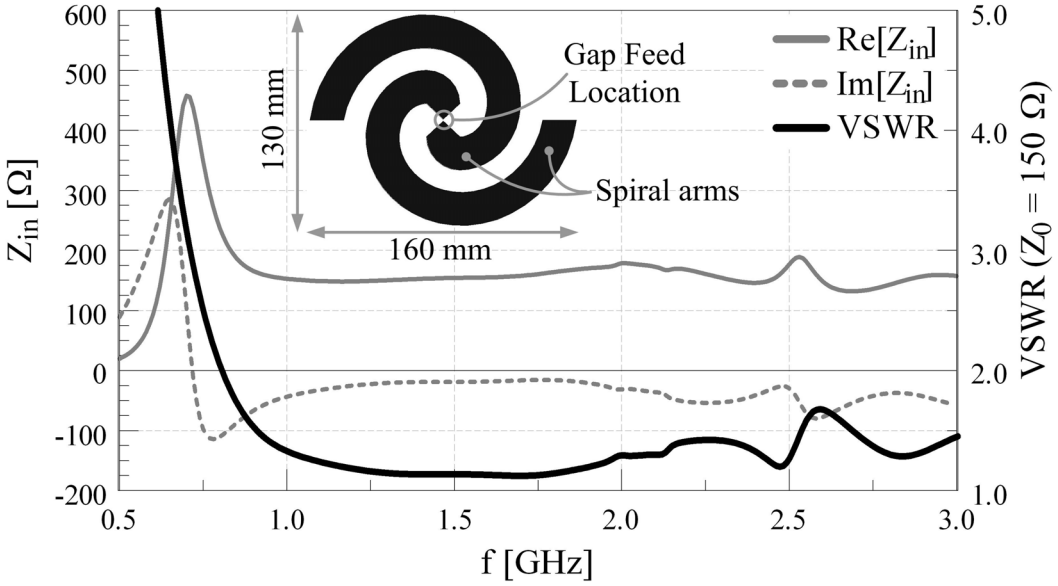

Fig. 2. Base spiral geometry (metal is hatched in solid black) with its simulated input impedance (left ordinate) and VSWR (right ordinate).

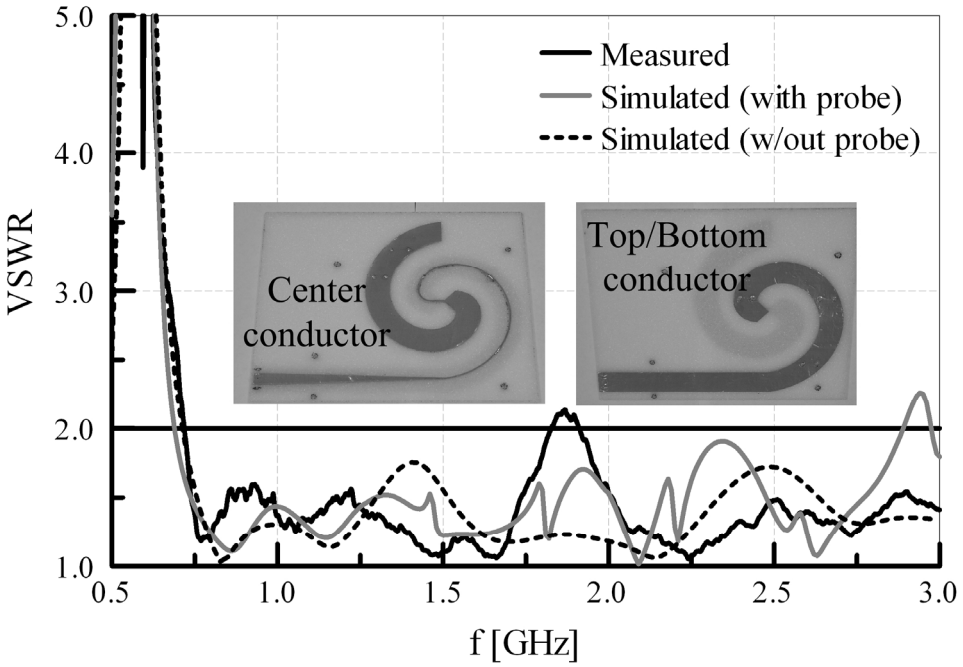

Fig. 3. Fabricated spiral antenna on Rochelle Foam with measured and simulated (stripline and SMA probe feed) VSWR for the fabricated.

5. Example 2: Internally-Fed Archimedean Spiral Aperchassis

The design in this section extends the aperchassis concept by examining the use of a non-unity dielectric substrate material, different spiral input impedance, a larger bandwidth, and a completely internalized feed network. This design has a slot-to-metal ratio of 1.25 (2.5 mm: 2 mm) and an input impedance of 160 Ω. It has been scaled up in frequency from UHF/VHF to S-band to eventually be compatible with mechanical milling constraints but the aperchassis concepts still apply. Fig. 4 shows the design of this structure, including the gap-fed, non-tapered stripline feed, and tapered stripline feed.

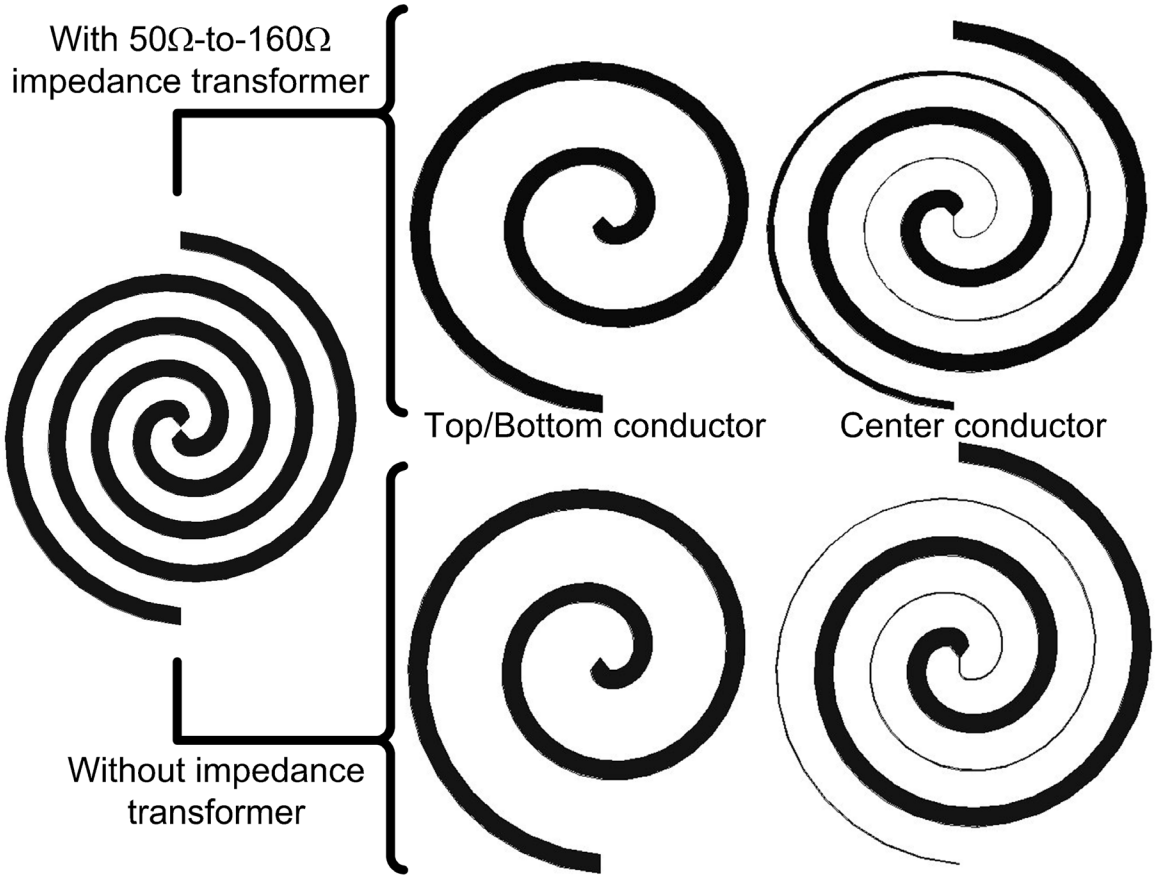

Fig. 4. Gap-fed spiral geometry (left) and stripline realization of the structure with a non-tapered and tapered feed section.

The tapered feed is 104 mm in length (approximately one turn) and remains conformal to the spiral. This section was synthesized using two additional spiral curves with growth rates that are adjusted to create a wider line-width at the input and intersect the non-tapered design. Duroid 5880 (ε_r = 2.2) substrates with a total height h = 1.16 mm (2×0.508 mm) were used to provide structural support. Fig. 5 shows the simulated VSWR for the three configurations of the spiral shown in Fig. 4 at the lower end of their bandwidth. The simulated gap-fed bandwidth spans 2.44 GHz (2.3 GHz using the 20.8 mm outer, resonant, osculating circular slot radius) to 12.67 GHz (11.93 GHz using the 4

mm inner, resonant, osculating circular slot radius taken at the end of the balun taper). Erratic impedance behavior develops with the larger electrical size of this structure and difficulties in obtaining a quality mesh for the longer, thinner stripline structure compared to the ½ turn externally-fed design.

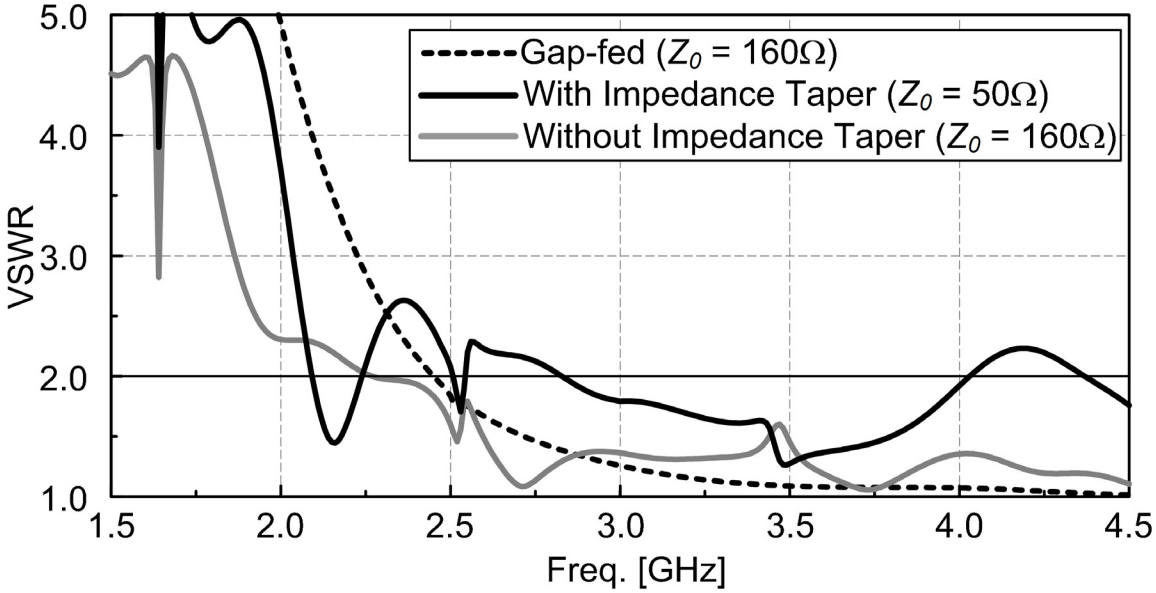

Fig. 5. Simulated VSWR of gap-fed spiral geometry and stripline realization of the structure with a non-tapered and tapered feed section from Fig. 4.

6. Radiation Behavior

The radiation behavior represents an equally important figure of merit given the diverse roles that UAVs and other potential platforms for the aperchassis. Given that circular polarization does not play a primary role in many of these circumstances (communicating with hand-held radios on the ground, beamforming in dynamic constellations, etc.), the ability to of the aperchassis to provide pattern coverage represents an important figure of merit. The mean effective gain (*MEG*) (1) [12] has been examined for this. The *MEG* takes into consideration the radiation behavior with both the distribution and polarization of incoming waves (2) (Gaussian distribution shown) and the time-average ratio (*XPR*) of their incident power (3).

$$MEG = \oiint_{\Omega}\left(\frac{XPR}{XPR+1}G_{\theta}(\Omega)P_{\theta}(\Omega)+\frac{1}{XPR+1}G_{\phi}(\Omega)P_{\phi}(\Omega)\right)d\Omega \quad (1)$$

$$P_{\theta,\phi}(\Omega)\rightarrow P_{\theta,\phi}(\theta)=A_{\theta,\phi}\exp\left[-\frac{(\theta-m_{\theta,\phi})^2}{2\sigma_{\theta,\phi}^2}\right] \quad (2)$$

$$XPR=\frac{\langle P_{\theta}(\Omega)\rangle}{\langle P_{\phi}(\Omega)\rangle}=1 \quad (3)$$

Results comparing the ideal (gap-fed) structure against the stripline based aperchassis across the matched impedance bandwidth have been omitted for brevity but they will be included in the presentation. However, Figs. 6-8 show the simulated, normalized radiation patterns (30 dB dynamic range) in the primary elevation planes at 4 GHz for the three antenna configurations. This illuminates the need for further investigation into the radiation behavior of the aperchassis. In the current configuration, the stripline configuration does not provide any shielding for the stripline from the radiating spiral mode and the asymmetry introduced by splitting the spiral mode between the two grounds has a pronounced effect on the radiation behavior.

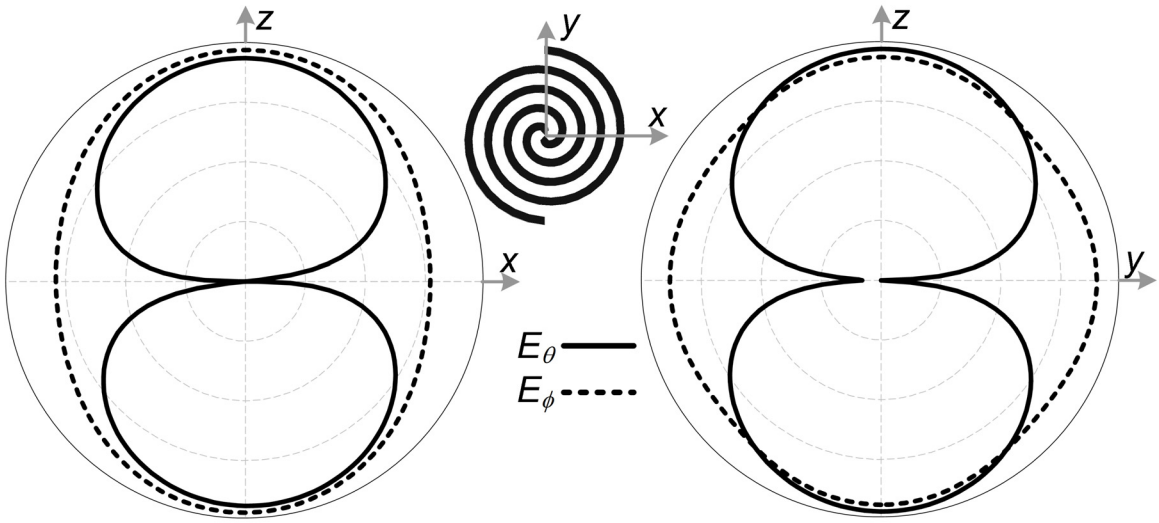

Fig. 6. Simulated radiation patterns at 4 GHz in the primary elevation cut-planes for the gap-fed spiral geometry in Fig. 4.

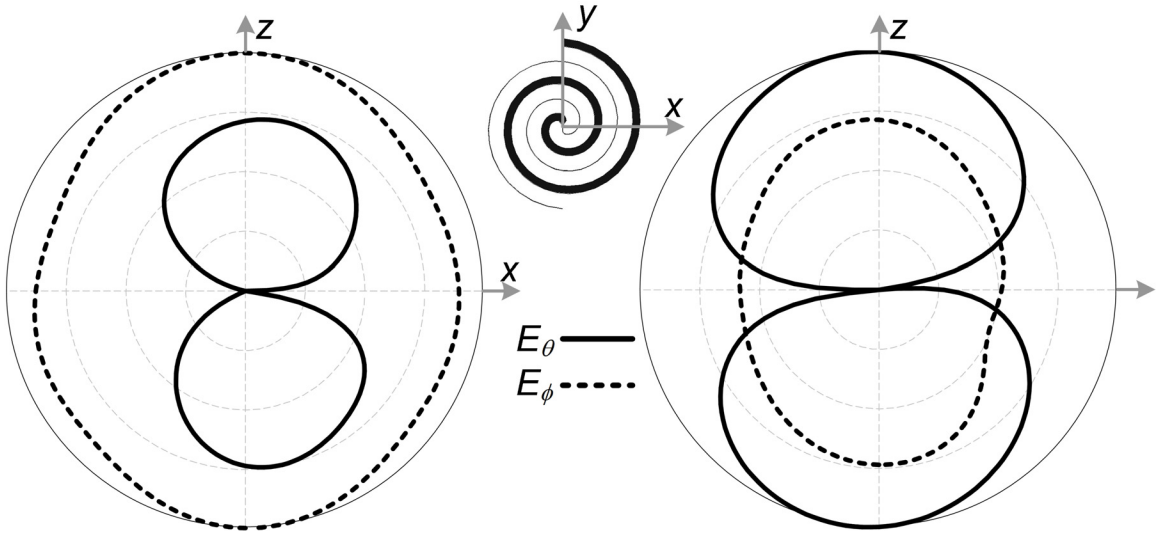

Fig. 7. Simulated radiation patterns at 4 GHz in the primary elevation cut-planes for the stripline realization of the structure with the non-tapered feed section from Fig. 4.

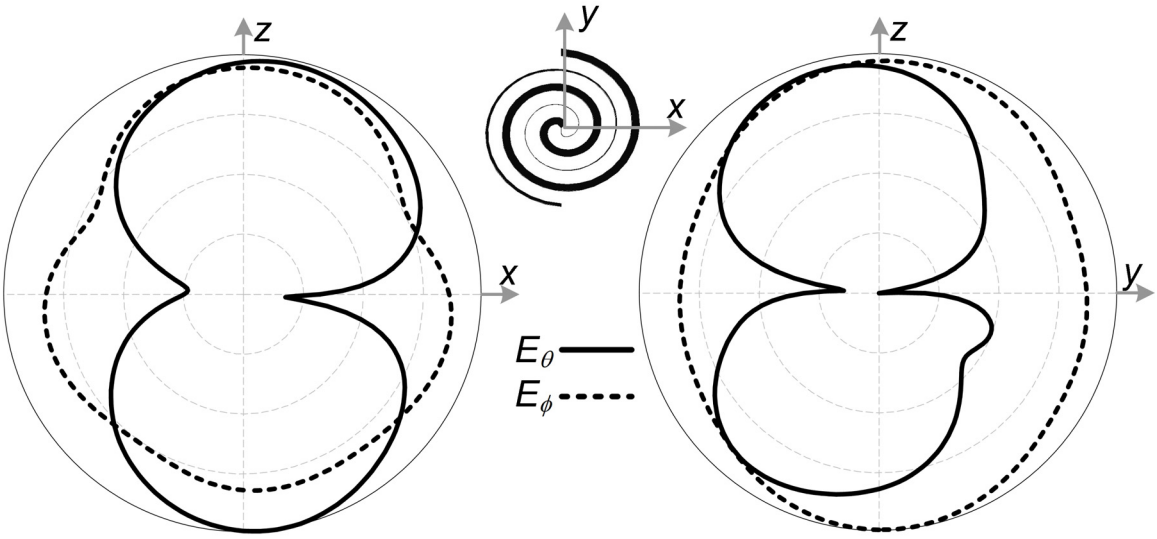

Fig. 8. Simulated radiation patterns at 4 GHz in the primary elevation cut-planes for the stripline realization of the structure with the tapered feed section from Fig. 4.

7. Conclusion

This work has provided the preliminary work in support of the aperchassis. This concept provides an internalized feed network and leaves surfaces and volumes to integrate subsystems to enable multifunctionality and thereby aid in the mitigation of size and/or weight constraints. Measured and simulated results in the first example demonstrated the basic design and operation of the structure. The second example showed the ability to provide a curvilinear, internally integrated impedance taper. Future and ongoing work will examine the structure in more detail and reduce the size of the impedance matching network and examine perturbation along the surface and volume of the structure. In addition to this, structurally functional materials are being investigated to facilitate load-bearing functionality. The effects of structural deformations are also under investigation.

8. Acknowledgements

The author gratefully thanks Tyrone L. Roach and the Electromagnetics Laboratory at the University of Illinois for the substrate materials and fabrication of the antenna.

9. Bibliography

[1] J. Dyson, "The equiangular spiral antenna," in *Proc. of Antenna Applications Symposium*, Monticello, IL, vol. ECM, October 1955, pp. 1-12.

[2] J. Dyson, "The equiangular spiral antenna," *IEEE Transactions on Antennas and Propagation*, vol. 7, pp. 181-187, April 1959.

[3] Kaiser, J.A., "The Archimedean two-wire spiral antenna," *IRE Transactions on Antennas and Propagation*, vol. 8, pp. 312-323, May 1960.

[4] P. E. Mayes, “Frequency-independent antennas and broad-band derivatives thereof,” Proceedings of the IEEE, vol. 80, pp. 103-112, January 1992.

[5] R. Bawer and J. Wolfe, “The spiral antenna,” *IRE International Convention Record*, vol. 8, March 1960, pp. 84 – 95.

[6] D. S. Filipovic, N. A. Stutzke, M. C. Buck, Q. Mu, N. W. Kefauver, “Unconventional spiral antennas and arrays,” *in Proc. of Antenna Applications Symp.*, Monticello, IL, September 2005, pp. 378 – 407.

[7] J. Thaysen, K. B. Jakobsen, J. Appel-Hansen, “Characterisation and optimisation of a coplanar waveguide fed logarithmic spiral antenna,” in Proc. of *IEEE-APS Conference on Antennas and Propagation for Wireless Communications*, November 2000, pp. 25 – 28.

[8] W.-H. Tu, M. Li and K. Chang, “Broadband Microstrip-Coplanar Stripline-Fed Circularly Polarized Spiral Antenna,” *IEEE Antennas and Propagation Society International Symposium*, July 2006, pp. 3669 – 3672.

[9] H. Nakano, K. Nakayama, K. Hirose, and J. Yamauchi, “A monofilar Archimedean spiral slot antenna fed by a triplate transmission line,” in Proc. of *IEEE Antennas and Propagation Society International Symposium*, June 1991, pp. 1106 – 1109.

[10] G. H. Huff and T. L. Roach, "Stripline-based spiral antennas with integrated feed structure, impedance transformer, and dyson-style balun," in *Antennas and Propagation International Symposium*, 2007 IEEE, 2007, pp. 2698-2701.

[11] Ansoft, HFSS© v10, Pittsburgh, PA 15219.

[12] T. Taga, "Analysis for mean effective gain of mobile antennas in land mobile radio environments," Vehicular Technology, IEEE Transactions on, vol. 39, pp. 117-131, 1990.

EVALUATION OF HUMAN BODY INTERACTION FOR THE ENHANCEMENT OF A BROADBAND BODY-BORNE RADIO GEOLOCATION SYSTEM

Arian Lalezari*[1,2], Farzin Lalezari[2], Bongsik Jeong[1], Dejan Filipović[1]

[1]Department of Electrical and Computer Engineering
University of Colorado at Boulder, UCB 425, Boulder, CO, USA 80309
[2]FIRST RF Corporation
4865 Sterling Dr., Boulder, CO, USA 80301

Abstract: The proliferation of RF devices in search-and-rescue and military applications has increased the demand for wideband body-borne RF geolocation systems. In this paper, a two-element antenna system is evaluated for application to broadband (100-750 MHz) body-borne radio geolocation. Full-wave simulations of the antenna system are used to generate free-space and body-borne data. These data are used to evaluate the impact of the human body on the amplitude and phase of the detected signal. Calibration techniques are established to characterize the impact of these effects. Raw detection values are evaluated and examined in order to exploit body interaction effects to improve the calibrated geolocation of an RF source. Simulations of the antenna system are validated with prototype measurements in free space. Relevant recommendations are made for future work.

1. Introduction

Technologies utilizing wireless links are simultaneously growing smaller, more prolific, and operating across larger portions of the radio frequency (RF) spectrum. To identify and locate these devices, there is a corresponding demand from commercial, consumer, and military users for direction finding and geolocation capabilities that match these trends in size, capability, and bandwidth. The main focus of this study is in the evaluation of radio direction finding (RDF) capabilities in a form-factor that is suitable for body-borne integration. There are two main objectives: 1) to unambiguously detect a wide variety of signals across a broad range of frequencies, and 2) to observe practical limitations for the size and weight of the RDF system to minimize impact on the user. These considerations influence the electrical size of the antenna system and limit the applicability of many conventional RDF techniques [1]. Next-generation RDF systems will require the versatility to use a suite of signal processing capabilities to maximize the accuracy of the direction finding solution [2,3], requiring efficient yet practical antennas and robust algorithms.

The focus of this study is on vertically-polarized signals, and the domain for the evaluation of the direction finding sensitivity is in the azimuthal plane ($\theta = 90°$). Vertical dipole elements are used as the baseline radiator, due to their polarization and good azimuth-plane gain coverage. Although it is commonly accepted that three antennas are required to unambiguously determine the angle and range of arrival of an RF signal from a fixed platform [4,5], a two-antenna system is explored in conjunction with the human body to examine methods of overcoming the inherent ambiguities of a two-antenna system. These ambiguities arise from the system geometry (illustrated in Figure 1), which collocates the antenna feeds in a common plane.

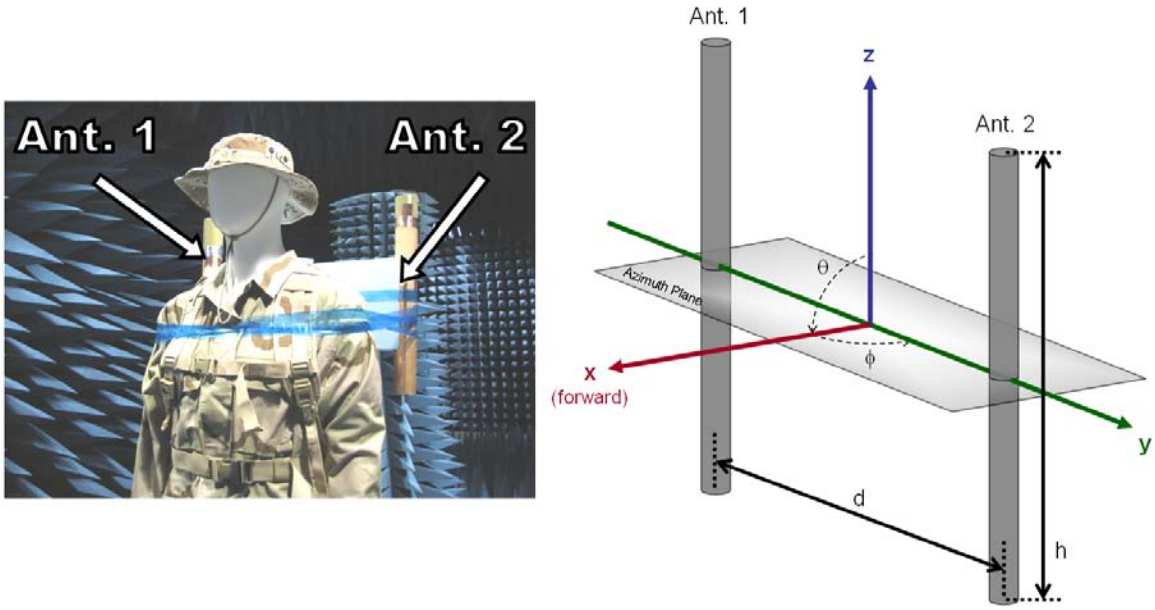

Figure 1: Illustration of system geometry, coordinate system, and body phantom used in the measurements.

Because the system has no aperture in the direction orthogonal to the plane containing the antennas (the y-z plane), there is an inherent ambiguity for incident signals from angles mirrored about this plane. That is, a signal from some angle, ϕ, will excite the two antennas in a manner that is identical to a signal from the angle $\phi' = 180°-\phi$, making it impossible to differentiate between the two signals without modifying the system, traditionally done by adding one or more additional antennas. The goal of this paper is to determine whether the introduction of a human subject will sufficiently perturb the system to reduce or resolve this ambiguity.

Several techniques exist for evaluating the performance of direction finding systems [6-8], including broadband self-calibration techniques [9,10]. Because the two primary metrics in this study are the accuracy of the direction finding solution and the errors caused by ambiguities in the system, an auto-correlating direction finding function (DFF) is adapted from the literature [11]. Specifically, the phase and amplitude of the currents excited at the ports of the antennas are characterized when illuminated by incident waves from all directions in azimuth. These data are characterized either independently or in

concert as functions of the angle of the incident wave, in order to identify accuracy and false detection rates, which are the two metrics used to evaluate the system performance.

The problem is evaluated using a conjunction of computer modeling and physical measurements to add confidence to the results. For computer simulations, a method of moments (MoM) code, FEKO [12], is selected. This tool is well-suited for this study due to the open domain nature of the problem and inherent surface equivalence principle (SEP) formulation for efficient modeling of dielectric media like the human body. More information about the modeling approach is provided in section 2. Using the results of these simulations, the amplitude and phase response of the antennas are utilized to estimate the angle of arrival of an impinging signal. The performance of the baseline geometry is presented in section 3. Finally, the results of these studies are summarized in section 4, and recommendations for future work are provided.

2. Modeling Set-up and Discussion

2.1. Validation

Because geolocation is a completely passive ("receive-only") function, the data that are collected in both computer simulation and physical measurements record the response of the antenna with an incident wave. In physical measurements, this is done by exciting a source and measuring the antenna response in an anechoic environment. In FEKO, the antennas are terminated with a resistive load, and the currents at these are recorded. In both cases, the incident-wave excitation is swept across the frequency range of interest.

In order to explore the challenges of a body-borne antenna system, limitations on antenna size are selected which enable realistic integration. Specifically, an antenna height of h = 16 inches (40.6 cm), antenna diameter of two inches (5.1 cm), and center-to-center antenna baseline of d = 20 inches (50.8 cm) are chosen. This configuration enables a backpack-mounted configuration like the one shown in Figure 1.

Additionally, a frequency band is selected to encompass not only a large selection of common RF devices, but also to cover a wide range of electrical sizes for the antenna and element-to-element baseline. The 100-750 MHz range covers sources such as television stations, radio navigation bands, and a variety of other fixed and mobile radio bands. However, due to size limitations in the anechoic chamber, only the 300-750 MHz band is measured. In this band, the antenna height ranges from approximately 0.4 wavelengths to approximately one wavelength, and the antenna baseline ranges from approximately 0.5 wavelengths to nearly 1.3 wavelengths.

For the direction finding system, the most important data are the phase and amplitude response of the antennas in the azimuth plane ($\theta = 90°$). Using a broadband log-periodic (LP) source antenna, measurements of the free-space performance of a prototype antenna are taken across the band of interest. A FEKO model is generated with the same antenna element, and simulated across the same band of interest. Shown in Figure 2 and Figure 3

are the data from the measured and computer simulation tests in free space at three frequencies spanning the band of interest.

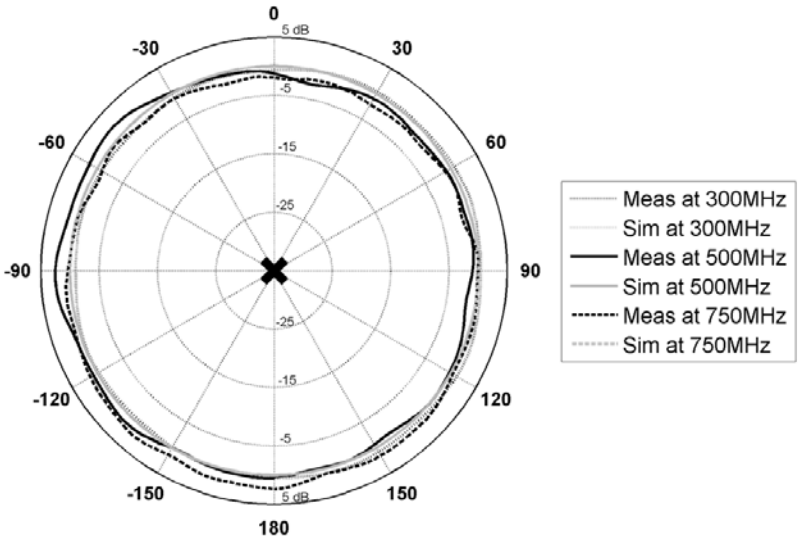

Figure 2: Measured (dark) and simulated (light) data of the amplitude response of the antenna element (black x) in free space.

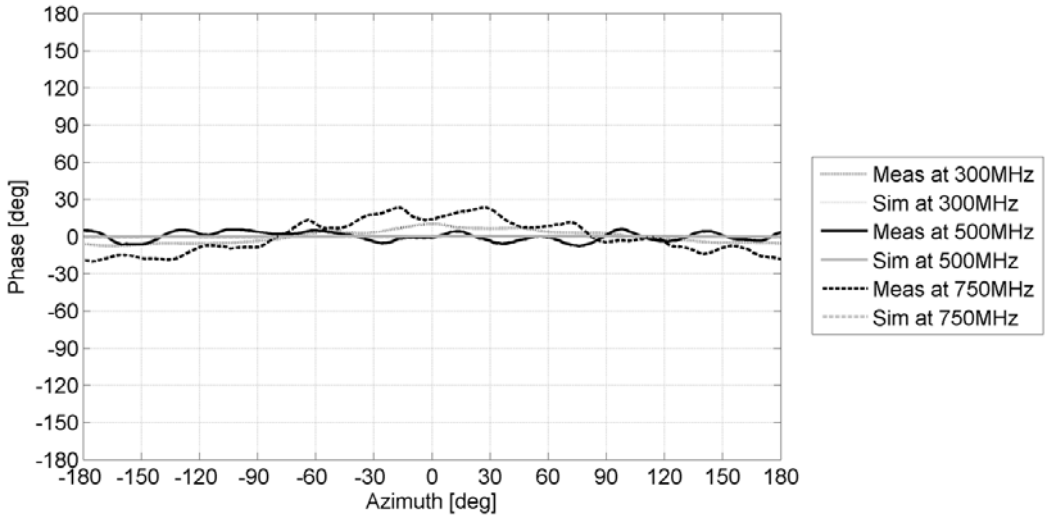

Figure 3: Measured (dark) and simulated (light) data of the phase response of the antenna element in free space.

Next, the two-element configuration is characterized (in free space) in measurement and simulation. For these tests, the center of rotation is the point directly between the antennas, such that the antennas are located at ±90° in azimuth, as illustrated in Figure 1. Again, the antennas are characterized in free space, with no obstructions other than the other antenna, which is terminated in a broadband resistive load. Received amplitude and phase data are gathered for both antennas, and measurements of the antenna located at +90° azimuth are presented in Figure 4 and Figure 5. Because the antenna is separated by d/2 from the center of rotation, its received phase varies like (d/2 sinϕ), where ϕ is the

azimuth angle. At the high end of the band, the magnitude of this variation is approximately 240°, so the phase has been "unwrapped", so that it may extend beyond ±180°.

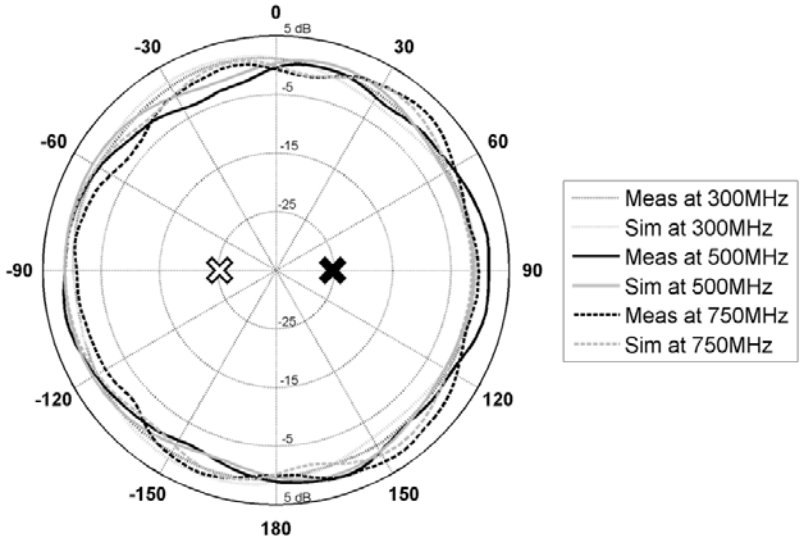

Figure 4: Measured (dark) and simulated (light) data of the amplitude response of one antenna (black x) of the two-element system in free space show.

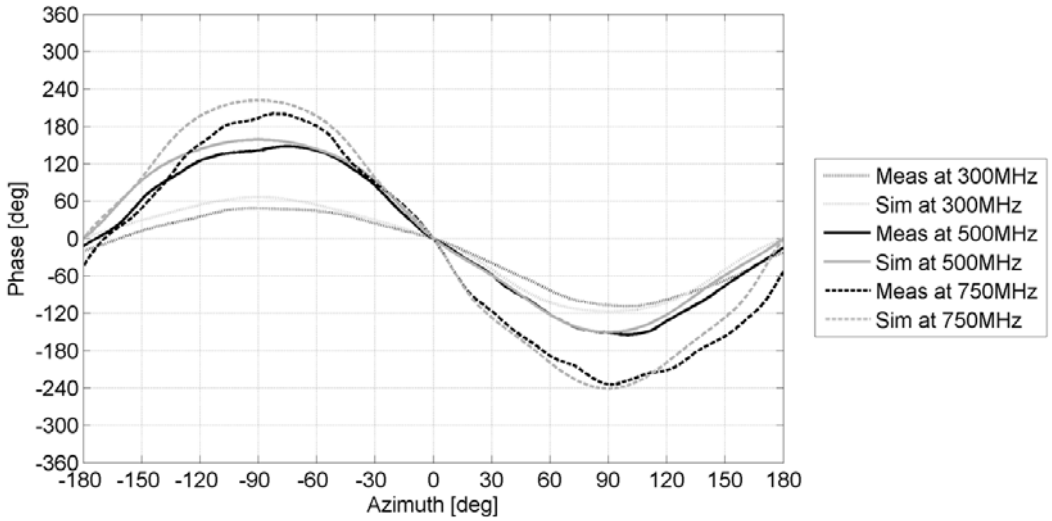

Figure 5: Measured (dark) and simulated (light) data of the phase response of one antenna of the two-element system in free space. The phase data have been normalized to the same value at $\phi = 0°$.

2.2. Modified Geometry

To improve computational efficiency, subsequent evaluations use a simpler system geometry. Instead of "thick" dipoles, wire dipoles are adopted. While there is some impact on bandwidth and efficiency, these antennas provide equivalent information about

the impact of the human body on direction finding performance, while allowing simpler computational evaluations. The dipoles are also modified to 20” (50.8 cm) in total length. This change compensates somewhat for the loss of low-end efficiency that is incurred by using wire dipoles.

There is a variety of data available on the electrical properties of the human body [13-15], and while these properties vary in different parts of the body and at different frequencies, a dielectric model is selected that is consistent with the available data at approximately 300 MHz, which is approximately the geometric mean frequency of the band of interest. A dielectric constant of $\varepsilon_r = 60$ and an electrical conductivity of $\sigma = 0.9$ S/m are chosen. To evaluate the impact of a human body, a simple cylindrical geometry is selected. The cylinder has an 18 inch (45.7 cm) diameter and is 6 feet (1.83 m) tall, as illustrated in Figure 6. To represent a realistic body integration scheme, the center of the cylinder is offset by 10” (25.4 cm) in the positive x-axis (forward) direction.

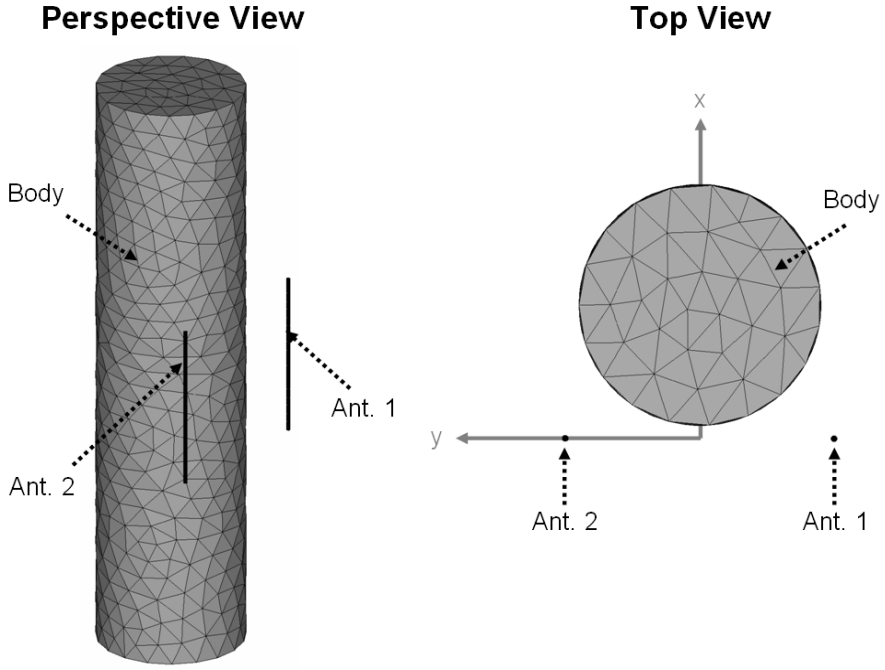

Figure 6: The human body model geometry from two perspectives, showing the relative size and orientation of the body and antennas in the baseline configuration.

3. System Performance

To understand the performance of the system, it is important to characterize it both in free space and in the presence of the human body.

3.1. Free-Space Performance

Prior to characterizing the effects of the human body on the system performance, it is important to understand the performance of the antenna system in free space. Here, the two dipoles are placed in free space, and subject to a series of plane wave excitations

every 5°, starting at ϕ = -180°, and ending at ϕ = 180°. In general, the raw values of the phase and amplitude of the received signal are functions of the electrical distance to the transmitter and are governed by Friis transmission formula. Of more importance are two relative values: the difference in phase between the two ports, and the ratio of the received amplitudes. These values are plotted versus incidence angle in Figure 7.

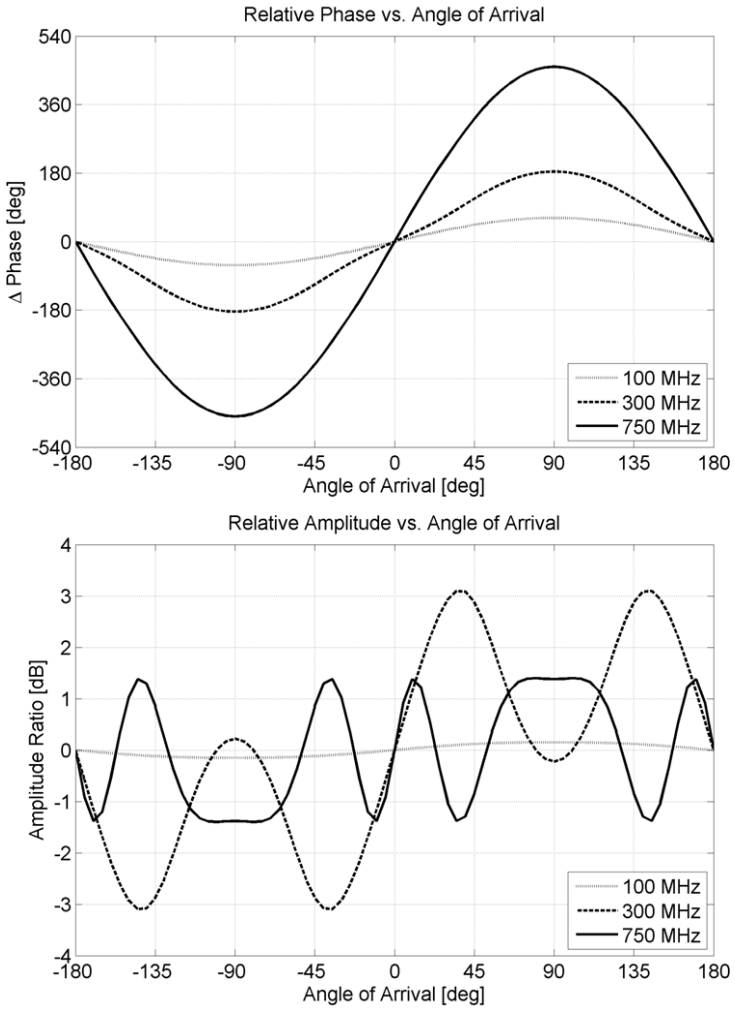

Figure 7: The relative phase (top) and amplitude (bottom) data are plotted versus the incidence angle of an incoming plane wave at three different frequencies.

From these plots, the inherent "hemispherical" ambiguity of the two-antenna system is evident. Specifically, the data inside [-90°, 90°] is mirrored about the ±90° coordinates, and is identically replicated in [-180°, -90°] and [90°, 180°]. Because the data traces are not one-to-one, a particular phase delta or amplitude ratio does not necessarily correspond to only one incoming signal. For example, if a 300 MHz signal has a relative phase of approximately 90° and relative amplitude of 3dB, then it is impossible to distinguish whether the signal is incident from ϕ = 40° or ϕ' = 180°-40° = 140°.

In order to better visualize this ambiguity, these signals are auto-correlated using a simple correlation function that produces a correlation error (called a direction finding function, or DFF). The auto-correlation function uses some signal response as its input, and identifies parts of the signal that match one another. This input is called a discriminator function, and is denoted as a function, S(ϕ). This function can be created using measured data for either the phase or amplitude response of the antenna system as a function of azimuth angle. By using this input, the auto-correlation function can associate the antenna response to the angle(s) of incidence which produce a particular excitation.

For example, for a signal incident from known angle ϕ_0, the auto-correlation is:

$$DFF_{\phi_0}(\phi) = S(\phi_0) - S(\phi). \quad (1)$$

The output of the auto-correlation function is identically equal to 0 when $\phi = \phi_0$, indicating a proper identification of a signal. However, it is possible that other angles may also minimize the DFF, producing false alarms. The output of this direction finding function is shown for three different incidence angles in Figure 8 and Figure 9, using phase and amplitude information, respectively, as the discriminator, S.

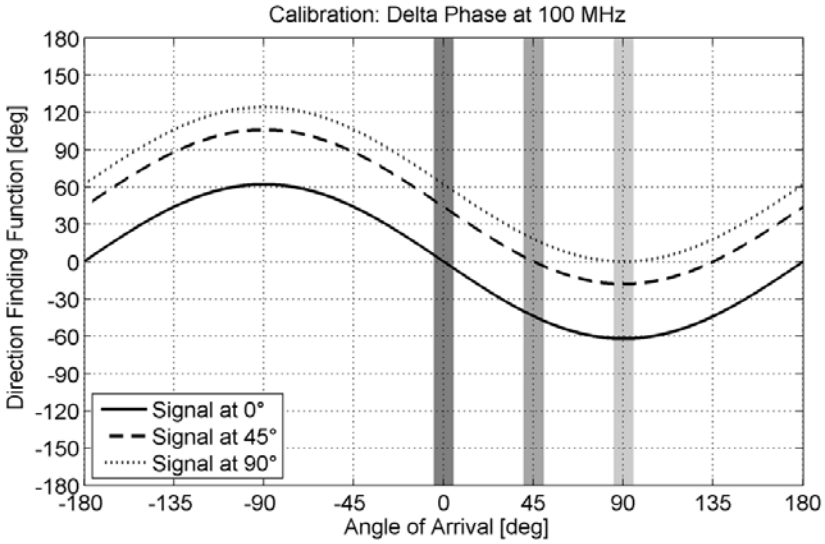

Figure 8: The direction finding function is evaluated using the relative phase data for incoming signals at 100 MHz from 0°, 45°, and 90°.

Note that the three bands highlight the areas where the three signals should have zero error (DFF = 0). Indeed, the dark band highlights the proper angle for the solid line (0°), the medium band highlights the dashed line (45°), and the light band highlights the dotted line (90°). However, ambiguities are also seen for the signals at 0° and 45°. The solid line (0°) has a zero crossing at $\phi_0 = 0°$, but another at $\phi_0' = \pm 180°$. Likewise, the dashed line (45°) has a zero crossing at $\phi_0 = 45°$, but another at $\phi_0' = 135°$. It is also worth noting that the data for the dotted line has only one zero crossing, at $\phi_0 = 90°$. This is because its "mirrored" angle has the same value: $\phi_0' = \phi_0 = 90°$. The ambiguity is graphically illustrated in Figure 10.

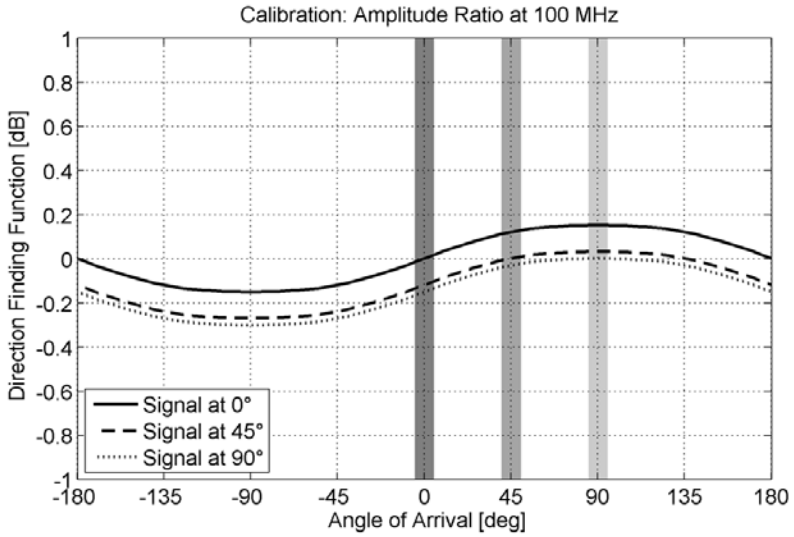

Figure 9: The direction finding function is evaluated using the relative amplitude data for incoming signals at 100 MHz from 0°, 45°, and 90°.

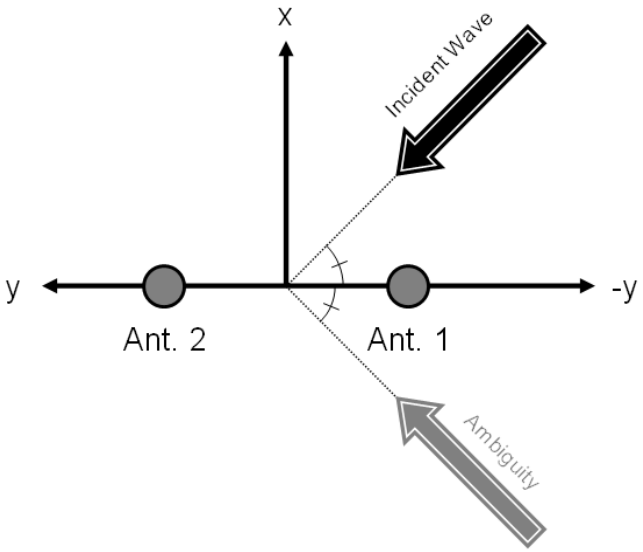

Figure 10: An incoming wave that approaches the antenna system (black arrow) at some angle away from the y-z plane (horizontal axis) is indistinguishable from a wave that is mirrored about this plane (gray arrow).

It is useful to compile the direction finding function for all angles into a single plot to produce a more complete sense of the spatially-dependent performance of the system. An example of this type of visualization is provided for both the phase and amplitude responses of the system in free space at 100 MHz in Figure 11 and 12, respectively.

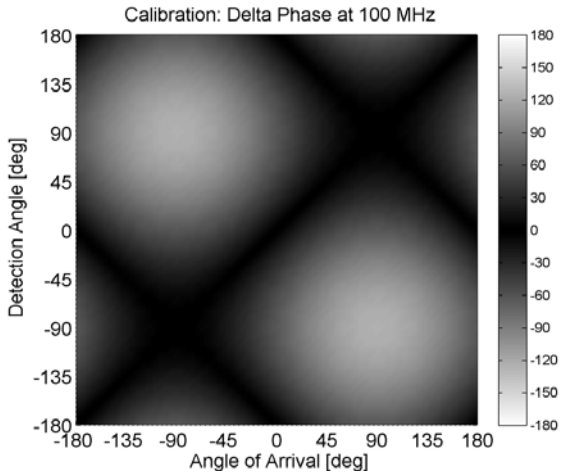

Figure 11: The free space direction finding function (DFF) is plotted for all possible angles of arrival (x-axis) and detection angles (y-axis), using the response at 100 MHz. Dark areas indicate areas of low correlation error, corresponding to solutions for the direction finding algorithms.

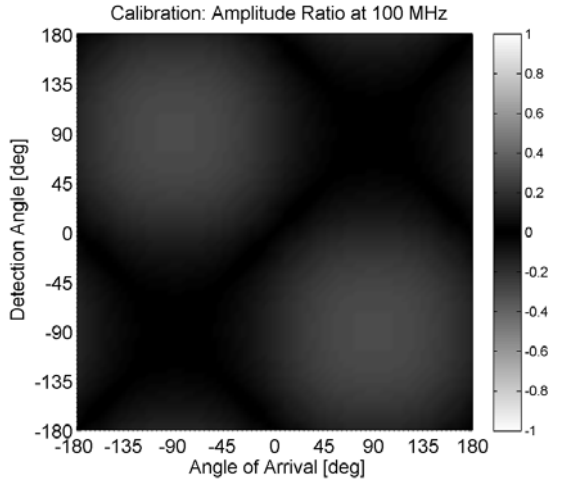

Figure 12: The free space direction finding function (DFF) is plotted for all possible angles of arrival (x-axis) and detection angles (y-axis), using the amplitude response at 100 MHz.

In these plots, it is possible to visualize both the detection accuracy and the incidence of false alarms. The main dark band from the lower left to the upper right corners of each plot is the band of proper detections. That is, these data correspond to an incoming wave with some angle of arrival ϕ_0 being detected at some detection angle ϕ_d that is at – or very near – the correct location in space. One can see that the accuracy of the system (characterized by the width of this band) is relatively small for ϕ_0 near 0° and ±180°, but somewhat larger for ϕ_0 near ±90°. Conversely, there are multiple regions of good correlation for ϕ_0 near 0° and ±180°, indicating false detections. Specifically, signals arriving from $\phi_0 \approx 0°$ have the same response – and therefore low DFF values – near ±180°. As previously noted, data near ±90° are unambiguously detectable.

In order to quantify these parameters, two statistics are generated. The first statistic describes the accuracy of the system, and is generated by determining the range of angles around a "proper" detection that falls below some "detection threshold". For direction finding schemes, this accuracy represents the uncertainty in the angle of a detected signal, so smaller values of this parameter are more favorable. The second statistic describes the false alarm rate, and is defined as the percentage of the signal that is not contained in the main detection, but which falls below the same detection threshold. This is explained in Figure 13 by looking back at the direction finding function for the free-space system at 100 MHz, using phase information as the discriminator function, S.

For this analysis, a detection threshold of ±10° is used. That is, signals whose expected relative phase lies within 10° of the relative phase of the arriving signal will be identified as "detections".

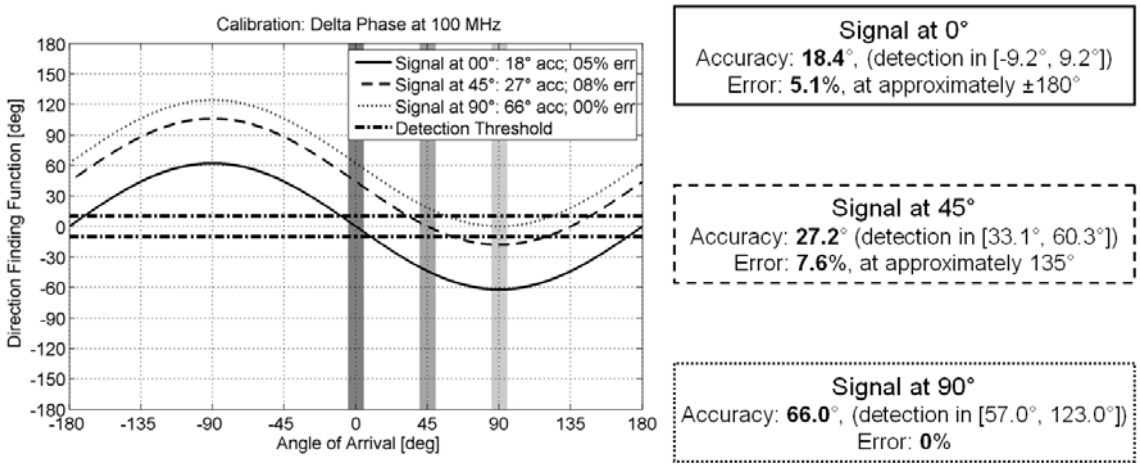

Figure 13: The direction finding function is evaluated using the relative phase data for incoming signals at 100 MHz from 0°, 45°, and 90°. Using a detection threshold of ±10°, the accuracy and error rate statistics are generated for each signal.

Averaged over all azimuth angles, the mean statistics for the free-space case are summarized in Table 1. For these tables, a detection threshold of ±10° is used for the phase data, and ±2dB is used for the amplitude data.

Table 1: The accuracy and error percentage statistics are shown for the free-space direction finding functions using both phase and amplitude.

Mean Detection Accuracy [deg]

Technique	Frequency [MHz]		
	100	300	750
Phase	**42.2**	**14.4**	**7.3**
Amplitude	**180.0**	**85.8**	**93.4**

Mean Error Percentage [%]

Technique	Frequency [MHz]		
	100	300	750
Phase	**4.2**	**4.3**	**2.8**
Amplitude	**N/A**	**26.2**	**49.1**

Note that at 100 MHz, the system is incapable of using only amplitude to determine the angle of arrival, due to the lack of sufficiently different responses from the antenna system as a function of azimuth angle. That is, the relative amplitude never changes by more than the detection threshold of 2dB, making an amplitude-only detection scheme impossible to use at these frequencies. It is important to note, however, that the phase-

only detection produces moderate results at this frequency, indicating that it may be favorable to use the two metrics in tandem to identify a signal. This is explored in more detail in section 3.2. To characterize the impact of the human body on the system, free-space statistics are compared to their equivalent cases in the presence of the human body.

3.2. Human Body Effects on Signal

Using the baseline system geometry and human body model described in section 2.1, the antenna response is re-characterized. The direction finding functions at 100 MHz are presented for three sample signals in Figure 14 and 15. The detection thresholds are set at ±10° for phase, and ±2dB for amplitude.

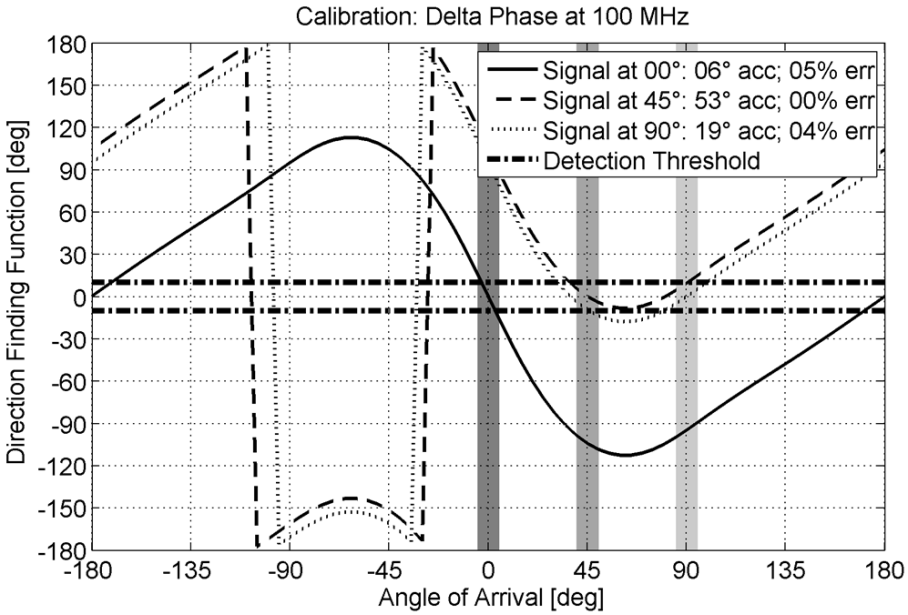

Figure 14: The direction finding function is evaluated using the relative phase data for incoming signals at 100 MHz from 0°, 45°, and 90° in the baseline human body model configuration.

The effects of the human body are immediately evident in both the phase and amplitude responses, as compared to the free-space data previously presented in Figure 8. Of particular interest is the perturbance of the location of the ambiguities. While there is no change in the location of the ambiguities for the signal at 0°, the other two signals exhibit a change in the location of their false detections. For example, the signal at 45° now has a false return at approximately 80° in the phase response, and approximately 120° for the amplitude response, instead of the expected ambiguity at the mirrored angle, $\phi_0' = 135°$. Interestingly, the signal at 90° was unambiguous in free space, but adopts an ambiguity in the phase DFF at approximately 35°.

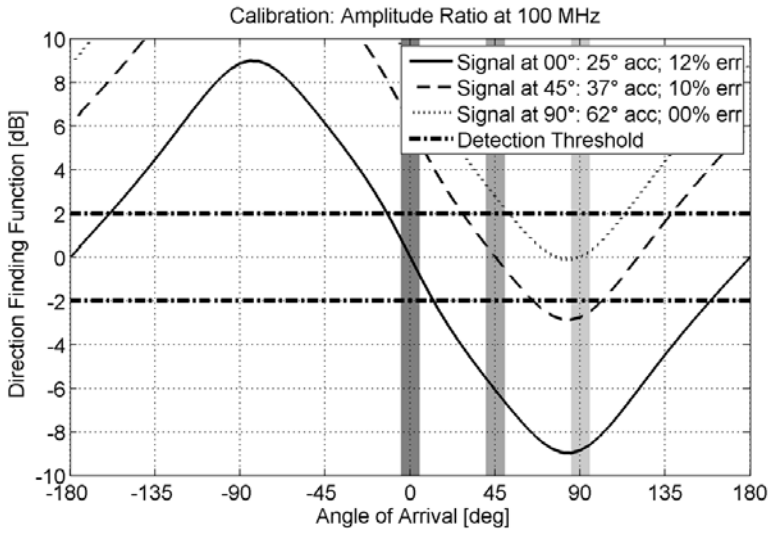

Figure 15: The direction finding function is evaluated using the relative amplitude data for incoming signals at 100 MHz from 0°, 45°, and 90° in the baseline human body model configuration.

Using these data, the same statistics characterizing accuracy and error rate are provided for the body-borne system in Table 2.

Table 2: The accuracy and error percentage statistics are shown for the body-borne direction finding functions using both phase and amplitude.

Mean Detection Accuracy [deg]

Technique	Frequency [MHz]		
	100	300	750
Phase	**22.6**	**9.7**	**5.5**
Amplitude	**48.2**	**32.0**	**37.9**

Mean Error Percentage [%]

Technique	Frequency [MHz]		
	100	300	750
Phase	**2.5**	**3.6**	**2.5**
Amplitude	**6.4**	**3.8**	**2.6**

In order to characterize the impact of the human body, the percent improvement in each parameter is tabulated in Table 3.

Table 3: The percent improvement of accuracy and error percentage between the body-borne geometry and the free-space geometry direction finding functions (DFFs) using both phase and amplitude are tabulated.

Delta Detection Accuracy [%]

Technique	Frequency [MHz]		
	100	300	750
Phase	**46.4**	**32.6**	**24.7**
Amplitude	**73.2**	**62.7**	**59.4**

Delta Error Percentage [%]

Technique	Frequency [MHz]		
	100	300	750
Phase	**40.5**	**16.3**	**10.7**
Amplitude	**93.6**	**85.5**	**94.7**

It is important to note that there is an improvement in every metric at all frequencies. The presence of the body shows a moderate improvement in the accuracy and error percentage of the direction finding function using phase information, ranging from about 10-45% improvement. However, the most significant improvements are experienced with the discrimination capability of the amplitude information, which improves accuracy by approximately 60-75%, and reduces false alarm percentages by at least 85% for all frequencies.As with the free space data, it is useful to visualize the complete spatial

response of the system in the presence of the body as well. These data are presented in Figure 16 and Figure 17, with the detection thresholds (±10° for phase, ±2dB for amplitude) highlighted by the broken white lines.

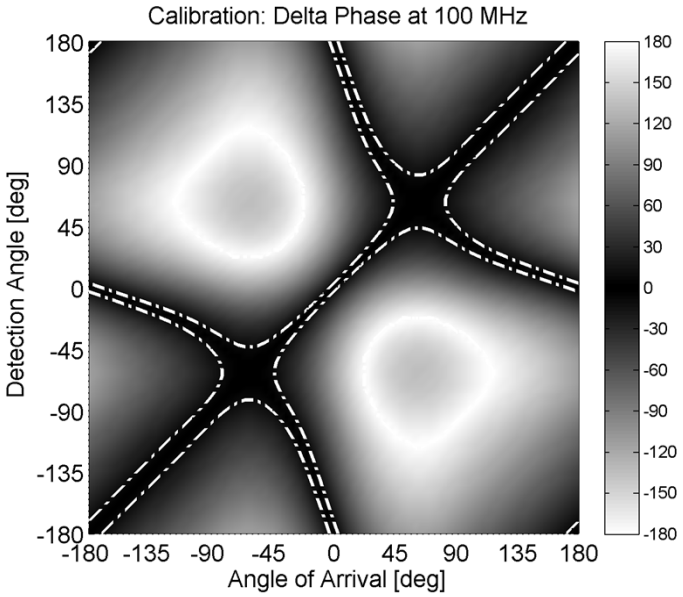

Figure 16: The direction finding function (DFF) is plotted for all possible angles of arrival (x-axis) and detection angles (y-axis), using the phase response of the baseline body geometry configuration at 100 MHz. Dark areas indicate areas of low correlation error, corresponding to solutions for the direction finding algorithms. The detection thresholds are highlighted by the broken white lines.

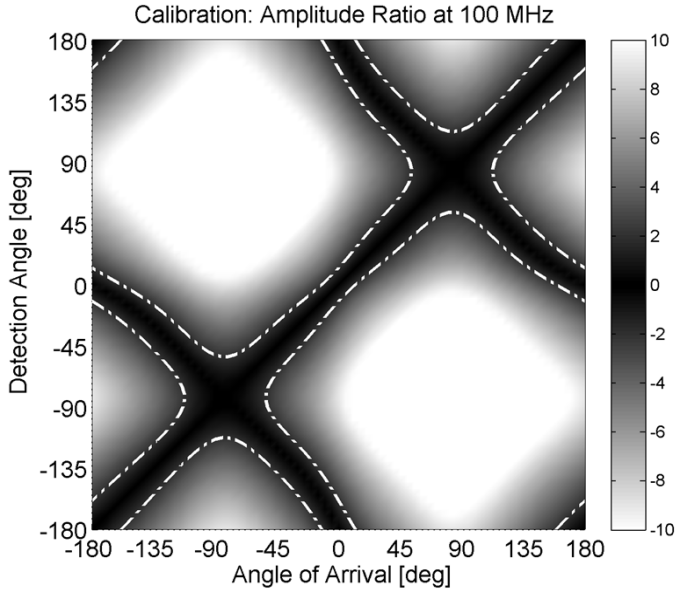

Figure 17: The direction finding function (DFF) is plotted for all possible angles of arrival (x-axis) and detection angles (y-axis), using the amplitude response of the baseline body geometry configuration at 100 MHz.

From these data, it is evident that the structured ambiguity characteristics that are present in free space have been altered by the presence of the human body. Most importantly, however, by observing the shapes of the dark regions inside the broken white lines, it is evident that the phase and amplitude responses of the system change in somewhat different ways. This final note is of special interest, because it indicates that the phase and amplitude information can be used in concert to achieve an even further improved detection capability. Specifically, by using the intersection of the detection regions in the phase DFF and the amplitude DFF together as a combined detection metric, it is possible to achieve significant improvements in performance. These are reflected in the values of the accuracy and error rate statistics for the "combined" approach, shown in **Error! Not a valid bookmark self-reference.**.

Table 4: The accuracy and error percentage statistics are shown for the body-borne direction finding functions using phase alone, amplitude alone, and using a combined detection.

Mean Detection Accuracy [deg]

Technique	Frequency [MHz]		
	100	300	750
Phase	**22.6**	**9.7**	**5.5**
Amplitude	**48.2**	**32.0**	**37.9**
Combined	**16.7**	**8.0**	**5.5**

Mean Error Percentage [%]

Technique	Frequency [MHz]		
	100	300	750
Phase	**2.5**	**3.6**	**2.5**
Amplitude	**6.4**	**3.8**	**2.6**
Combined	**1.4**	**0.5**	**0.3**

These results clearly show that if one considers only detections which simultaneously satisfy the phase and amplitude criteria, there is a significant improvement in accuracy and false alarm rates. That is, the interaction of an incoming signal with the body changes the received phase and amplitude of the signal in such a way that the sensitivity of the system's angle of arrival prediction is improved and its susceptibility to false alarms is reduced. These improvements are quantified as percent improvements over the mean performance of a phase-only or amplitude-only system in Table 5.

Because the body perturbs the system's ambiguities in different ways for phase and amplitude, it is possible to use the information from these two returns independently to resolve many of them, resulting in improved accuracy of at least 52% and reduced error rates of at least 68% across the band of interest.

Table 5: The percent improvement of accuracy and error percentage between the combined DFF detection compared to the mean performance of the phase-only and amplitude-only DFF detections are tabulated.

Delta Detection Accuracy [%]

Technique	Frequency [MHz]		
	100	300	750
Combined	**52.8**	**61.6**	**74.7**

Delta Error Percentage [%]

Technique	Frequency [MHz]		
	100	300	750
Combined	**68.5**	**86.5**	**88.2**

It is useful to visualize the spatial response of the combined metric in a similar fashion to the individual DFF responses, as shown in the combined metric at 100 MHz in Figure 18.

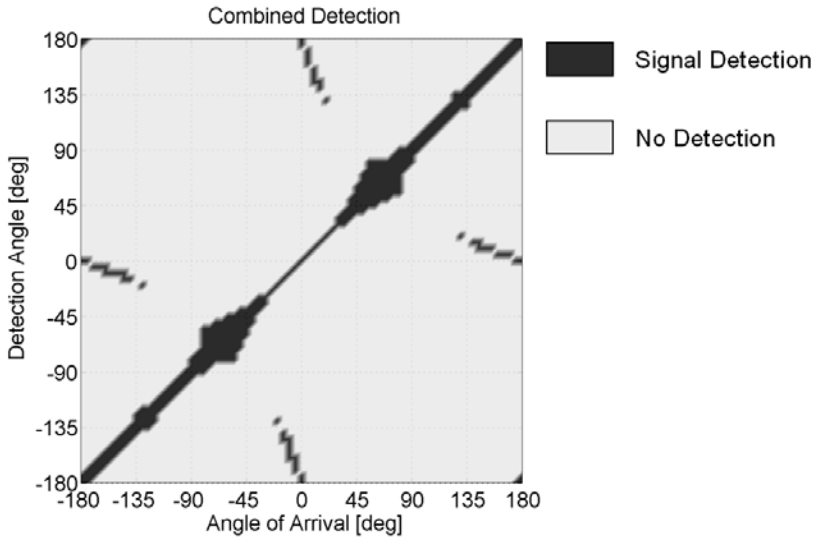

Figure 18: By combining the detection regions for the phase DFF and the amplitude DFF at 100 MHz, a combined DFF is obtained with improved accuracy and reduced false alarm rates.

As with previous DFF plots, the detection region is shown in the dark color, and the rejection region is shown in the light color. As previously discussed, the correct rejection band is the main band from the lower left to the upper right corner of the plot. Only four regions of ambiguities appear at this frequency, shown as the four dark regions away from the main detection region. Similar results are seen at 300 and 750 MHz:

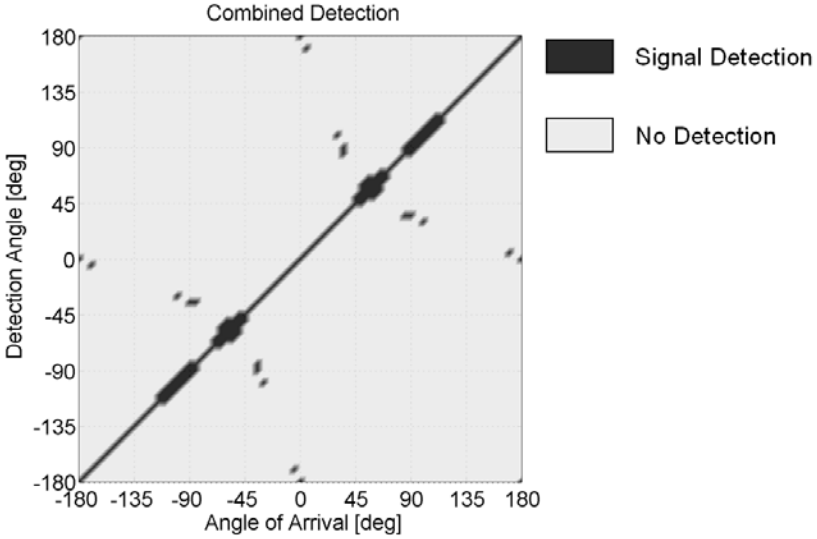

Figure 19: By combining the detection regions for the phase DFF and the amplitude DFF at 300 MHz, a combined DFF is obtained with improved accuracy and reduced false alarm rates.

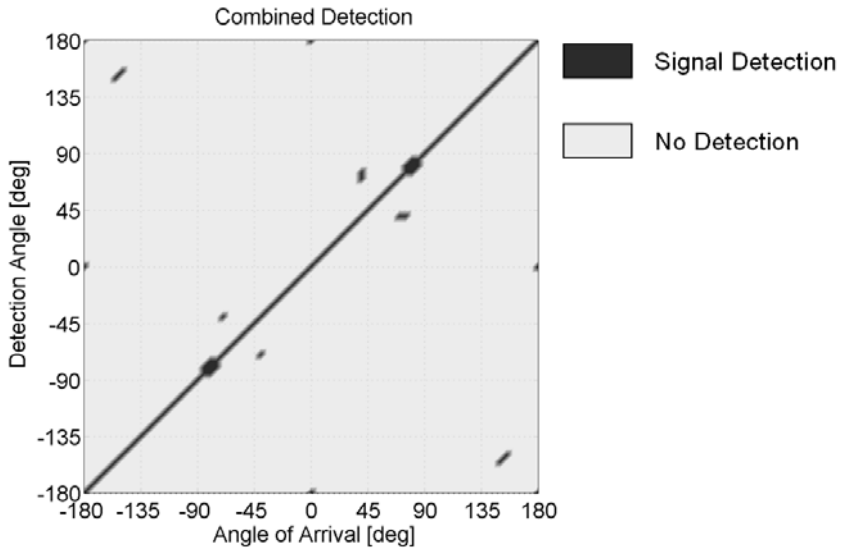

Figure 20: By combining the detection regions for the phase DFF and the amplitude DFF at 750 MHz, a combined DFF is obtained with improved accuracy and reduced false alarm rates.

4. Summary

In this paper, we describe a study which demonstrates that the effects of human body interaction can be favorably exploited to significantly improve the accuracy and reduce the false alarm of a two-antenna direction finding system. The amplitude and phase of a signal received by the system in the proximity of the body is perturbed sufficiently to exhibit an improvement of at least 52% in accuracy, and a reduction of at least 68% in false alarm rates across the band of interest. While this study did not generate a case that completely eliminates the ambiguities, it is anticipated that additional modifications to the geometry can be imposed to yield further improvements. It is noted that the current model has perfect symmetry about the x-z plane, and identical separation between both antennas and the body. It is anticipated that real-world perturbations of these parameters might further improve the performance of the system.

To exploit these effects, however, it is important to understand the sensitivity of various system parameters. The future studies will investigate the sensitivity of: the antenna-body spacing, the shape and size of the body phantom, the electrical properties of body phantom, the antenna size and baseline separation, and the antenna termination impedance.

5. References

[1] H. H. Jenkins, Small-Aperture Radio Direction-Finding, Boston, Artech House Publishers, 1991.

[2] D.W. Watson and H.E. Wright, Radio Direction Finding, New York, Van Nostrand-Reinhold, 1971.

[3] P.J.D. Gething, Radio Direction Finding and Superresolution, London, Peregrinus, 1991.

[4] R.C. Johnson, Antenna Engineering Handbook, Third Edition, United States, McGraw-Hill, 1992.

[5] Hall, David L., James Llinas, and Steven Strauss. Handbook of Multisensor Data Fusion. New York: C R C P LLC, 2001.

[6] Gething, P. J. Radio Direction Finding. Washington, D.C.: Institution of Engineering and Technology (IET), 1991.

[7] Chandran, Sathish, ed. Advances in Direction-of-Arrival Estimation. New York: Artech House, Incorporated, 2006.

[8] Lipsky, Stephen E. Microwave Passive Direction Finding. Grand Rapids: SciTech, Incorporated, 2003.

[9] Lie, Joni P., Chong M. See, and Boon P. Ng. "Ultra Wideband Direction Finding using Digital Channelization Receiver Architecture." IEEE Communications Letters 10 (2006): 85-87.

[10] Ng, Boon P. "Array Shape Self-Calibration Technique for Direction Finding Problems." IEE Proceedings-H 139 (1992): 521-25.

[11] Bellion, Anthony, Cyrille Le Meins, Anne Julien-Vergonjanne, and Thierry Monédière. "Generation of Calibration Tables for Direction Finding Antennas Using FEKO." 24th Annual Review of Progress in Applied Computational Electromagnetics (ACES) (2008): 903-08.

[12] FEKO, http://www.feko.info, by EM Software & Systems, commercially licensed software.

[13] Ito, Koichi. "Numerical and Experimental Human Body Phantoms." IET Seminar on Antennas and Propagation for Body-Centric Wireless Communications, 2007 (2007): 6-12.

[14] Barnes, Frank S., and Ben Greenebaum. Bioengineering and Biophysical Aspects of Electromagnetic Fields. New York: C R C P LLC, 2006.

[15] Youngs, I. J., A. S. Treen, G. Fixter, and S. Holden. "Design of Solid Broadband Human Tissue Simulant Materials." IEE Proceedings on Science and Measurement Technology 149 (2002): 323-28.

INVESTIGATION OF GROUND PLANE SLOT DESIGNS FOR ISOLATION OF COSITED MICROSTRIP ANTENNAS

K. C. Kerby and J. T. Bernhard
Electromagnetics Laboratory
Department of Electrical and Computer Engineering
University of Illinois at Urbana-Champaign
Urbana, IL 61801
http://antennas.ece.uiuc.edu/
kkerby@illinois.edu, jbernhar@illinois.edu

ABSTRACT: Ground plane slot designs have been reported that can improve isolation between antennas that share a ground plane. However, no systematic model for design or scaling of such slots presently exists. As part of an investigation that aims to arrive at generalized design guidelines for ground plane slot structures, this work examines the response of ground plane slot structures' excitation to different antenna orientations.

1. INTRODUCTION

In systems with multiple cosited antennas, coupling between adjacent antennas can degrade performance. The antennas may be in the same system, as in a phased array. Alternatively the antennas may belong to different systems, such as the Bluetooth and WLAN systems on a mobile phone.

The two simplest ways to reduce coupling between two antennas are based on the basic properties of propagation. By moving the antennas further apart or intentionally mismatching their polarizations, one can reduce the signal from one antenna that is received at the other. However, in many situations those approaches are impossible. Arrays, for instance, have prescribed spacing and operate on the assumption that the elements are identically oriented. Also, in small wireless devices, antenna designers usually have little or no control over antenna placement in packages.

When the easy approaches are not feasible, most methods of improving isolation between antennas involve including some structure between them that prevents propagation in that direction: an electronic band gap (EBG) structure [1], [2], a resonant cavity [3], or resonant-length slots in the ground plane [3], [4]. Ground plane slots add no extra weight or volume to the system, require no vias, and have less stringent manufacturing tolerances than EBG structures, so for many applications they may be the most promising approach. However, there is no analytic model for ground plane slot structures, and there is no systematic scaling method for adapting existing slot designs to new systems. Therefore, as part of an ongoing project to develop an understanding of ground plane slot

structure behavior and a system of design guidelines, this work examines the effect of antenna orientation on the excitation of ground plane slot structures.

2. BACKGROUND

Ground plane slot structures have been reported by Alvey [3] in 2006 and by Chiu et al. [4] in 2007. The Alvey slot design, pictured in Figure 1, consists of a row of meander-line block elements. The total path length of each meander-line element is approximately a half wavelength in the effective medium of the slots. Reported S parameters for this design are shown in Figure 2, compared to the S parameters of a base case without the slots.

The Chiu slot design, pictured in Figure 3, is composed of some number of parallel end-to-end pairs of slots. Each slot touches the edge of the ground plane on one end and extends partially across the ground plane towards the center. The design we focus on uses two pairs of slots. The total length of each end-to-end slot pair (which is also the total width of the ground plane) is approximately a half wavelength in the effective medium of the slots. Reported S parameters for this design are shown in Figure 4, compared to the S parameters of a base case without the slots.

In an earlier part of this project, these two reported ground plane slot designs were compared to one another [5]. The Chiu design was scaled to operate on the same base configuration as the Alvey design in order to facilitate comparison. In the course of that investigation, some trials showed that the slots responded differently depending on the orientation of the antennas. In this paper, scaled versions of the Chiu design will be used to illustrate the effects of antenna orientation on slot excitation.

3. SLOT EXCITATION BEHAVIOR

Figure 5 shows one scaled version of the Chiu slot design, operating at 2.2 GHz on a substrate with dielectric constant 2.2 and thickness 1.575 mm. The antennas are aligned so that the slot structure crosses their H-plane. In this case, the antennas and ground plane are proportionally the same as the original Chiu base design and were scaled together. The slots' dimensions were multiplied by a scaling factor, with the constraint that the slots must always reach the edge of the ground plane. Simulated S_{21} values for this design with different slot scaling factors are plotted in Figure 6. The slots induce a dip in S_{21} that does not change frequency as the scaling factor is varied.

Figure 7 shows another version of the Chiu slot design, in which the slots cross the antennas' E-plane. This design operates at 2.375 GHz on the same substrate material as the design in Figure 5. Simulated S_{21} values for this design with different slot scaling factors are plotted in Figure 8. In this case, the features of the S_{21} plot can be seen to change in frequency as the slots are scaled. This orientation of the Chiu slot design also

seems to reduce coupling over a wider bandwidth than the original Chiu design, whose antennas were in the H-plane orientation, reported.

4. ANALYSIS

The same slot structure responds differently to scaling when adjacent antennas are oriented in different directions. This leads one to reason that the slots operate by a different method in each case. Consideration of the slots' electrical dimensions in concert with the field distribution along the adjacent radiating antenna edge sheds some light on the two excitation methods. The slots' behavior will be similar to that of a printed antenna not backed by a ground plane, so that the effective resonant wavelength of the slots depends on a weighted average of the dielectric constants of the substrate and air.

Based on this effective wavelength, the width of the substrate (which is also the total length of the slot structure) in the H-plane orientation case is about 0.65 λ_{eff} at 2.2 GHz, but it is approximately 0.5 λ_{eff} at 1.65 GHz, the frequency of the S_{21} dip. In the E-plane orientation, the width of the substrate is about 0.84 λ_{eff} at 2.375 GHz, where the slots' response is clearly noticeable. The slots' individual lengths, however, are 0.25 λ_{eff} at that frequency.

The field distributions along the adjacent edges of the antennas in each orientation are as shown in Figure 9. When the slots cross the antennas' H-plane, the fields vary along the adjacent edge of the antenna. In this case, the slots would be excited in a dipole-like mode, with different polarities at either edge of the substrate. This excitation would exist when the slots were a half wavelength long, which agrees with our previous evidence. This is the mode in which the original design operated; all of the test configurations placed the slots in the antennas' H-plane. When the slots cross the antennas' E-plane, the fields do not vary along the adjacent edge of the antenna. In this case, the slots are excited independently of one another and the individual slot length therefore matters more than the width of the substrate. Here, since the slots are a quarter wavelength long, they transform the apparent "open" at the edge of the ground plane into a "short" near the center, effectively shorting out the currents on the ground plane that contribute to coupling the two antennas.

5. CONCLUSIONS

The effect of antenna excitation on the orientation of ground plane slot structures has been examined. It has been shown that slot response depends heavily on the orientation of adjacent antennas. Two fundamentally different modes of operation have been described for one previously reported slot structure. The fact that slots respond differently to different field polarizations will be crucial in the design of ground plane slot isolation structures for polarization-agile or circularly-polarized antenna systems.

6. ACKNOWLEDGMENT

This work has been supported by a Bell Labs Graduate Research Fellowship.

7. REFERENCES

[1] D. Sievenpiper, L. Zhang, R. F. Jimenez Broas, N. G. Alexopoulous, and E. Yablonovitch, “High-impedance electromagnetic surfaces with a forbidden frequency band," *IEEE Transactions on Antennas and Propagation*, vol. 47, pp. 2059-2074, Nov. 1999.

[2] M. F. Abedin and M. Ali, “Effects of a smaller unit cell planar EBG structure on the mutual coupling of a printed dipole array," *IEEE Antennas and Wireless Propagation Letters*, vol. 4, pp. 274-276, 2005.

[3] G. Alvey, “Investigation of techniques for isolating cosite microstrip patch antennas," M.S. thesis, University of Illinois at Urbana-Champaign, 2006.

[4] C. Chiu, C. Cheung, R. Murch, and C. Rowell, “Reduction of mutual coupling between closely-packed antenna elements,*" IEEE Transactions on Antennas and Propagation*, vol. 55, pp. 1732-1738, June 2007.

[5] K. Coles, K. C. Kerby, and J. T. Bernhard, “Comparisons of Ground Plane Techniques for the Isolation of Cosited Microstrip Antennas,” *Proc. IEEE Antennas and Propagation Symposium*, San Diego, CA, July 2008.

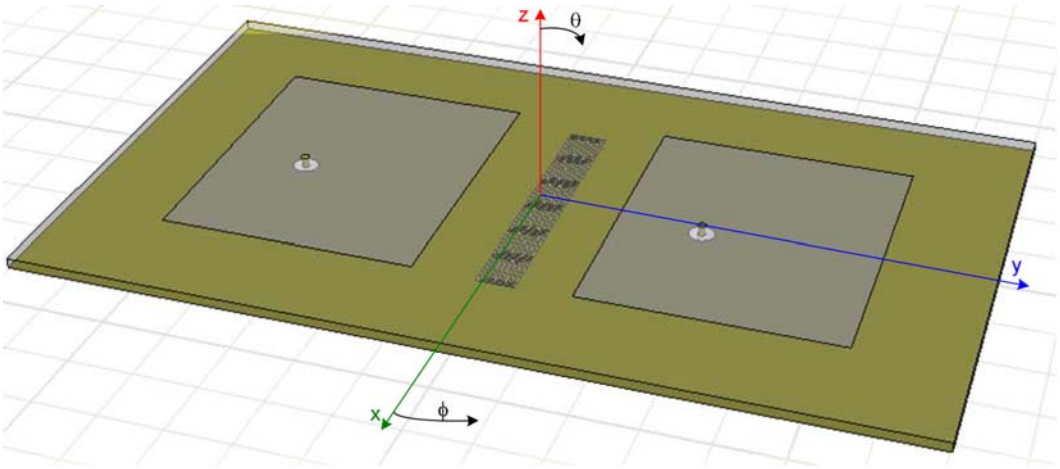

Figure 1: Ground plane slot design reported by Alvey [3].

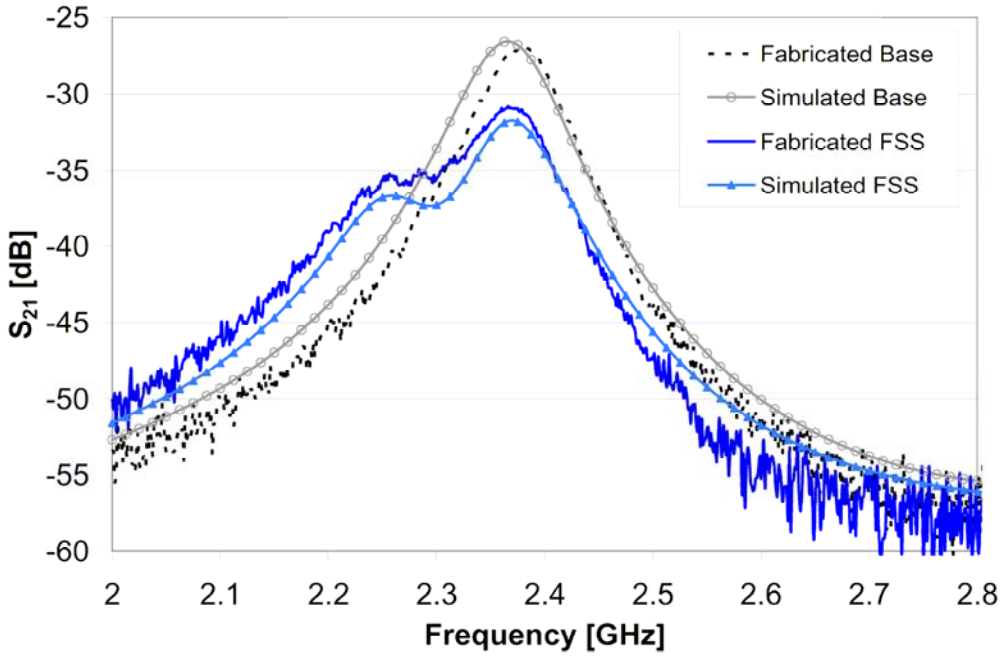

Figure 2: Simulated and measured S-parameters reported by Alvey [3].

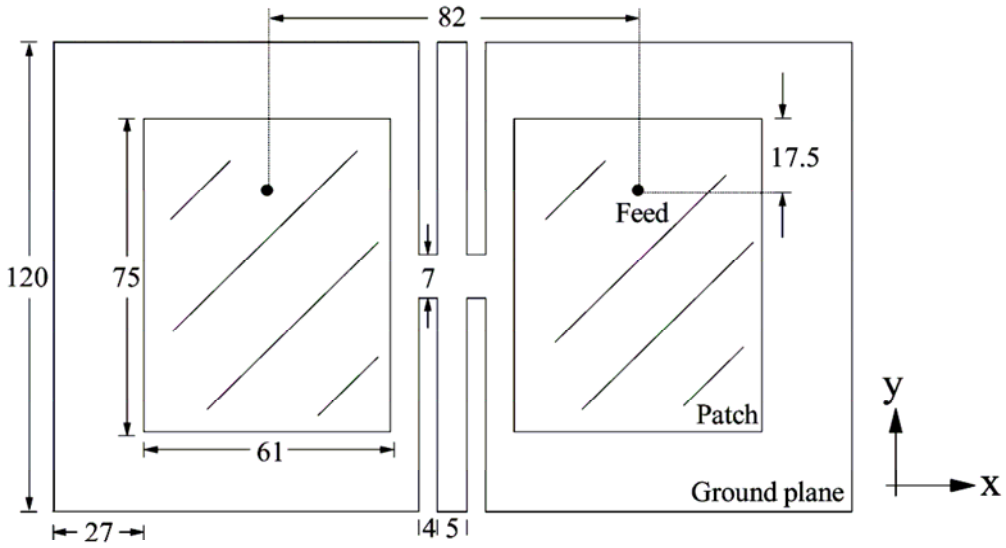

Figure 3: Ground plane slot design reported by Chiu et al. [4].

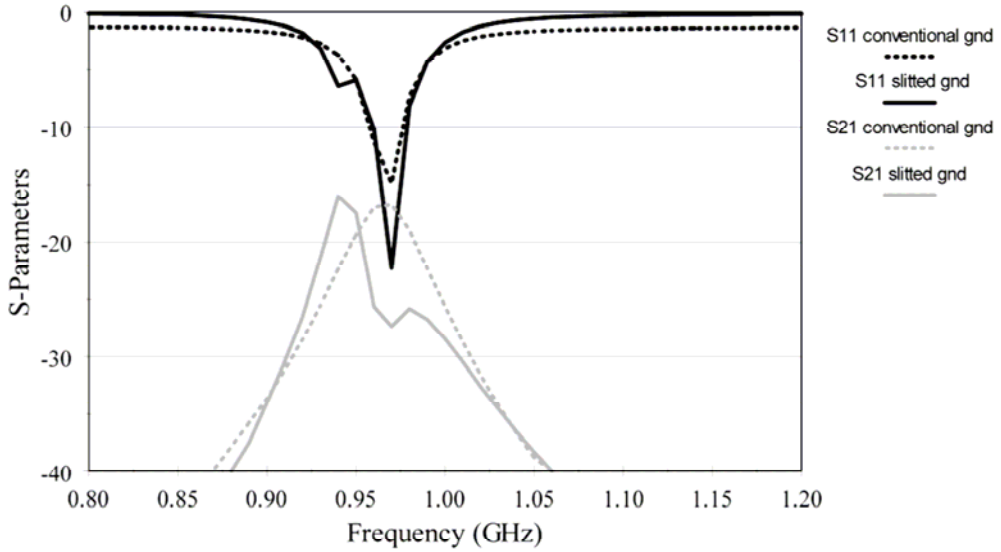

Figure 4: Measured S-parameters reported by Chiu et al.

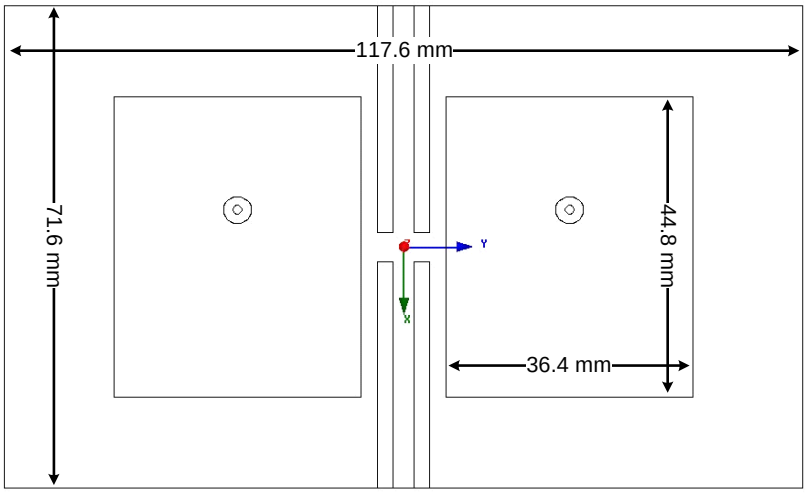

Figure 5: Scaled Chiu design, slot structure crossing antennas' H-plane.

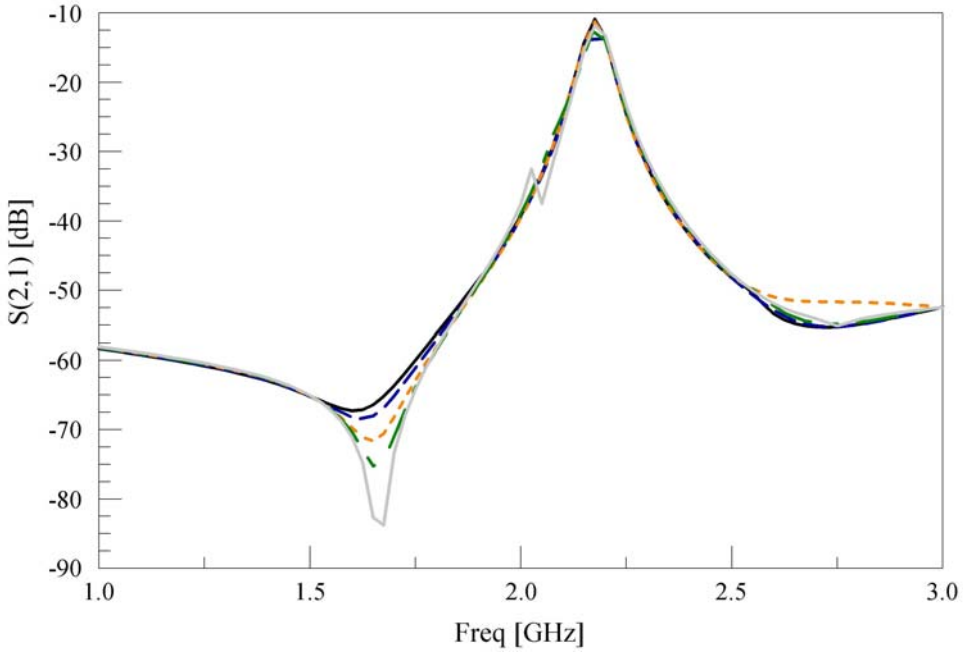

Figure 6: S_{21} for scaled Chiu design with slots crossing antennas' H-plane, slot scaling factor = 0.4 (solid black line), 0.42 (dashed line), 0.46 (dotted line), 0.48 (dot-dashed line), 0.5 (solid gray line).

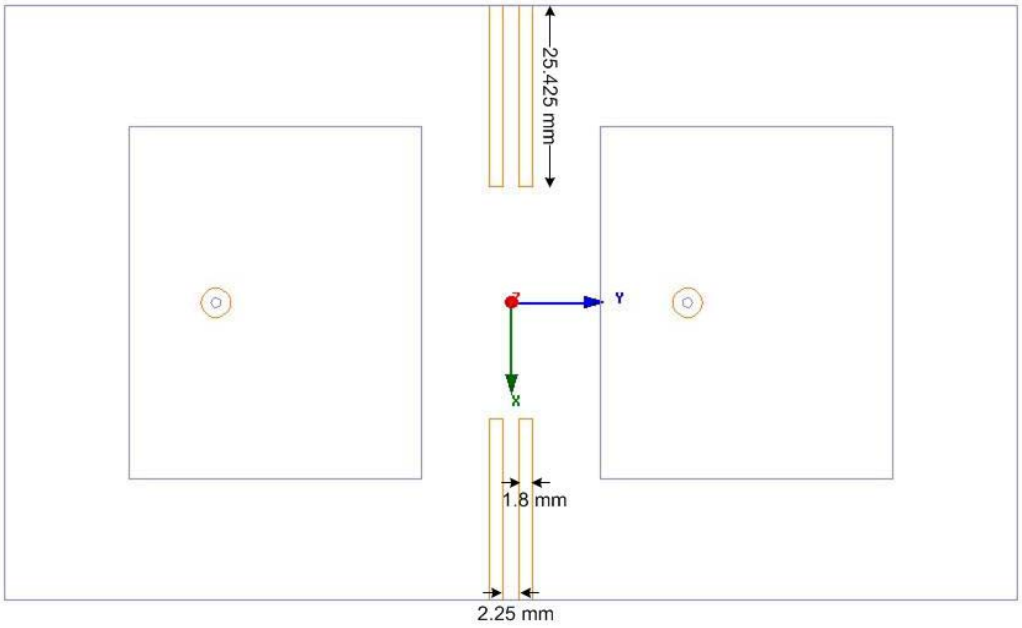

Figure 7: Scaled Chiu design, slot structure crossing antennas' E-plane.

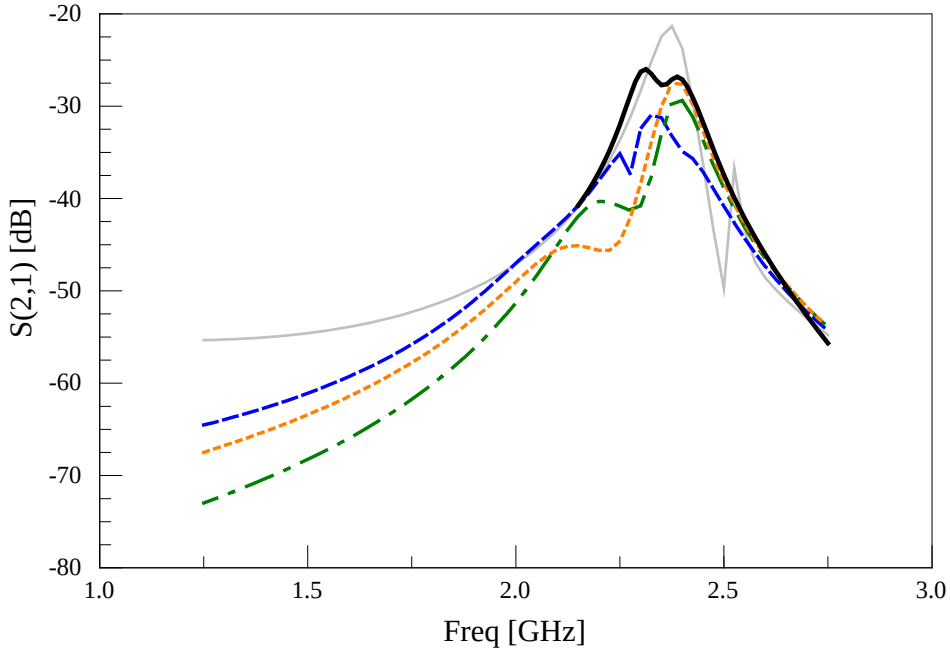

Figure 8: S_{21} for scaled Chiu design with slot structure crossing antennas' E-plane, slot scaling factor = 0.4 (solid gray line), 0.45 (dashed line), 0.5 (dotted line), 0.55 (dot-dashed line), with the base case for comparison (solid black line).

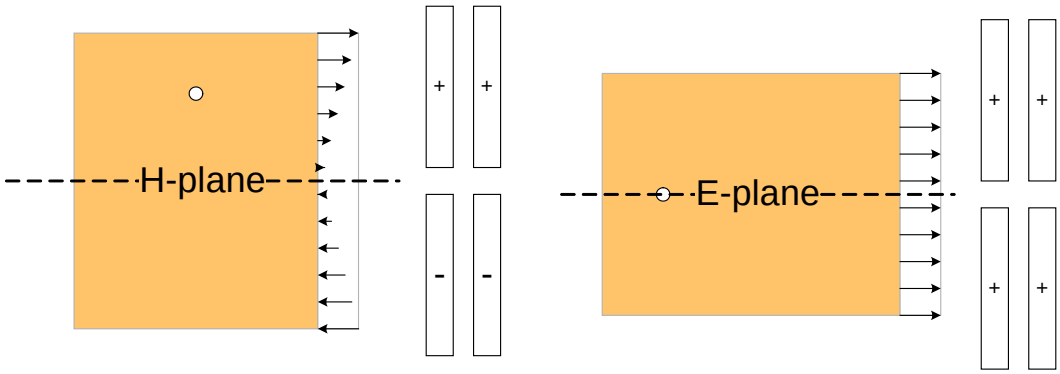

Figure 9: Diagram of slot excitation and patch edge fields in H-plane and E-plane orientations.

A NEW RADIO DIRECTION FINDER FOR WILDLIFE RESEARCH II

Todd A. Borrowman, Steven J. Franke and George W. Swenson, Jr.
Department of Electrical and Computer Engineering
University of Illinois at Urbana-Champaign

Abstract

The direction-finding system described at the 2007 Allerton Conference has been re-designed for 302 MHz and horizontal polarization. The new design involves a novel bent-dipole array configuration, 4-channel software-defined receivers and improved detection, classification and direction-finding algorithms. Target azimuth estimation is accomplished on a single 20 millisecond received pulse and many transmitters on incrementally different frequencies can be received and processed simultaneously.

1 INTRODUCTION

This paper reports a continuation of the work on the development of a radio direction finder (RDF) for tracking radio-tagged wildlife. The new RDF is to operate in the VHF band, to receive pulsed or otherwise modulated signals, to estimate target azimuths instantaneously, and to do so simultaneously on substantial numbers of targets.

The previous antenna design [1] was for a 164.5 MHz vertically polarized antenna. Several antenna configurations were simulated in NEC-Win-Pro [2], tested in direction-finding algorithms, and the complex radiation pattern of the best performing configuration was verified in the field. Lastly a field test was performed to show the validity of this direction finding technique. That field test will be revisited later in this paper. In anticipation of a practical field test to be conducted in a biological research site, a similar series of simulated tests has been performed on the design of a new horizontally-polarized antenna array and a new receiver system to meet the technical requirements of the site. Specifically, the vertical polarization of the earlier system has been changed to horizontal in the new system, and the operating frequency has been raised to 302 MHz.

2 COMPUTER SIMULATIONS

A site at a biological field station has been chosen as a test bed for the prototype direction finder. There are several birds that have been tagged with pulse transmitters. These transmitters operate at 302 MHz and due to the backpack configuration used to attach them on the birds, the signals are horizontally polarized. Because of these requirements, a new antenna array was designed.

As discussed in previous work [1], Monte Carlo computer simulations are useful in assessing an antenna pattern's direction finding performance. Multiple antenna geometries were tried using simple dipole antenna elements in various horizontal configurations. The standard deviation of the errors produced in the trials was calculated for multiple signal-to-noise ratios (SNRs).

The criteria used for selecting the best direction finder are complex. The difficulty lies with the fact that the precision of the estimation changes non-linearly with SNR. At high SNR the distribution of errors is dependent on the shape of the pattern near the angle of arrival of the signal. One should

maximize the rate of change of the pattern over azimuthal angle. This is reflected in the Cramer-Rao lower bound (CRLB) being proportional to the inverse of the square of the derivative of the antenna pattern versus azimuthal angle [3].

However at low SNR, symmetries in the pattern can cause ambiguities in the estimate and thus a wide range of estimation errors. Because these ambiguities are prevalent at widely separated angles this is not shown in the CRLB. Therefore the best direction finder has the lowest standard deviation of errors at high SNR without having large standard deviation at low SNR due to ambiguities. The chosen antenna's results are given in figure 1. The figure on the left displays the results from computer simulations with high SNR. This is in the regime where the CRLB gives values consistant with the Monte Carlo results. The figure on the right shows the results with a lower SNR. At this SNR the ambiguities begin to show themselves as areas of high standard deviation.

Owning to the inability of the CRLB to detect ambiguities, a different statistical method was investigated to determine the best direction finder. The "confusion matrix" shows these ambiguities. As presented in [4], the confusion matrix is given as

$$\chi_{ij} = \frac{a(\theta_i)^* a(\theta_j)}{\|a(\theta_i)\| \, \|a(\theta_j)\|}, \tag{1}$$

where * is the conjugate transpose and $\|\cdot\|$ is the norm of the vector. The value of χ_{ij} is unity if the steering vectors are co-linear (and thus ambiguous) and zero if they are orthogonal.

These confusion matrices show the 180 degree ambiguities that occur at the antenna's boresight (Figure 2). These ambiguities are what cause the differences in the graphs of the Monte Carlo results. This feature seems to be characteristic of four element symmetric antenna arrays.

The modeled antenna was built (figure 3) and its far-field pattern was measured. The antenna elements are 9.5 mm aluminum tubing cut into 23.2 cm long sections (figure 4). They are mounted into a square of Lexan plastic and held in place by set screws. The antenna feed is a coaxial cable connected to lugs which are screwed into the ends of the antenna elements at the center point. Ferrite beads were placed at 1/4th wavelength intervals along the feed lines to suppress RF surface currents.

The antenna pattern was measured using a network analyzer. One antenna of the array at a time was measured while the other three were terminated by 50 Ω loads. A simple dipole was used as the target antenna and was located 24 m away from the array. The array was placed on a rotating platform so a full 360 degree pattern could be measured.

As seen in figures 5 and 6 the patterns match fairly well with the calculated values. The phase angle matches extremely well with the calculated values. This indicates that the array was spaced correctly in construction. The gain pattern is similar to the calculated pattern with a few inconsistencies. The front-to-back ratio was measured to be higher than calculated. This can be attributed to the construction of the antenna, namely the mounting hardware which attaches the antenna to the mast. Secondly there are asymmetries in both lobes and between the nulls. The cause of this probabily lies with the unbalanced feed line to the antennas.

3 TARGET TRANSMITTER TESTS

In the previous paper [1], results were presented from a transmitter target test which was performed using a previous antenna design. A transmitter was driven around a field site with a global positioning satellite (GPS) receiver. This gave a measurement of the true bearing of the target which could be compared to an estimated bearing. The received signal was recorded and processed using prototype algorithms and the results were presented (reprinted here in figure 7).

Since that work, newer algorithms have been developed. The detection and estimation can now be processed in real-time. The new estimation algorithm also gives more statistics about the received signals that can be used to refine the bearing estimates.

Initially the signals are filtered based on center frequency and estimated signal bandwidth. Since the target frequency is known it is a simple matter of marking signals outside the target frequency as false positives. An additional check of this signal validation proceedure is the fact that false positives due to random noise will have a wider bandwidth estimation than the true positives. These true positives are presented in figure 8.

The large errors that remain are due to the ambiguities which are inherent to the antenna design and construction. By examining the likelihood statistic used by the estimation algorithm (figure 9) a "smooth" track can be seen, which closely corresponds to the actual bearing. By assuming that the high probabilities at the beginning and the end of the data give the true bearing, and then limiting the angular speed of the estimates to be less than fifty degrees per second (a conservative limitation), the track given in figure 10 is produced.

This method of using previous estimates to eliminate ambiguity errors becomes more powerful when used in a fully deployed system. A position estimation system using these direction finders will need at least two installations receiving a signal to triangulate the position. Because the ambiguities are approximately one-hundred eighty degrees apart, if two installations receive a signal only one pair of the four possible bearing pairs will give reasonable results and intersect at a point. This method gets stronger the more signals one receives.

4 CONCLUSION

Simulations and actual field tests of the radio direction finder previously described [1], designed for vertical polarization and operation on 164.5 MHz, have demonstrated a workable system capable of very fast operation, simultaneous estimation of azimuths on many moving targets, and very respectable precision of azimuth estimation. A second version of the instrument, designed for horizontal polarization and 302 MHz operation, has in simulation demonstrated similar capabilities. Field tests of the horizontally polarized antenna array show close replication of the simulated complex pattern. Thus, this novel direction-finding technique involving simple antenna structures, use of complex analytic signals, modern statistical estimation algorithms and multiple software-defined receivers can be used in either horizontally- or vertically-polarized configurations and over a wide range of VHF frequencies.

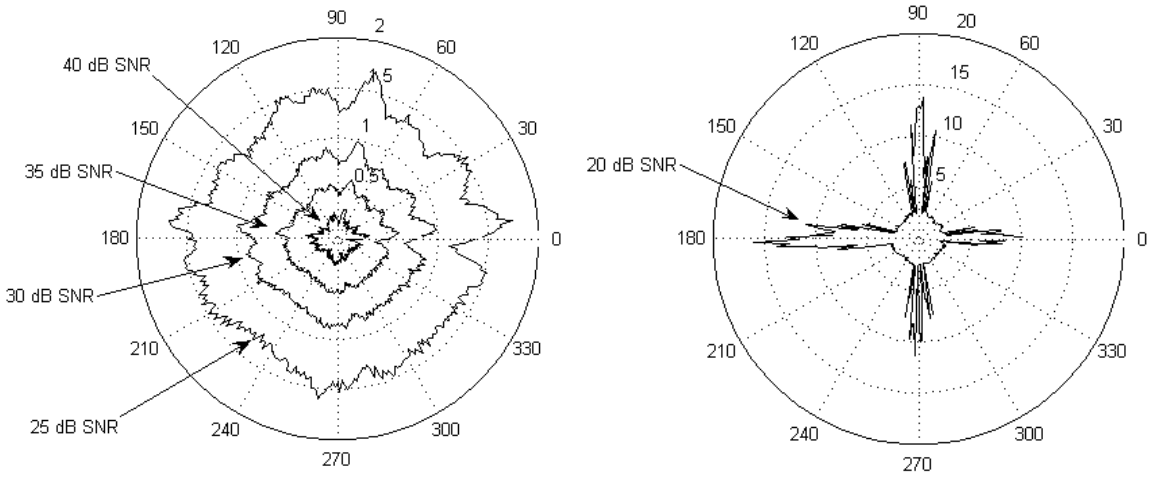

Figure 1: Results from Monte Carlo direction finding simulations. The radial scale is the standard deviation of errors in degrees. This reported SNR does not account for the receiver configuration in a real world implementation. The SNR must be adjusted for both the transmitter bandwidth and the noise bandwidth of the system to reflect this. For the current receiver implementation the SNR should be reduced by 13.6 dB.

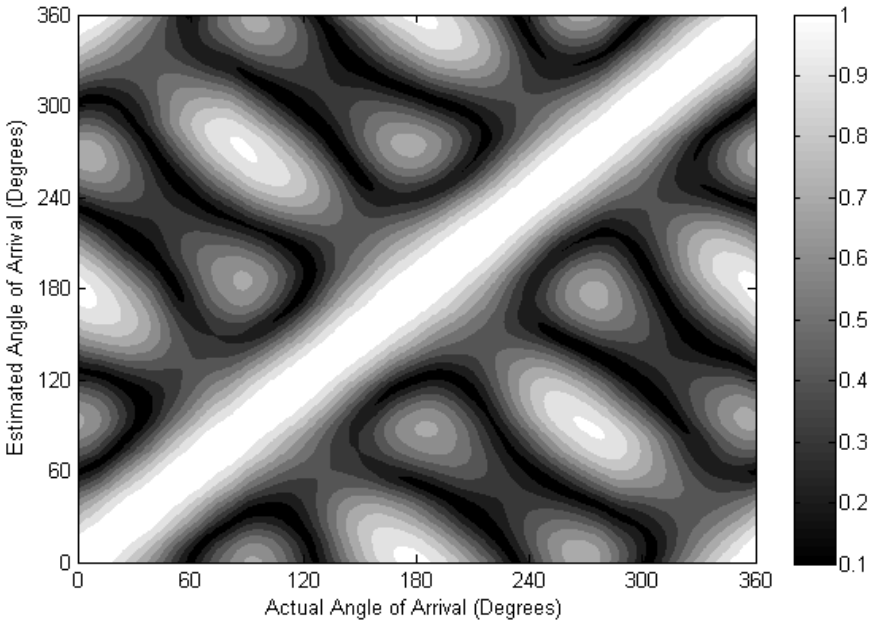

Figure 2: Confusion matrix for the measured antenna pattern of the four-element horizontal bent dipole array

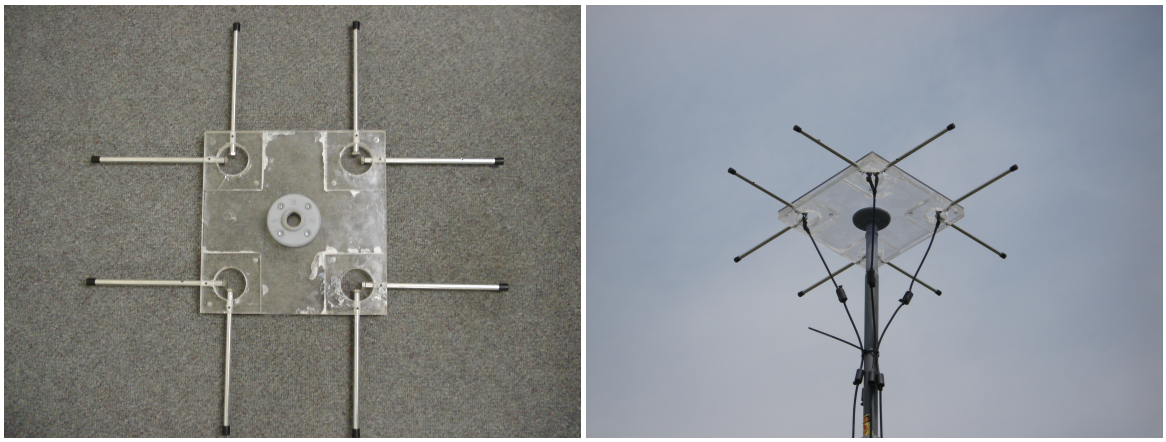

Figure 3: Constructed Antenna.

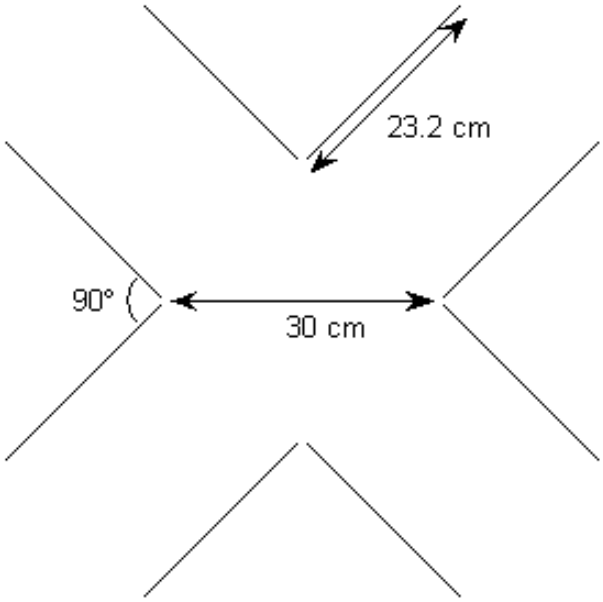

Figure 4: Layout of four-element horizontal bent dipole array.

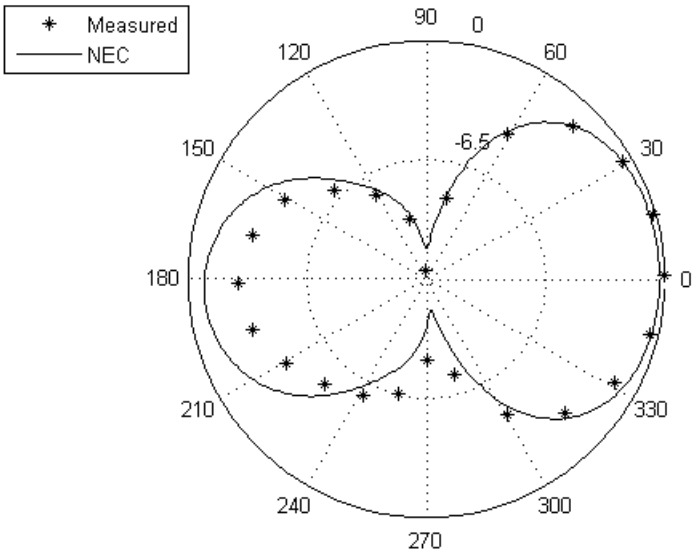

Figure 5: Comparison of NEC simulation and measured four-element horizontal bent dipole array magnitude pattern at a frequency of 302 MHz. The radial axis is in dB.

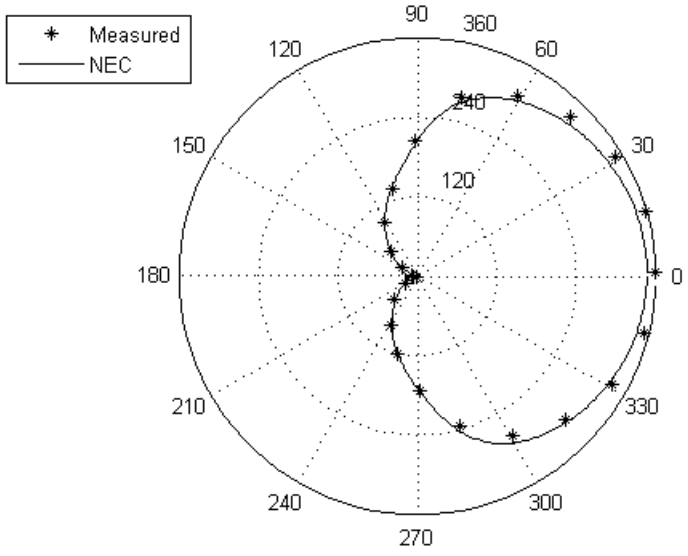

Figure 6: Comparison of NEC simulation and measured four-element horizontal bent dipole array phase pattern at a frequency of 302 MHz. The radial axis is in degrees.

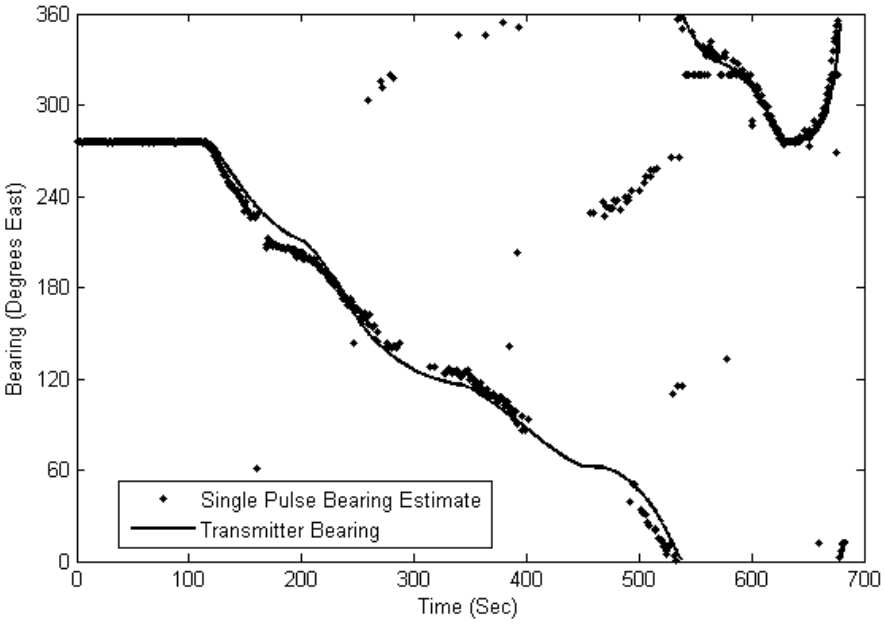

Figure 7: Single pulse bearing estimation of the target trasmiter. This figure was presented in the previous paper [1].

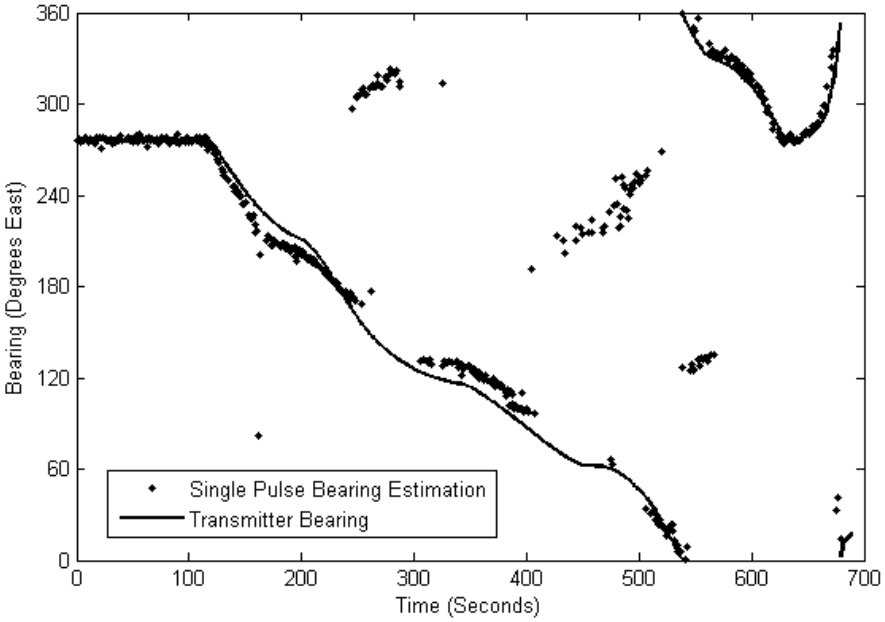

Figure 8: Single pulse bearing estimation of the target transmiter using real-time algorithms. These data points have been filtered to eliminate false positives.

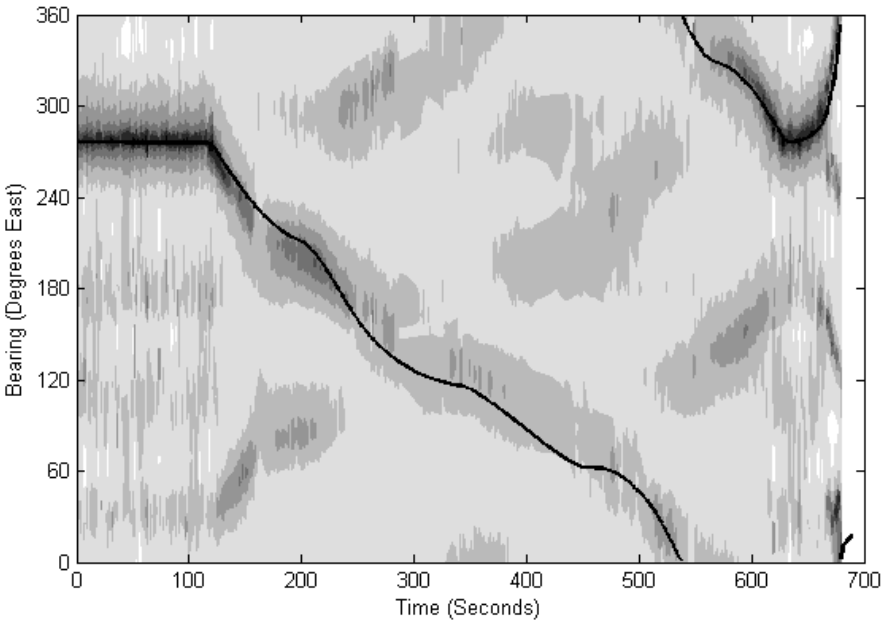

Figure 9: Contour plot of the estimator values. Dark areas represent higher probability.

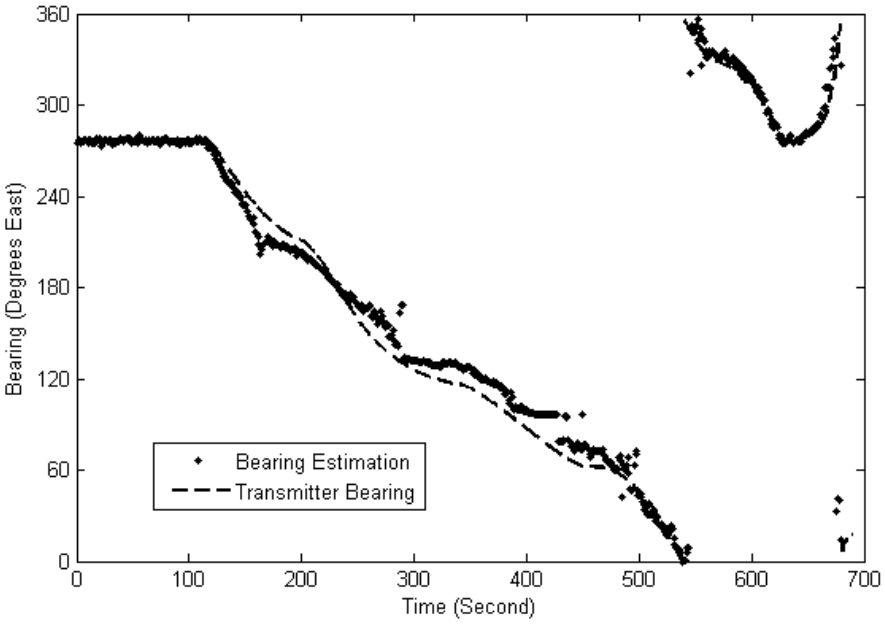

Figure 10: Bearing estimations based on a smooth tracking curve.

Acknowledgement

This work was supported financially by CESU Agreement No.W9132T-06-2-0011 between the U.S. Army Engineer Research and Developement Center, Construction Engineering Research Laboratory and the Department of Electrical and Computer Engineering, University of Illinois at Urbana-Champaign.

References

[1] T.A. Borrowman, S.J. Franke, and G.W. Swenson Jr., "A new direction finding system for wildlife research," in *Proceedings of the 2007 Antenna Applications Symposium, Allerton Park*, 2007, pp. 384-394.

[2] Nittany Scientific Inc., "NEC-Win Pro," 2003, http://www.nittany-scientific.com/nwp/index.htm.

[3] B. Friedlander and A.J. Weiss, "Direction finding in the presence of mutual coupling," in *IEEE Transactions on Antennas and Propagation*, Vol. 39, No. 3, 1991, pp. 273-284.

[4] M. Erić, A. Zejak, and M. Obradović, "Ambiguity characterization of arbitrary antenna array: type I ambiguity," in Proceedings of the 1998 IEEE 5th International Symposium on Spread Spectrum Techniques and Applications, Vol. 2, 1998, pp. 399-403.

Pillbox Antenna with a Dipole Feed

W.R. Pickles and M.G. Parent
U.S. Naval Research Laboratory
Washington DC 20375

Abstract: The Naval Research Laboratory is designing an azimuthally scannable phased array with a large vertical aperture. A pillbox design is being used because it achieves a large vertical aperture with the simplicity of a space feed. Commonly, pillbox antennas are fed with waveguide horns. For this design, however, a dipole feed was chosen, to reduce the size of the feed network and to relieve the congestion of having many adjacent coaxial transmission line to waveguide transitions. Calculated and measured responses for the antenna and feed network are presented.

1. Introduction

The U.S. Navy at the Naval Surface Warfare Center, Dahlgren Division, under sponsorship of the Office of Naval Research, is constructing a Digital Array Radar (DAR) test bed as a means to reduce risk for future large, multi-mission, S-band radars. The goals of the DAR test bed are to demonstrate calibration, high clutter rejection, and wideband high range resolution imaging in a 64-channel system where each channel contains its own receiver and exciter. The objective of the DAR program is to develop the distributed receivers and exciters, digital beamforming, and back end signal processing subsystems required in future systems; construction of the test bed is necessary as a means to test the hardware developed to date. The Naval Research Laboratory (NRL) is supporting the effort through the design of a novel pillbox antenna array that offers high gain, low loss, and simple fabrication. Additional requirements for the DAR antenna are that it have an impedance mismatch of less than −17 dB from 2.9 to 3.5 GHz.

2. Antenna Considerations

NRL chose a pillbox design (Fig. 1) for the phased array elements because this design offers a large vertical aperture with a very simple feed network. An H-plane horn design, such as that of the Navy's AN/SPS-67 antenna, was rejected because it would require too much depth for the large aperture sizes being considered. Other types of radiators considered by NRL incorporated power divider networks that would incur electrical losses, increase complexity, or both. Air dielectric designs are used as much as possible in this antenna to maintain consistency between elements and to reduce losses. Initially, every attempt was made to minimize the use of connectors, for the same reason.

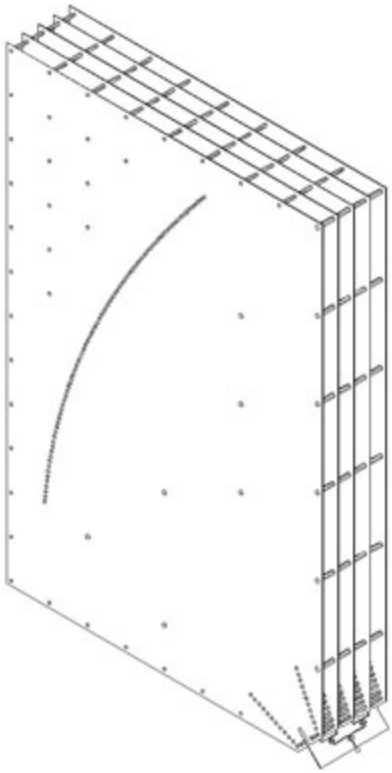

Figure 1 – NRL 4-element pillbox antenna with 4-way Wilkinson feed.

The pillbox array element was developed with the aid of Ansoft HFSS, an electromagnetic simulation computer program employing the finite element method. The majority of this analysis was performed with HFSS version 8.5. The entire pillbox presented too large a project to yield converged results, so only the feed horn was analyzed. Ansoft recommends that radiation boundaries be offset one quarter wavelength from the structure of the antenna, so the project was analyzed in a wedge-shaped environment.

2.1 Control of Current Flow

To build a pillbox array, it would be simplest to construct each pillbox element separately and then install them in an overall array structure. However, variations in the flatness of the pillbox elements could cause unevenness in the line of contact between adjacent elements, which in turn could cause irregularities in the current flow across such boundaries. This concern arose during consideration of the SPS-67 antenna design. The SPS-67 is a low sidelobe design consisting of 64 H-plane horns (see the simplified sketch in Figure 2). As shown in the inset view of Figure 2, the horns have exterior machined edges that are slightly raised. This ensures predictable contact between adjacent elements along the edges. The SPS-67 horns are about 6 inches high, whereas the DAR pillboxes are about 4 feet high. It would be difficult to construct large elements with such careful control of edge contact. The DAR array is not explicitly a low sidelobe array. However, DAR has performance goals that

may require control of low-level currents equivalent to the control required for low sidelobe arrays.

For the NRL pillbox antenna design, it was decided to make the partitions between unit cells common to each cell. This eliminated concern about uneven current flow across the edges between adjacent elements, although it complicated the construction.

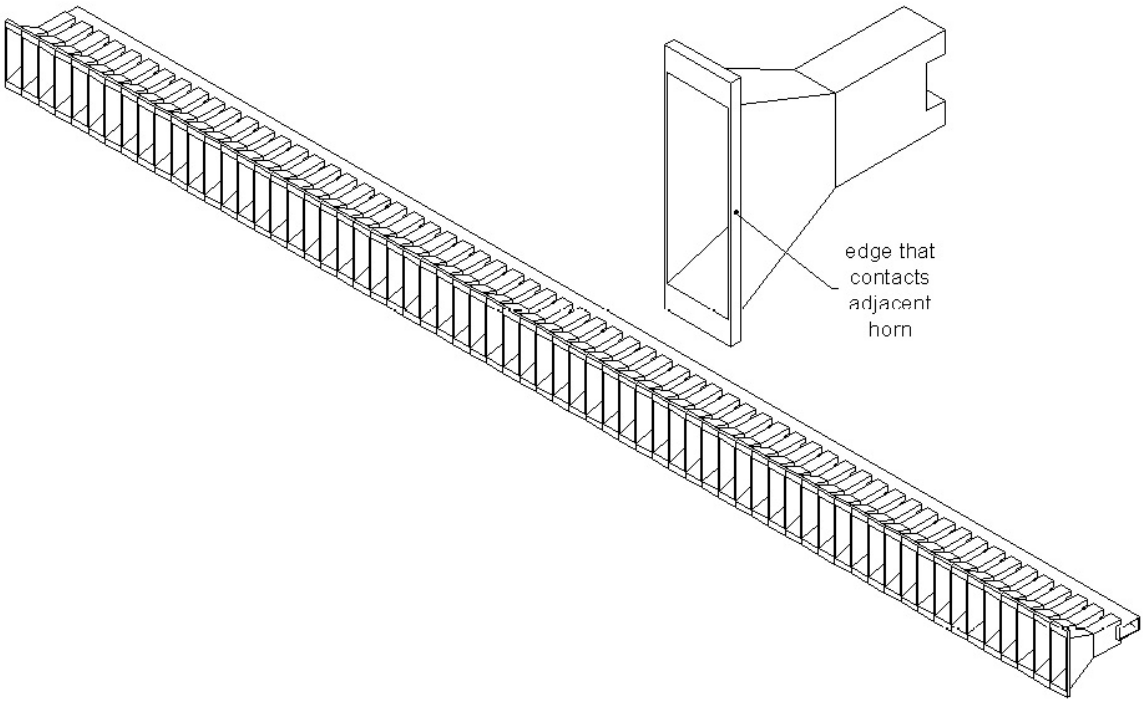

Figure 2 – SPS-67 antenna.

2.2 Waveguide Feed Design

Commonly, a pillbox antenna has a waveguide horn feed. In NRL's pillbox array configuration, this presented concerns about accessibility of connectors and joining hardware. In order to reliably stabilize each feed horn with respect to each pillbox element, at least two attachment points would be required, as shown in the sketch in Figure 3. However, access to screw heads and nuts in the confined space between the pillbox partitions would be difficult. Waveguide horns, coaxial connectors, and coaxial elbow adaptors all would have to fit in the space between adjacent pillbox elements. The congestion might preclude the use of broad wall coax to waveguide transitions.

Another waveguide feed option is to construct the broad walls of the waveguides from the same metal sheets that form the partitions between pillbox antennas, and to form the narrow walls from metal spacers between. With this arrangement, it might be difficult to maintain

good continuity from broad wall to narrow wall. Ideally this joint would be welded or brazed.

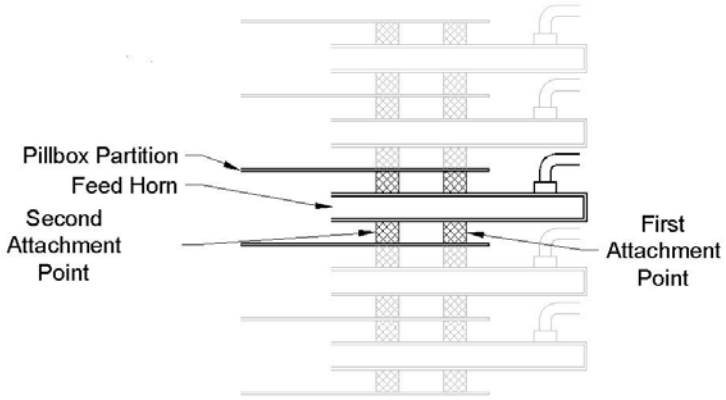

Figure 3 – Working design showing region where pillbox array interfaces with feed horn array.

Another possibility would be to construct the narrow wall from a line of standoffs or posts, as shown in Figure 4. This would allow positive contact to be ensured by tightening each standoff individually. HFSS simulations of this scheme showed that radiation leaked out between the posts in the vicinity of discontinuities. The polarization of the strongest leakage component, which is close to 0 dBi, is shown by the E vector in Figure 4. To control this leakage, the standoffs would have to be placed so close together that they could not be grasped with a wrench during construction. Smaller diameter standoffs could be used to get closer spacing, but in deference to the technicians who have to assemble the full-scale array, it was decided not to use screws smaller than 6-32.

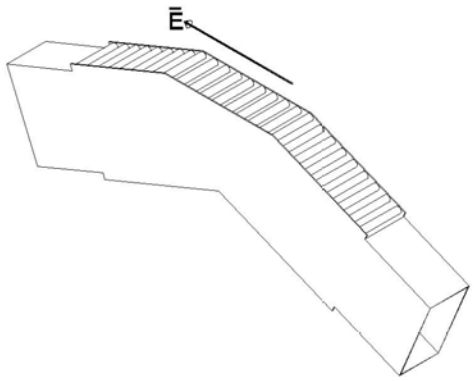

Figure 4 – Waveguide constructed with sheet metal broad walls and columns of posts for narrow walls. Radiation leakage at discontinuities is a problem.

Ultimately, a variation of this last concept was chosen. A feed horn composed of rows of posts was constructed internal to the pillbox at the lower front corner. A double balun dipole [1] was inserted at the base of the horn to excite it. Details of both are given in the next section.

3. Design of the Pillbox

The design of the pillbox followed two of the guidelines given by Gambahaya and Inggs [2, 3]. The first guideline was to use a focal length to diameter ratio (f/Dp) of 0.3 for a good compromise between maximizing gain and minimizing cross-polarized radiation. Dp refers to the diameter of the parent paraboloid of the pillbox antenna reflector. Here, Dp/2 as shown in Figure 5 is the vertical distance from the focus F to the top of the parabolic reflector. The second guideline was that the edge illumination of the parabolic reflector should be approximately –10 dB with respect to the peak.

The element spacing for the array was chosen to be 1.65 inches, which is one half wavelength at 3.5 GHz. This permits scanning to all angles at all frequencies in the operational bandwidth. This may be more conservative than necessary. A slightly higher radiation pattern gain could be obtained with a larger element spacing, but at the expense of scanning performance. The material chosen for the pillbox partitions was 1/16 inch aluminum, resulting in a 1.5875 inch spacing between partitions.

The parabolic reflector was formed by a series of standoffs between the plates forming the sides of the pillbox. The feed horn was constructed in the same way: with standoffs. A double balun dipole was placed at the base of the horn. The standoffs were carefully tightened to provide good electrical contact to adjoining pillbox partitions. Measurements of 150 standoffs revealed that they had been machined with an accuracy of about ±0.5 mils. A single machined piece of metal the size of the parabolic reflector would have a considerably larger tolerance and could be subject to some warpage from the machining process.

The initial layout of the pillbox is shown in Figure 5. An area 48 inches high with indeterminate width was marked out. A series of parabolas with an f/Dp ratio of 0.3 and focus at point F were drawn in this region until a size that neatly filled the available space was found. The corresponding focal length and diameter were 24.3 inches and 81 inches, respectively. An approximately sized H-plane sectoral horn was drawn at the focus to aid in the layout. Angles were measured from the plane of the focus to the lower edge and upper edge of the parabola. The difference between these two was calculated to be 69 degrees.

The feed horn then was designed separately with HFSS 8.5 so that its 10 dB beamwidth was equal to 69 degrees. This is shown in Figure 6. Note that only half of the feed is simulated. This is because the double balun dipole is electrically symmetric and may be modeled by only one monopole, one balun, and one feed line. The narrow walls of the wedge-shaped environment were modeled as radiation boundaries and are shaded. The broad walls of the environment were modeled as electric walls. The broad wall which cuts off the feed monopole from its mirror image is also designated as a symmetry boundary. It was verified

that the radiation patterns were altered by changes in the pattern of the standoffs, but not by variations in the shape of the wedge-shaped simulation environment. The positions of the standoffs forming the horn were adjusted to obtain a 10 dB beamwidth of 69 degrees. The dimensions of the dipole were adjusted to obtain the best impedance match across the operational frequency band. The axes in Figure 6 show the origin of the coordinate system in HFSS. The horn was moved up and down along the z-axis to obtain the flattest phase response within the 69 degree beamwidth as shown in Figure 7. In this way the origin was made to correspond with the phase center of the horn.

It was noted earlier in relation to Figure 4 that radiation could leak out between the standoffs in the vicinity of discontinuities in the line of standoffs. However, HFSS simulations indicated that any cross-polarized components of radiation emanating from the horn in Figure 6 were at least 50 dB down from the co-polarized components.

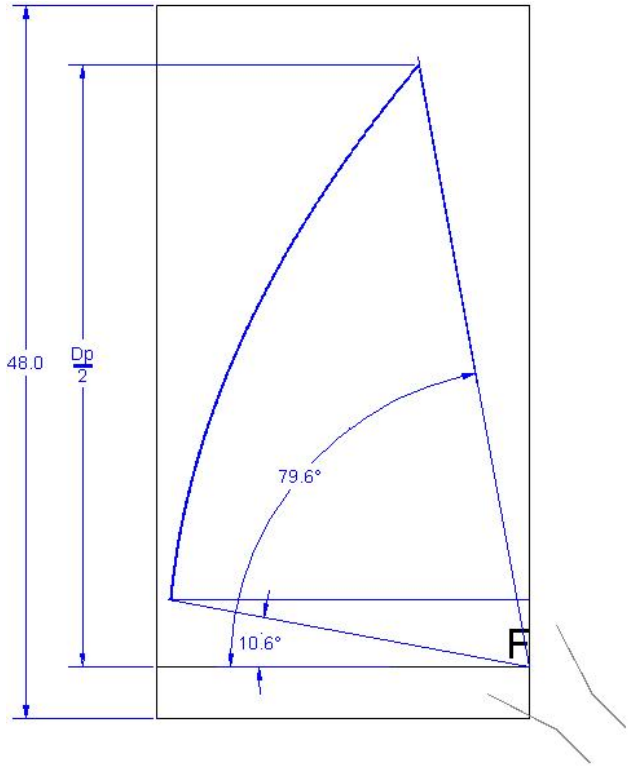

Figure 5 – Initial layout of pillbox antenna.

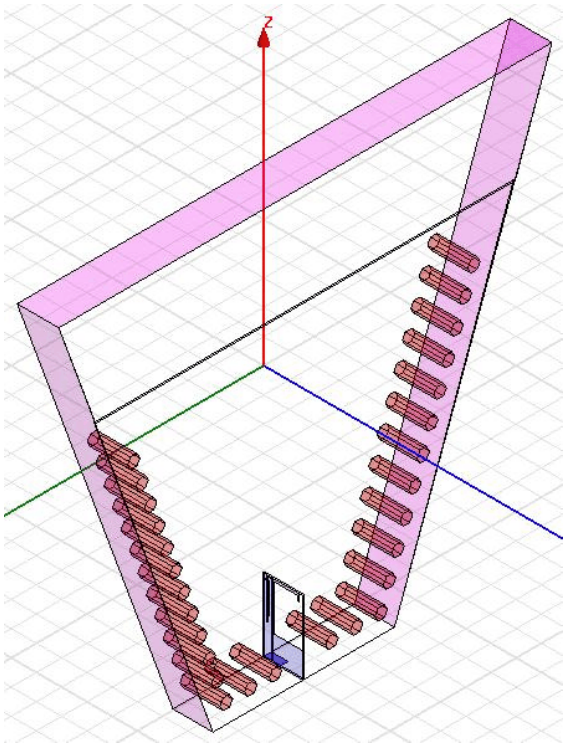

Figure 6 – HFSS model of (half of) a pillbox feed horn (x-axis to left, y-axis to right).

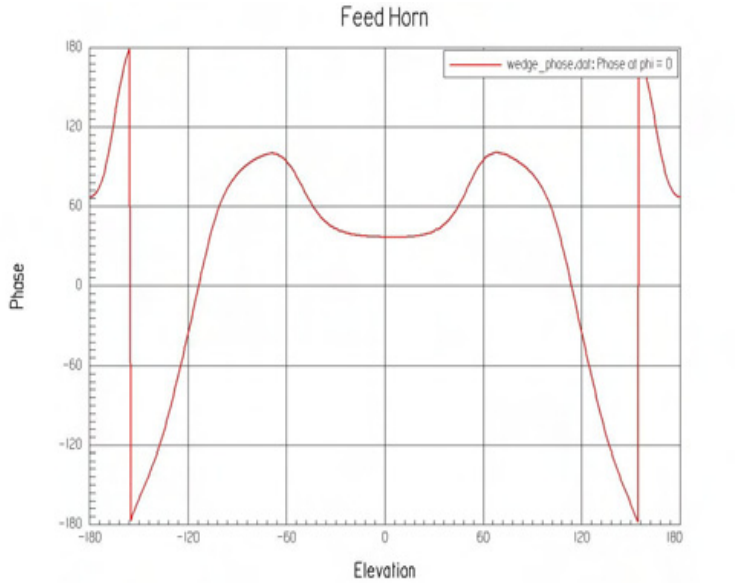

Figure 7 – Radiation phase pattern of pillbox feed horn.

The optimized, phase-centered horn design was exported from HFSS 8.5, converted to AutoCAD format, and inserted in the pillbox design of Figure 5, as shown in Figure 8. Standoffs were employed to form the parabolic reflector. The loci of the centers of the standoffs were found by offsetting the parabola by a distance equal to the radius of the standoffs, and then dividing it into intervals one half inch long. For continuity of the microwave signal, it might be desirable to have the standoffs a little closer together—about 1/10 wavelength[1] —but then they would be too close for easy construction. On the other hand, the standoffs are thick enough that the space between standoffs, as opposed to distance between centers, is much less than 1/10 wavelength.

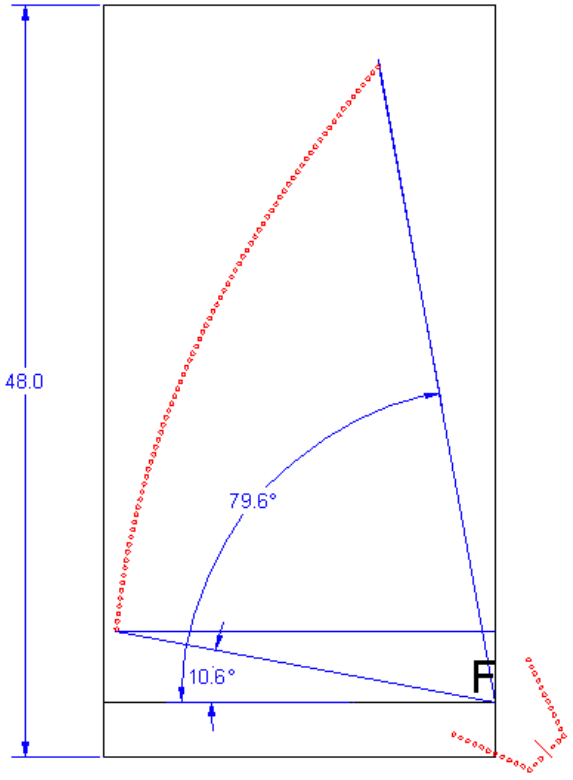

Figure 8 – Positions of the standoffs which form the feed horn and parabolic reflector.

The design of the pillbox was completed by adding structural standoffs to keep the plates parallel. The structural standoffs were added on a 4 inch grid, the size chosen for convenience only. The layout was slightly enlarged so that standoff holes on the edges of the panel would fit. Standoffs remote from the radiation path are identical to the electrically significant standoffs. Standoffs in or near the radiation path were constructed of Delrin

[1] Empirically it has been found that discrete contacts approximately 1/10 wavelength apart satisfactorily approximate a continuous connection.

(acetal resin polymer). It was found that the regular pattern of dielectric standoffs caused diffraction lobes to appear in the radiation patterns. This was remedied by removing as many dielectric standoffs as possible while still retaining sufficient stiffness of the pillbox. Finally, microwave-absorbing foam was added around the edges of the parabola to stop low-level radiation from the feed horn spilling past the parabola. The final configuration of the pillbox is shown in Figure 9.

A double balun dipole was employed to excite the horn because it exhibits a combination of low reflection and wide bandwidth. The dielectric material for the dipole circuit board is 30 mil Rogers RO4350 ($\varepsilon_r = 3.48$, $\tan \delta = 0.0031$). HFSS simulations indicated that the arms of the dipole would be too close to the walls of the pillbox for even moderate power operation. This was remedied by adding a downward protruding “dog-leg” at the end of each dipole arm, as shown in Figure 10. The space between the end of the dipole arm and the wall of the pillbox is 69 mils and the length of the dog-leg is 144 mils. A dipole was checked for overheating as follows. A continuous 10-watt signal in the band between 2.9 and 3.5 GHz was applied to the dipole, apart from the rest of the pillbox antenna. The dipole was periodically viewed with an infrared thermometer. The infrared thermometer indicated perhaps a 5 °F rise, although the readings were uneven. Immediately after the test was completed, it was noted that the dipole was not warm to the touch.

In Figure 11, a photograph of a partially disassembled pillbox array shows the position of the dipole relative to the horn. The base of the dipole is positioned flush with the bottom of the horn.

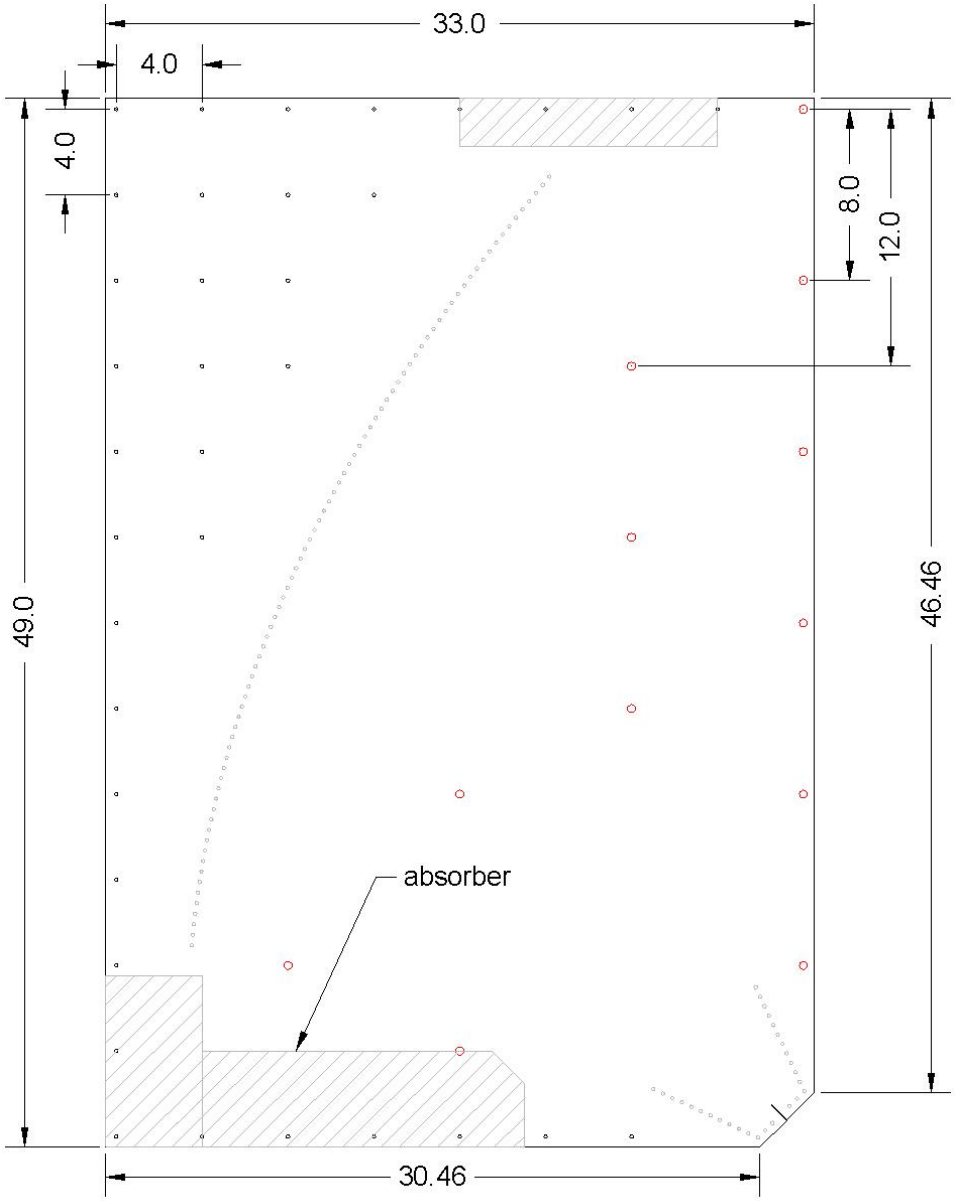

Figure 9 – Completed design of pillbox antenna.

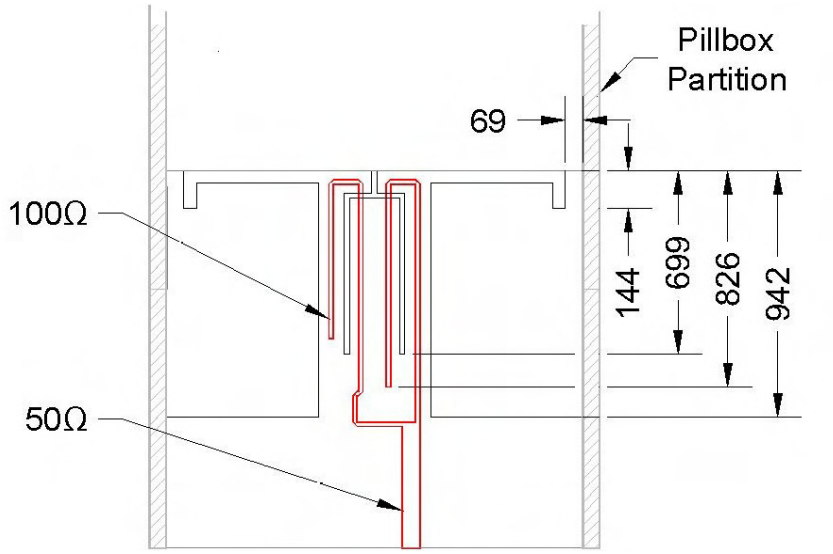

Figure 10 – Dimensions in mils of the dipole exciting the feed horn in the pillbox antenna.

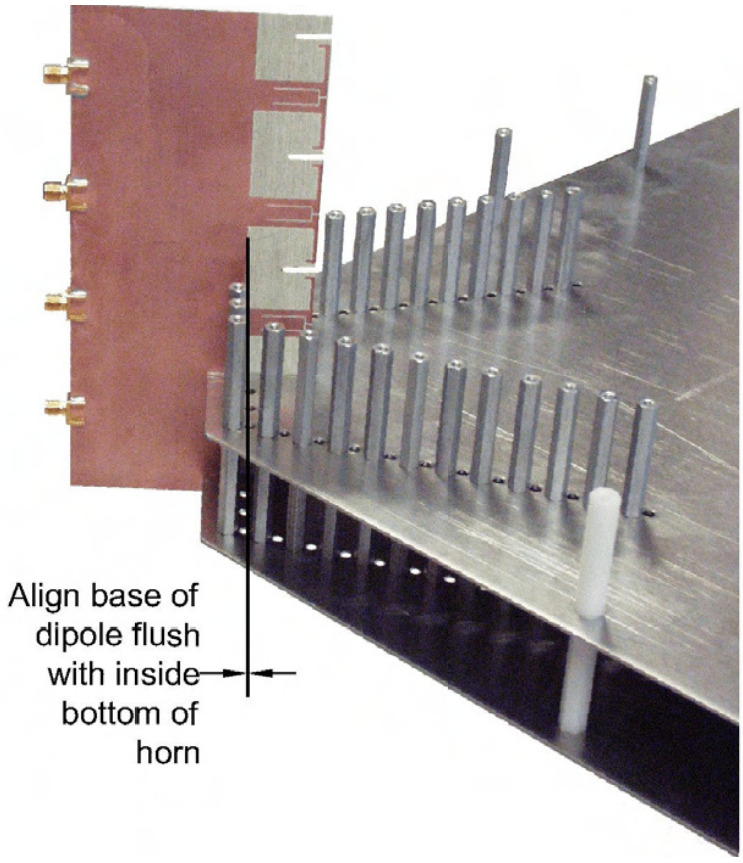

Figure 11 – Partial assembly of pillbox array showing dipole position relative to feed horn.

Shortly before this article was written, the NRL Radar Division's Antenna Section upgraded to HFSS version 11. HFSS version 11 has an improved meshing algorithm that allows it to analyze antennas as large as (and larger than) the pillbox antenna discussed here, incorporating details as small as the dipole feed. Figure 12 shows the HFSS 11 pillbox model. Both broad walls were modeled as perfect electric walls. Furthermore, the inside wall was designated as a symmetry plane. The outside wall has a 31 mil step at the lip of the pillbox to model the thickness of the partitions between pillbox elements. This is shown in Figure 13, which is a rotated detail view of the pillbox model in the vicinity of the dipole. The vantage points in Figures 12 and 13 may be reconciled by noting the coordinate axes in each view. The electric walls on the two sides of the model simulate an infinite array condition in the x-direction. The shaded edges of the model in Figure 12 designate surfaces with radiating boundary conditions while the unshaded edges designate perfect electric boundaries. Only the top edge corresponds to a real radiating surface. The other edges were made radiating surfaces instead of perfectly matched non-radiating boundaries to simulate the presence of absorber. This shortcut was employed because the purpose of the model was to optimize the feed. The simulation was run both including and excluding the thinned dielectric standoff configuration shown in Figure 9.[2] The standoffs did not change the radiation patterns significantly. However, they did increase the reflection coefficient by about 6 dB.

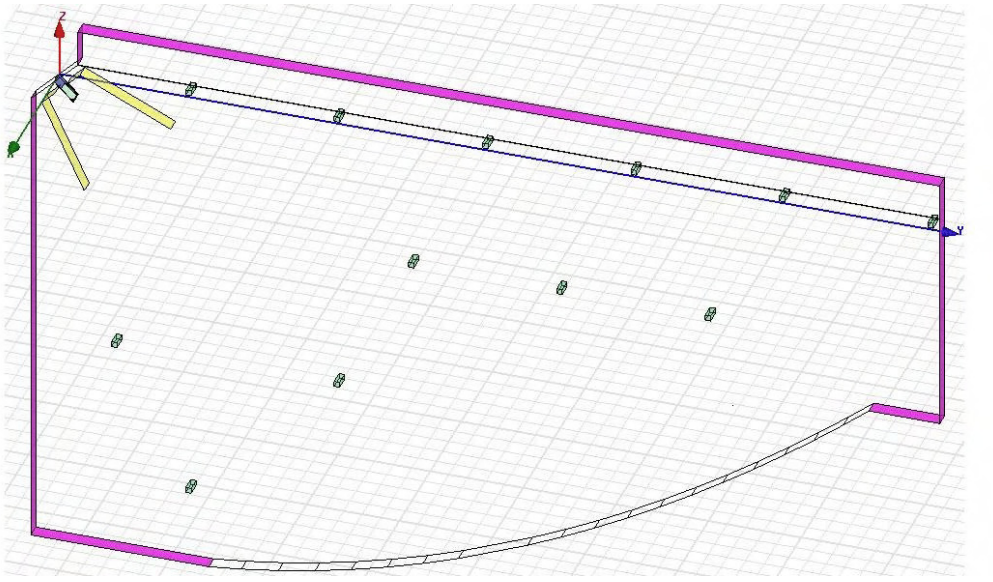

Figure 12 – HFSS model of pillbox with dielectric standoffs. Shaded edges indicate locations of radiation boundaries.

[2] Delrin was modeled with the same dielectric properties as Rogers RO4350, as published dielectric constant values for Delrin range from 3.1 to 3.7.

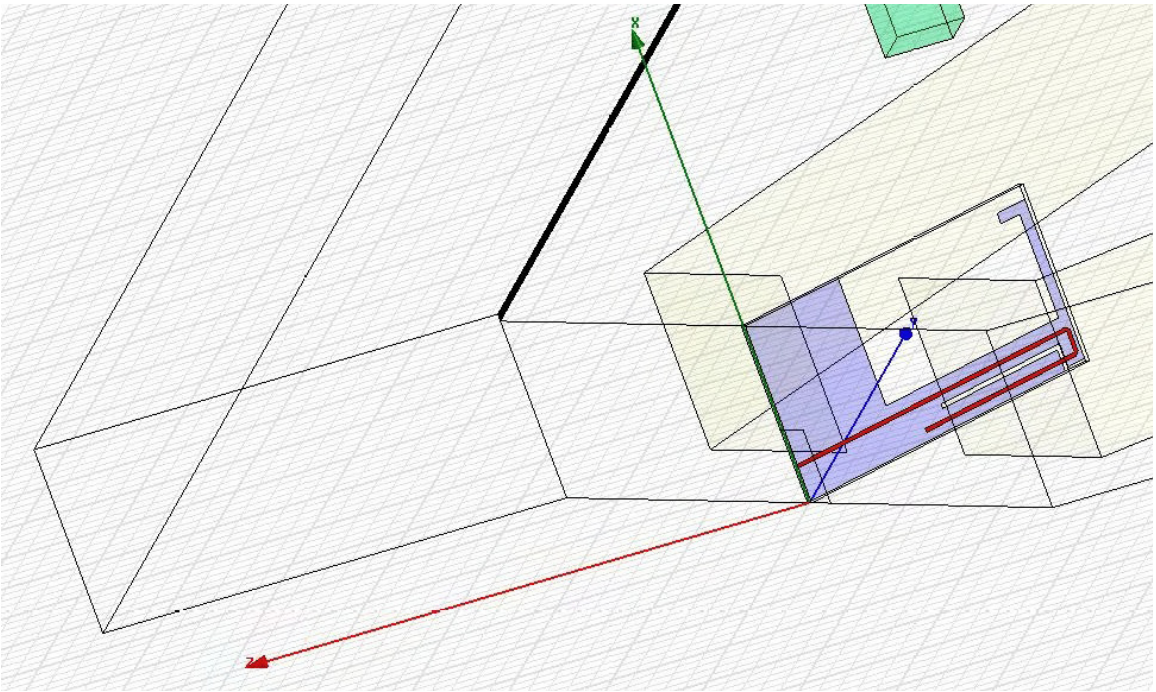

Figure 13 – Detail view of pillbox showing dipole feed and step (dark line) in outside electric wall implemented to model pillbox partition.

4. Comparison of Simulated and Measured Results

Figure 14 shows a plot of the measured coupling between adjacent elements. The coupling is close to the desired level of reflection for the pillbox elements, which serves to emphasize the importance of measuring the active reflection coefficient of the pillbox element. The active reflection coefficient is obtained when all elements of the array are excited by generators with uniform amplitude and linearly progressive phase [4]. The currents that are measured returning to a given antenna port in the array are a combination of the element's self-coupled currents and the mutually coupled currents from all the other elements in the array. In lieu of performing a true active reflection measurement, the four elements of the pillbox array were excited in tandem with a 4-way Wilkinson power divider, which attenuates out-of-phase reflections and passes in-phase reflections. The resulting reflection measurement is then an average of two end elements and two interior elements.

The boundary conditions used in HFSS simulated an element in an infinite array, so the impedance predicted by HFSS is the active impedance. Measuring the impedance of four elements simultaneously with a power divider is a closer approximation of this condition than is the measured impedance of one element excited with other elements passively terminated.

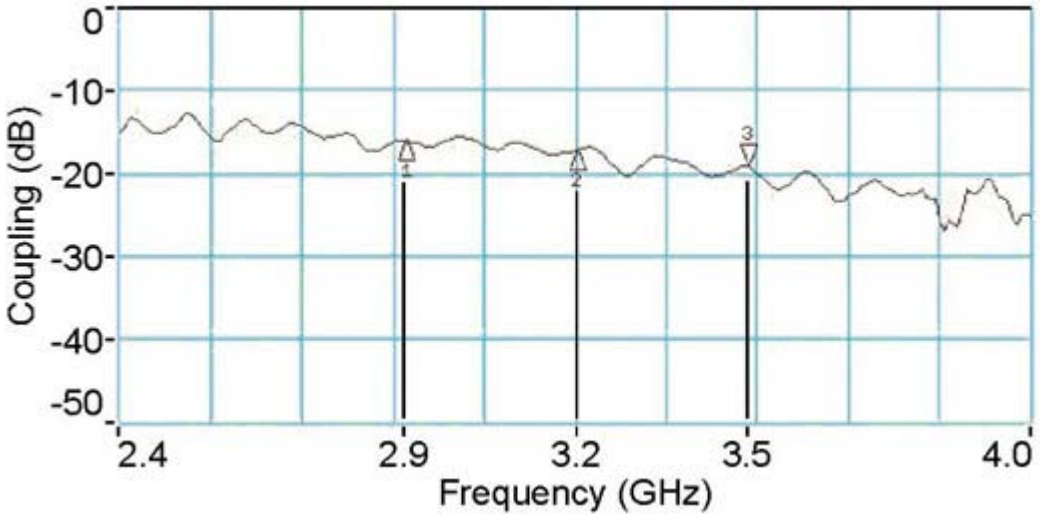

Figure 14 – Measured coupling between adjacent elements in 4-element pillbox array.

Figure 15 shows a comparison of three related reflection coefficients:

1. "measured": The measured reflection coefficient for a 4-element array. The ports of the four pillboxes are combined with a Wilkinson power divider network.
2. "pillbox": The simulated reflection coefficient for (half of) one element with infinite array boundary conditions.
3. "wedge": The simulated reflection coefficient for (half of) just the feed horn in a wedge-shaped environment with infinite array boundary conditions.

The worst measured pillbox reflection is −16 dB and the worst simulated pillbox reflection is −19 dB. Furthermore, it may be anticipated that the measured reflection will improve if a larger power divider is used because there will be more interior elements while still only two exterior elements. For the most part, the differences between the measured and simulated reflection occur at levels below −20 dB, so the agreement between the two may be judged good. The third curve, the simulated reflection for the feed horn alone, has fewer ripples, which is to be expected for a shorter signal path. It is not inconsistent with either the measured or simulated reflection curves for the full pillbox.

It should be noted that the −16 dB reflection at 2.96 GHz is above the design requirement. However, it is anticipated that this level would be lower in larger arrays as the infinite array condition modeled in HFSS is approached.

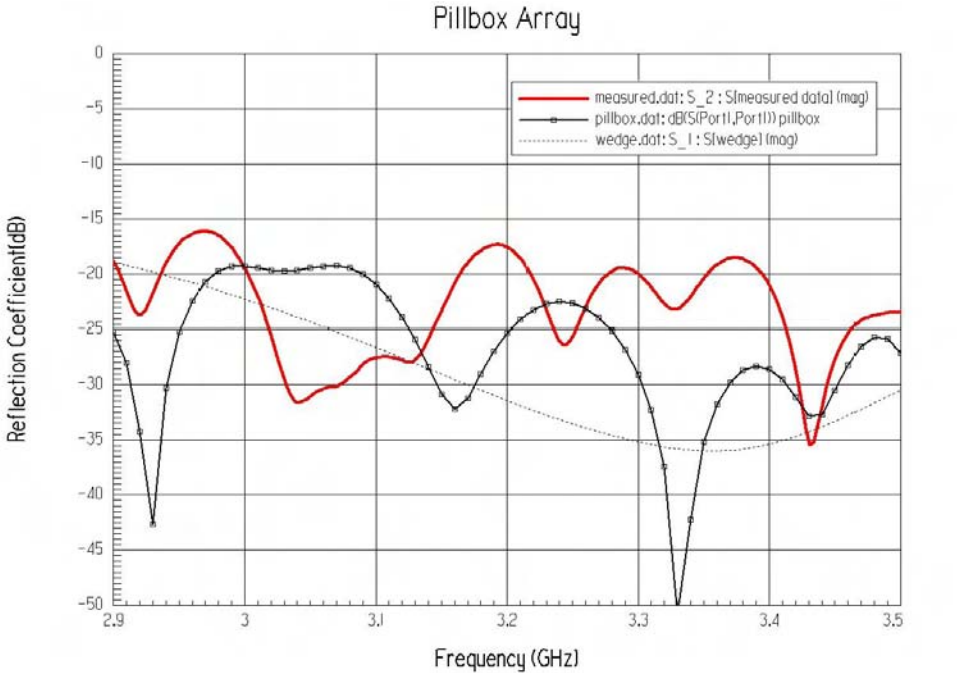

Figure 15 – Measured and simulated reflection coefficients for pillbox antenna.

Figures 16, 17, and 18 show measured and simulated radiation patterns for 2.9 GHz, 3.2 GHz, and 3.5 GHz, respectively. The measured patterns are for a 4-element array fed in tandem with a 4-way Wilkinson power divider. The simulated patterns are for the HFSS model shown in Figure 12. The difference between the peaks of the measured and simulated patterns is fairly close to 6 dB, as would be expected. The most significant difference between the measured and simulated patterns is in the far out sidelobes. The simulated results show higher sidelobes. This is to be expected because the absorber shown in Figure 9 was not included in the HFSS simulation. As noted earlier, the primary reason for running the HFSS simulation was to optimize the design of the dipole shown in Figure 10. From the viewpoint of the dipole it does not matter whether the fields that spill past the parabolic reflector are removed by absorber or radiation boundaries. Either way, they are not reflected back to the dipole.

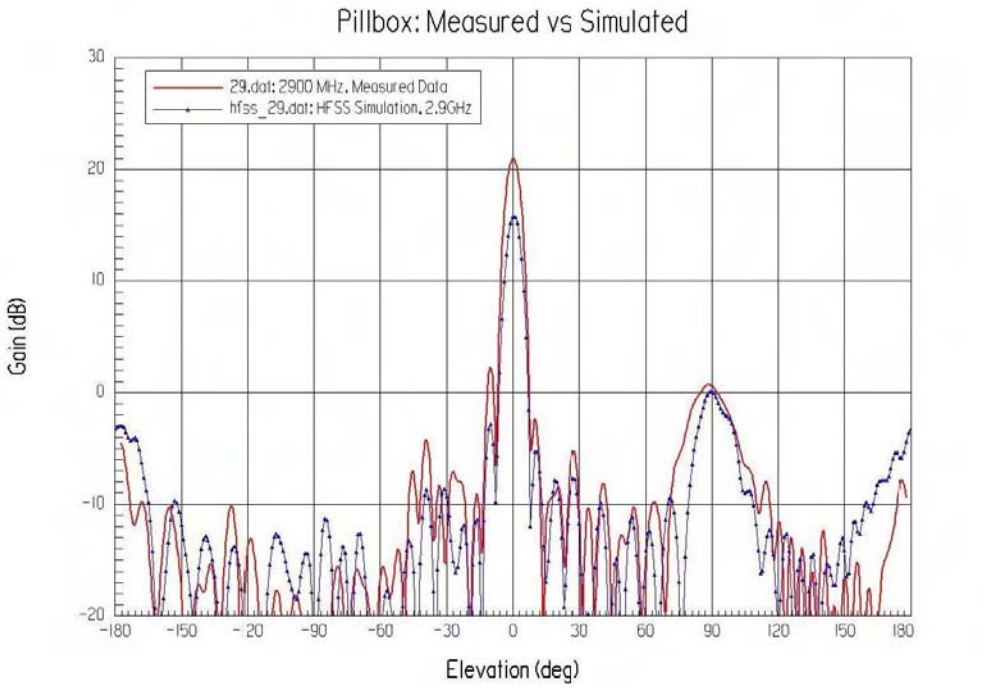

Figure 16 – Measured and simulated radiation patterns for pillbox antenna at 2.9 GHz.

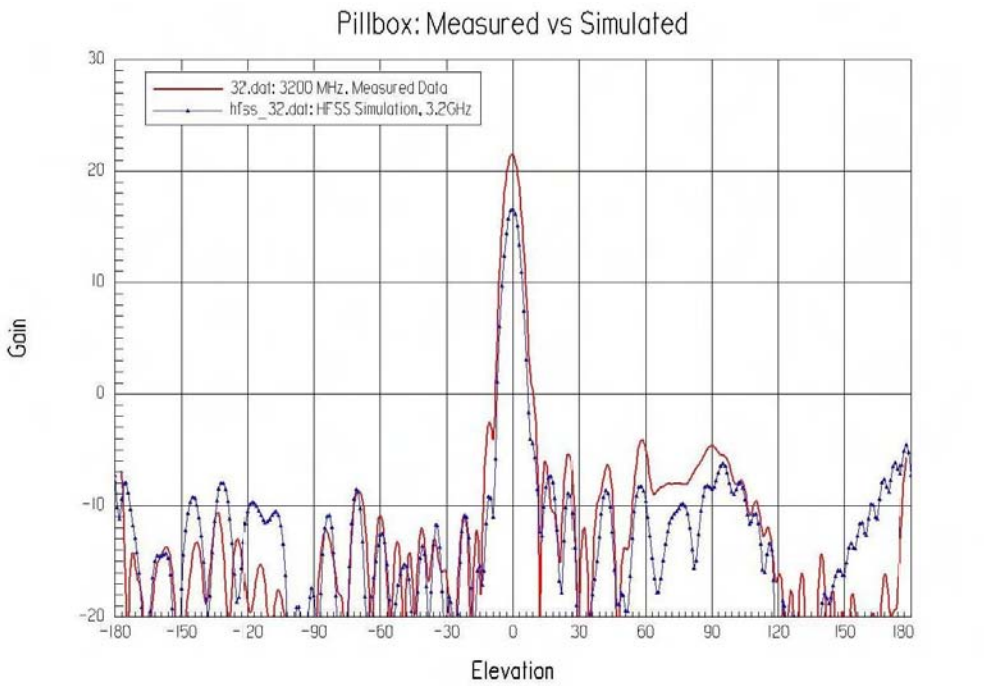

Figure 17 – Measured and simulated radiation patterns for pillbox antenna at 3.2 GHz.

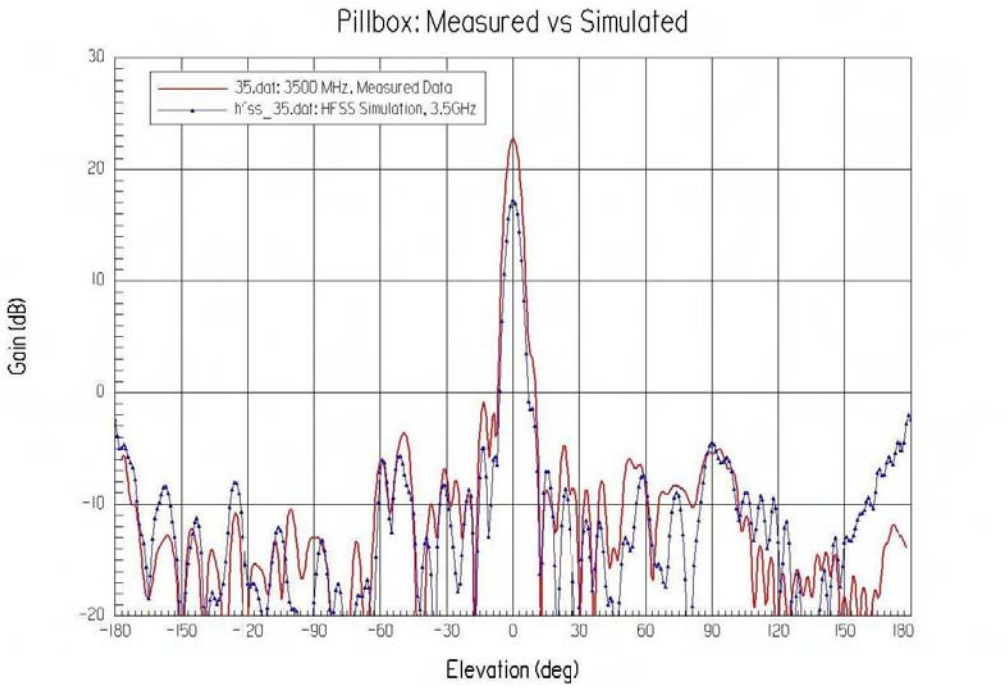

Figure 18 – Measured and simulated radiation patterns for pillbox antenna at 3.5 GHz.

The directivity for a rectangular aperture antenna with uniform illumination [5] is given by

$$D = \frac{4\pi}{\lambda^2} L_x L_y \ , \tag{1}$$

where λ = wavelength, L_x = aperture length, and L_y = aperture width.

For the pillbox antenna discussed here, the vertical extent of the parabolic reflector is 36 inches. Each element has a width of 1.65 inches, so the width of the 4-element array is 6.6 inches. However, the illumination of the aperture is not uniform. The feed horn was designed so that its 10 dB beamwidth corresponded to the angular width of the parabola as viewed from the phase center of the horn. A better approximation of the illumination of the parabola would be a cosine on a 10 db pedestal distribution. The aperture efficiency is derated by a factor of 0.92 for such an illumination taper [6]. Equation (1) multiplied by this factor is plotted in Figure 19 and is designated "Theoretical." The measured peak gains are also shown in Figure 19. Accounting for the losses in the power divider used to excite the array would further improve the comparison. The output ports of the power divider are not accessible, so its losses cannot be measured. However 0.5 dB is a reasonable estimate. With these considerations, the pillbox antenna may be seen to have a measured gain within 1 dB of theoretical, which is more than satisfactory.

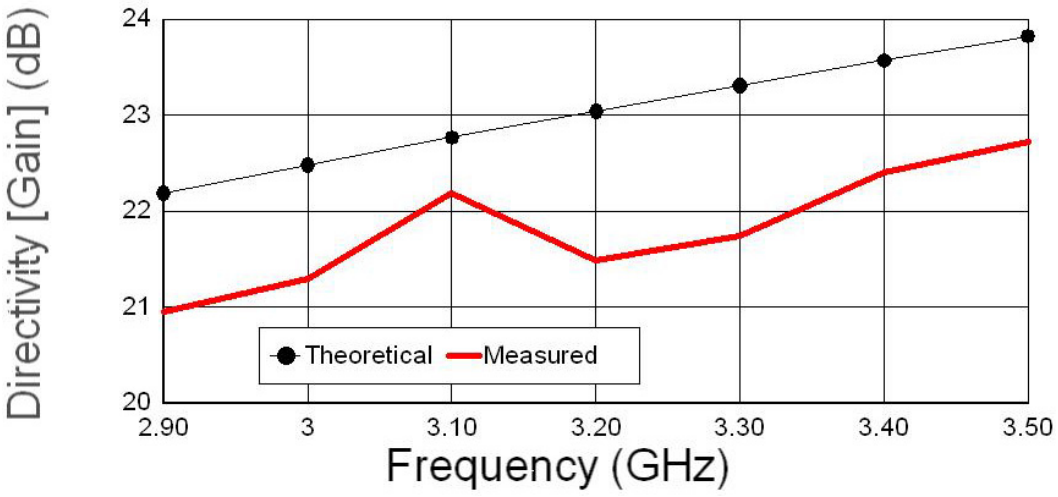

Figure 19 – Theoretical directivity and measured gain for pillbox antenna.

The beamwidth for a line source with a cosine on a 10 dB pedestal illumination taper [7] is given by

$$BW = 1.03\frac{\lambda}{L}\ , \tag{2}$$

where λ = wavelength and L = aperture length.

Using 36 inches for L, the theoretical ("Calculated") and measured beamwidths in the elevation plane are plotted in Figure 20. Although only three data points define the measured curve, the general trend is that the measured beamwidth is slightly thinner than the theoretical beamwidth at low frequencies and slightly fatter than the theoretical beamwidth at high frequencies. This is reasonable. The feed horn was designed to have a 69 degree beamwidth at 3.2 GHz. At 2.9 GHz the feed horn beamwidth should be slightly more, increasing the edge illumination of the parabolic reflector and decreasing the overall beamwidth. At 3.5 GHz, the opposite would be true.

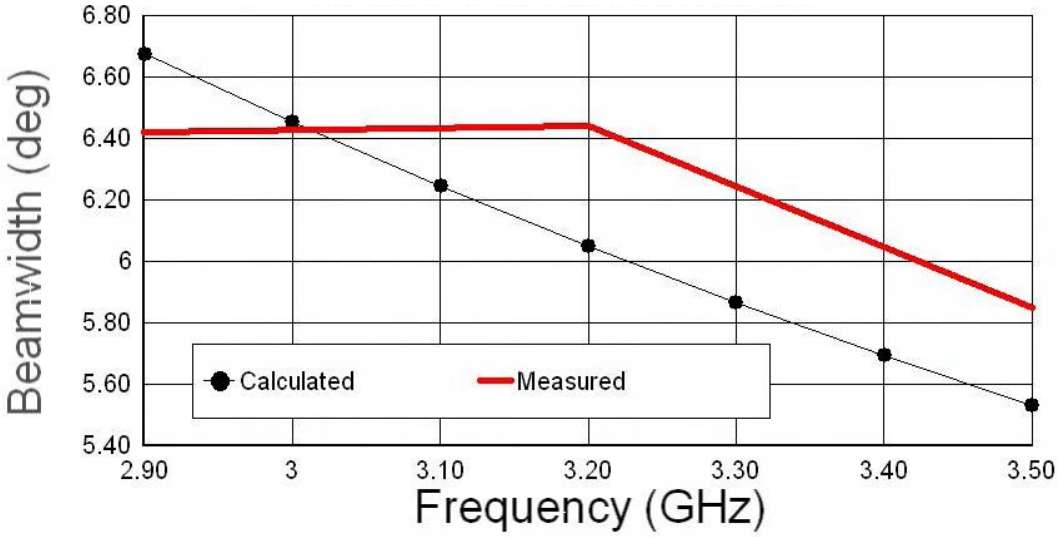

Figure 20 – Theoretical and measured elevation beamwidth for pillbox antenna.

5. Conclusion

This report describes the development of a pillbox antenna with a dipole feed in lieu of a waveguide feed. The main advantage of a dipole feed is that it relieves the congestion that would result from an array of waveguide feeds joined to an array of pillbox antennas. The pillbox antenna described in this report exhibited low losses. This supports the choice of a pillbox element for the DAR array.

6. Acknowledgments

The authors gratefully acknowledge the support of Michael Pollock at the Office of Naval Research and Ron Stapleton at the Naval Surface Warfare Center, Dahlgren Division.

7. References

[1] W. R. Pickles and W. M. Dorsey, "Proposed Coincident Phase Center Orthogonal Dipoles", Antenna Application Symposium, Monticello, IL, Sept. 2007, pp. 107-124.

[2] S. B. Gambahaya, "Design and Implementation of the Pillbox Antenna for SASARII", Masters Thesis, University of Cape Town, Cape Town, South Africa, Dec. 2005.

[3] S. B. Gambahaya and M. R. Inggs, "Design and Implementation of a Pillbox Antenna for an Airborne Imaging Radar", internal paper, Radar Remote Sensing Group, Department of Electrical Engineering, University of Cape Town, South Africa, June 23, 2006. Available at www.rrsg.uct.ac.za/members/sifiso/paper1.pdf (accessed 21 July 2008).

[4] W. Kahn, "Active reflection coefficient and element efficiency in arbitrary antenna arrays", IEEE Trans. Ant. Propagat., vol. 17 (5), pp. 653-654, Sept. 1969.

[5] W. L. Stutzman and G. A. Thiele, Antenna Theory and Design, p. 390, New York: John Wiley & Sons, 1981.

[6] Stutzman and Thiele, p. 188.

[7] Stutzman and Thiele, p. 188.

THE STATE-OF-THE-ART IN SMALL WIDEBAND ANTENNAS

Steven R. Best
The MITRE Corporation
202 Burlington Road
Bedford, MA 01730
sbest@mitre.org
(781) 271-8879

ABSTRACT: In this paper we discuss the performance challenges and fundamental design approaches used in the development of small wideband omnidirectional antennas. The paper begins with a brief review of fundamental antenna performance limitations as a function of antenna size relative to the operating wavelength. We review and discuss a number of small, wideband antenna designs focusing on the techniques used to achieve an impedance match over a wide bandwidth. We compare a number of past and current antenna designs with the intent of identifying the current state-of-the-art in this area.

1. Background Discussion

With the advancement of software defined radios, there is an increasing capability to develop modulated signals (waveforms) that encompass or occupy very wide frequency bandwidths. Often, the usable spectrum or operating bandwidth of the radio itself exceeds the individual waveform bandwidths. Operating bandwidth capabilities of these radios can exceed ratios well in excess of 100:1 and even 1000:1.

At the same time, the size of the associated RF electronic components and IC's continues to decrease. With increasing radio bandwidth and decreasing electronic component size, it is natural that there is a similar desire within the wireless community to simultaneously increase the bandwidth and decrease the size of the system antenna.

However, with any omnidirectional antenna, the operating bandwidth is fundamentally limited by the antenna's volume [1]. For an omnidirectional resonant antenna[1], the approximate limit on operating bandwidth can be determined from the

[1] We define a resonant antenna as one exhibiting a single impedance resonance [$X_A(\omega_0) = 0$, $X'_A(\omega_0) > 0$] or antiresonance [$X_A(\omega_0) = 0$, $X'_A(\omega_0) < 0$] within it defined VSWR bandwidth. ω_0 is the resonant (or tuned) radian frequency, $2\pi f_0$, where f_0 is the frequency in Hz.

inverse of the lower bound on quality factor (Q) as defined by Chu [2] and later refined by McLean [3]. The lower bound on Q or the *Chu limit* is given by

$$Q_{lb} = \eta_r \left(\frac{1}{(ka)^3} + \frac{1}{ka} \right) \tag{1}$$

where η_r is the antenna's radiation efficiency, k is the free space wave number $2\pi/\lambda$, and a is the radius of an imaginary sphere circumscribing the maximum dimension of the antenna. Given the following inverse relationship between the resonant antenna's Q and its fractional matched VSWR bandwidth[2], FBW_V, [4]

$$Q(\omega_0) \approx \frac{2\sqrt{\beta}}{FBW_V(\omega_0)}, \qquad \sqrt{\beta} = \frac{s-1}{2\sqrt{s}} \le 1, \tag{2}$$

one can derive an upper bound on fractional matched VSWR bandwidth by substituting (1) into (2), which results in:

$$FBW_{Vub} = \frac{1}{\eta_r} \frac{(ka)^3}{1+(ka)^2} \frac{s-1}{\sqrt{s}} \tag{3}$$

where s is an arbitrary choice of maximum VSWR defined at the band edges. This upper bound on bandwidth for the resonant antenna is an approximate limit for achievable bandwidth as one can mismatch the antenna at resonance ($s \neq 1$ at ω_0) and achieve a slightly greater bandwidth than with a perfectly matched antenna.

The actual values of Q and bandwidth achieved with a resonant antenna are primarily determined by how effectively the antenna structure fills the spherical volume defined by the value of ka. For small values of ka ($ka << 1$), full utilization of the spherical volume allows the antenna Q to be within approximately 1.5 times the lower bound as demonstrated with the folded spherical helix antenna described in [5] and [6]. Subsequent work on radiation Q limits by Thal [7] showed that realizing a Q within 1.3 to 1.5 times the lower bound, at small values of ka, is the best that can be achieved with a spherical-shaped antenna.

In many practical applications, a spherical-shaped antenna is not a viable option and a cylindrical-shaped antenna is often preferred or necessary, particularly for vehicular platforms. The volume of a spherical-shaped antenna is fixed and conveniently defined

[2] Fractional matched VSWR bandwidth is defined as $(\omega_+ - \omega_-)/\omega_0$, where ω_+ and ω_- are the frequencies above and below the resonant frequency ω_0, respectively, where the VSWR is equal to an arbitrary chosen maximum value s. The VSWR as a function of frequency is determined relative to a characteristic impedance equal to the antenna's resistance at the resonant frequency ($s = 1$ at ω_0).

by any stated value of *ka*. The volume of a cylindrical-shaped antenna is defined by its overall length and diameter and for the same fixed value of *ka*, there are a number of length-to-diameter ratios (or cylindrical volumes) that can be chosen to fit within the same spherical volume. The practical consideration in optimizing the performance of a cylindrical-shaped antenna is that for a fixed value of *ka*, the minimum achievable antenna *Q* (and therefore maximum bandwidth) varies as a function of length-to-diameter ratio. For the same value of *ka*, the spherical-shaped antenna can achieve a lower *Q* than the cylindrical-shaped antenna.

To address the issue of relating the relative performance of cylindrical- and spherical-shaped resonant antennas, a number of efforts have focused on deriving a lower bound on *Q* for arbitrarily shaped antennas. Hansen and Adams address the problem by deriving lower bounds for prolate and oblate spheroids that they apply to cylindrical-shaped antennas [8] – [9]. Gustafsson et al derived fundamental limits for arbitrary-shaped antennas [10] – [11]. As part of their general work, Gustafsson et al derived a lower bound for cylindrical-shaped antennas as a function of their length-to-diameter ratio. Figure 1 presents a graph showing the ratio of the lower bound for cylindrical-shaped antennas ($Q_{lb\text{-}cyl}$) to the lower bound for spherical-shaped antennas (Q_{lb}). For the result shown in Figure 1, it is assumed that the antenna is vertically polarized, electrically small ($ka \leq 0.5$), has a maximum directivity of 1.5, and it exhibits a single impedance resonance within its defined VSWR bandwidth.

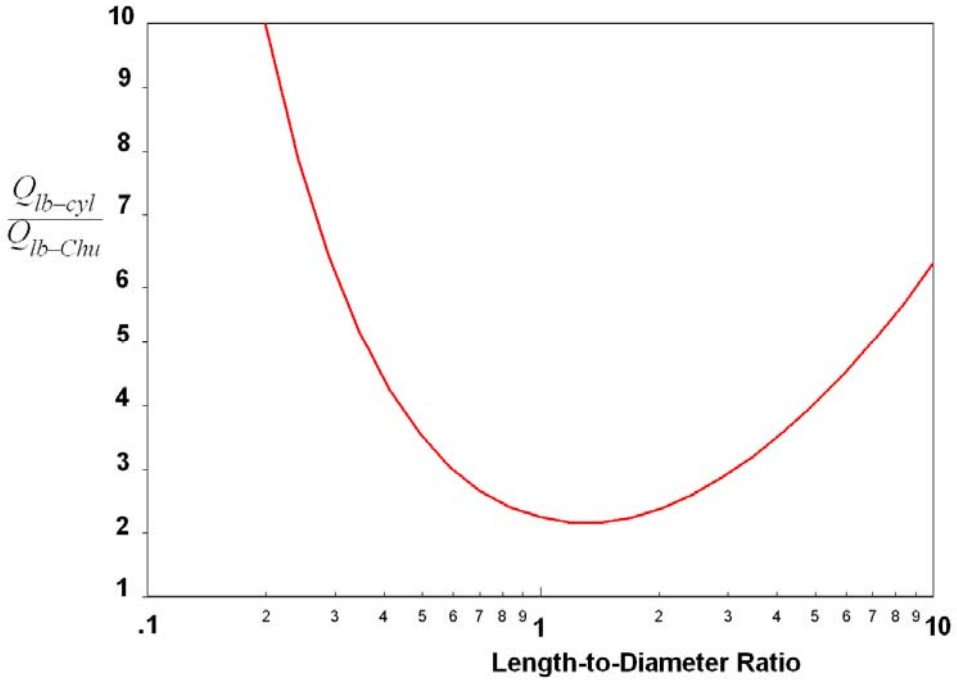

Figure 1. The ratio of the lower bound on *Q* for a cylindrical-shaped antenna to the lower bound on *Q* for a spherical shaped antenna.

To achieve an impedance match and increase the operating bandwidth of a resonant antenna beyond these theoretical limits, one can utilize external reactive matching components in the design of the antenna system. When using lossless, external reactive components to impedance match the antenna, the Bode-Fano limits on matched bandwidth [12] – [14] apply. For an infinite number of impedance matching sections, Bode showed that the maximum achievable bandwidth is given by

$$BW_{\infty} = \frac{1}{Q}\frac{\pi}{\ln\left(\frac{1}{|\Gamma|}\right)} \tag{4}$$

where Γ is the usual reflection coefficient. Substituting the lower bound on Q from (1) into (4), and expressing $|\Gamma|$ in terms of VSWR, s, the maximum fractional VSWR bandwidth that can be achieved with an infinite number of matching sections is

$$FBW_{V\max} = \frac{1}{\eta_r}\frac{(ka)^3}{1+(ka)^2}\frac{\pi}{\ln\left(\frac{s+1}{s-1}\right)} \approx \frac{1}{\eta_r}\frac{\pi(ka)^3}{\ln\left(\frac{s+1}{s-1}\right)};\quad (ka << 1) \tag{5}$$

For a 2:1 maximum VSWR at the band edges, there is a 4.04 times increase in the upper bound on fractional bandwidth relative to that defined in (3) for the same antenna Q. Hansen points out that the Bode bandwidth formula in (4) unrealistically assumes that the reflection coefficient is constant over the bandwidth and that it increases to infinity at the band edges. Hansen [13] - [14] presents corrections to the Bode-Fano matching coefficients and shows that for the 2:1 VSWR bandwidth, the maximum achievable increase in bandwidth is a factor of approximately 3.8 not 4.04.

When impedance matching with external reactive elements, the maximum increase in relative bandwidth occurs with the addition of the first matching section. For a maximum VSWR of 2:1 at the band edges, the maximum increase in bandwidth with a single matching circuit is approximately 2.31 [14]. The relative increase in bandwidth diminishes quickly with an increasing number of sections. Additionally, any loss within the matching elements will increase bandwidth at the expense of overall efficiency. In the design of many wideband antennas, the trade-off between bandwidth and efficiency is an acceptable design compromise.

Instead of adding matching or tuning elements ("circuits") external to the antenna, it is possible to add tuning elements within the antenna design. These matching or tuning elements do not have to be lumped circuit components, rather, their electrical equivalent can be integrated directly within the antenna structure. When integrating equivalent matching circuits within the antenna structure, the Bode-Fano matched bandwidth limits

may provide insight into the achievable increase in bandwidth but they should not necessarily be taken as strict fundamental limits [15].

When integrating impedance matching techniques within the antenna structure with the objective of designing a wideband antenna, it is necessary to develop multiple impedance resonances (and antiresonances) within the defined VSWR bandwidth. With some multiple-resonant antennas, the inverse relationship between *Q* and bandwidth may not hold and it is possible to design the antenna to have a bandwidth greater than the inverse of the lower bound on *Q* for the single resonant antenna [15] - [16]. In designing wideband, multiple resonant antennas, it must be recognized that higher-order modes are likely present and the radiation pattern of the antenna may not be consistent with that of a fundamental dipole (monopole) over the entire operating band.

The final points addressed here are the usual performance trade-offs that occur in the design of small wideband antennas. Typically, the significant design challenge is achieving a matched VSWR at the low end of the operating band where the antenna may be electrically small. The next design challenge is usually maintaining acceptable radiation patterns over the entire operating band, particularly at the upper frequencies where the antenna may be electrically large.

Oftentimes, the design engineer chooses the maximum antenna size based on maintaining reasonable radiation patterns over the entire bandwidth and then optimizes the design for the best impedance match at the low end of the band. In many instances it may not be possible to achieve an acceptable match at the low end of the band, particularly if high radiation efficiency is desired. Many times, radiation efficiency is sacrificed over the entire bandwidth to achieve the desired impedance match. In these designs, the radiation efficiency and gain is usually lowest at the lowest frequency.

This raises the issue of defining a limit on realized gain as a function of antenna size and achievable bandwidth. If it is assumed that the antenna is matched over some defined bandwidth, so that mismatch loss is not a significant factor in establishing realized gain, it is desirable to be able to define a limit on gain as a function of the antenna's electrical size (*ka*) at the lowest end of the operating band and the desired bandwidth. In this case, reduced gain at the low end of the band is primarily established by reduced radiation efficiency. It is assumed that the antenna is electrically small at the lowest operating frequency and that its directivity would be approximately 1.5 for a dipole or 3 for a monopole. At this point, a fundamental gain limit of this type does not exist and it is not possible to compare practical antennas against fundamental limits.

2. The Goubau Antenna

One of the most referenced, small wideband antennas is the Goubau antenna [17] - [19], depicted in Figure 2. It is often considered to be the standard to which other small,

wideband antennas should be compared. The antenna was developed by Georg Goubau and Felix Schwering in the mid-1970's. It has an overall height of 4.3 cm (1.7 in.) and a cylindrical diameter of 12.3 cm (4.84 in.). Goubau's measured results indicate that the antenna operates with a maximum 2:1 VSWR over a frequency range of approximately 470 – 890 MHz, a 1.9:1 bandwidth ratio.

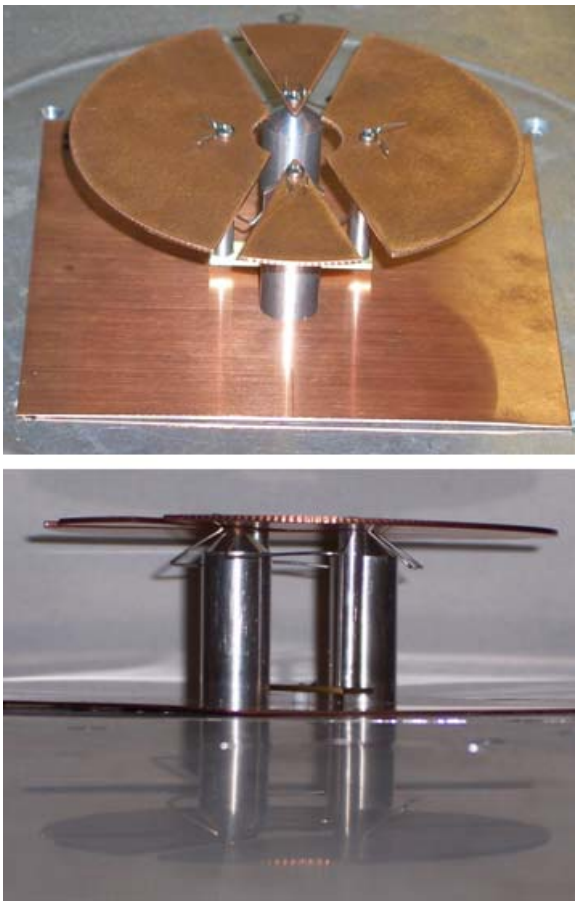

Figure 2. Photograph of the Goubau antenna. The antenna has an overall height of 4.3 cm and a cylindrical diameter of 12.3 cm.

The design and operation of the Goubau antenna are described in detail in the open literature [17] – [19] and will not be presented here. The performance properties of the Goubau antenna shown in Figure 2 were measured and simulated using CST's Microwave Studio [20]. Measured and simulated VSWR of this antenna are shown in Figure 3. With the simulated antenna, the design focused on achieving a VSWR less than 2:1 over the entire operating band. The operating frequency range for the simulated antenna with this criterion is 490 – 865 MHz, a bandwidth ratio of 1.77:1, slightly less than that described by Goubau. In the case of the fabricated antenna, the design focused

on maximizing the antenna's bandwidth. The antenna operated over a frequency range of 463 – 916 MHz, a bandwidth ratio of 1.98:1, however, the maximum VSWR over this operating band is 2.43:1. For many wideband applications, this is considered an acceptable VSWR.

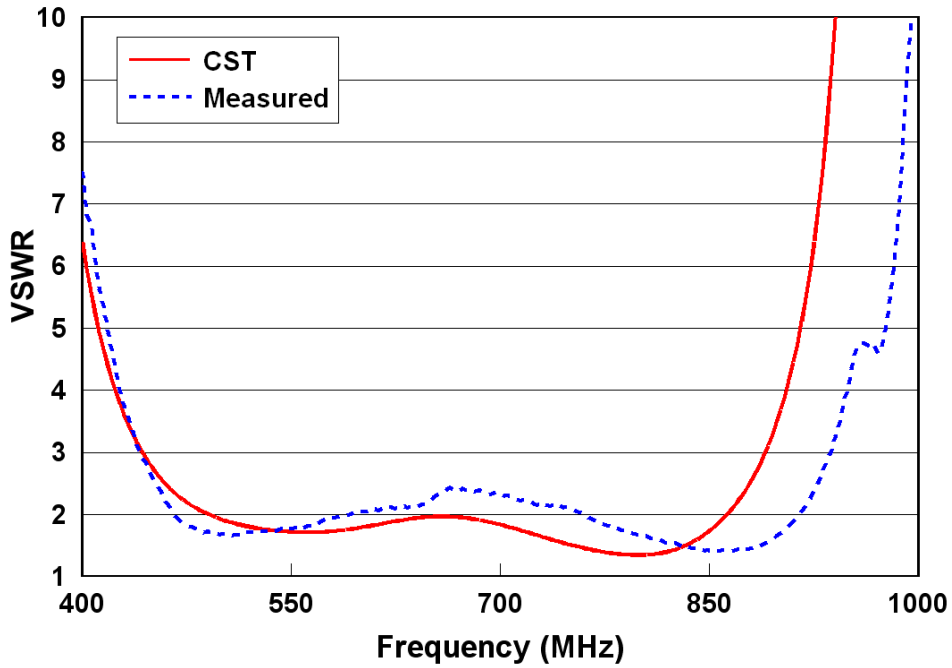

Figure 3. Simulated and measured VSWR of the Goubau antenna.

Comparing the bandwidth of the Goubau antenna to the theoretical limits on bandwidth involves two issues that must be considered. First, there is the issue of choosing the frequency at which to define the value of *ka*. With a resonant antenna, *ka* is defined at the resonant frequency, which is approximately at the center of the operating band. Considering a wideband antenna, the center frequency of the operating band may not be relevant since the real design challenge is achieving the desired impedance match at the lowest frequency in the operating band. For this reason, we choose to compare the relative performance of the wideband and resonant antennas at a *ka* determined for the lowest operating frequency of the wideband antenna. For a relatively small value of *ka* ($ka << 1$), the operating band of the resonant antenna will likely not extend much below this lowest frequency and the comparison will be valid. If the value of *ka* approaches or exceeds 1, then a relative comparison is probably of minimal interest since the antennas are not electrically small.

The second issue that must be considered is the fact that to achieve a wide bandwidth with a relatively small antenna, the structural design of the antenna must be such that multiple impedance resonances are formed within the antenna's operating band.

This multiple resonance impedance matching is illustrated with the simulated impedance of the Goubau antenna shown in Figure 4. The impedance characteristics shown in Figure 4, where there is a resonance, antiresonance and resonance is often referred to as double-tuning. When an antenna exhibits multiple impedance resonances, the fundamental limits defined for the resonant antenna do not apply. The question to consider is the following: Does comparison to these limits provide some insight into how well the wideband antenna performs?

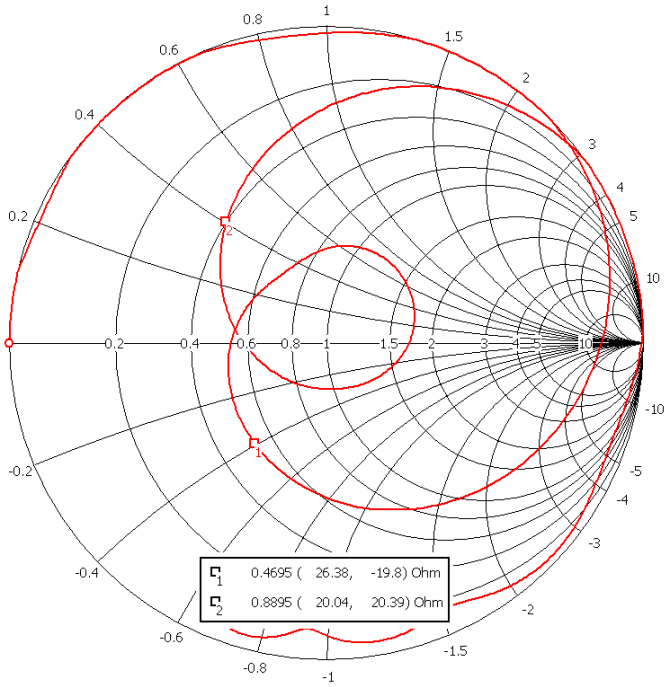

Figure 4. Simulated impedance of the Goubau antenna.

The Goubau antenna has an overall height of 4.3 cm and a cylindrical diameter of 12.3 cm. For these dimensions, the value of a is approximately 7.5 cm. The cylindrical length-to-diameter ratio is approximately 0.7. Note that the calculation of the length-to-diameter ratio must include the antenna's image in the ground plane. Choosing the lowest operating frequency of 490 MHz (for the simulated antenna), the value of ka is approximately 0.77. From (3), with s = 2 and η_r =1, the maximum achievable fractional matched VSWR bandwidth for a resonant, spherical-shaped antenna is determined to be approximately 20.3%. Considering that a resonant, spherical-shaped antenna can, at most, achieve a bandwidth within 76.9% of this value[3] [7] and that the resonant, cylindrical-shaped antenna can achieve a bandwidth within 37.6% of the spherical-

[3] At a ka of 0.65, Thal showed that the Q of the spherical-shaped antenna can approach the Chu lower bound to within a factor of approximately 1.3.

shaped antenna (from Figure 1), the maximum achievable bandwidth for the cylindrical-shaped antenna, for ka = 0.77, is approximately 5.87%. Considering the Bode-Fano matching limits with an infinite number of tuning circuits, this bandwidth could increase by a factor of 3.8 to 22.3%. This roughly translates into a bandwidth ratio of approximately 1.23:1. The bandwidth ratio of the simulated Goubau antenna is approximately 1.77:1, illustrating how well the multiple resonant antenna performs and that comparing its bandwidth to the fundamental limits for a single resonance antenna is not relevant.

3. The Freidman Antenna

When evaluating the performance of the Goubau antenna, Friedman [19] presented another wideband antenna design, shown in Figure 5. This antenna was designed for the purpose of achieving a 2:1 VSWR over a 2:1 frequency band. Friedman's antenna has an overall height of 6.48 cm and a cylindrical diameter of 18.42 cm. These dimensions represent an approximate physical scaling factor of 1.5 relative to the Goubau antenna. The antenna's length-to-diameter ratio is 0.7, essentially the same as that of the Goubau antenna. The operating frequency range of the antenna, as measured by Friedman, is approximately 327 – 610 MHz, an actual bandwidth ratio of 1.86:1, which is similar to that of the Goubau antenna.

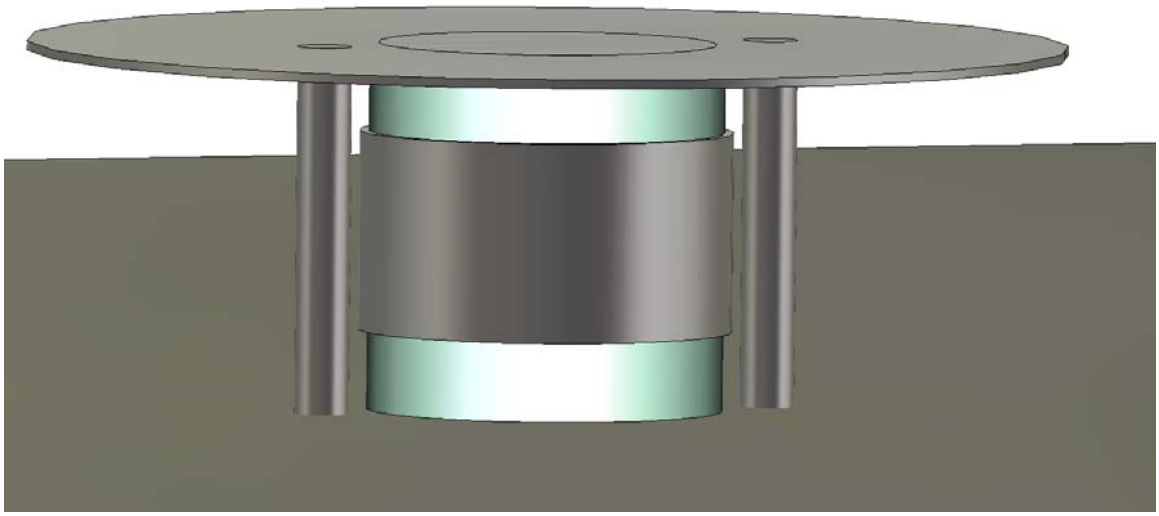

Figure 5. The Friedman wideband antenna. The antenna has an overall height of 6.48 cm and a cylindrical diameter of 18.42 cm.

Microwave Studio was used to verify and characterize the performance of the Friedman antenna. The simulated VSWR of the antenna is presented in Figure 6. The

antenna operates over a frequency range of 328 MHz – 618 MHz, a 1.88:1 bandwidth ratio. The maximum VSWR over the operating band is approximately 2.43:1. These performance characteristics differ from the Freidman measurements but they are very similar to the results achieved with the fabricated Goubau antenna shown in Figure 2. When the Friedman antenna was slightly modified to achieve a maximum VSWR of 2:1 over its operating band, the frequency range decreased to 342 – 596 MHz, a 1.74:1 bandwidth ratio. The VSWR of the modified antenna is shown in Figure 7. These results are very similar to those of the simulated Goubau antenna, where the maximum VSWR was also kept under 2:1 over the operating band. As expected in both cases, allowing a higher VSWR in the middle of the operating band allows the antenna to exhibit a wider bandwidth.

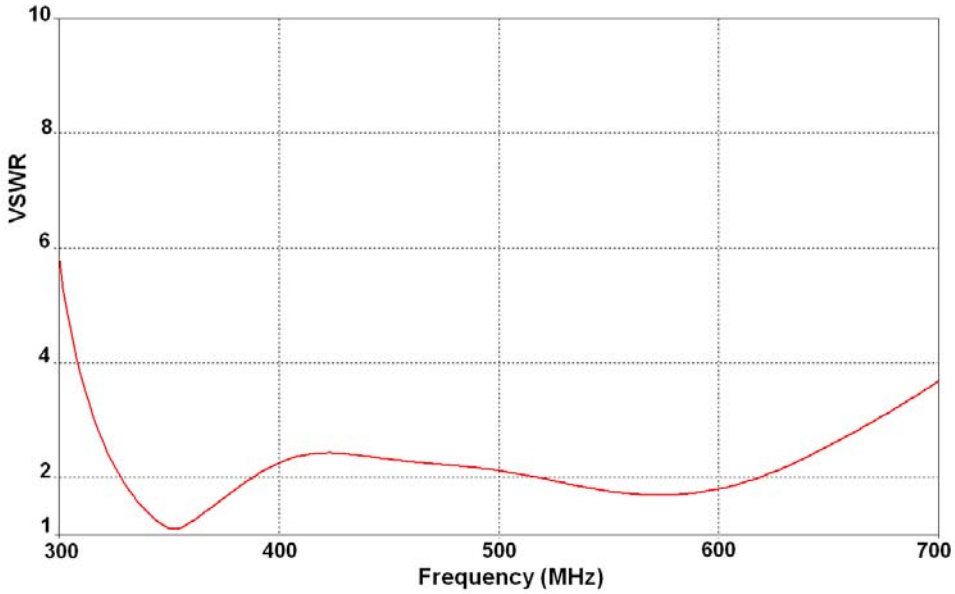

Figure 6. Simulated VSWR of the Friedman antenna. The antenna operates with a maximum VSWR of 2.43:1 over a frequency range of 328 – 618 MHz, a 1.88:1 bandwidth ratio.

There are two issues that will be consider using the Friedman antenna. The first is a direct comparison to the Goubau antenna so that we can establish a reasonable method of comparing wideband antennas that have different dimensions and operate at different frequencies. The second is an evaluation of the design process used to achieve the multiple impedance resonances or double-tuning.

If several wideband antennas have the same dimensions and are matched at the same low-end frequency, a direct comparison of antenna bandwidth is meaningful. If the antennas do not have the same dimensions and/or do not operate over the frequency

range, a direct comparison of the antenna designs in terms of only their bandwidths may be misleading.

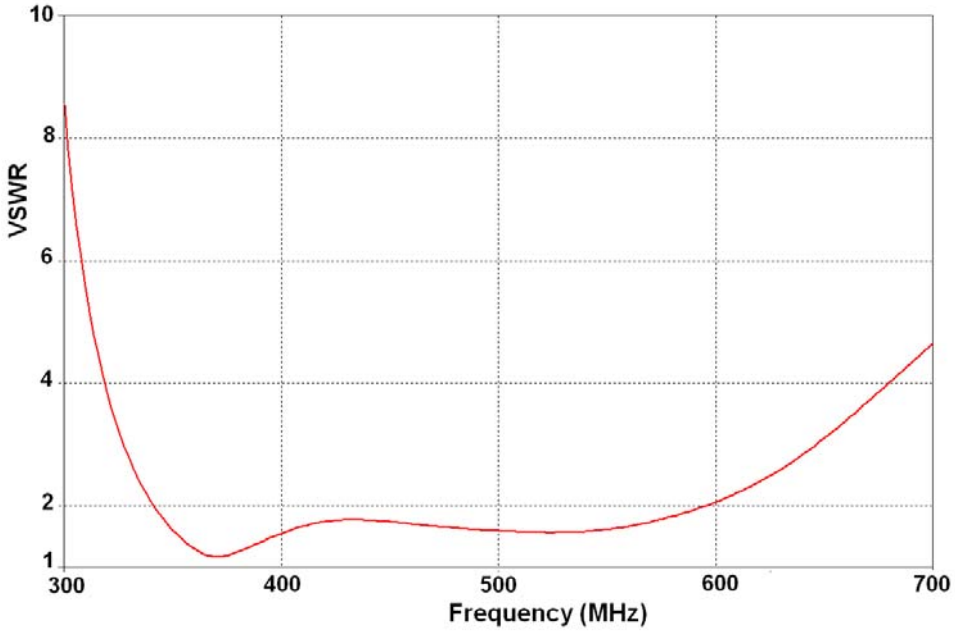

Figure 7. Simulated VSWR of a modified Friedman antenna. The antenna operates with a maximum VSWR of 2:1 over a frequency range of 342 – 596 MHz, a 1.74:1 bandwidth ratio.

At the most fundamental level, the maximum achievable operating bandwidth is directly a function of the antenna's volume [1]. For spherical-shaped antennas, the maximum achievable bandwidth is directly a function of $(ka)^3$, as stated in (3). For cylindrical-shaped, vertically-polarized antennas, the maximum achievable bandwidth is a function of volume and to a great extent the overall height [21].

If the cylindrical volume were the only factor defining maximum achievable bandwidth, the minimum ratio of $Q_{lb\text{-}cyl}/Q_{lb\text{-}Chu}$ in Figure 1 would occur at a value of $1/\sqrt{2}$ (0.707), the value of length-to-diameter ratio necessary for achieving maximum cylindrical volume in a sphere of any radius a. The minimum value of $Q_{lb\text{-}cyl}/Q_{lb\text{-}Chu}$ occurs at a length-to-diameter ratio of approximately twice this value, $\sqrt{2}$ (1.41), illustrating that height, in addition to volume, is substantial in establishing bandwidth.

The issue now is to define some criterion for stating the relative effectiveness of the cylindrical-shaped antenna design in establishing bandwidth so that different design approaches can be compared. The primary issue to consider in this criterion is the fact that antennas having smaller values of ka at their lowest operating frequency are not

theoretically able to achieve as much bandwidth as antennas having larger values of *ka*. The proposed criterion to compare the achieved bandwidth for the designs considered in this paper (the Comparison Factor) is

$$CF = \frac{BWR}{(ka)^3}\frac{d}{l} \tag{6}$$

where *BWR* is the operating bandwidth ratio, *d* is the antenna's overall diameter and *l* is the length or height of the antenna, including its image in the ground plane. A higher value of CF implies that a given antenna design is better at achieving wide bandwidth in combination with its size and lowest matched operating frequency. This proposed comparison factor is not intended to guarantee that the antenna with the highest CF value is the best choice for a given application. Oftentimes, trade-offs between size and bandwidth are a necessary part of the design process. For the Goubau and Friedman antennas having VSWR's less that 2:1 over their entire operating bands, the values of CF are 11.09 and 9.4, respectively, indicating that the Goubau antenna is a slightly better design. No attempt was made to reduce the size of the Friedman antenna to match that of the Goubau antenna since its overall dimensions are essentially scaled by a factor of 1.5.

From this point forward, the focus will turn to an examination of the design approach used to implement multiple resonances or double-tuning within the Friedman antenna structure. The primary starting point of the Friedman design is the central conical-cylinder and top-hat shown in Figure 8. While the parallel capacitance within the structure is the dominant factor, both the series inductance and parallel capacitance establish the primary resonance. The series inductance is established by the conductor length along the outside of the conical-cylinder structure while the parallel capacitance is established by the conical section near the feed point and the top-hat. The impedance of this antenna is shown in Figure 9. Its first resonance occurs at a frequency of 332 MHz, where the antenna is not well matched.

The next step in the design process is to introduce another tuning circuit and create the impedance loop that is characteristic of a double-tuned antenna or circuit. The additional tuning circuits are the shorting posts shown in Figure 10, which predominantly have the effect of parallel inductors. Note that they are not placed at the feed point so they do not have the same effect as placing parallel inductors at the feed point. Their number, placement and diameter have a significant effect on the antenna impedance. Note also that full equivalent circuit models of the antenna structure are provided by Freidman [19] and are not repeated here.

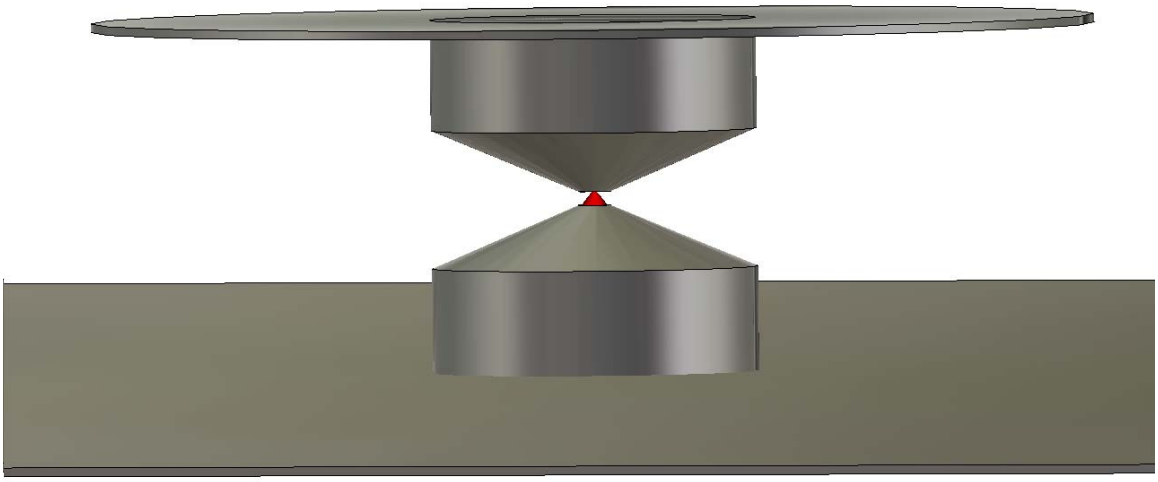

Figure 8. Depiction of the basic structure of the Friedman antenna. The central conical-cylinder structure and top-hat are primarily utilized to add parallel capacitance.

The impedance of the antenna with the two shorting posts is presented in Figure 11. The impedance loop associated with the double-tuning is now evident, however, the antenna is not yet matched. The next step in the matching process is to move the impedance loop so that it is closer to the center of the Smith chart. This is accomplished by adding parallel capacitance near the feed point. In Friedman's design, parallel capacitance is added by placing a metal sleeve around the central cylinder structure of the antenna. The metal sleeve stands off of the central cylinder via a Teflon sleeve. This final configuration was previously shown in Figure 5. The final impedance of the Friedman antenna is shown in Figure 12. The movement of the impedance loop to the center of the Smith chart is evident.

Recently, there have been a number of small, wideband antennas presented in the literature. All essentially incorporate the same basic principles that were used with the design of the Freidman antenna. Each has a central structure and top-hat to introduce parallel capacitance. This is followed by the addition of secondary structures to introduce double-tuning. Finally, series inductance and/or parallel capacitance are added to the antenna structure to achieve an impedance match. We will consider several of these recent designs in the next section.

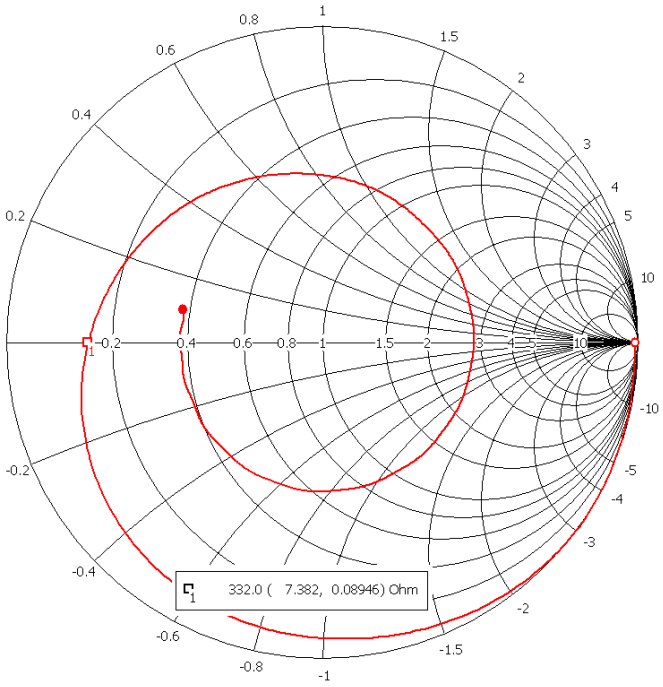

Figure 9. Impedance of the basic structure of the Freidman antenna. With the parallel capacitance being the dominant tuning circuit, the characteristic loop associated with double-tuning is not yet present.

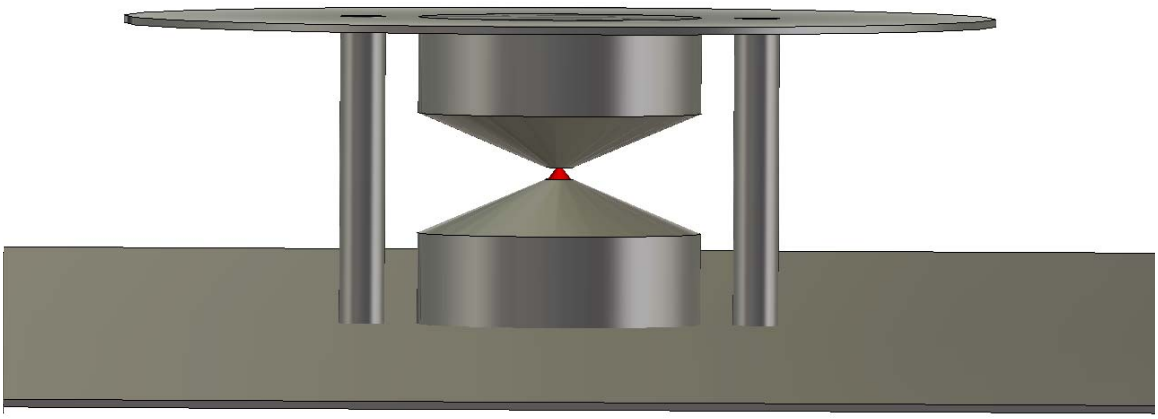

Figure 10. Depiction of the Friedman antenna with the two shorting posts included in the design.

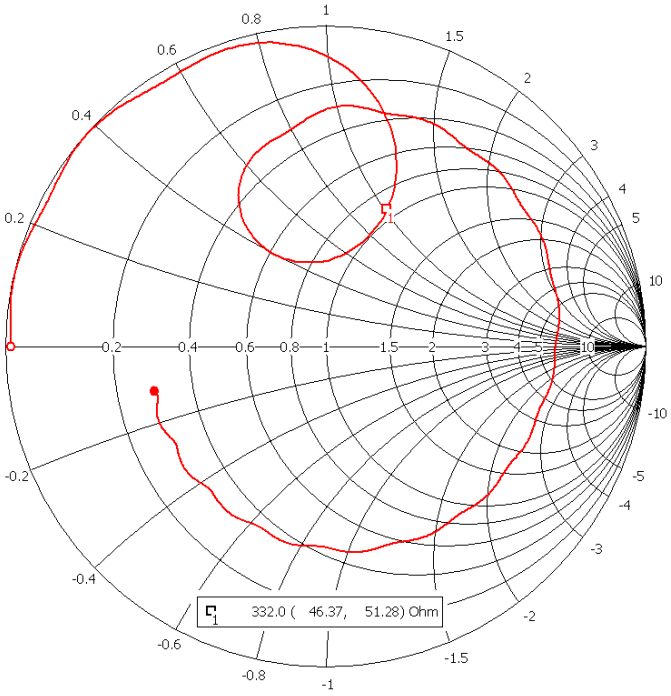

Figure 11. Impedance of the basic structure of the Freidman antenna with the shorting posts added. The impedance loop that is characteristic of a double tuned circuit is now evident.

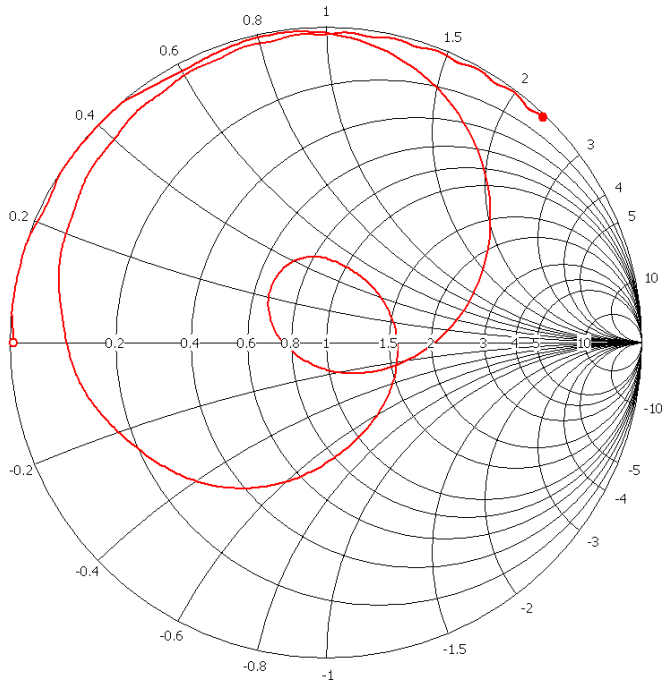

Figure 12. Impedance of the matched Freidman antenna.

4. Recent Small Wideband Antenna Designs

There have been several small wideband antennas described in the recent literature. When these designs are described, there is usually no comparison with existing wideband designs and the reader is uncertain if the design provides a fundamental improvement in the bandwidth-to-size ratio. The designs considered here include one described by the author at the 2006 *Antenna Applications Symposium* [22], another by C. B. Ravipati [23], and one by Nakano et al [24].

The first of these designs considered is the small wideband antenna described in [22]. The antenna is shown in Figure 13. It has the same dimensions as the Goubau antenna, a height of 4.3 cm and an overall diameter of 12.3 cm. The antenna's impedance and VSWR properties are presented in Figures 14 and 15, respectively. Similar to the Friedman antenna, the intent of this design was to achieve a 2:1 VSWR in excess of a 2:1 frequency band. This objective was marginally exceeded in that the antenna exhibits a frequency bandwidth of 2.32:1, operating from 547 – 1272 MHz.

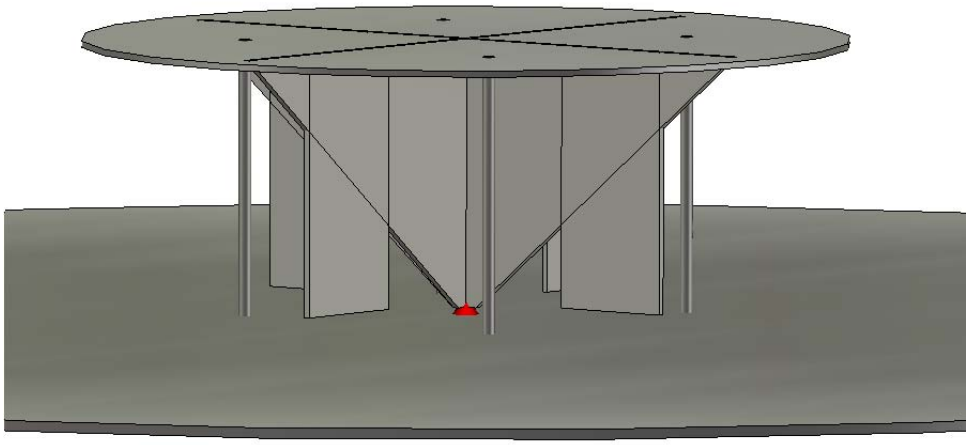

Figure 13. Depiction of the small wideband antenna described in [22].

While this antenna has a wider frequency bandwidth than the Goubau antenna, its lowest operating frequency is substantially higher, resulting in a larger value of *ka* at the low end of the band. The value of *ka* at 547 MHz is approximately 0.86. With a larger value of *ka* at the lowest operating frequency, the antenna naturally has the capability of achieving a wider bandwidth. This is consistent with concept that if the volume of the Goubau antenna were increased, a wider bandwidth should be realizable. To appropriately compare the two antennas, the values of CF are compared. The CF value of this antenna is 5.23 versus Goubau antenna's CF value of 11.09. The Goubau antenna is a more effective design in terms of its bandwidth-to-size ratio.

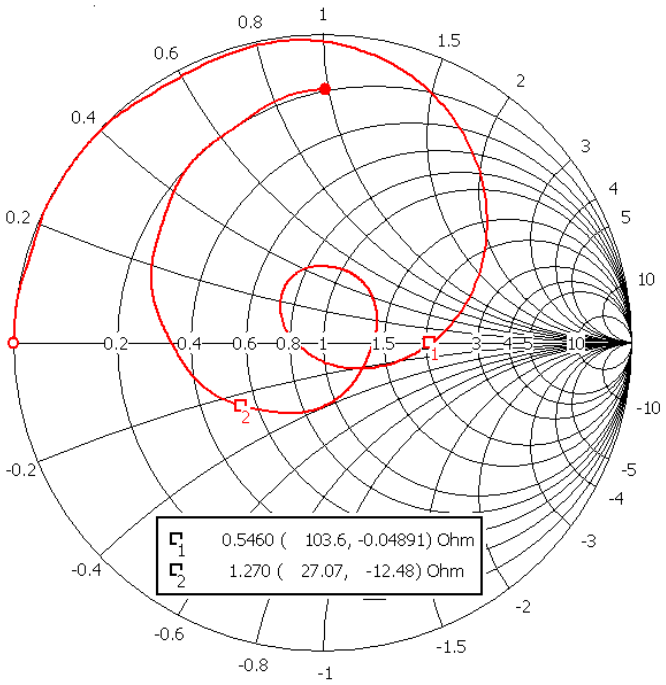

Figure 14. Simulated impedance of the small wideband antenna described in [22].

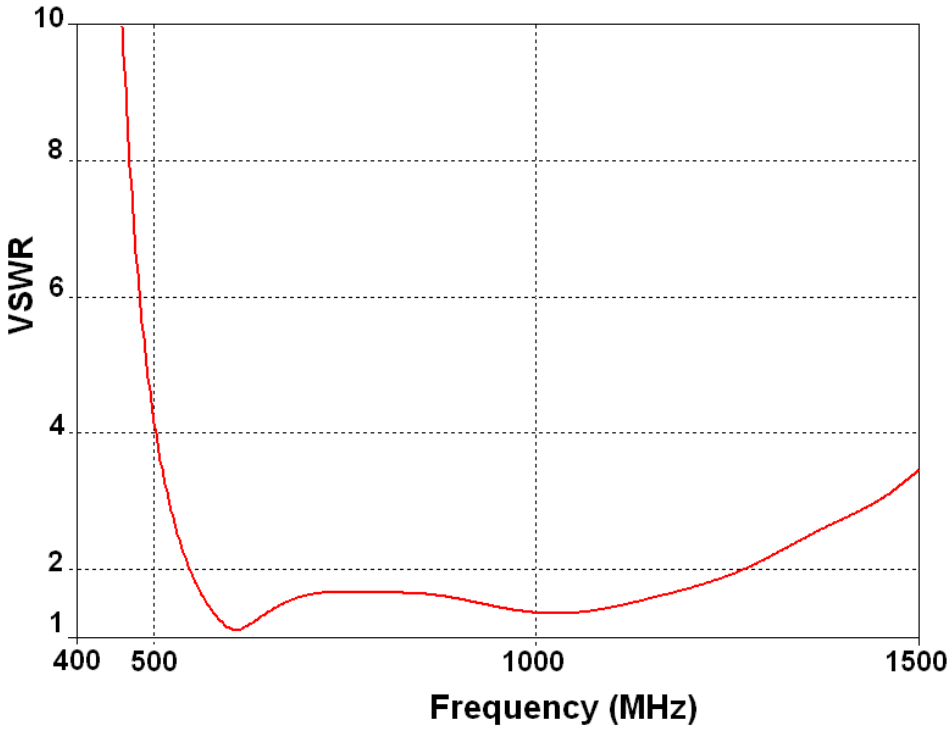

Figure 15. Simulated VSWR of the small wideband antenna described in [22].

The approach used in the design of this antenna is similar to that used in the design of the Friedman antenna. The design begins with a central symmetric structure and top-hat to achieve a lower resonant frequency than achievable with a thin, straight-wire monopole of the same height. The beginning structure and its impedance are presented in Figures 16 and 17, respectively. The next step in the design process is to add the shorting posts to the structure to implement double-tuning, which is characterized by the impedance loop shown in Figure 18. The final step in the design process is to add parallel capacitance to the structure to move the impedance loop to the center of the Smith chart as shown in Figure 14. The parallel capacitance is added using the wide, vertical plates shown in Figure 19. No attempt has been made to modify the design to achieve the same lowest operating frequency of the Goubau antenna.

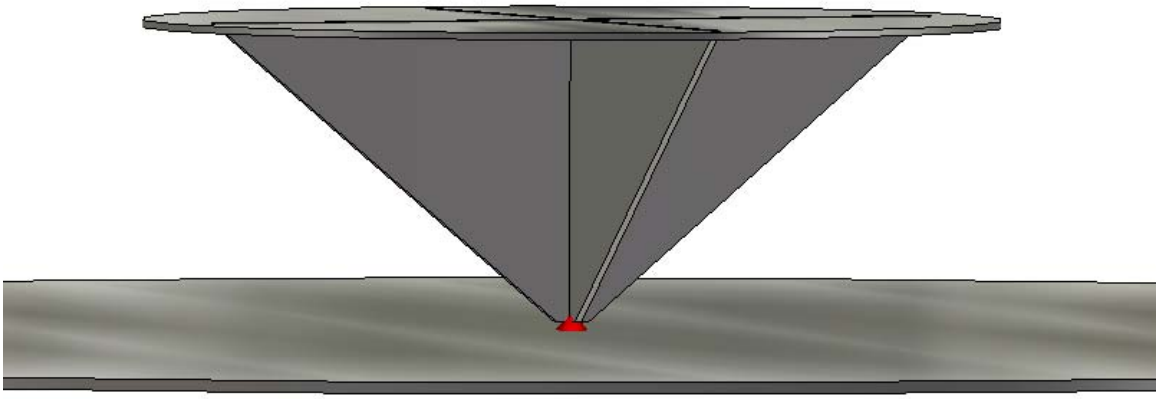

Figure 16. Beginning antenna structure of the small wideband antenna described in [22].

The next antenna considered is the wideband antenna designed by C. B. Ravipati [23]. This antenna, shown in Figure 20, also has the same dimensions as the Goubau antenna. Its VSWR (simulated and measured) and impedance (simulated) are shown in Figures 21 and 22, respectively. Considering the measured VSWR and ignoring the very narrow frequency range at the low end of the band where the VSWR is just over 2:1 (actually 2.07:1), the operating band covers a frequency range of 547 - 2603 MHz, a 4.76:1 frequency bandwidth. At 547 MHz, the value of *ka* is 0.86. The value of CF for this antenna is 10.7, almost matching that of the Goubau antenna.

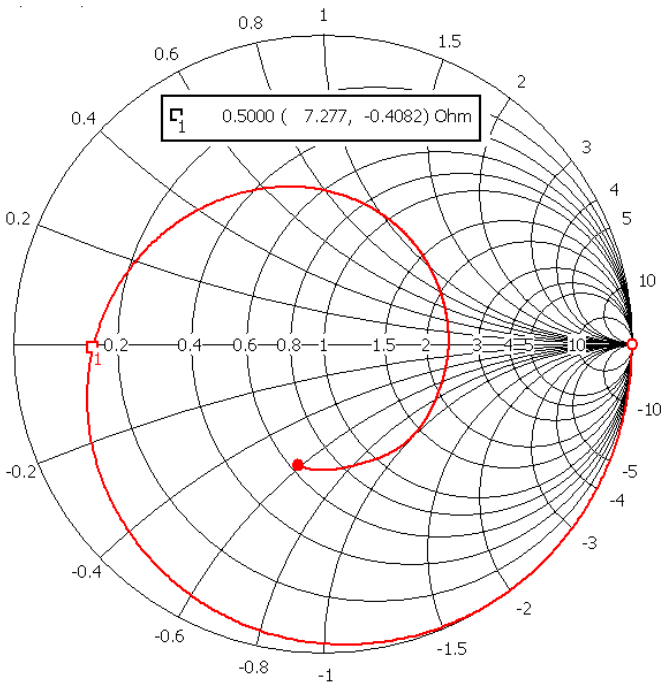

Figure 17. Simulated impedance of antenna shown in Figure 16.

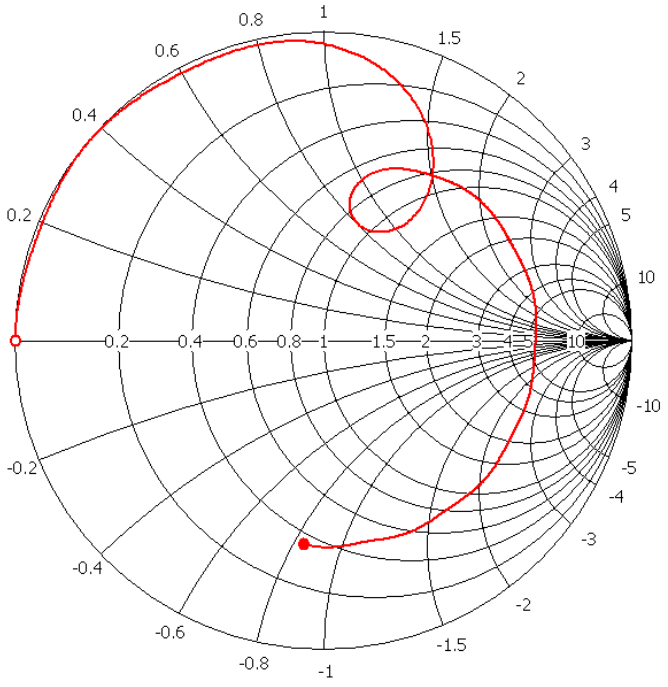

Figure 18. Simulated impedance of antenna shown in Figure 16 with the shorting posts added between the top-hat and the ground plane (see Figure 13).

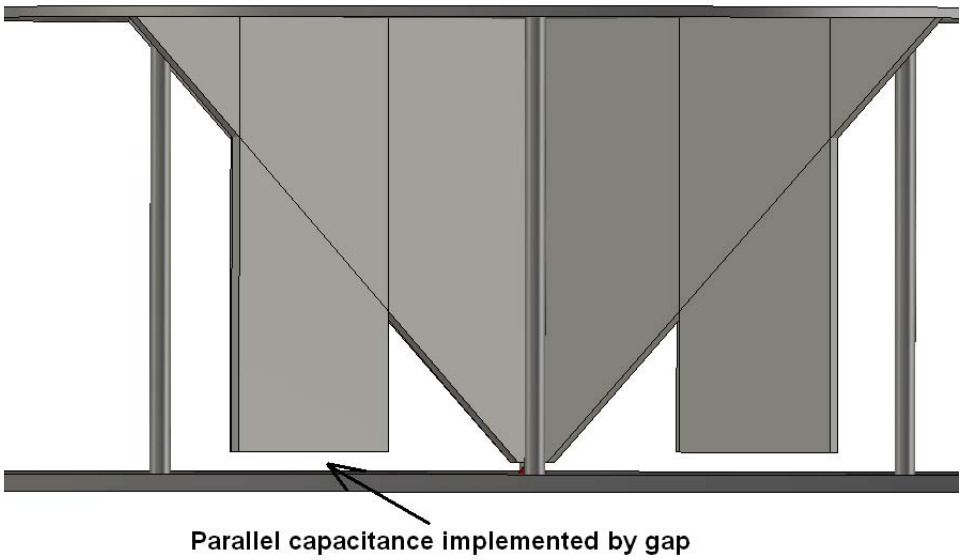

Figure 19. Illustration of how the parallel capacitance is added to the antenna structure to move the impedance loop to the center of the Smith chart.

The difference in CF value between the Ravipati and Goubau antennas raises two issues: 1) is the relative difference in the CF values meaningful, since in this case it implies that the Goubau antenna is slightly better in terms of its bandwidth-to-size ratio, and 2) if the Ravipati antenna were modified to begin operating at approximately 490 MHz or lower, would it achieve more or less bandwidth than the Goubau antenna? The question raised is whether the larger electrical size of the Ravipati antenna is fundamentally necessary to achieve the much wider bandwidth? Answering these questions is necessary to understanding the advantages of the Ravipati design versus the Goubau design. These questions are currently being addressed and are not considered further here. In many practical applications, the bandwidth-size trade-off with the Ravipati antenna (a larger antenna with more bandwidth) is an acceptable design compromise.

An important characteristic of the Ravipati antenna to consider is the multiple-tuning that occurs in the impedance match as shown in Figure 22. The previous antennas considered had a double-tuned impedance match, characterized by a single loop in the impedance curve. The Ravipati antenna has two loops in the impedance curve. The design approach with the Ravipati antenna is similar to that of the previous designs in that it begins with a central symmetric structure and a top-hat for capacitive loading. The next step in the design process is different in that the antenna configuration is not optimized for double-tuned matching, rather it is optimized for multiple-tuning.

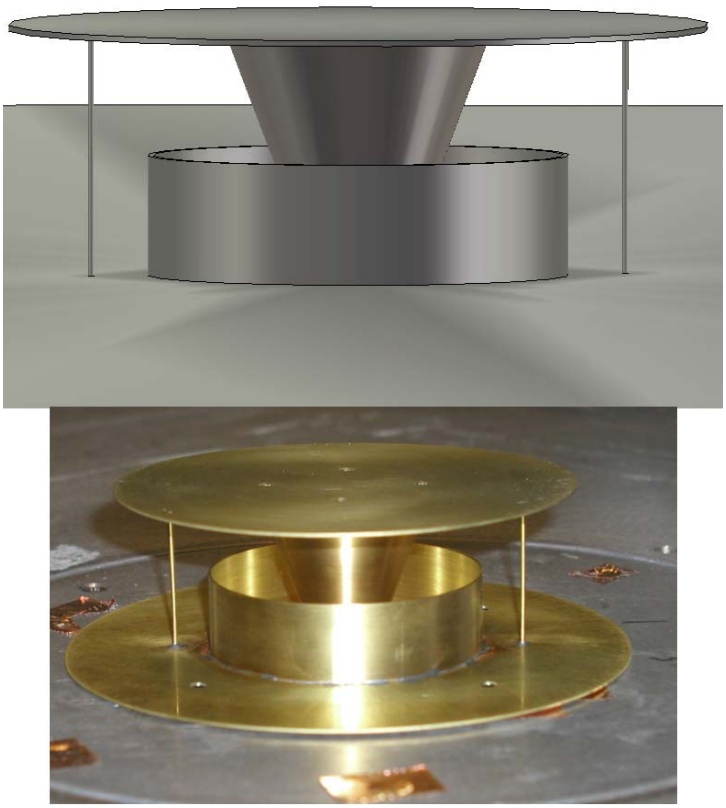

Figure 20. The Microwave Studio model and fabricated version of the Ravipati antenna. The antenna has a height of 4.3 cm and a diameter of 12.3 cm.

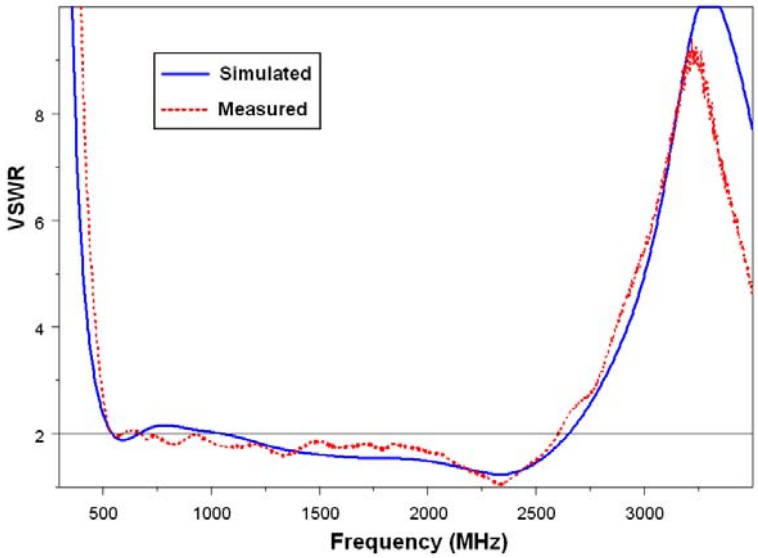

Figure 21. Simulated and measured VSWR of the Ravipati antenna.

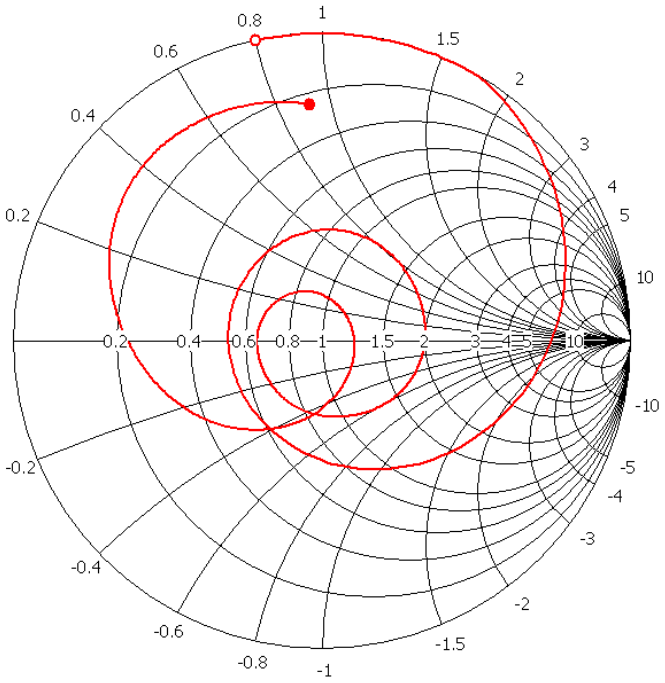

Figure 22. Simulated impedance of the Ravipati antenna.

Since the central conical body-of-revolution (BOR) structure is solid, it provides additional parallel capacitance so that when the two shorting posts are added, the double-tuned impedance is centered on the Smith chart but the impedance is not well matched. The impedance of the antenna without the short cylindrical sleeve is shown in Figure 23. The frequency range encompassed by the double-tuned impedance loop is approximately 460 – 1500 MHz. The further addition of the cylindrical sleeve provides the multiple-tuned impedance match that is shown in Figure 22.

From another perspective, the cylindrical sleeve can be added to the central conical body-of-revolution and top-hat structure, implementing double-tuning at a higher frequency. The impedance of the Ravipati antenna without the shorting posts is shown in Figure 24. The frequency range of the double-tuning is approximately 940 – 2890 MHz. The further addition of the shorting posts provides the multiple-tuned impedance match that is shown in Figure 22.

The design of this antenna is achieved using two double-tuning "circuits" that are together optimized to achieve the desired impedance match. Since the tuning circuits are coupled they must be designed together in order to implement the final match. The variables include the location and diameter of the shorting posts and the location and height of the cylindrical sleeve.

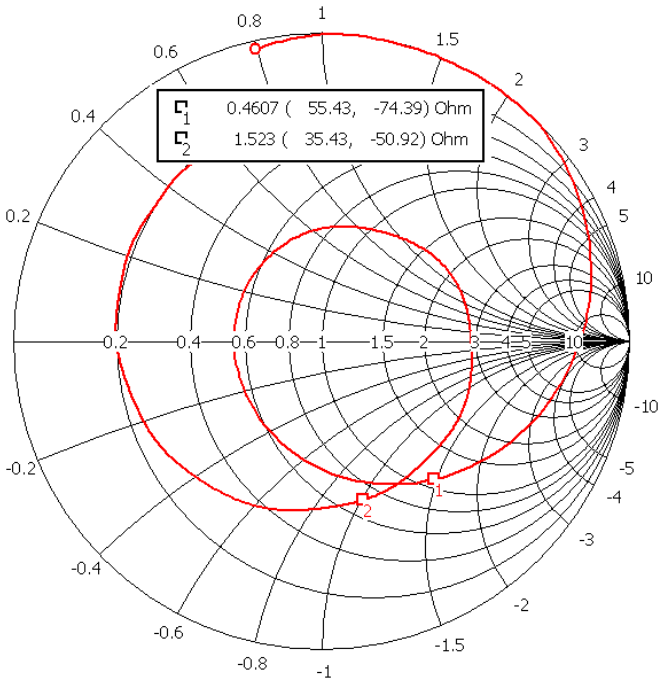

Figure 23. Simulated impedance of the Ravipati antenna without the cylindrical sleeve.

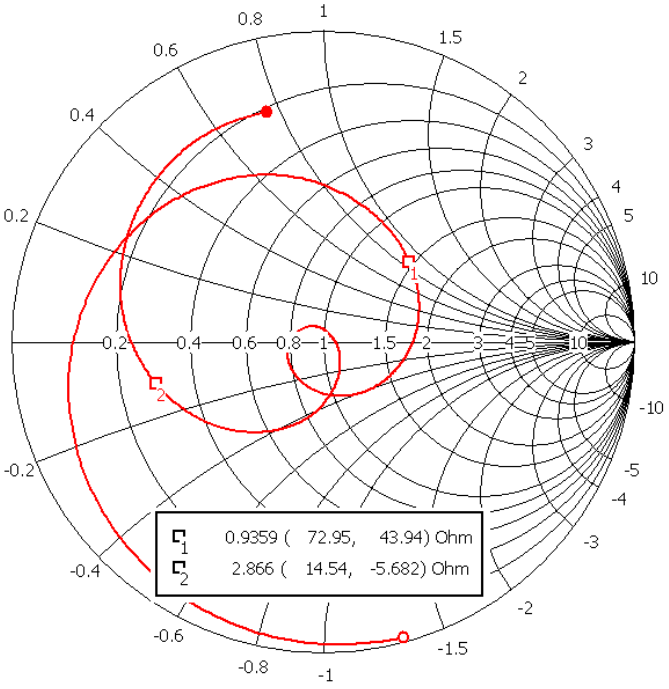

Figure 24. Simulated impedance of the Ravipati antenna without the shorting posts.

The final antenna considered was recently presented by Nakano et al [24]. It is a wideband antenna described as consisting of a conducting body of revolution and a shorted parasitic ring. The antenna is shown in Figure 25. In [24], the antenna was designed to operate from approximately 2 – 15 GHz. Here, the antenna was scaled to have the same overall height of the Goubau antenna, 4.3 cm. It has an overall cylindrical diameter of 17.2 cm, substantially larger than that of the Goubau antenna. The length-to-diameter ratio of the antenna is 0.5. The antenna's VSWR and impedance are presented in Figures 26 and 27, respectively. The impedance is shown for a frequency range of 500 - 5000 MHz.

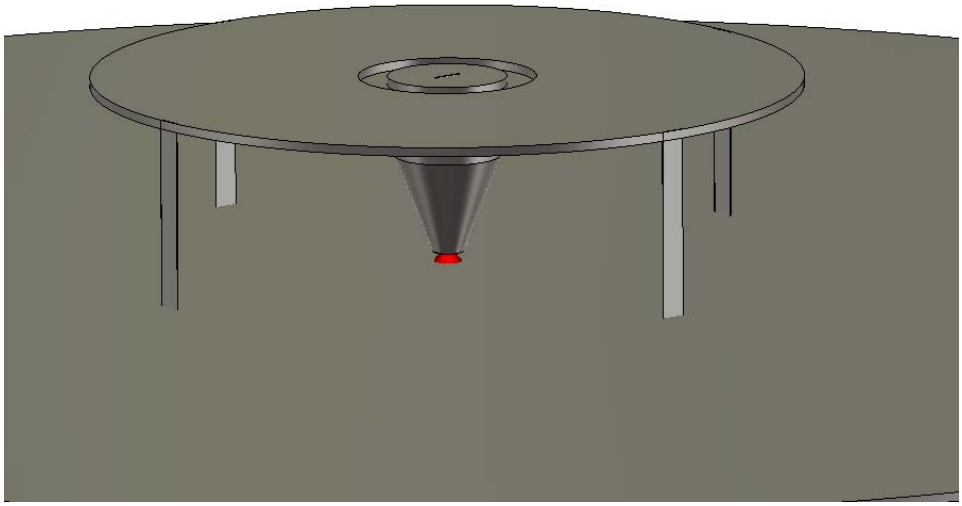

Figure 25. The Microwave Studio model of the Nakano antenna.

The simulated VSWR is presented for a frequency range of 400 – 5000 MHz. The antenna first exhibits a 2:1 VSWR at a frequency of 490 MHz, consistent with the lowest operating frequency of the matched Goubau antenna. The VSWR curve shows several frequency regions where the VSWR is slightly greater than 2:1. This is consistent with the measurement data presented in [24]. If this is ignored and the operating band is defined as 490 – 5000 MHz, the operating bandwidth of the antenna is approximately 10.2:1. At the lowest frequency, the value of *ka* is 0.99. The CF value for this antenna is 21.2, almost twice that of the Goubau antenna. This implies that this antenna is a better design in terms of the bandwidth-to-size ratio. Again, this raises the issue of the validity and practical value of the CF values determined here. To resolve any issue regarding the CF values, all of the designs considered should be optimized where all have the same physical dimensions and where they are all matched at the same lowest frequency. This is an effort currently being pursued.

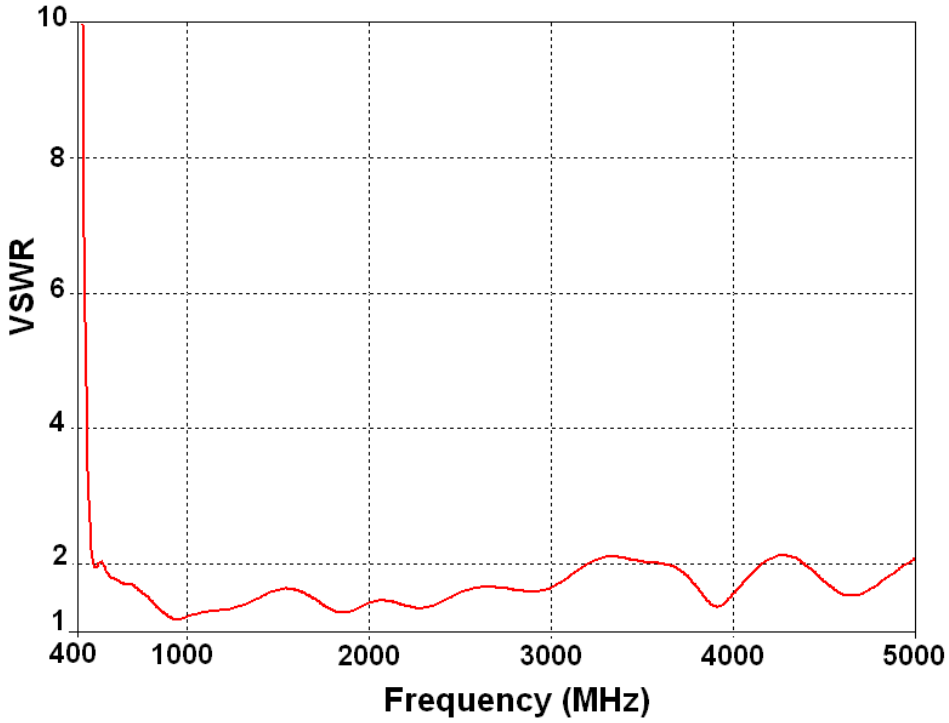

Figure 26. The simulated VSWR of the Nakano antenna.

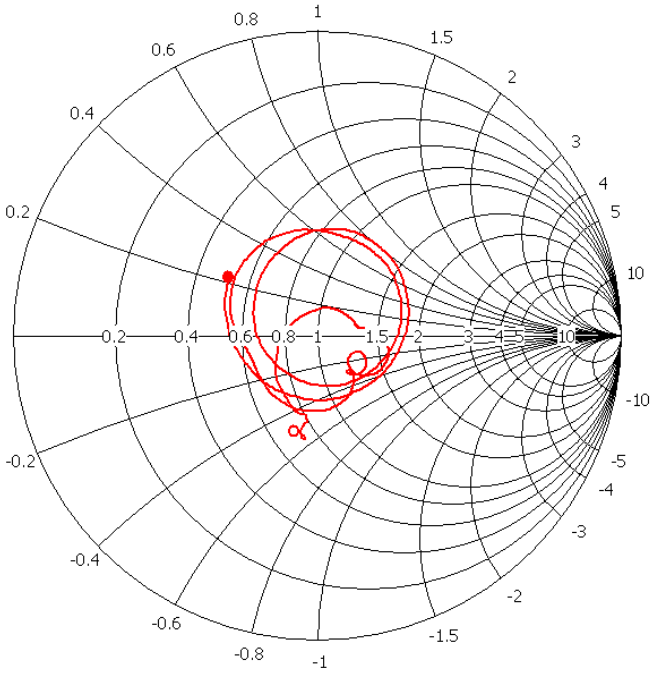

Figure 27. The simulated impedance of the Nakano antenna over a frequency range of 500 - 5000 MHz.

The design of the Nakano antenna follows a similar approach used with the other antennas in that it begins with a central structure and top-hat. The design continues with the inclusion of the shorting posts and the gap in the top-hat. The impedance of the central support structure and the solid top-hat is shown in Figure 28. Up to 2 GHz, the impedance of the basic structure is similar to that of the other antennas. Above 2 GHz, the impedance is nearly centered on the Smith chart and it exhibits an impedance loop, consistent with that of double-tuning, from 4 - 5 GHz. The other antennas were not characterized in this frequency range at this point, so relative comparisons cannot be made.

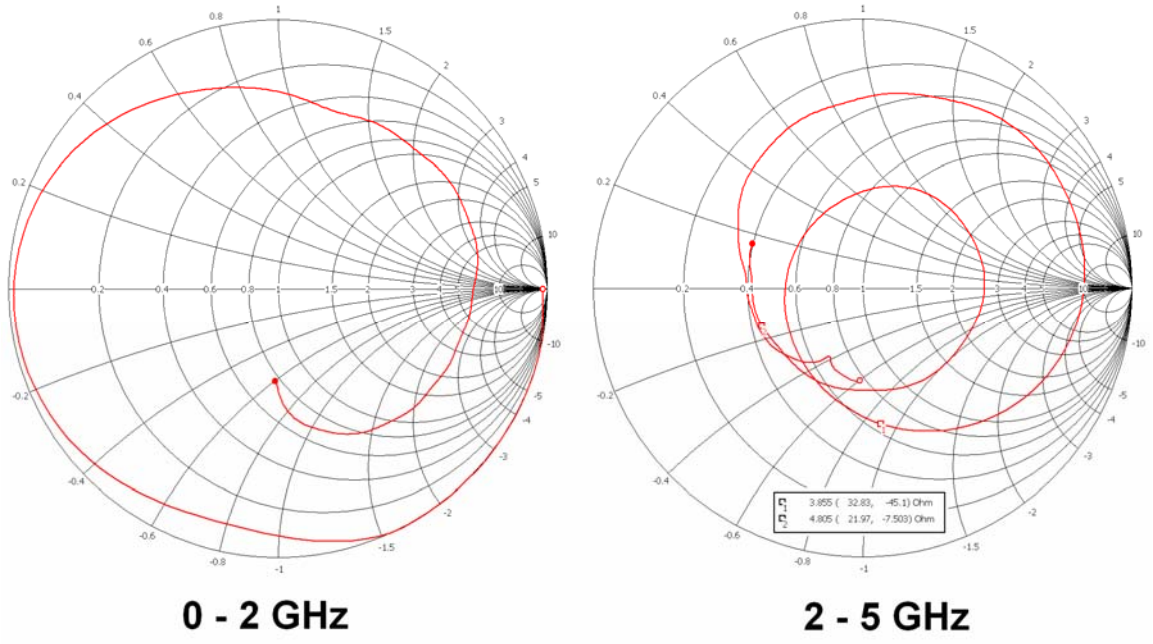

Figure 28. The simulated impedance of the basic structure of the Nakano antenna up to 5 GHz.

The next issues considered are the design effects of the shorting posts and the gap in the top-hat. The impedances of the Nakano antenna without the gap in the top-hat (showing the effects of the shorting posts) and without the shorting posts (showing the effects of the gap) are shown in Figures 29 and 30, respectively. With only the shorting posts included in the design, an impedance loop, consistent with double-tuning, forms over a frequency range of approximately 500 - 1000 MHz. This is similar to the other antennas but with slightly wider bandwidth. The shorting posts also have an impact on the upper frequencies, improving the impedance match over the range of the impedance loop that exists near 4 GHz.

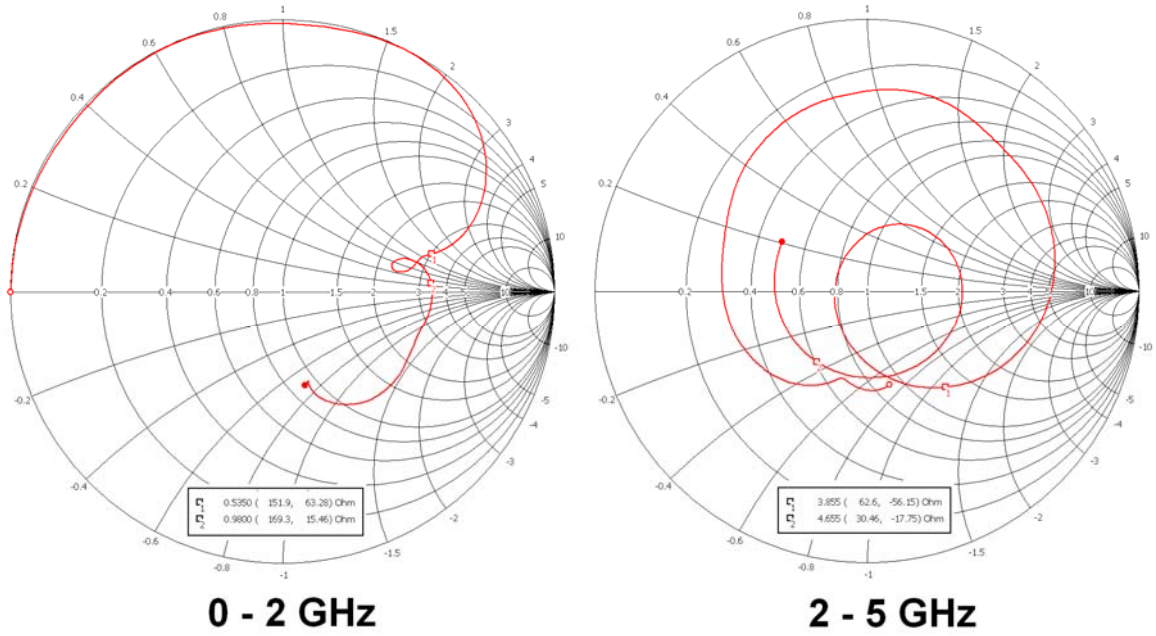

Figure 29. The simulated impedance of the Nakano antenna with the gap in the top-hat removed to illustrate the effect of the shorting posts.

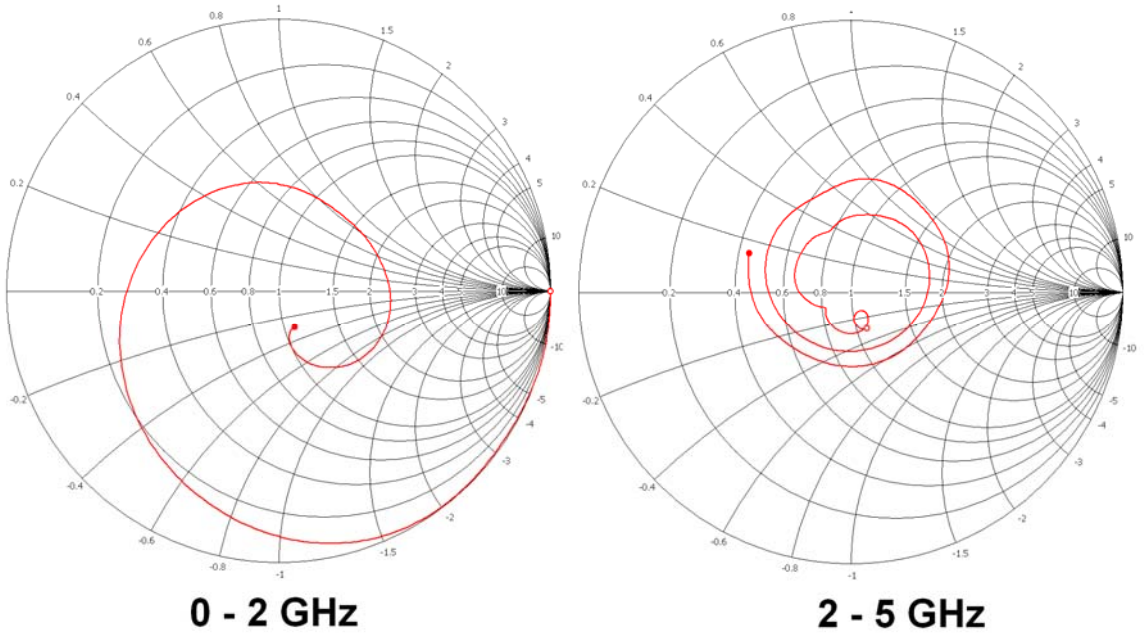

Figure 30. The simulated impedance of the Nakano antenna with the shorting posts removed to illustrate the effect of the gap in the top-hat.

With only the gap in the top-hat included in the design, there is only a marginal effect on the antenna's impedance below 2 GHz. There is a significant effect on the impedance above 2 GHz, where the impedance is essentially matched up to 5 GHz. This illustrates that the shorting posts are significant to the overall impedance match below 2 GHz and the gap in the top-hat is significant to the overall impedance match above 2 GHz. However, the effects of the shorting posts and the gap in the top-hat are not mutually exclusive. Both effect the impedance over the entire range of frequencies from 490 - 5000 MHz and both must be optimized together to implement the desired impedance match over the entire operating band.

The final point addressed is the effect of reducing the diameter of the Nakano antenna to match that of the Goubau antenna. The resulting VSWR is presented in Figure 31. The antenna exhibits a wide bandwidth, operating from approximately 663 MHz to over 5 GHz. There are regions in the operating band where the VSWR slightly exceeds 2:1. The value of CF for this smaller version of the Nakano antenna is 13.3 just slightly higher than the CF value of the Goubau antenna. Again, a fairer comparison would occur if the lowest operating frequency of this antenna were set to match that of the Goubau antenna.

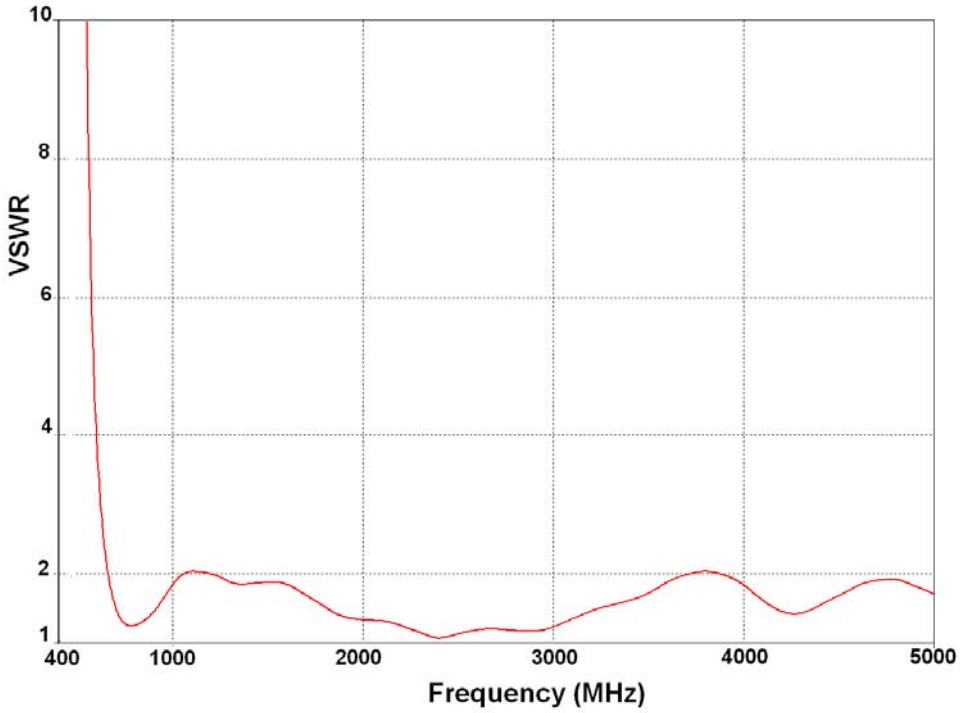

Figure 31. The simulated VSWR of the Nakano antenna having the same overall diameter as the Goubau antenna.

5. Higher Order Modes

In the design of the Goubau, Friedman and Ravipati antennas, one of the primary objectives was to maintain fundamental monopole patterns over the entire operating band. Meeting this objective is a factor limiting the bandwidth of the antenna. If higher-order modes are created and exhibit substantial radiation, the operating bandwidth of the antenna can be increased. This was demonstrated with an asymmetric design described in [22].

The radiation patterns of the Goubau and the Ravipati antennas at the highest frequency in their operating band are presented in Figure 32. An infinite ground plane is assumed. The Goubau antenna is omnidirectional to within ±0.3 dB, while the Ravipati antenna is omnidirectional to within ±2.8 dB. The Ravipati antenna would exhibit improved omnidirectionality if 4 shorting posts were used in the design rather than 2.

Radiation patterns of the Nakano antenna are presented in Figure 33 for 2.45 GHz and 4.95 GHz. At 2.45 GHz the Nakano antenna is omnidirectional to within ±1.1 dB. At 4.95 GHz it is omnidirectional to within ±4.5 dB. At 4.95 GHz, the pattern peak does not occur at the antenna horizon.

Ultimately, the design objective for the small wideband antenna is to achieve as low an operating frequency as possible, maximum bandwidth and fundamental monopole patterns over the entire operating band.

6. Discussion

In this paper, the design of several wideband antennas was considered. The antennas presented here included the Goubau antenna, the Friedman antenna, the Ravipati antenna, the Nakano antenna and an antenna designed by the author. The basic structures of these antenna were considered in detail and features within the antennas necessary to achieve an impedance match over a wideband were discussed. At the most fundamental level, all of the antennas are designed using similar principles.

A numerical comparison factor was introduced to compare the bandwidth of the antennas in relation to their electrical size at the lowest operating frequency. The validity of this comparison is, in the author's opinion, questionable. In order to validate the value of the comparison factor, and the relative merit of the designs considered here, each should be limited to the same physical dimensions and be required to exhibit the same lowest operating frequency. This is an effort that is currently underway.

From an engineering perspective, the effects of inclusions within the antenna structure were considered. It was demonstrated that the effects of the inclusions on the antenna's impedance are not mutually exclusive and that the each must be optimized

simultaneously in order to achieve the desired bandwidth. Finally, as one would expect, antennas with larger physical volume are capable of achieving wider impedance bandwidths.

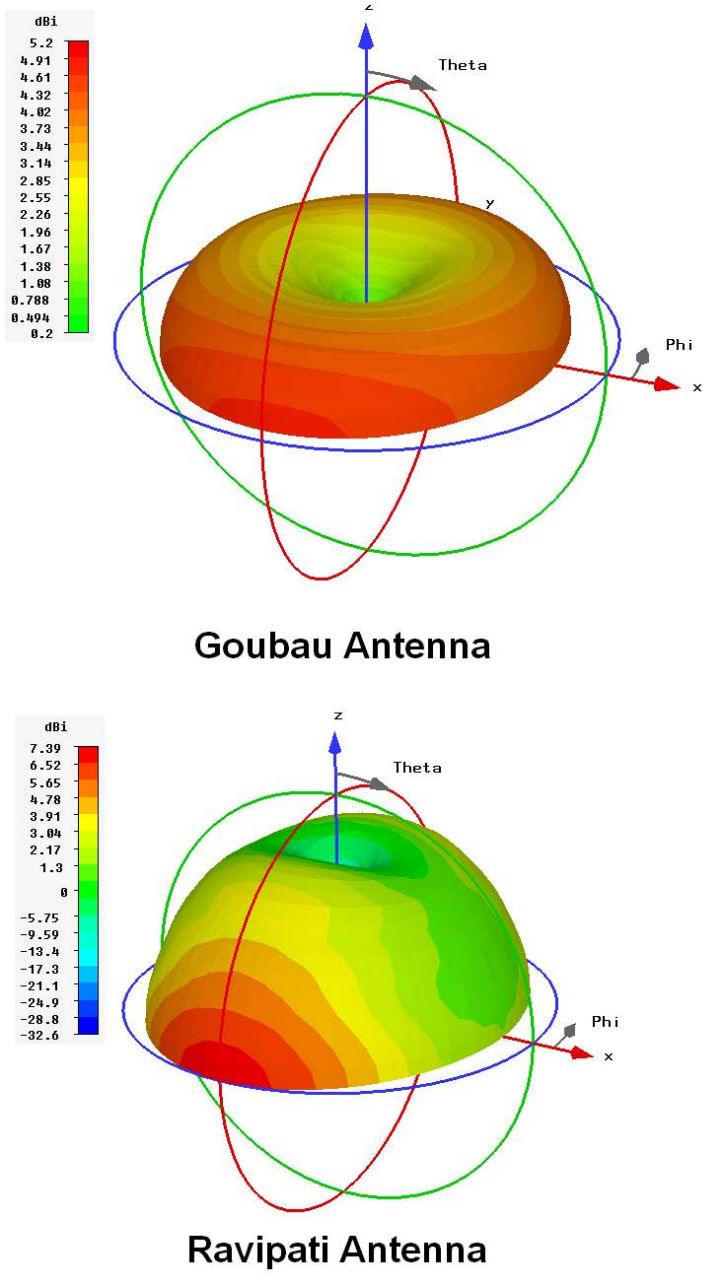

Figure 32. Radiation patterns of the Goubau and Ravipati antennas at the highest frequency in their operating band.

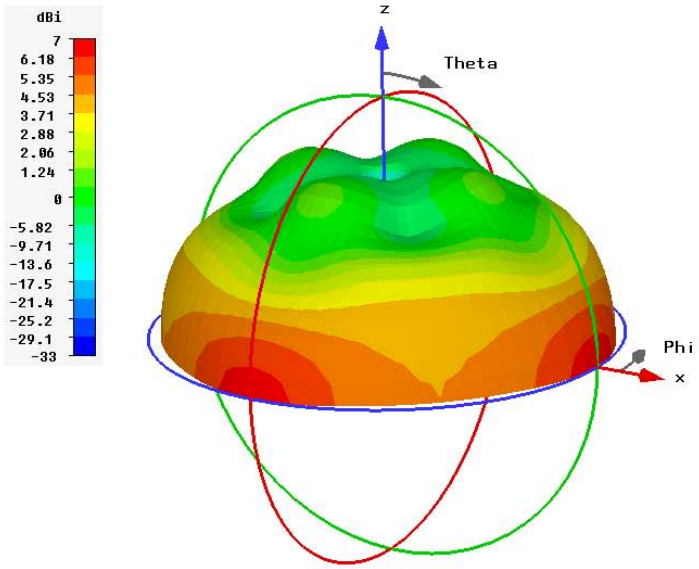

2.45 GHz

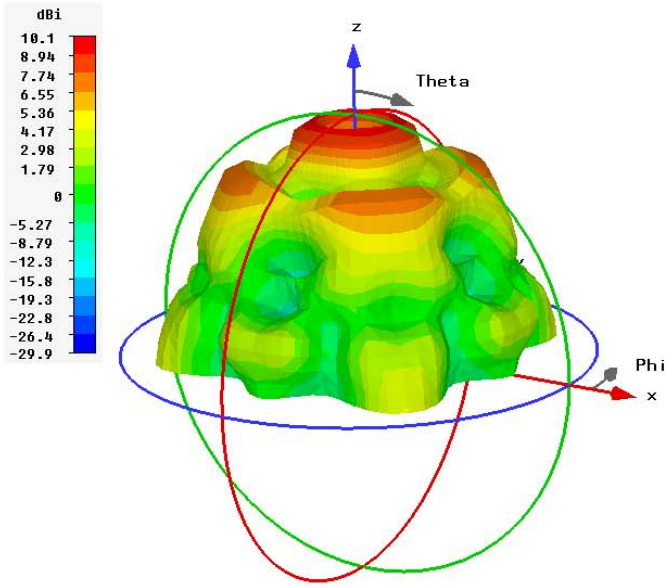

4.95 GHz

Figure 33. Radiation patterns of the Nakano antenna at 2.45 and 4.95 GHz.

7. References

[1] H. A. Wheeler, “Fundamental limitations of small antennas,” *Proceedings of the IRE*, Vol. 35, pp. 1479-1488, Dec. 1947.

[2] L. J. Chu, "Physical Limitations on Omni-Directional Antennas," *J. Appl. Phys.*, Vol. 9, pp. 1163-1175, 1948.

[3] J. S. McLean, “A Re-Examination of the Fundamental Limits on the Radiation Q of Electrically Small Antennas,” *IEEE Trans. Antennas Propagat.*, Vol. 44, pp. 672-676, May 1996.

[4] A. D. Yaghjian and S. R. Best, “Impedance, Bandwidth and Q of Antennas,” *IEEE Trans. Antennas and Propagat.*, Vol. 53, No. 4, pp. 1298-1324, Apr 2005.

[5] S. R. Best, “The Radiation Properties of Electrically Small Folded Spherical Helix Antennas,” *IEEE Trans. Antennas Propagat.*, Vol. 52, No. 4, pp. 953-960, Apr 2004.

[6] S. R. Best, “Low Q Electrically Small Linear and Elliptical Polarized Spherical Dipole Antennas,” *IEEE Trans. Antennas Propagat.*, Vol. 53, No. 3, pp. 1047-1053, Mar 2005.

[7] H. L. Thal, “New Radiation *Q* Limits for Spherical Wire Antennas,” *IEEE Trans. Antennas Propagat.*, Vol. 54, No. 10, pp. 2757-2763, Oct 2006.

[8] R. C. Adams and P. M. Hansen, “Evaluation of the Minimum Radiation Q for Electrically Small Antennas in Spheroidal Coordinates,” 2008 *IEEE AP-S Symposium*, Paper 110.4, July 2008.

[9] P. M. Hansen and R. C. Adams, “Radiation Q of Practical Electrically Small Cylindrical Antennas as a Function of Aspect Ratio – Comparison to Minimum Q Formulas,” *2008 IEEE AP-S Symposium*, Paper 110.5, July 2008.

[10] M. Gustafsson, C. Sohl, and G. Kristensson, “Physical Limitations on Antennas of Arbitrary Shape,” Lund University Report: LUTEDX/(TEAT-7153)/1-36/(2007), July 2007.

[11] M. Gustafsson, C. Sohl, and G. Kristensson, “Physical limitations on scattering and absorption of antennas,” *Second European Conference on Antennas and Propagation (EuCAP 2007)*, Edinburgh, U.K., November 2007.

[12] R. M. Fano, Theoretical Limitations of the Broadband Matching of Arbitrary Impedances,” *J. Franklin Inst.*, Vol. 249, Nos. 1-2, pp. 57–83 and pp. 139–154, January – February, 1950.

[13] R. C. Hansen, ”Fano Limits on Matching Bandwidth,” IEEE AP Magazine, Vol. 47, No. 3, pp. 89-90, June 2005.

[14] R. C. Hansen, *Electrically Small, Superdirective, and Superconducting Antennas*, John Wiley and Sons, 2006.

[15] H. R. Stuart and S. R. Best, “A Small Wideband Multimode Antenna,” *2008 IEEE AP-S Symposium*, Paper 209.2, July 2008.

[16] H. R. Stuart, S. R. Best, and A. D. Yaghjian, “Limitations in Relating Quality Factor to Bandwidth in a Double Resonance Small Antenna,” *IEEE Ant. Wireless Prop. Lett.*, Vol. 6, pp. 460-463, 2007.

[17] G. Goubau, "Multi-element monopole antenna," *Proceedings of the ECOM-ARO Workshop on Electrically Small Antennas*, Fort Monmouth, NJ, pp. 63-67, October 1976.
[18] G. Goubau, N. N. Puri and F. Schwering, "Diakoptic theory for multielement antennas," *IEEE Trans. Antennas Propag.*, Vol. 30, No. 1, pp. 15-26, January 1982.
[19] C. H. Friedman, "Wide-band matching of a small disk-loaded monopole," *IEEE Trans. Antennas Propag.*, Vol. 33, No. 10, pp. 1142-1148, October 1985.
[20] Microwave Studio, www.cst.com
[21] H. A. Wheeler, "Small Antennas," *IEEE Trans. Antennas Propag.*, Vol. 23, No. 4, pp. 462-469, July 1975.
[22] S. R. Best, "Progress in the Design of a Small Wideband Antenna," *2006 Antenna Applications Symposium*, Monticello, IL, September 2006.
[23] C. B. Ravipati, *Private Communications*, 2006 – 2008.
[24] H. Nakano, H. Iwaoka, K. Morishita, and J. Yamauchi, "A Wideband Low-Profile, Antenna Composed of a Conducting Body of Revolution and a Shorted Parasitic Ring," *IEEE Trans. Antennas Propag.*, Vol. 56, No. 4, pp. 1187-1192, April 2008.